Diffuse Fe-Kα line emission tracing the recent history of our Galactic Centre

Renzo Capelli

SIGILL. UNIVERSITAT. LUDOVIC. MAXIM.

München 2011

Diffuse Fe-Kα line emission tracing the recent history of our Galactic Centre

Renzo Capelli

Dissertation
an der Fakultät für Physik
der Ludwig–Maximilians–Universität
München

vorgelegt von
Renzo Capelli
aus Bergamo, Italy

München, den 21. Oktober 2011

Erstgutachter: Prof. Dr. Werner Becker
Zweitgutachter: Prof. Dr. Thomas Preibisch
Tag der mündlichen Prüfung: 02. Dezember 2011

To my parents, Gisella and Andrea,
my grandmother Olga,
and to the dearest memory of my grandfather Renzo.

Contents

List of Figures

List of Tables

Summary

The centre of the Milky Way is populated by what is reasonably considered the most interesting and puzzling astrophysical object, a supermassive black hole (SMBH). Such SMBHs appear to occupy the centres of most galaxies. The radiative counterpart of the SMBH in the Galactic Centre (GC), known as Sgr A*, is unusually dormant compared to other detected radiatively emitting black holes, with a total luminosity of about 10^{-8} its Eddington limit. Over the years, scientists have been trying to unveil the mystery of this low activity in Sgr A*. An important piece of the puzzle is to uncover the history (recent and less recent) of our own Galaxy, in order to discover if Sgr A*'s dormant nature is usual, or if it has perhaps been brighter in the past. However, observations of the Galactic Centre, despite its proximity, are not straightforward because of the eight kiloparsec thick blanket of diffuse radiation and interstellar matter in the line of sight.

The first observation to present evidence for past high activity of the SMBH in the GC was the discovery of fluorescent emission from neutral Fe within the massive molecular complexes which lie in the central molecular zone (CMZ), a layer of molecular material distributed along the galactic plane in the inner 200 parsec of the Galaxy. This fluorescence is observed in the standard X-ray energy band, at 6.4 keV. The first detection was made only in 1994, when the newly launched Japanese X-ray observatory ASCA first observed the Galactic Centre. Immediately after the discovery of the Fe-Kα line emission, it was interpreted as the fluorescence echo of past (few hundred years ago) high energy activity of Sgr A*. The atoms which produce the fluorescent line X-ray photons are ionised in this scenario by X-ray photons propagating towards the cloud from Sgr A* (or other putative source), and therefore the cloud itself is generally referred to as an X-ray Reflection Nebula (XRN). The first measurements of the 6.4-keV line flux from the first XRN discovered in the GC region (Sgr B2 and Sgr C) immediately revealed that this line emission is unlikely to be produced by other sources than Sgr A*, given that the X-ray luminosity required to produce the observed fluorescent photons was too high to be attributed to other X-ray sources (e.g., X-ray binaries and supernova remnants).

In the last decade, XRN all over the inner CMZ have been proposed to be the actual *smoking gun* of the past low AGN activity of Sgr A*, which is suspected to have undergone a flare about 10^4 times brighter than the brightest flare ever measured ($L_X \sim 10^{35}$ erg s^{-1}). This enhanced X-ray activity must have left a trace in the diffuse emission permeating the GC region, especially in the ionisation of molecular clouds (MCs) in the CMZ seen through the Fe fluorescent line at 6.4 keV, and the Thomson-Compton scattering of hard

X-rays into the line of sight by the MCs. The picture is however still unclear and partly confusing, since energetic phenomena associated with the particle bombardment of a MC can also produce a detectable Fe-Kα line emission. This thesis work strives for a complete and consistent picture of the recent history of the SMBH Sgr A* through the study of the spectral and timing properties of the XRN in the GC region. Nowadays, among the biggest challenges in the study of the GC is the confirmation of the reality of past AGN activity of Sgr A*, which could open new exciting horizons on the study of Galactic formation and evolution.

This thesis work is essentially derived into two parts: in the first three Chapters we will introduce the reader to the subject of the work, the phenomenology of the X-ray emission by neutral Fe from MCs in the GC region, whereas in the Chapters 4 to 6 we will present the work carried out during the doctoral studies and published in international Journals of Astrophysics.

In Chapter 1 we are going to discuss in detail the physics of the interstellar medium (ISM), focussing on the molecular phase. We briefly describe the physical properties of the gaseous phases of the ISM and how they were discovered, introducing the observational techniques which have been developed to detect and study them. Since this thesis work is mainly devoted to the study of the XRN in the GC region, we will discuss in detail the physics and phenomenology of the molecular phase of the ISM, aiming at showing the strong peculiarity of the CMZ, where the most massive clouds are found to be highly shocked and far from virialised; basically, the GC is a highly turbulent region, where highly energetic phenomena interplay with one another to continuously influence the physical conditions of this peculiar environment.

The second subject of Chapter 1 is the phenomenology of cosmic rays (CR); in fact, these highly energetic charged particles are of great importance to the ionisation of molecular clouds. We are going to introduce the reader to the aspects of the CR physics which are also relevant for our work, these being their composition, energetics, energy spectrum and acceleration mechanisms. We will also briefly present two of the most important observations which led to the discovery that the GC region is populated by CR in all forms and energies (at least up to 10^{15} GeV); *i.* the discovery of bright radio filaments and threads running perpendicular to the galactic plane, strong evidence of the higher concentration of CR electrons with GeV energies interacting with strong magnetic fields (B$\sim$mG), and *ii.* the discovery of TeV diffuse emission resembling the distribution of the molecular material in the innermost $\sim$200 pc of the Milky Way, which showed that the CMZ is filled with a recently accelerated component of hadronic (i.e. protons) CR. Sub-relativistic CR electrons and protons are of extreme interest for the topic of our thesis work because they might be a significant source of ionisation for the neutral gas populating the innermost CMZ.

To conclude Chapter 1, we will give a brief introduction to the object that might turn to be the main character of all the story we are going to tell: the SMBH Sgr A*; in fact, we will first summarise the history of discoveries which led to the firm evidence that the GC is populated by a SMBH with a mass of $\sim 4\times10^6 M_\odot$, and later discuss its broad band (radio to X-ray) emission and the phenomenology of the currently observed infrared and

X-ray flares.

It is important to comment that the three subjects of this first Chapter are not lonely characters playing their own part on an empty stage, but they are instead dynamic entities which together contribute to create and shape the structure of the entire GC region and its phenomenology.

In Chapter 2 we will concisely review the physics of ionisation. First, we give a brief introduction to the element which is subject of our thesis, iron; in fact, this is the element which better traces the ionisation products because of the combination of high fluorescence yields and cross section for bound-free absorption. We are going to describe the ionisation process in the context of the atomic structure of Fe, giving a particular emphasis to the two mechanisms through which the Fe atom can relax after losing an electron from the inner K shell, fluorescence and emission of an Auger electron. Fluorescence is an efficient relaxation mechanism for heavier elements ($Z \gtrsim 40$, among which is iron), whereas the emission of an Auger electron is more likely for light elements. Since the Fe-Kα is a fluorescent line, in Chapter 2 we will describe the physics of Fe ionisation, focussing on the phenomenology of the 6.4-keV line and the reflected continuum: these are indeed the most important quantities to characterise the ionisation process at the origin of the Fe-Kα line emission. A further topic of our discussion is the physics of the XRN; we are going to present the calculations which led to hypothesis that Sgr A* is the putative illuminating source at the origin of the XRN in the CMZ, together with the results of some simulations performed by Sunyaev & Churazov (1998) which are relevant for our work, since they show the surface brightness distribution of the 6.4-keV line emission as expected in different configurations of the source-cloud-observer geometry.

The second part of Chapter 2 is devoted to the other physical mechanism which can produce Fe fluorescence, namely particle bombardment. We will show that the stopping range for electrons and protons (i.e. the column density they have to cross to come at rest given a certain initial kinetic energy) are significantly different, the one for protons being about two orders of magnitude higher; this feature contributes to make bombardment by protons more efficient than the electronic one in producing steady and diffuse 6.4-keV line emission.

To conclude, we will describe the theory and phenomenology of the electron and proton bombardment of a cold absorbing medium, depicting the features that arise in the X-ray spectra of particle-illuminated molecular clouds; we will also emphasise the shapes and strengths of the cross sections of each of the two processes.

Chapter 3 is devoted to the phenomenology of the diffuse X-ray emission which is observed throughout the whole GC region; this is basically given by the contribution of three different components, which we call warm plasma, hot plasma and non-thermal X-rays. Each component has its own tracer and all three can be simultaneously studied in a typical spectrum of the diffuse X-ray emission from the CMZ; after introducing the physical parameters of the two thermal plasmas, which have typical temperatures of about 1 keV and 6.5 keV respectively, together with their energetics and the possible contributors to this diffuse emission, we will mainly focus on the third component, whose tracer is the subject of this thesis work, i.e. the Fe-Kα line at 6.4 keV. We are going to describe the close connection between the Fe fluorescent line and the non-thermal continuum, particularly a recent theory which proposed this continuum emission to be due to a stellar accretion event onto the SMBH Sgr A*, thus releasing a huge amount of energy in the form of sub-relativistic protons with kinetic energies up to hundreds of MeV; this theory provides a very efficient mechanism to produce both the continuum and, in part, the 6.4-keV line emission.

The second part of Chapter 3 is entirely dedicated to the history of the discoveries related to the topic of this thesis which have been achieved in the last ~15 years; we divided this temporal window in three parts which resemble the three different epochs of scientific research related to the nature of the XRN in the CMZ and the possible connection with the past low AGN activity of Sgr A*. We divided this time window into three different epochs describing the *status quo* of the field, i.e. the achievements that have been reached before my doctoral work has been carried out; it is interesting to see that the nature of the ionising source of the XRN in the innermost ~30 pc of the Galaxy has for a long time been debated, and specifically that the most likely source has been thought to be, from time to time, Sgr A*, low energy CR (mainly electrons), and finally back again to Sgr A*.

Chapter 4 is the first Chapter presenting the results of our doctoral research. In particular it shows the results of the studies we have been carrying out on the XRN closest to the position of Sgr A*, using the large dataset of XMM-Newton data targeted at the GC. In terms of time, this are the last results that we have achieved in our research, which resulted in a paper to be submitted soon to the Astronomy & Astrophysics Journal. We have studied the temporal variability and the spectral features of the Fe-Kα line in several molecular clouds which lie in the inner ~30 pc of the Galaxy (in projection). Previous studies of these clouds only based on the temporal variability of the 6.4-keV line have built a model for the illumination scenario in which Sgr A* is the primary source of ionisation for all the XRN in the GC region; as such, its X-ray luminosity should have been constant for more than 200 years at a level of a few 10^{39} erg s^{-1}, about 10^4 times brighter than the brightest flares ever measured (which have an averaged duration of about 1 hour). The main motivation of our work is to study, with much deeper insight, the ionisation processes working in these molecular clouds, particularly the spectral parameters which are the tracers of a plausible past illumination, namely the equivalent width of the Fe-Kα line measured in the X-ray spectra of the clouds and the absorption feature imprinted in the reflected continuum at the characteristic energy of the Fe-K edge (7.1 keV). These spectral parameters are intimately related to each other and to the ionisation process, and cannot be disregarded in the attempt to model the past high energy activity of the putative illumination source.

Furthermore, there are two tricky parameters which must be considered when attempting to reproduce the temporal behaviour of the ionising source and the three dimensional distribution of the clouds in the CMZ: the column density of the molecular cloud and its Fe abundance. In a different approach, compared to the publications which preceded our

Ph.D. studies, we devised a way to directly measure them and therefore be less dependent on assumptions; in particular we presented a new method for estimating the cloud density directly from the X-ray spectrum, and used a theoretical treatment to derive the averaged Fe abundance within the molecular clouds studied, which resulted in 1.56 times the solar value.

As we will argue in Chapter 4, our findings are significantly different from what has been assumed before; as a result, we give a different interpretation on the overall illumination setting. Basically we find that the MCs in the immediate vicinity of Sgr A* require the illumination scenario to be more complex than the single flare model recently suggested in the literature. The results we will present in Chapter 4 show that in order to reproduce the Fe-Kα line flux and variability measured in these clouds, a variable X-ray flux from Sgr A* is needed, in the range 10^{37}-10^{38} erg s^{-1}, significantly lower than the one deduced to be at the origin of the Fe fluorescence in the Sgr B2 complex. Moreover, together with a more active past X-ray life than the one previously suggested for Sgr A*, we also found evidence for a significant contribution from low energy CR bombardment, which might be the source of the steady component of the 6.4-keV line flux observed in at least some of the lightcurves of the clouds we have studied.

In Chapter 5 we present the results of our first study of the Fe-Kα line emission from molecular clouds in the GC region. The clouds we have specifically studied here are in the vicinity of the Arches cluster, a young (~2 Myr) stellar cluster among the densest and most massive in the whole Galaxy, which lies about 20 pc (in projection) from Sgr A*. We used the same dataset of the research presented in Chapter 4 in order to study the ionisation process in these clouds; as a first application, we tested the XRN/Sgr A* scenario which was proposed recently in the literature (before our publications), and since then has been favoured for the interpretation of XRN phenomenology in the GC region. We discovered that this model cannot properly describe the Fe fluorescence which is observed in the Arches cluster surroundings; moreover, the X-ray luminosity of the Arches cluster itself is too low ($L_X \sim 10^{34}$ erg s^{-1}) in order to reproduce the amount of Fe fluorescence observed in the nearby molecular clouds. We therefore interpret this fluorescence in terms of particle bombardment, where the measured CRs energy density is ~100 times higher than the one estimated for the Galactic Ridge diffuse emission; this higher density can be reasonably attributed to the acceleration of particles in situ through shocks involving massive colliding winds binaries. The fluxes from these molecular clouds must be solely due to particle bombardment, and we consider them prototype examples.

About 15 pc (in projection) West of the Arches cluster we discovered the XRN displaying the fastest variability of the Fe-Kα line flux ever found in the GC region, the only one where both the rise and the decrease of the 6.4-keV flux has been monitored. The fast variability and the measurement of the Fe-Kα line flux allow us to completely rule out Sgr A* to be the source of the primary ionizing flux in this case. We therefore interpret the lightcurve and the spectrum as the superposition of a constant particle bombardment (to explain the constant level before the onset of the variability) and an external irradiation by an X-ray transient source.

These molecular clouds were not previously studied by other authors; we discovered that the Fe-Kα line phenomenology in the GC region is much richer than previously thought; we showed that rather than being produced only by a past high energy activity of Sgr A*, this fluorescent line can also be created in response to an enhanced cosmic ray flux or to the activity of a powerful X-ray transient source. The peculiar physical conditions of the GC environment support these findings and aid us in suggesting that a multi source scenario for the whole Fe-Kα line emission is very likely.

In Chapter 6 we report the results of a study we carried out on the temporal and spectral variability of the Arches cluster. Although this subject is not directly related to the Fe-Kα line emission observed from molecular clouds in the GC region, we report the results of this research because of their importance for future directions and further studies (see Chapter 6).

The Arches cluster provides an excellent opportunity to study the X-ray activity in a massive star cluster; its high stellar concentration ($\rho \sim 10^5$ M$_\odot$ pc^{-1}) gives rise to its enhanced X-ray luminosity (L$_X$ $\sim 10^{34}$ erg s^{-1}) through the process of wind-wind collisions. Before our study, the Arches cluster has been observed several times in the X-rays, with different observatories tracing the general features of the X-ray emission; ours was the first investigation of the temporal properties of the X-ray emission within the cluster. In fact, we used the same dataset (8 years of observations) as for the previous studies to perform a temporally resolved spectral analysis of this cluster, which enabled us to discover the first evidence for X-ray flaring activity in a massive stellar cluster located at the GC.

The analysis of XMM-Newton data allowed us to place a lower limit to the duration of the flare of about 4 days, with an emission measure of 1.2×10^{57} cm^{-3}, significantly higher than that usually detected in stellar flares ($\sim 10^{55}$ cm^{-3}). The origin of the flaring activity must be attributed to a massive colliding wind binary, where the increase in the flux might be due to the collision of clumps within the winds and/or to an orbital modulation of the X-ray emission from supersonic colliding winds (flare in periastron due to the 1/D dependance of the X-ray luminosity, with D distance between the stars). All these processes contribute to the total high energy budget of the GC region, and therefore they might be discovered in the near future also to make a contribution to the total diffuse Fe-Kα line flux in some peculiar regions, like the ones studied in Chapter 5.

In Chapter 7 we are going to present our conclusions, providing the outlook for further studies which can be carried out in the near future also with the help of the next generation X-ray telescopes which will contribute to expand the horizons of astronomical research.

Chapter 1

The Galactic Centre environment

> Is there any reasonable amount
> of matter in ordinary regions of space
> between the stars?
> Sir A.S. Eddington, 1926.

Along the $\sim$ 8kpc line of sight between the sun and the centre of the Milky Way lies a dense blanket of clouds and gas (interstellar medium, or ISM), making the Galactic Centre (GC) inherently difficult to observe. Due to this, much of the progress in the understanding of our galactic centre has occurred only recently, thanks to the development of new observational techniques and instrumentation; including for example adaptive optics of infrared images on ground-based telescopes (VLT, Keck), X-ray space observatories, and the new generation radio interferometers like the VLA and VLBI.

The GC region is visible from Earth at radio wavelengths; both continuum and molecular line emission is observed. It then becomes obscured in the far infrared band due to high foreground emission from dust, heated up to a few tens of degrees Kelvin by starlight The centre of the Milky Way is again visible in the near-infrared (NIR), where the emission is produced mainly by stars (the low energy tail of the black body spectrum); once again, even in the NIR band stars are only visible if their positions do not intersect the sightline of a dense cloud of dust and/or molecules, otherwise the reddening (visual extinction) would be so high that no signal could be detected. The large amount of dust along the line of sight, which absorbs most readily at UV wavelengths, completely prohibits observation in the visible and ultraviolet (UV) bands. The GC is visible once again in the high energy electromagnetic domain of X-rays and γ-rays, which can easily penetrate the thick layer of ISM along the Galactic Plane. Because of the opacity to X-rays and γ-rays of the Earth's atmosphere, the study of the GC in these energy domains requires the deployment of space observatories.

Numerous kinds of astrophysical sources are found in the GC region, including (to name a few) X-ray binaries, stellar clusters like the Arches and Quintuplet clusters, the most massive and densest stellar clusters in the galaxy, non thermal radio filaments, and, of course, the nearest Super Massive Black Hole (SMBH), Sgr A*. All these sources are embedded in a smooth (on large scales) distribution of ISM, which permeates all the Galaxy in its various phases of temperature and density. Although the distances are *astronomical*, let me point out that the total absorption through the ISM from Earth to the GC is only about 6×10^{22} Hydrogen (H) atoms per squared centimenter, which corresponds to the thickness of a sheet of paper like the page you are now reading.

In this chapter I will focus on the ISM, and try to explain in detail the physical and chemical properties of this important building block of the Galaxy. Moreover, I will introduce to the reader two other important inhabitants of the GC region: Cosmic Rays (CR) and magnetic fields. All these components, ISM, CR and magnetic fields, are not independently and stably populating the inner region of the Galaxy, but rather are continuously developing and interacting with one another. At the end of the chapter, I will also give a brief and essential introduction to the most extraordinary source populating the GC region; the 4×10^{6}M$_{\odot}$ SMBH, Sgr A*.

1.1 Interstellar Medium and molecular clouds

Galaxies are made of more than just stars. Perhaps the first to see an indication of this fact was William Herschel, who, in the eighteenth century, noticed that some regions of the sky, particularly along the Galactic plane, seem to have a marked absence of stars. It was not until the beginning of the 20th century, however, that Edward Barnard demonstrated that these dark zones are due to the presence of cold and dense matter, blocking the light from the stars behind them. Now it is well known that the space between the stars is filled with tenuous matter, of varying composition, temperature and density. In the solar neighbourhood, the ISM density varies from $\sim10^{-26}$ g cm^{-3} in hot gas to 10^{-20}-10^{-18} g cm^{-3} in the coldest molecular clouds. The ISM is made up of (solid state particles) and gas (molecules, atoms, ions and electrons), and can be observed via the absorption, reddening and polarization of starlight, as well as via direct emission lines. Other emission mechanisms, moreover, like synchrotron emission, inverse Compton and bound-free emission can also provide evidence of the presence and distribution of ISM throughout the Galaxy.

1.1.1 The different phases of the ISM

Increasing in temperature and decreasing in density, four typical phases of the ISM (in the gaseous form) are usually identified: molecular, atomic, warm ionised and hot ionised. The typical temperatures and densities of these gaseous phases are presented in Table 1.1. We begin by introducing the atomic, warm and hot ionised phases, as well as dust, which is the only phase of the ISM to be in a solid state. In Section 1.1.2 we describe the phase which is most important for our work, the molecular gas.

Table 1.1: Parameters of the different gaseous phases of the ISM. Here we quote the typical values of the temperature and the density (adapted from Ferrière, 2001).

Component	T(K)	n (cm^{-3})
Molecular	10-20	10^2-10^6
Cold atomic	50-100	20-50
Warm ionised	~8 000	0.2-0.5
Hot ionised	$\sim 10^6$	$\sim 10^{-3}$

Neutral atomic gas

We first want to clearly state that there is not actually a clear distinction between atomic and molecular clouds; most realistic scenarios would correspond to a cloud that have a molecular core and an atomic halo. Neutral H (HI) is spread in the whole Galaxy, and it is most likely found in the ground state because of the low collision rate in typical conditions (e.g. Ferrière, 2001). The electronic transitions of H relative to the n=1 state lie in the UV regime of the electromagnetic spectrum; electron transition between the level n=1 and a higher, more energetic, levels form the so called Lyman (Ly) lines series. The least energetic of these lines, the Ly$_\alpha$ line, has an energy of ~10.2 eV, and lies in the middle of the UV band. Besides being seen in emission, these lines can also be seen in absorption: for example, surveys of ISM (Galactic and extragalactic) based on the study of the Ly$_\alpha$ absorption allowed astronomers to study the distribution of the atomic galactic and extragalactic ISM (see for example Shull & van Steenberg, 1985).

A real breakthrough that opened the window of spectral line radio astronomy was the prediction (van de Hulst, 1944) and following first observation (Ewen & Purcell, 1951) of the HI hyperfine structure line at 21 cm (1420 MHz). In contrast to the UV starlight, this long wavelength photon can penetrate a dust cloud, allowing the measurement of the total amount of HI along a certain sight line. This line is produced by a hyperfine transition of the H atom; the ground 1s state of the H atom has two levels because of the interaction between the electron spin and the nuclear (proton) spin. The two spin vectors can be parallel (higher state) or antiparallel (lower state). The energy difference between these two quantum states of the H atom is 5.9×10^{-6} eV, very small compared to the electronic ground state binding energy of 13.6 eV. The radial extension of the HI in the Galactic disk extends out to 30 kpc from the GC (Diplas & Savage, 1991); the thickness of this HI layer decreases to less than 100pc in the inner ~ 3kpc, essentially because of the stronger vertical gravitational field. For comparison, the same quantity for radial distances to the GC larger than R$_\odot$ increases more than linearly with R , reaching ~3 kpc at the edge of the Galaxy (Diplas & Savage, 1991).

Another interesting tool to investigate the distribution of atomic ISM along the line of sight, of essential importance in all our work, is the absoprtion of X-ray sources. The effect of photoelectric absorption in the spectrum of an X-ray source is the absorption of the softest part of the spectrum, depending on the total amount of matter along the sight

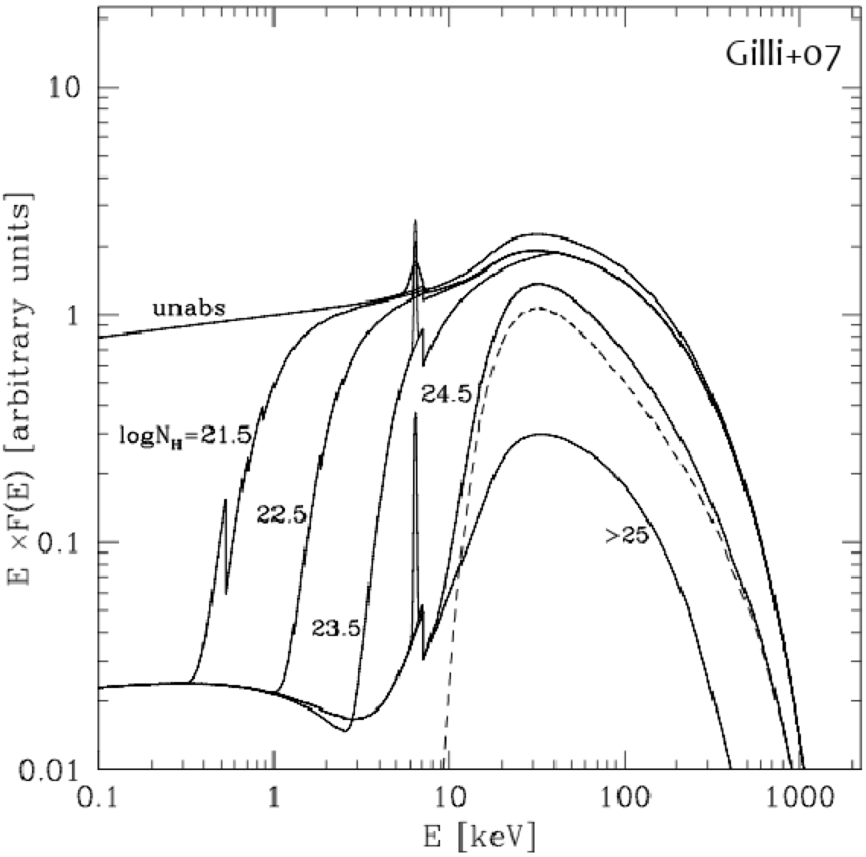

Figure 1.1: Effect of the X-ray absorption on a power law spectrum as a function of the N_H amount along the line of sight (Gilli et al., 2007).

line. The main elements in the ISM which absorb soft X-rays are Oxygen, Neon and Iron, with a lower contribution by Carbon, Nitrogen, Magnesium, Sulphur and Silicon. Most of these atoms have their absorption edge in the soft X-ray band (~0.1-3 keV); at the higher energies, the ISM is transparent to the X-ray radiation because of the very steep energy dependence ($\sigma \propto E^{-3}$) of the cross section for photoelectric effect, which decreases rapidly with increasing energy of the incoming photon (see Chapter 2). The transparency of the ISM to the hard X-ray radiation allows us to observe regions of the Universe which otherwise would be totally hidden, because they cannot be observed in the optical or UV domain; a valuable example is the Galactic Centre, where the typical optical extinction (A_V) has been estimated to be about 30 mag. The photoelectric absorption by neutral metals along the line of sight is visible and measurable through the presence of edges in the X-ray spectrum of the source of interest; assuming a certain abundance of the elements (and their ratio with respect to the abundance of the most abundant H) it is possible to derive the equivalent column density of H atoms along the same sight line, usually indicated with the symbol N_H and measured in units of atoms per squared centimetre (cm^{-2}). Note however that the terminology might be misleading, since the effective photoelectric absorption in the X-ray band is not produced by H atoms, but rather by metals; accordingly the N_H value is derived from the assumed elemental abundance. In Fig.1.1 we show the effect of the absorption of soft X-rays in the spectrum of an X-ray source (here described by a simple powerlaw) by the ISM in the line of sight; we can see that for an $N_H \gtrsim 10^{23}$ cm^{-2} the source flux is strongly suppressed below 1 keV. The typical column density measured in the spectra of X-ray sources in the GC region is on the order of 10^{22-23} cm^{-2}, with a mean value across the innermost region of 6×10^{22} cm^{-2} (Predehl & Schmitt, 1995).

Warm ionised gas

O and B stars, the most massive and therefore most luminous stars which populate the Universe, emit a significant amount of radiation in the UV band, especially at energies higher than 13.6 eV; this is the threshold energy for ionisation of the K shell of Hydrogen (e.g. Rybicki & Lightman, 1979). As a result, in regions where star formation occur and the conditions for the formation of the most massive stars are satisfied, we can observe the warm component of the ISM, ionised gas with a temperature of about 10^4 K and density of about 0.1 cm^{-3}, the so called HII regions (HII refers to the ionisation state of the H atom, i.e. Hydrogen is ionised, whereas HI means that the H atom is neutral). These regions are often found in association with molecular clouds, the material from which the most massive stars are formed and that they ionise and blow away. As a result, the typical spectrum of an HII region shows strong emission lines from various elements heavier than H; these lines are excited by different physical mechanisms such as recombination, fluorescence and electron collisions (for a nice textbook review, see Osterbrock & Ferland, 2006).

Within an ionised region, the electrons are mostly free to travel in the sea of ions (mostly protons) and being scattered via electric interactions. As a consequence, besides photoionisation and recombination processes, the other emission mechanism typical of an HII region is the bremsstrahlung emission produced by the acceleration of the free electrons in the electric field of the protons/ions. The bulk of this continuum emission can be seen in radio regime (NRAO , 2010).

An interesting physical parameter associated to an HII region is the size of the ISM cloud which is ionised by the central star, often called the Strömgren sphere, which can be derived postulating the equilibrium between the ionisation produced by the underlying star and the recombination experienced by free protons and electrons after the H atom has been ionised; until this equilibrium phase is not reached, the size of the HII region continuously increases (see the original paper by Strömgren, 1939). For example, assuming that $\dot{N}_{OB} \gtrsim 10^{49}$ is the number of photons more energetic than 13.6 eV emitted per second by an O6 type star, it is possible to estimate the radius of the HII region to be $R_S \sim 0.3$ pc for a typical density of the nearby cloud $n_H \sim 5000$ cm^{-3}. More generally, the radius of the Strömgren sphere can be written as $R_S \sim (3\dot{N}_{OB}/4\pi\alpha)^{1/3} n_H^{-2/3}$; these dependence on the type of star and on the density of the nearby ISM are simply understood if we think that more ionising photons produce a radiation pressure which acts at enlarging the HII region, whereas a higher density of the surrounding medium would absorb more efficiently the ionising photons closer to the stellar surface [1].

Hot ionised gas

This is the hottest phase of the ISM, with temperatures that can easily reach 10^{6-7}K. If this hot gas has to be in pressure equilibrium with the ambient medium, i.e. with the other components of the ISM, its density must be very low. Indeed, as we can see from Table 1.1, the typical densities for the hot ionised ISM is 0.01-0.001 cm^{-3}. The existance of such a hot component has been first postulated by Spitzer (1956) in order to provide the pressure environment to confine the observed high latitude interstellar clouds; the presence of such clouds is well explained in terms of a pressure balance/equilibrium of the cold ISM with a hot, rarefied gas which composes the Galactic corona (Spitzer, 1956).

Together with filling the Galactic corona, hot ISM is found also in Galaxy Clusters, the so called intracluster medium, where a gas with a typical temperature of about 10^8K is found to fill the space between galaxies; the origin of such a hot plasma is thought to be the gravitational energy released during the formation of the cluster itself. This gravitational energy is converted into thermal energy of the particles which compose the medium, which because of the extremely high temperature are fully ionised and therefore emit X-rays via thermal bremsstrahlung emission (Boehringer & Werner, 2009).

For what concerns the presence of hot ISM in the Milky Way, the ROSAT satellite first could give a unbiased view of this hot ISM thanks to the high soft X-ray sensitivity and the improved angular resolution with respect to the previous X-ray observatories; the results were published by Snowden et al. (1997), who also found an enhancement of this diffuse emission towards the Galactic Centre region. These authors found for the bulge soft X-ray emission a density of the hot plasma of $\sim$0.0035 cm^{-3}, a scale height of $\sim$ 2kpc and a temperature of the hot plasma of $10^{6.6}$K; the total X-ray luminosity of this emission is in the order of 10^{39}erg s^{-1} (Snowden et al., 1997). The nature and physical properties of the hot gas which fills the GC region will be discussed in details in Chapter3.

The hot component of the ISM is heated via injection of mechanical energy; the first and likely sources of this energy are SN explosions and stellar wind driven bubbles. For what concerns the cooling of the hot phase of the ISM, this can be achieved via different processes (Draine, 2011): collisional ionisation of H, He and heavier elements, as well as free-free continuum emission. The cooling from different species is dominant at different temperatures (Gaetz & Salpeter, 1983). For example, H and He dominate at temperatures lower than 40000K, while for higher temperatures the low density cooling species are important, such as Oxygen, Silicon, Nitrogen, Carbon, and further hot, Iron. Free-free emission becomes the dominant cooling process at temperatures higher than 10^{6-7}K, and remains up to the highest temperatures (Gaetz & Salpeter, 1983). The cooling rate for thermal bremsstrahlung emission scales as $T^{1/2}$; this has also contribution by metals, for which the cooling rate scales as the nuclear charge Z^2 (Rybicki & Lightman, 1979). This cooling process is clear in the spectra of the hot diffuse X-ray emission permeating the

---

[1] This calculation has been taken from the lecture notes of the International Max Planck Research School on Astrophysics Introductory course.

GC region, where a hot plasma with a temperature of ∼1keV ($\sim 10^7$K) is found to be homogeneously distributed along the inner galactic plane (e.g. Koyama et al., 2007a).

Dust

There is a last cold state of the ISM, which is not in the form of gas but solid: dust grains, basically formed of dielectric and refractory elements. We introduce here the basics of dust astronomy, mostly some quantites which will be helpful in the discussion of Fe ionisation and abundance in the GC region (For a complete and detailed treatment of the physical properties of dust grains see the review by Draine, 2003); basically, all iron found in MCs in the CMZ is depleted, i.e. found in form of dust grains. The dust represents only a small part of the interstellar mass, but it has an enormous importance in the balance of chemical and physical processes involving the other phases of the ISM. Dust grains participate to the chemistry of the interstellar matter, providing direct sinks and sources of gas; in cold and dense molecular clouds, dust grains act at accreting particles from the gas state to enlarge their body size, whereas in the warmer medium which fills the intracloud space dust particles lose their volatile mantle, returning elements to the gas phase (Ferrière, 2001). Moreover, when interested by the passage of a blast wave produced by a SN explosion, the dust grain is partially vaporised, and as a result it participates at the chemical enrichment of the ISM (Ferrière, 2001). Dust grains contribute to the formation and mantainance of the molecular Hydrogen in two ways: dusty particles act as catalysts by allowing H atoms to combine on their surface and form the H_2 molecule, and they also shield the previously formed H_2 molecules from the strong diffuse UV radiation, preventing their photodissociation (Ferrière, 2001). Being a dynamical phase of the interstellar matter, dust can be heated or cooled in several ways: the main heating processes are the absorption of star light, the collisions with atoms, collisions with cosmic rays and other dust grains, and the absorption of energy released by chemical reaction in the grain surface (e.g. by the formation of the H_2 molecule). On the other hand, the physical processes leading to the cooling of dust grains are thermal emission, collisions with cold atoms and/or molecules, and ejection of atoms from the outer layer of the grain (sublimation).

We know about the presence of dust in the ISM in two main ways: the extinction of starlight and the thermal infrared emission from heated dust grains. But how important is it in the Galaxy structure and evolution? The gas to dust ratio in the Milky Way, i.e. the ratio between the number of atoms in the gaseous form to the number in the solid form, is about 100/1, meaning that elements in the form of dust grains are (in number) only 1% of the elements in the gas form; moreover, the baryionic mass of the Galaxy is only 10% of its total mass, therefore reducing the impact of the dust grains to the total galactic matter to about 0.1%. Although these numbers might give the impression that dust can be neglected in the discussion about the ISM within the Galaxy, we note that dust is responsible for the absorption (and re-radiation via FIR continuum emission) of about 30-50% of all the starlight produced in the Milky Way (see Draine, 2003).

The total amount of the visual extinction A_V along a certain line of sight is strongly correlated with the total amount of cold neutral ISM along the same line of sight. Predehl

& Schmitt (1995) found an empirical relation that connect these two quantities:

$$\frac{N_H}{A_V} = 1.79 \times 10^{21}\ \mathrm{cm}^{-2}\mathrm{mag}^{-1} \tag{1.1}$$

Besides the extinction of the radiation field coming from a distant source, dust particles also emit continuum radiation. Mainly two components of continuum emission can be ascribed to dust particles: extended red emission, a broad continuum peaking between 6100 and 8200 A due to photoluminescence (absorption of a UV/optical photon followed by re-emission in the near IR band), and a thermal continuum from dust grains heated up to few tens of K, which peaks in the FIR (Draine, 2003).

1.1.2 Molecular clouds

Molecular gas makes up the coldest and densest phase of the ISM. The first molecules in interstellar space to be observed were CH and CN, via the optical absorption lines that they produce in the spectra of stars. The most abundant molecules in the Galaxy are however H_2 and Carbon Monoxide (CO), observed first through absorption lines in stellar spectra in the UV (respectively Carruthers, 1970; Smith & Stecher, 1971). Radio observations are needed, however, in order to study the densest condensations of molecules, molecular clouds (MC), in which the density can reach a value of 10^6 H atoms per cm^3, making them optically thick to UV radiation (Snow & McCall, 2006). In the radio (at submm wavelengths), the rotational transitions of the most abundant polar molecules take place (see section 1.1.3 for a quantitative description).

The H_2 molecule, being homonuclear, is highly symmetric and does not have any permanent electric dipole moment, therefore all the rotational-vibrational transitions within the electronic ground state have low coefficients for spontaneous emission (Habart et al., 2005); this because they are quadrupole transitions, of higher order with respect to dipole ones which for the H_2 molecule are forbidden due to the structural symmetry (the dipole is null). The H_2 molecule exists in two forms, depending on the relative orientation of the nuclear spins, namely para-H_2 (spins antiparallel) and ortho-H_2 (spins parallel); radiative transitions between these two states of the H_2 molecule are forbidden, although conversion between the two states might occur in response to a charge exchange reaction (Eisberg & Resnick, 1985). The H_2 molecule can be excited in several ways (Habart et al., 2005): (i) it can suffer electronic transition from the ground level to the more energetic ones via absorption of UV radiation ($\lambda \leq 912$ A) from nearby stars and/or absorption of X-rays from nearby X-ray sources in dense regions opaque to UV radiation; as the molecule relaxes into the original ground state, all the other vibrational and rotational energy levels are populated, this cascade originating optical to infrared fluorescent emission; (ii) when the H_2 gas density and temperature are high enough ($n_H \gtrsim 10^4\ \mathrm{cm}^{-3}$, $T \sim 500$ K, see Section 1.1.3), the molecular excitation is driven by collisions of the gas particles. Together with being observed at UV and optical wavelength, the H_2 molecule can be observed in the infrared in its roto-vibrational transitions, which are very faint because of the very low emission coefficient (quadrupole emission, Habart et al., 2005).

The other abundant molecule, the CO, has a permanent dipole moment and therefore can be easily observed in the radio regime through line emission due to rotational transitions; the fundamental rotational transition (J=1-0) has λ=2.6 mm (115 GHz), it therefore lies the heart of the radio band (for comparison, we calculated the fundamental frequency of the J=1-0 rotational transition of the H_2 molecule to be 1.46 THz, λ ~20mm). The first large scale surveys of the CO J=1-0 emission were performed in the 1970s (Scoville & Solomon, 1975; Burton et al., 1975); the main results of these first attempts to investigate the distribution of the cold molecular matter within the Galaxy were the discovery of a strong concentration of molecular material in the inner half a kpc of the Galaxy and the fact that most of the molecular gas (besides the one liying in the GC region) is distributed in a so called molecular ring which is radially extended between 3.5 and 7 kpc.

The MCs in the Galaxy are hierarchically distributed in size and mass: from the biggest complexes, with sizes of dozens of parsec and masses in the range 10^5-10^6 $M_\odot$ (the Sgr B2 MC in the GC region is the largest, with a size of 40 pc and a mass close to 10^6 $M_\odot$), they scale down to the smallest and densest cores only a few parsec in size with densities $\gtrsim 10^4$ cm^{-3}. Indicating with G the gravitational constant, with M the mass of the cloud, L its size and σ the internal velocity dispersion of the molecules, the majority of molecular clouds obey the virial theorem relation (GM/5L $\sim \sigma^2$, if a spherical cloud is assumed), meaning the clouds are approximately virialized (i.e. the gravitational potential of the cloud is balanced by the kinetic energy of its molecules, therefore preventing collapse or evaporation). Larson (1981) found three empirical powerlaw relations which bound M, L and σ, studying the physical properties of CO selected molecular clouds in the Galaxy (see Fig.1.2):

$$\sigma \text{ (km s}^{-1}) = 0.42 \left(\frac{\mathrm{M}}{\mathrm{M}_\odot}\right)^{0.2} \tag{1.2}$$

$$\frac{2GM}{\sigma^2 L} = 0.92 \left(\frac{L}{pc}\right)^{0.14} \tag{1.3}$$

$$< n_{H_2} > (cm^{-3}) = 3.4 \times 10^3 \left(\frac{L}{pc}\right)^{-1.1} \tag{1.4}$$

Equation 1.2 relates the velocity dispersion measured in the MC and the cloud mass; Equation 1.3 relates the ratio between the velocity dispersion as calculated from the virial theorem (σ^2 ~GM/L) and the one measured via radio observations; the last, Equation 1.4 relates the density of a MC with its size. The presence of these three empirical correlations can be understood if the MCs are bound by self-gravity.

Typical temperatures measured in MC cores are only tens of degrees Kelvin (10-20 K Goldsmith, 1987). The root mean square speed for a thermal distributed set of molecules is given by the Maxwell-Boltzmann distribution as $\bar{v} = \sqrt{3kT/m_{H_2}}$. For the typical temperatures of MC cores quoted above, the thermal velocities are in the range 0.35-0.5 km s^{-1}. These velocities are significantly lower than the dispersion velocity measured in the CO J=1-0 emission line profiles of the MCs (several tens of km s^{-1}), therefore indicating

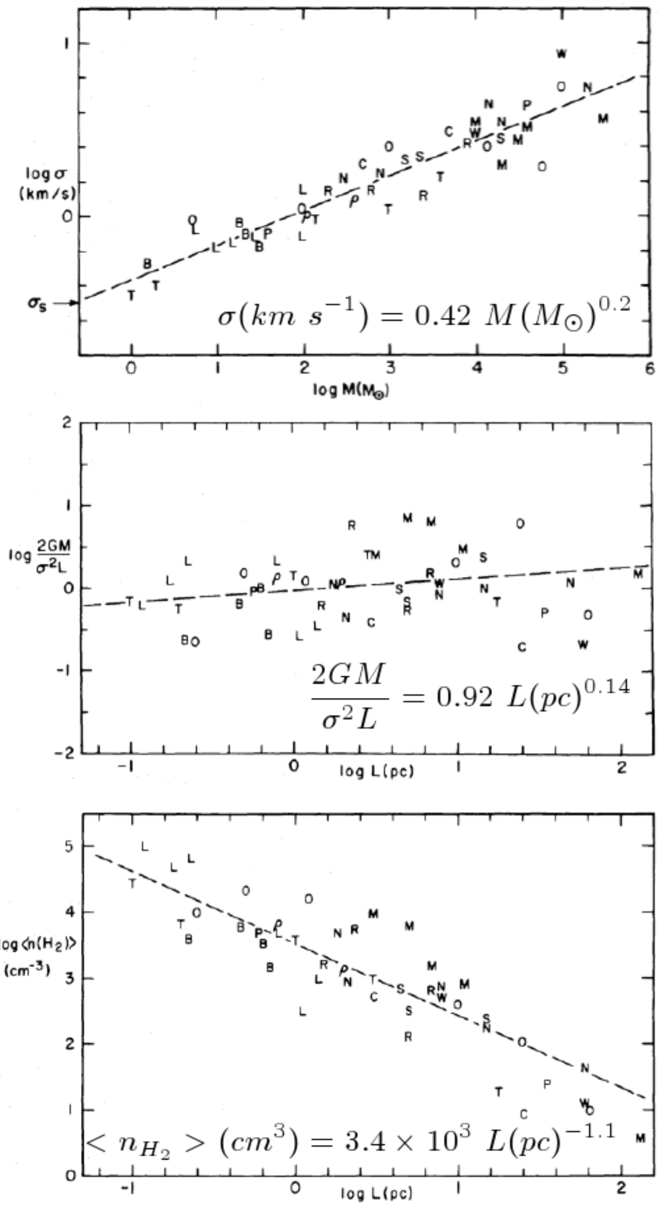

Figure 1.2: The three correlations found by Larson (1981); . The dashed lines in each panel represent the three best fit functions (see text) also reported in the plots. The letters refer to the different MCs selected in Larson's paper.

that the internal dynamics of MCs is dominated by turbulence (e.g. Larson, 1981). For what concerns MCs in the GC region we will show in Section 1.1.4 that, although these clouds are also dominated by turbulence like the ones in the bulge and the disk, the internal physical conditions are completely different, i.e. the virial mass of the clouds in the GC is generally significantly higher than the measured mass (Miyazaki & Tsuboi, 2000; Oka et

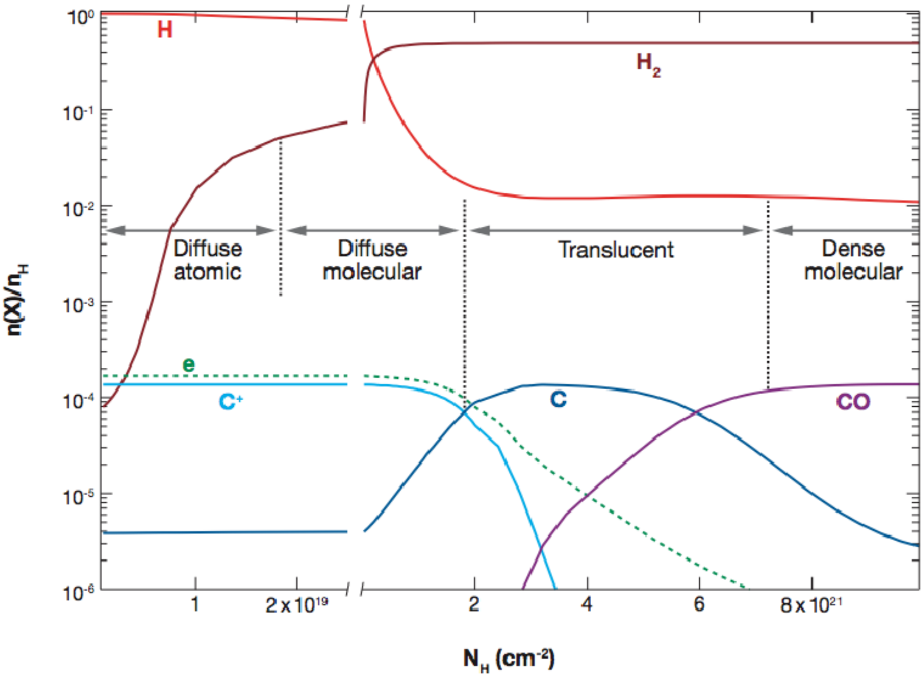

Figure 1.3: Revised definitions of molecular and atomic clouds (adapted from Snow & McCall, 2006).

al., 2001).

As for the more general concept of the ISM, the molecular phase comprises different kinds of clouds, which themselves span a wide variety of physical and chemical conditions. In Fig.1.3 we present a classification proposed by Snow & McCall (2006) based on the concentration of the ionization states of the different elements (or molecules), especially those of H_2 and CO. [2]. These authors classified the molecular phase of the ISM in four different types, depending on the physical state of the most abundant molecules. For an H column density (N_H) lower than 1-2×10^{19} cm^{-2}, the background radiation field can fully penetrate the cloud, producing the photodissociation of all the H_2 molecules; looking at the low N_H side of Fig.1.3 it can be seen that all H is in the atomic state (for this reason these clouds are called *atomic diffuse*), the concentration of electrons is the highest and also almost all the C available is in the ionic form C^+. The N_H range here considered is a transition region for the H_2 molecule, which increases in fraction of about three orders of magnitude towards the higher densities.

The second range of column density considered is 2-5×10^{19}-2×10^{21} cm^{-2}. This is a transition region for all the most abundant components of MCs, here called *diffuse*

---

[2] We are however aware of the fact that all the classifications are to be intended in broad terms as guidelines, and that most of the MCs populating the Galaxy cannot be classified entirely in one class, but they most likely present an onion like structure, with the densest core at the center, and optically thinner and more tenuous structures in the outer layers

molecular clouds. In this regime the interstellar radiation field is sufficiently low to allow the atoms to bind and form molecules. As a consequence, the fraction of H atoms reaches the minimum plateau value (see Fig.1.3). Carbon also experiences a transition in these density range; some of the the ionic C^+ recombines with free electrons, increasing the number of C atoms found in the cloud. However, enough interstellar radiation is still present to ionize part of the C and to photodissociate CO; indeed, the photon energy required to dissociate an H_2 molecule (4.52 eV) is higher than the one required for CO dissociation (3 eV). These clouds have typical densities in the range 100-500 cm^{-3} and temperatures of 30-100K (Snow & McCall, 2006).

In the column densities range 2-7$\times10^{21}$ cm^{-2} the Hydrogen is mostly found to be in the molecular form. The amount of matter found in these *Translucent clouds* is sufficient to shield C atoms and let them transite from the ionized to the neutral form. Moreover, part of the atomic C also binds with Oxygen (O) to form the CO molecule. The free electrons density decreases towards the higher N_H therefore decreasing the amount of free charge distributed in the MC. Typical temperatures are slightly lower than in diffuse clouds, T$\sim$15-50 K, and densities are higher (Snow & McCall, 2006).

At the upper limit of the N_H axis (see the right side of Fig.1.3), for typical values higher than $10^{22}cm^{-2}$, lie the dense molecular clouds, of the kind that we will consider throughout all our work on the Fe-K_α line in the GC region. As clearly shown in Fig.1.3, in these clouds CO is finally formed and also the available H is entirely in the molecular form. Moreover, no free electrons are theoretically found here, unless injected from the ambient surrounding the cloud like it might happen in the GC region (cosmic ray ionization). Typical densities of this type of clouds are higher than 10^4 cm^{-3}, with the lowest temperatures found among condensed structures in the Galaxy.

1.1.3 How to observe molecular clouds: rotational, vibrational and electronic spectra of molecules

Depending on the distribution of the electric charge within a molecule, molecules in the ISM divide in polar and non polar, depending on whether their structure displays a net separation of charge. For example, being H_2 a homonuclear diatomic molecule, it has no net separation of charge and therefore no permanent electric dipole moment. For what concerns direct observations of the ISM, this has a huge impact on the quantity of informations that we can derive for the chemical and physical state of this molecule, compared, for example, to a polar molecule like the CO. Molecules with a permanent electric dipole moment are carriers of fundamental informations about the physical state of the ISM; they undergo rotational, vibrational and electronic transitions, which emit radiation at specific wavelengths from radio to optical-UV. Here, we discuss the physics of these transitions, focusing on the physics of the rotational lines emission[3].

---

[3] The formulas and the derivation of the different physical quantities reported in this section have been taken from the Radio astronomy course by the National Radio Astronomy Observatory (NRAO) (NRAO , 2010), which can be found at the http://www.cv.nrao.edu/course/astr534/ERA.shtml.

From the classical view of the Bohr atomic structure, we can write the angular momentum of an electron rotating around the nucleus as the product of its distance (assumed to be constant) and the momentum (also assumed to be constant). If we then consider the quantization rule of the angular momentum L, we can see that there are only certain values permitted for the electron radii a_n, whose formula can be written as (e.g. Eisberg & Resnick, 1985)

$$L = m_e v a_n = n\hbar \Rightarrow a_n = \frac{n\hbar}{m_e v}, \tag{1.5}$$

where m_e is the electron mass, v its velocity and $\hbar$ the Planck's constant. This formula is also valid for atoms in a molecule. In the following we consider the simple model of a diatomic molecule whose two atoms A and B are separated by a distance $r_e = r_A + r_B$. In the center of mass frame, the molecule can be seen as a point mass $\mu=\left(\frac{m_A m_B}{m_A+m_B}\right)$ rotating with an angular frequency ω, hence having a total angular momentum $L=I\omega$ which can be derived from

$$I = m_A r_A^2 + m_B r_B^2 \qquad \rightarrow \qquad L = (m_A r_A^2 + m_B r_B^2)\omega \tag{1.6}$$

For our purposes, it is convenient to write the expression for the angular momentum in terms of the reduced mass of the molecule μ; in formula

$$L = \mu r_e^2 \omega \tag{1.7}$$

From classical mechanics we can write the rotational kinetic energy of the molecule as

$$E_{rot} = \frac{I\omega^2}{2} = \frac{L^2}{2I} \tag{1.8}$$

and hence having the expression of the energy associated with the molecular rotation as a function of its angular momentum. As introduced above, in a mechanical system L is quantized and can only be integer times $\hbar$; from the formula 1.8 we therefore deduce that the rotational energy of the molecule is also quantized, and its values can be calculated to be

$$E_{rot} = \frac{J(J+1)\hbar^2}{2I}, \tag{1.9}$$

where J is the rotational quantum number, which can have only integer values, starting from 0 (e.g. Eisberg & Resnick, 1985). We note that the rotational energy has a zero point, correspondent to $J = 0$, which means that the molecule can be rotationally still. Another important characteristic of the rotational energy of a molecule is its dependence on the inverse inertia, $E_{rot} \propto I^{-1}$; as a consequence, only the most massive molecules have rotational energy states excited by collisions. As a counterexample, the minimal rotational energy ($E_{rot}^{J=1}$) allowed for the lightest H_2 molecule is about 500K, far beyond the actual temperature inferred from the cold dense molecular clouds (kT∼50-100K) (NRAO , 2010); the H_2 molecules inside the cloud do not have enough energy to excite their own rotational levels via collisions. On the contrary, more massive molecules like the CO and CS can be found in different rotational levels excited by collisions. The only rotational transitions allowed are the ones for which the variation in the rotational quantum number J satisfies the relation ΔJ=±1; as a consequence, the frequency of a rotational line increases linearly towards higher J. For example, the energy E of the line emitted in the rotational transition J→J-1 is

$$E_{rot} = [J(J+1) - J(J-1)]\frac{\hbar^2}{2I} = \frac{\hbar^2 J}{I}, \tag{1.10}$$

from which the frequency of the emitted photon can be calculated as

$$\nu = \frac{\Delta E_{rot}}{h} = \frac{\hbar J}{2\pi I}, \qquad J = 1, 2, ..., \tag{1.11}$$

where J is the rotational quantum number correspondent to the more energetic level. Written as a function of the reduced mass μ and the equilibrium separation r_e between the atoms within the molecule, this frequency becomes (NRAO , 2010)

$$\nu = \frac{hJ}{4\pi^2 \mu r_e^2}, \qquad J = 1, 2, ... \tag{1.12}$$

As a result, a diagram showing the energetic levels of a certain molecule looks like a ladder whose steps are increasingly spaced towards higher energies. Alternatively, given the selection rule $\Delta J = \pm 1$, we can see that the emission lines in the spectrum are equally spaced in energy, frequency and wavelenght. Moreover, the frequency of rotational lines only depends inversely on the moment of inertia of the molecule; accordingly, the most massive molecules are found to emit at cm wavelengths, while intermediate mass molecules like CO and CS are emit in the *mm* range. Having understood the basic physics of the rotational energy and transitions in molecules, we have now to answer the question how these levels are excited, and how intense the line will be. Molecules are excited to energetic rotational states by foreground radiation and collisions with other gas particles. Comparing the thermal energy of a molecule in a gas described by a temperature T, i.e. E∼kT, with its rotational kinetic energy E_{rot}, we can give a rude estimate of the minimum temperature that a gas must have in order to collisionally excite the molecular rotational levels. This is

$$T_{min} \approx \frac{J(J+1)h^2}{2Ik4\pi^2} = \frac{hJ}{4\pi^2 I}\frac{h(J+1)}{2k} \tag{1.13}$$

As a result, the minimum temperature required to excite the J→J-1 transition at frequency ν can be approximated by the expression

$$T_{min} \approx \frac{\nu h(J+1)}{2k} \tag{1.14}$$

With this formula, we can calculate that the minimum temperature needed in order to have significant excitation of the $^{12}C^{16}O$ J=1→0 line at ν=115GHz is ∼5.5K, condition that is easily satisfied in basically all the coldest observed molecular clouds.

About the line flux, we remind here that rotational lines are emitted via electric dipole transitions; if we consider a radiative trasition between two energetic levels labeld U and L, we can write the emission coefficient A_{UL} (spontaneous emission, in units of s^{-1}) as a function of the total power radiated at the transition frequency (NRAO , 2010)

$$A_{UL} = \frac{|P|}{h\nu_{UL}} = \frac{64\pi^4}{3hc^3}\nu_{UL}^3|\mu_{UL}|^2 \tag{1.15}$$

In this formula, P is the power radiated at the frequency ν as given by the Larmor's formula; in fact, the component perpendicular to the line of sight of the electric dipole moment of a rotating molecule is an oscillating function of time of the form $qr_e \exp(-i\omega t)$ (NRAO , 2010). In formula 1.15, ν_{UL} represents the frequency of the rotational line and μ_{UL} is the averaged electric dipole moment.

An interesting characteristic of this emission coefficient is its dependence on the third power of the frequency; consequently, radio transitions with higher frequency will show more prominent lines in the spectrum. The intensity of the electric dipole moment of the J=1→0 transition is

$$|\mu_{J\rightarrow J-1}|^2 = \frac{\mu^2 J}{2J+1} \tag{1.16}$$

For example, the A_{10} emission coefficient of the CO J=1→0 transition is 7.1×10^{-8} s^{-1}; this translates in a typical time for the spontaneous emission of a photon of $\sim10^7$ s (NRAO , 2010), much longer than the typical collision time between molecules in a dense molecular cloud. As a consequence, collisions between gas particles can sustain the process of rotational line emission for the CO molecule.

A critical density, in units of cm^{-3}, can also be defined for every transition; following (NRAO , 2010):

$$n^* \approx \frac{A_{UL}}{\sigma v}, \tag{1.17}$$

where σ is the cross section for molecular collisions and v their typical velocity. For densities above n^* the rate of encounters $n\sigma v$ can balance the rate of spontaneous emission. Molecules with high A_{10} only radiate at the higher densities. For example, the HCN J=1→0 line at ν=88.6GHz has $A_{10}=2\times10^{-5}$ (NRAO , 2010); as a result, the rotational transitions of this molecule are significantly excited at densities in the order of 10^5 cm^{-3}, very high compared with the typical tracers of cold molecular ISM like CO and CS, which are more widely distributed within the interstellar space.

Together with the rotational transitions, molecules can undergo vibrational and electronic transitions. In increasing energy we first discuss the main properties of the vibrational lines. Within a molecule described by a certain electronic level, the nuclei do not mantain a fixed separation because the molecule is not a rigid rotating body. Besides rotating, molecular nuclei vibrate about a certain equilibrium separation, whose energy is quantized in such a way that

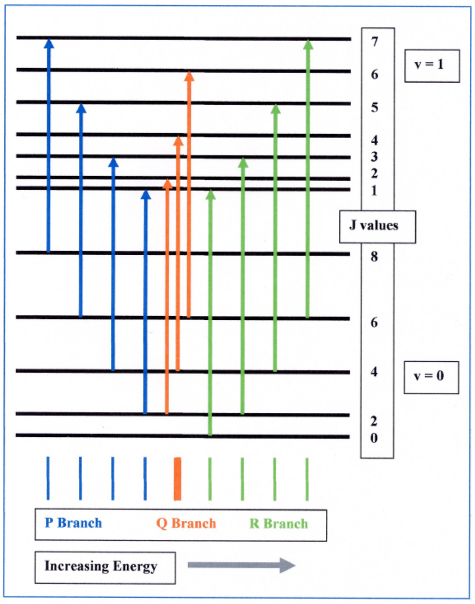

Figure 1.4: Rotovibrational energy levels diagram. The diagram shows the different energy scales for the vibrational and rotational energies; within a vibrational state, several rotational levels can be found, with energies which increase towards higherJ quantum numbers. THe arrows show the different transitions (in absorption) allowed; the P, Q and R branches are defines as transitions with ΔJ=-1, 0, +1 respectively.

$$E_v = (v + 1/2)h\nu_0 \tag{1.18}$$

where the fundamental frequency is ν_0=1/2$\pi\sqrt{C/\mu}$, with μ the reduced mass of the system and C the force constant, so that the molecular potential can be approximated by the parabolic shape V(x)=Cx^2 in the vicinity of the equilibrium point. In a different way with respect to what we saw for the molecular rotational levels, the energy between two adjacent vibrational levels is the same for every level v (the selection rule for vibrational transitions is $\Delta\nu = \pm 1.$). Indeed,

$$\Delta E_{v+1\rightarrow v} = h\nu_0[(v + 1 + 1/2) - (v + 1/2)] = h\nu_0 \tag{1.19}$$

which is independent on the vibrational quantum number v. The resulting spectral lines lie in the infrared band, with a wavelength between 8000$\mathring{A}$ and 50000$\mathring{A}$ for most of the molecules (Eisberg & Resnick, 1985). As a consequence of the quantization of the energy, the ground state for vibration of molecules cannot be zero, therefore a molecule is in perpetual vibration about the equilibrium separation. Moreover, as we previously introduced, the rotational transitions involve a lower energy difference. Therefore, every vibrational level is populated by many rotational levels; we can represent these two energetic structures of molecules in a diagram, as shown in Fig.1.4[4].

At higher energies, a molecule can also be described by its electronic level, whose selection rules are the same as in quantum theory of the atomic spectra (Δl=±1 and Δm=0,±1). Neglecting coupling between electronic, vibrational and rotational levels, we can simply write the energy of a particular physical state as the sum of the three energies related to the electronic, vibrational and rotational level, i.e. $E = E_e + E_v + E_r$. As a result of a transition between the upper energetic level and a lower one (U→L), the radiation emitted as a photon will have an energy

$$\Delta E = \Delta E_E + (E_v^U - E_v^L) + (E_r^U - E_r^L) \tag{1.20}$$

The vibrational selection rule remains unchanged, i.e. the selection rules for an armonic oscillator, whereas the selection rule for the rotational level is now broader because it encompasses also the case ΔJ=0, since in case also an electronic transition occurs, the parity constraints on the rotational transitions derived from quantum mechanics are no longer valid (Eisberg & Resnick, 1985).

1.1.4 Molecular clouds in the Galactic Centre region

The GC region is unique for many aspects, and one of this is the presence of the most massive and dense molecular clouds in the whole Galaxy; the so-called Central Molecular Zone (CMZ), a molecular layer about 400 pc in size, hosts a large concentration of mostly molecular gas ($\sim 10^8 M_\odot$) which account for about the 10% of the total mass of the Galaxy (Güsten & Philipp, 2004). Despite the high gas surface density ($\geq$100M$_\odot$/pc^2), the GC region is higly depleted with only a small fraction of matter in the gaseous form, about 1%. The distribution of matter with respect to the position of Sgr A* is asymmetric, with more gas concentrated at positive longitudes and the surface density peaked at the position of the Sgr B2 MC, the most massive molecular complex in the CMZ. Moreover, the distribution of the mass is not smoothed and homogeneous, but rather inhomogeneous and concentrated in massive molecular complexes. The most important (for our work) of these MCs are the innermost, which approximately lie in the Galactic plane; these are Sgr A, Sgr B (B1 and B2), Sgr C and Sgr D. In a face-on view of the GC region these massive clouds would be located in a circular ring; however, when measuring the intensity of a certain molecular line produced within the clouds, which give us a measurement of the total mass and the physical conditions within the cloud, we do not constrain the position of the material along the third dimension, the line of sight. To identify coherent molecular structures astronomers build the so-called *lb* and *lv*-diagrams, which display the total emission in a sky map and in a longitude-velocity plot, respectively. While the first diagram represents the 2D distribution of the molecular gas observed in a particular emission line, the *lv*-diagram shows the range of relative velocities along the line of sight over which the line-emitting molecular complex is distributed; for example, in the GC radio map observed in the CO J=1-0 and CS J=2-1 lines, respectively Oka et al. (1998) and Tsuboi et al. (1999) (see Fig.1.5), we can see

---

[4] from http://www.barrettbellamyclimate.com

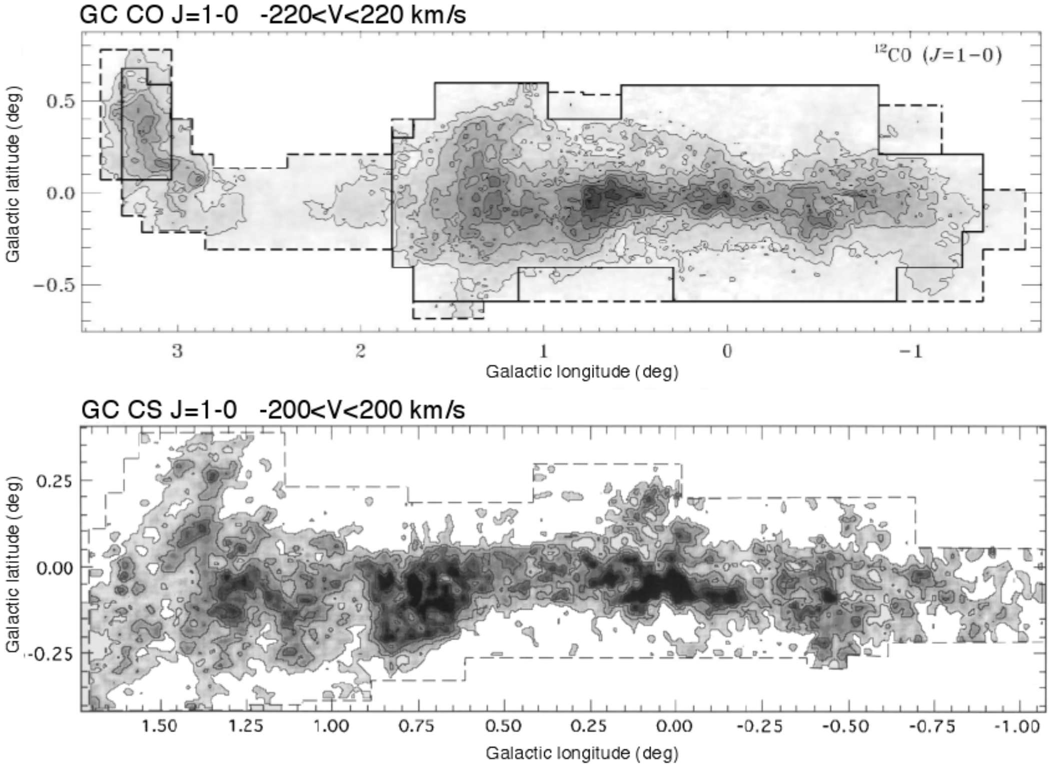

Figure 1.5: *Upper panel*: Maps of the ^{12}CO J=1-0 line emission in the GC region integrated over the velocity range V_{LSR}=40 to 50 km s^{-1}. Contours are drown at every 200 K km s^{-1}. (from Oka et al. (1998)). *Lower panel*: Velocity integrated CS J=1-0 emission in the GC region. The data have been numerically convolved with a 60" circular Gaussian beam. The velocity integrated range is from 40 to 50 km s^{-1}. Contour interval and first contour level are both 35.7 K km s^{-1} in T_{MB}. (from Tsuboi et al. (1999)). Both CO and CS data have been taken with the 45 m telescope at the Nobeyama Radio Observatory.

that isolating the line emission within different velocity ranges is the main way to identify coherent molecular structures.

The lv-diagrams of the molecular emission observed in the GC region show that, together with circularly rotating molecular complexes located close to the geometric centre of the Galaxy, the so called Central Molecular ring (CMR), there are many structures corresponding to MCs which move in non circular trajectories; this might be the resulting response of the clouds to a bar potential (e.g. Binney et al., 1991). An exhaustive representation of the geometrical structure of the CMZ has been presented by Rodríguez-Fernández (2006, see Fig.1.6); besides the CMR, the CMZ is populated with molecular clumps and molecular filaments few hundreds pc long.

The MCs in the CMR are warm (temperature up to 150 K) and dense (10^4 cm^{-3}). The heating mechanism which have been proposed encompass the photoionisation of the ex-

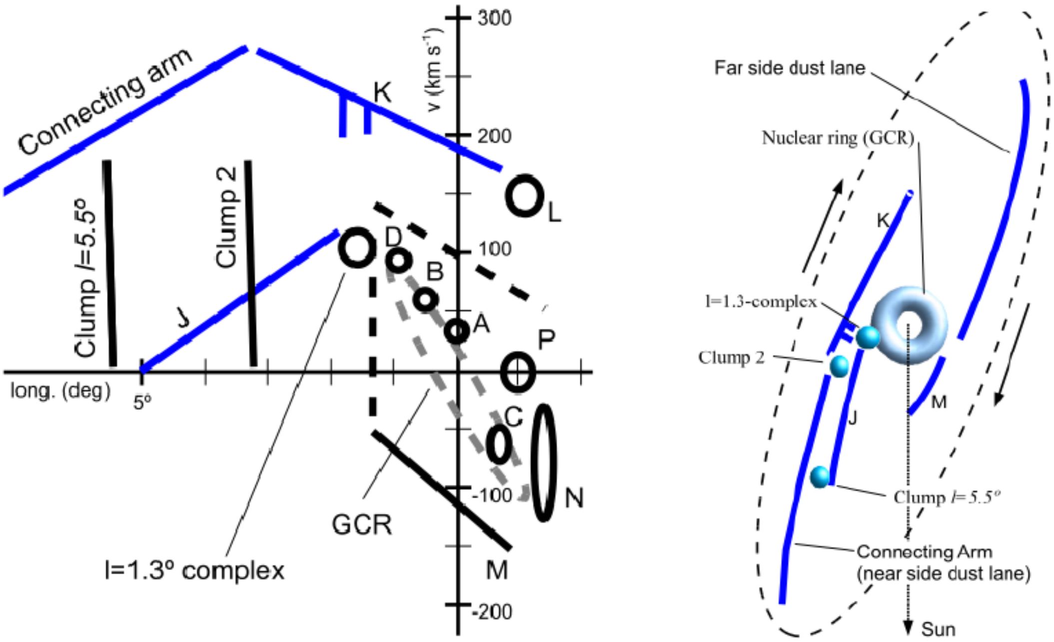

Figure 1.6: *Left panel*: diagram of the main kinematical structures visible in the *l*-*v* diagram of the inner CMZ. The labels A-D represent the main molecular complexes in the GC region, from Sgr A to Sgr D. The other letters represent other structures, reported in the text. *Right panel*: Possible face on view of the CMZ, with the same structures as highlighted in the left panel (Rodríguez-Fernández, 2006).

ternal layers of a molecular cloud (photo-dissociation regions) and magneto-hydrodynamic shocks (Rodríguez-Fernández & Martín-Pintado, 2005); while the presence of sources of ionising continuum in the CMZ is certain, and includes massive stars, stellar clusters (i.e. Arches and Quintuplet) and X-ray binaries, the presence of propagating shocks in the CMZ is less straightforward to demonstrate. In fact, molecular abundances in the CMR suggest that the UV radiation from massive stars or foreground emission can only account for the heating of 10 to 30% of the molecular gas (Rodríguez-Fernández et al., 2004). On the other hand, there are observations of molecules abundances (SiO and organic molecules like CH_3OH) which clearly point in favor of an important contribution by shocks to the heating of the molecular gas in the CMR and the l=1.3° complex; for example, the abundance of CH_3OH and C_2H_5OH is high in MCs which are not associated with thermal continuum sources, whereas their abundances decreases by more than a factor of ten in clouds associated with thermal continuum sources (Martín-Pintado et al., 2001). Contrarily, the clouds in non-circular orbits do not present signs of star formation (Oka et al., 1998); the physical conditions of these clouds are not well known because less observed. However, dense CS-emitting clouds ($n>10^4 cm^{-3}$) are seen in both the CMR and all the other kinematic components of the *lv*-diagram shown in Fig.1.6.

As already discussed, there are many heating mechanisms which, all together, might account for the warm temperature typically measured in MCs within the CMZ; exposition to UV radiation from young stars and/or stellar clusters, magnetic viscous heating (which requires mGauss magnetic fields within the clouds), cosmic rays bombardment, and dissipation of supersonic turbulence (e.g. Huettemeister et al., 1993). Heating by collisional dissipation of kinetic energy via dust particles cannot account for the warm temperature in the MCs because of the homogeneous low temperature of the dust found in the CMZ, $T_d \ll T_{gas}$ (Pierce-Price et al., 2000); the same condition for the dust temperature seems to suggest that the gas heating is unrelated to UV radiation.

However, all these mechanisms must be able to supply enough heating in order to compensate a cooling rate of $\Lambda \sim 6 \times 10^{-22}$ erg s^{-1} cm^{-3} (Güsten & Philipp, 2004). From this cooling rate it is also possible to estimate the time scale for thermal cooling of molecular clouds; Goldsmith & Langer (1978) have quantified this timescale to be less than about 10^5 years for gas densities in the range 10^3-10^4 cm^{-3}. In formulas (Goldsmith & Langer, 1978)

$$\tau_\Lambda = 1.5kT \left[\frac{\Lambda}{n_{H_2}}\right], \tag{1.21}$$

where Λ is the cooling rate and n_{H_2} is the gas density. Because the cooling timescale il short in cosmic standards, there must be a heating mechanism able to supply the energy able to mantain the clouds in thermal equilibrium. Here, we write the formulas for the heating of the molecular gas produced by the dissipation of supersonic turbulence and cosmic ray bombardment; the first one can be written as (Güsten & Philipp, 2004)

$$\Gamma_{tur} \sim 3.5 \times 10^{-28}\ v_t^3\ n_{H_2}\ (1\mathrm{pc/l}) \qquad [\mathrm{erg\ s^{-1}\ cm^{-3}}], \tag{1.22}$$

where v_t is the turbulent velocity inside the MC, and n_{H_2} and l are its density and size (Güsten & Philipp, 2004). If we assume a size of 5 pc, a turbulent velocity of 15 km s^{-1} and a density of 10^3 cm^{-3}, the resulting heating rate turns out to be 5×10^{-22} erg s^{-1} cm^{-3}, very similar to the Λ value previously written for the cooling rate. Looking now at the second mechanism, the cosmic ray bombardment, we can write the heating rate produced by this as (Goldsmith, 1987)

$$\Gamma_{CR} \sim 4 \times 10^{-28}\ n_{H_2} \left(\frac{\xi_p}{4 \times 10^{-17}}\right) \frac{\epsilon_h}{6\ \mathrm{eV}} \qquad [\mathrm{erg\ s^{-1}\ cm^{-3}}], \tag{1.23}$$

where ϵ_h is the typical mean energy heating input per primary ionisation, typically estimated to be 5-7 eV (Black, 1987) for protons with typical energies of some 10 MeV. Furthermore,

$$\xi_p = \frac{\xi_0}{1+\phi} \tag{1.24}$$

is the primary ionisation rate (s^{-1}), with ξ_0 the total ionisation rate (comprehensive of the secondary products of ionisation) and ϕ a constant factor which takes into account the different contributions by first-secondary-third ionisations (~0.7 for the secondary, van Dishoeck & Black, 1986). The typical value for the ionisation rate measured in the Sun neighbourhood is 3×10^{-17} s^{-1} (Webber, 1998), while the study of molecular lines of ionised species like the H_3^+ and H_3O^+ show that in the GC region the same parameter can be up to 100 times higher than in the solar environment, with a typical value in the order of 2-7×10^{-15} s^{-1} (Oka et al., 2005). Recently, Crocker et al. (2007) estimated for the Sgr B2 MC an ionisation rate due to cosmic ray interaction with the gas particles of 4×10^{-16} s^{-1}, therefore still significantly higher than what found in outer regions of the Galaxy. Also the cosmic ray bombardment can provide the amount of heating necessary to keep the molecular gas warm; specifically, assuming a density of the MC of 10^4 cm^{-3} and ξ_p ~4×10^{-15} s^{-1}, the resulting heating rate Γ_{CR} perfectly matches the relative cooling rate $\Lambda \sim 6 \times 10^{-22}$ erg s^{-1} cm^{-3}.

Now we move on to discuss the statistical properties of the MCs in the CMZ. We first define the virial mass of a MC as the mass that the cloud must have in order to avoid rapid dissociation by internal turbulence; as we previously discussed, the MCs in the GC region show a very large range of turbulent velocities, sometimes as large as 30-40 km s^{-1}. In order to avoid rapid dissociation due to the turbulent motion of the gas particles, a MC has two ways to behave: either it is massive enough to stay gravitationally bound or, otherwise, it must be confined by some kind of pressure that counterbalances (inwards) the turbulent pressure which tends to dissociate the cloud (outwards). In the presence of an external pressure P_{ext} which acts against the cloud dissociation, the equation of the virial theorem can be written as (Spitzer, 1978)

$$4\pi R^3 P_{ext} = 3M\sigma_v^2 - \frac{3GM^2}{5R}, \tag{1.25}$$

where R is the radius of the cloud, M its mass and σ_v the velocity dispersion (Miyazaki & Tsuboi, 2000). In case there is no external pressure (P_{ext}=0), the solution of the above equation gives the expression for the *virial mass*, i.e. the mass of a cloud gravitationally bound in equilibrium (no gravitational collapse, no turbulent disruption, i.e. the kinetic energy of the molecules is balanced by the gravitational potential of the cloud). This mass can be written as

$$\frac{M_{vir}}{M_\odot} \approx 10^3 \left(\frac{R}{\mathrm{pc}}\right) \left(\frac{\sigma_v}{\mathrm{km\ s^{-1}}}\right)^2, \tag{1.26}$$

assuming that the cloud has a spherical shape and uniform density (of course, an idealized model). As first pointed out by Larson (1981), the MCs in the disk of the Galaxy are approximately in a virial equilibrium, since their virial mass is equal to the mass of the cloud measured from line intensity measurements. The situation dramatically changes for MCs in the GC region; Miyazaki & Tsuboi (2000) showed that the virial masses of the MCs studied in the CMZ through CS emission line at 49 GHz are typically one order of magnitude larger than the measured masses. This is shown in the left panel of Fig.1.7, where the virial mass of the MCs is plotted against the measured mass for MCs in the disk and in the GC region, to emphasize the difference; the filled symbols are the GC clouds,

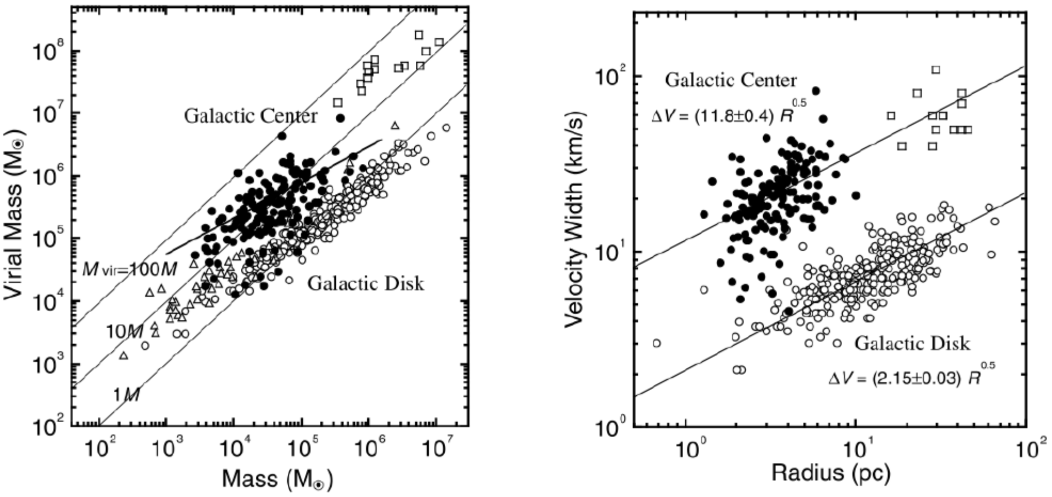

Figure 1.7: *Left panel*: comparison between the virial mass of the MCs and their measured mass (through CO-CS line intensity). Empty circles are for Galactic disk structure, whereas black points are for GC complexes; the empty squares represent the most massive structures in the CMZ. The thick solid line represents the best fit function (power-law) for the GC MCs; the other solid lines shows the M$_{vir}$=100M, M$_{vir}$=100M and M$_{vir}$=M respectively (Miyazaki & Tsuboi, 2000). *Right panel*: comparison between the velocity width (Δv) size relation for MCs in the Galactic disk (empty points), and the GC region (black). The solid lines show the best fit power law functions to the data, whose equations are reported on the plot and in the text (Miyazaki & Tsuboi, 2000).

with the empty squares on the top being the most massive of the molecular complexes lying in the GC region identified in the CO J=2-1 survey (Oka et al., 1998). The lowest solid line represents the analytical function M$_{vir}$=M, which is fairly well populated by the empty circles representing the MCs in the disk; spannig the plot upwards, we see the other two lines which identify the functions M$_{vir}$=10M and M$_{vir}$=100M.

We can clearly see that the black and white circles are two distinct populations, with the black circles well distributed around the M$_{vir}$=10M curve and therefore indicating that these clouds must be bound by an external pressure. Fitting the virial mass of the GC MCs as a function of the measured mass, Miyazaki & Tsuboi (2000) found an empirical relation between these two quantites which can be expressed as:

$$\frac{M_{vir}}{M_\odot} = (1.2 \pm 1.1) \times 10^3 \left(\frac{M}{M_\odot} \right)^{0.57 \pm 0.07} \tag{1.27}$$

This relation states that, for GC clouds, the M$_{vir}$ $\propto$ M$^{2/3}$; this result is also consistent with the predictions of some theoretical models in which the molecular clumps are confined by magnetic pressure (e.g. Bertoldi & McKee, 1992), in which the magnetic energy of the cloud is comparable with the its kinetic energy. In conclusion, we saw that most of the MCs in the GC region are higly turbulent, not gravitationally bound, and the dissociation due to the high kinetic energy of the particles is avoid by the presence of an external pressure. The favoured interpretation (nowadays) is that the gravitationally unbound MCs are kept in equilibrium by magnetic pressure, where the magnetic fields required to provide such a high pressure are in the order of few mGauss (which have indeed been observed in GC MCs, e.g. Crocker et al., 2007). The GC region is also filled by a diffuse emission usually modeled with two thermal plasmas with temperatures of kT_{warm} ∼1 keV and kT_{hot} ∼6.5 keV (Koyama et al., 2007a); the thermal pressure estimated for these two diffuse components of the ISM medium surrounding the clouds is on the order of 10^{-10} and 10^{-9} erg cm^{-3} respectively (Muno et al., 2008), insufficient to confine the highly turbulent clouds, whose turbulent pressure has been estimated to be on the order of 10^{-8} erg cm^{-3}; on the other hand, a magnetic field B∼mGauss has a energy density (pressure) $B^2/8\pi \approx 10^{-8}$ erg cm^{-3}, and therefore could bind the cloud, solving the issue.

As a further application, Miyazaki & Tsuboi (2000) plotted the velocity dispersion measured in the CS J=1-0 maps against the radius of the clouds. The σ_v-R relation was first reported by Larson (1981, see Fig.1.2) and investigated by many authors over different mass ranges. In the right panel of Fig.1.7 we show the σ_v-R plot for the GC clumps as well as for the clouds in the Galactic disk. As we can see from the plot, for a certain size of the cloud, the GC MCs are much more turbulent (and generally more massive, given the higher densities found in the GC region). A least squared fit to the data gives

$$\sigma_{\rm v}({\rm km\ s^{-1}}) = (11.7 \pm 1.4) \left(\frac{\rm R}{\rm pc}\right)^{0.50 \pm 0.08} \tag{1.28}$$

The index is 0.5, approximately equal to the value found for the same σ_v-R relation in disk clouds (e.g. Dame et al., 1986). For these periphery clouds, the constant coefficient which quantifies the turbulence in the cloud is a factor of 5.5 lower than that found in GC clouds, i.e. 2.15±0.03 (see right panel of Fig.1.7, Miyazaki & Tsuboi, 2000). Also in this plot, the massive complexes in the GC are reported in empty squares, at the top right of the diagram; these clouds also well obey the relation found for smaller clumps.

Last but not least, we want here to present the mass and size spectra observed for GC MCs, shown in Fig.1.8. Assuming a power law distribution of the masses of the form $dN/dM \propto M^{-\gamma}$, the best fit function to the mass spectrum has been measured to be

$$dN/dM \propto M^{-1.59 \pm 0.7} \qquad (M \geq 10^4 M_\odot) \tag{1.29}$$

The best fit value for the spectral index has been measured to be 1.59±0.7 (Miyazaki & Tsuboi, 2000), in very good agreement with the spectral index values (in the range ∼1.3-1.9) of other MCs spread around the Galaxy and surveyed in different molecular emission lines. Of course, the sensitivity limit and angular resolution of the surveys influence the turnover at the low mass stage of the curves. The so-derived mass spectrum of GC MCs is shown in the left panel of Fig.1.8, for MCs more massive than $10^4 M_\odot$.

The other physical quantity which has been studied by Miyazaki & Tsuboi (2000) is the size spectrum of the MCs. This is shown in the right panel of Fig.1.8, for MCs radii

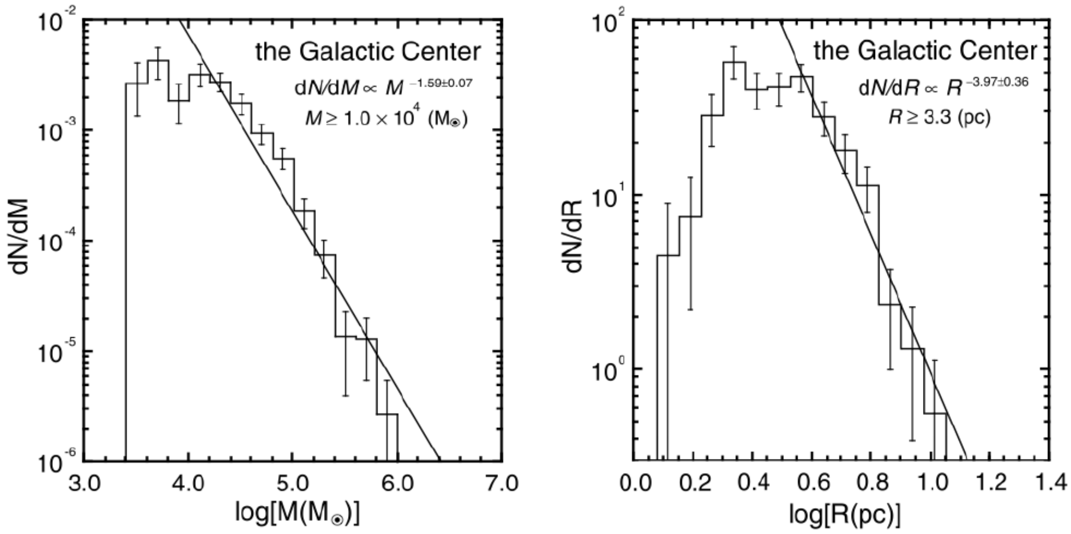

Figure 1.8: Mass (left) and Radius (right) spectra of the MCs in the GC region. The solid lines shows the best fit power law function whose equations is also written in the plots (Miyazaki & Tsuboi, 2000).

longer than 3.3 pc (due to angular resolution limitations). A fit to the data with a power law of the form $dN/dR \propto R^{-\gamma}$, returns the best fit function

$$dN/dR \propto R^{-3.97\pm0.36} \qquad (R \geq 3.3pc) \tag{1.30}$$

For the disk clouds, Elmegreen & Falgarone (1996) found $dN/dR \propto R^{-3.3}$, which, although lower than what found for the GC MCs, is still consistent with it if statistical uncertainties are taken into account.

A further fundamental result of the CO J=1-0 survey (Oka et al., 1998) is the discovery of high velocity compact clouds (HVCCs), molecular complexes described by compact size and very large velocity widths, which translate in enormous kinetic energies and short expansion times.

In the panel (a) of Fig.1.9 we can see that most of the discovered HVCCs are associated with the locations of the most massive molecular complexes found in the CMZ, whereas only few of them are isolated (Oka et al., 2010). The panel (b) represents the position of these peculiar clouds in the σ_v-R diagram; the HVCCs can be defined to be a new (different) population of MCs peculiar of the GC region, to be compared with the ones in Fig.1.7. The velocity widths well distribute around 100 km s^{-1}, a value much higer than what found in other clouds in the CMZ and in the Galactic disk; as a result, the ratio between the virial mass of these compact clouds and the observed mass is very high, due to the high turbulence which characterise these structures. Also the energetic of these clouds is unique; the kinetic energy derived for the discovered HVCCs is plotted in the panel (c) of Fig.1.9, where approximately 2/3 of the clouds have kinetic energies higher

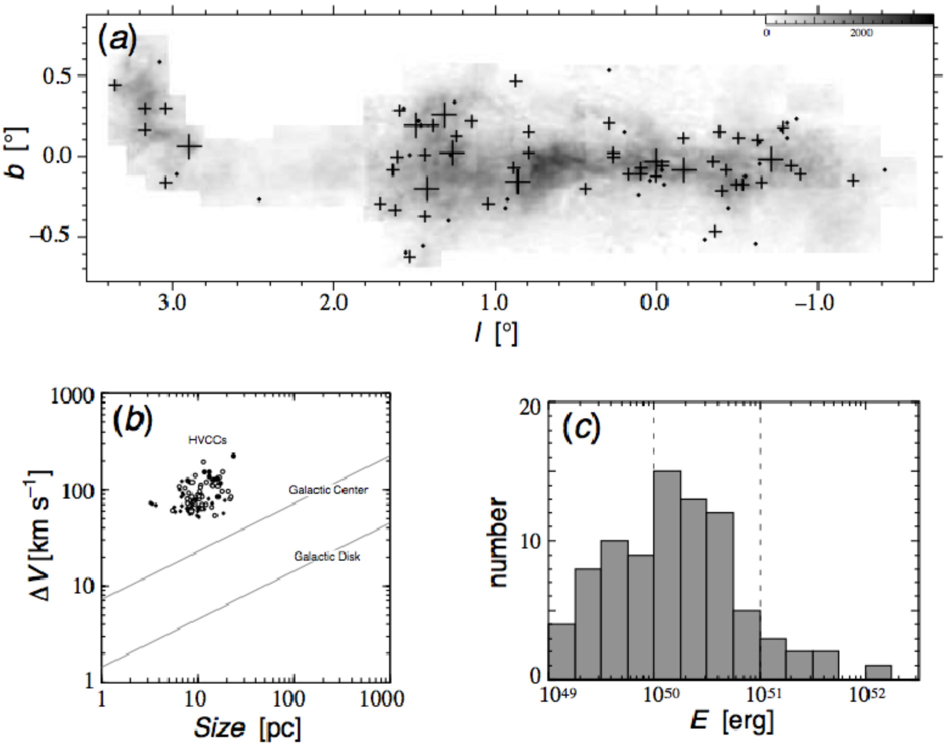

Figure 1.9: *(a)*: The position of the HVCCs in the CMZ (plus) on the background of the CO J=1.0 line intensity. The size of the + sign indicates the magnitude of the kinetic energy associated to the cloud. *(b)*: velocity dispersion - size plot for the HVCCs. The two solid lines shows the best fit power laws for MCs in the GC region and in the Galactic disk (see also Fig.1.7). *(c)*: histogram distribution of the kinetic energy of the HVCCs (Oka et al., 1998).

than 10^{50}erg s^{-1}, and where there are clouds with a kinetic energy which is higher than the energy released in a supernova detonation ($\sim 10^{51}$erg s^{-1}). Generally, the CO J=3-2/J=1-0 ratio ($R_{3-2/1-0}$) is thought to be a good indicator of the kinetic temperature and the density inside the cloud, when the CO column density per unit of velocity width ($N_{CO}/d\sigma_v$) is not too large (e.g. Oka et al., 2010). For example, high $R_{3-2/1-0}$ values have been found in the outer layers of MCs irradiated by the UV radiation from a massive star (White et al., 1999), as well as in the shocked molecular gas adjacent to SNR (Dubner et al., 2004); the $R_{3-2/1-0}$ is higher than $\sim$1 when the rotational level J=3 is well termalised. These HVCCs are defined by size and line intensity ratios; regarding the last, Oka et al. (2010) defined a lower threshold for the $R_{3-2/1-0}$ ratio to 1.5; for $R_{3-2/1-0}$ $\geq$1.5 the MCs density can be estimated to be in the order of n_{H_2} $\geq 10^4$cm^{-3} and the kinetic temperature to be 50K when $N_{CO}/d\sigma_v = 10^{17}$cm^{-2}(km s^{-1})$^{-1}$. As a reference, the main $R_{3-2/1-0}$ value for MCs in the Galactic disk is $\sim$0.4 (Oka et al., 2007), whereas the GC region is about 0.7 (Oka et al., 2010); accordingly, the HVCCs seem to be a peculiar state of the molecular gas found in the GC region. The origin of such a high $R_{3-2/1-0}$ ratio deals, once again, with shocks; its spatial distribution is clumpy and spotty, which suggest its origin to be connected with explosive events like SN explosions. But what is the origin of these HVCCs? An interesting suggestion was given recently by Oka et al. (2010); if the high turbulence measured inside an HVCC is produced by a supernova explosion, and since where SN are there must be a high concentration of mass, these peculiar turbulent molecular structures must be spatially associated with young stellar clusters, which cannot be observed because of the thick layer of ISM they are embedded in. Within this scenario, it is possible to convert the kinetic energy histogram of the HVCCs in the mass of the stellar clusters which might be responsible for the high SN explosion rate. As a result, the cluster masses range from $10^2/\eta$ $M_\odot$ to $10^5/\eta$ $M_\odot$, where η parametrise the efficiency of energy conversion from mechanic to kinetic (Oka et al., 2010).

An interesting source in this mass range located at the GC, only about 20 pc in projection from Sgr A*, which will be subject of study in this thesis, is the Arches cluster, the most massive and densest stellar cluster in the Galaxy; this unique source age is estimated to be $\sim$2 Myr and hence did not experience a supernova explosion yet, and indeed there is no spatial correspondence between the position of the Arches cluster and an HVCC. However, the presence of the Arches cluster suggests that other massive young clusters could lie in the GC region, and therefore contributing, through SN explosions, to produce the observed turbulence in nearby MCs.

1.2 Cosmic rays

Besides the different phases of the interstellar medium presented in the last section, the interstellar space is filled with another important component, cosmic rays (CR). The term *rays* is slightly misleading since it is not light that we are talking about; CR are the most energetic particles populating the Universe, with energies up to 10^{20} eV. CR are charged particles, either electrons or atomic nuclei, completely ionised; for this reason it is impossible to trace the original trajectory of the detected particles, since a charged particle is randomly scattered by galactic (and intergalactic) magnetic fields. If a broader definition of CR is considered, then we can also include in this population neutrinos and γ-rays (from nuclear de-excitation) which, due to their electric neutrality, can trace directly their primary source. Due to the low fluxes of particles with energies in excess of 1 TeV (e.g. Nagano & Watson, 2000), most observations are ground based, making use of different techniques; the fluxes being very low, a detector as large as possible is needed in order to get enough statistics for astronomical studies, and this is achieved using the Earth's atmosphere as a *giant* detector.

Primary CR are those particles that are accelerated in astrophysical sources (SNR, PWN, etc.); these are basically electrons, protons and atomic nuclei like Carbon, Oxygen and Iron and the other nuclei produced by stellar evolution. Other nuclei such as lithium, beryllium and boron, which are not abundant products of stellar nucleosynthesis, are called *secondaries*, because they are the results of the interaction of the primary CR with the

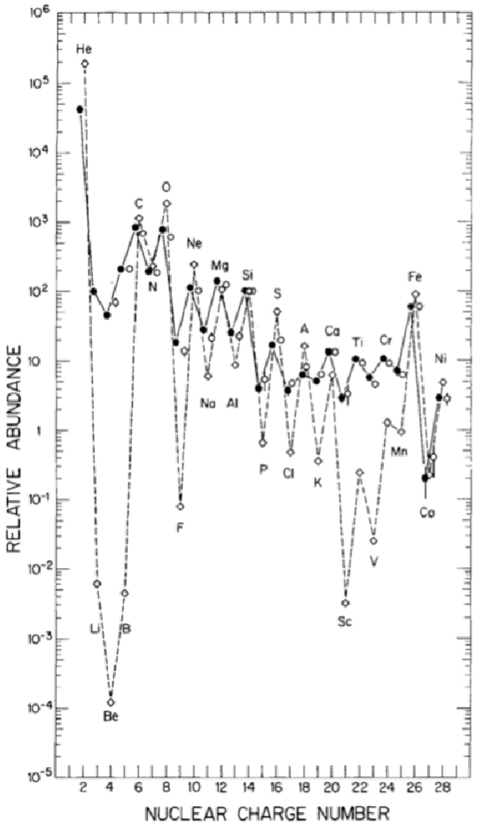

Figure 1.10: The element abundances of cosmic rays as measured at Earth compared to the solar abundances, all measured with respect to Silicon. Empty circles are solar abundances, whereas black points represent CR (Simpson, 1983).

ISM. In the GeV regime, CR from outside the Solar system are strongly modulated by the solar wind, which decelerates, and partly shields, the lower energies (up to GeV) CR; as a result, the intensity of any component of CR in the GeV range depends both on time and location (e.g. Cronin, 1999).

1.2.1 Composition

The composition of primary CR depends on which part of the spectrum is observed; generally, about 90% of the CR outside the Earth's atmosphere are protons, almost 9% are Helium nuclei (α particles) and the rest are electrons and heavier nuclei which are produced by stellar nucleosynthesis (e.g. Eidelman et al. , 2004). Light nuclei which are not final products of the stellar evolution, are found in CR with a much higher abundance relatively to their abundance in the Solar vicinity (Solar abundances); Fig.1.10 shows the element abundance found in CR as measured at Earth, compared to the solar system abundances (Simpson, 1983).

The most evident difference is the abundance of the light elements Li, Be and B; these are indeed some 10^{5-6} more abundant in CR than in the solar neighbourood. This difference in the relative abundance of the light elements is a consequence of the way secondary CR are produced. When the heavy nuclei like C and O collide with the ISM, they break up into the lighter nuclei of lithium, beryllium and boron; this process is called CR spallation, a form of natural nuclear fission (e.g. Gaisser, 2005). Moreover, the Li, Be and B energy spectra are found to be steeper than those of C and O, suggesting that the spallation process has an inverse dependence on the energy of the primary CR, i.e. less CR spallation occurs for the higher energy nuclei, most probably because the most energetic nuclei can more easily escape the Galactic magnetic field that keeps the low energy particles bound to the Galactic disk (e.g. Gaisser, 2005). Spallation is also responsible for the high abundances (compared to solar) of Scandium (Sc), Titanium (Ti), Vanadium (V), and Manganese (Mg) nuclei in CR, which are produced by collisions of Fe and Ni nuclei with the ISM (see Fig.1.10 Simpson, 1983).

1.2.2 Energetics

The relative abundance of secondary CR in the Galaxy is a measure of the propagation time of these particles before they succeed in escaping from the Galaxy. The equation of diffusion of CR in the Galaxy, which relates the observed element abundances and spectra to the original quantities (Gaisser, 2005)

$$\frac{N_i(E)}{\tau_{esc}(E)} = Q_i(E) - \left(\beta c n_H \sigma_i + \frac{1}{\tau_i}\right) N_i(E) + \beta c n_H \sum_{k \geq i} \sigma_{k \to i} N_k(E), \tag{1.31}$$

where $N_i(E)$ is the density of CR nuclei with mass i, n_H is the density of target nuclei in the ISM, $Q_i(E)$ is the number of primary CR (mass i) accelerated per cm^3 per second, and σ_i ($\sigma_{k\to i}$) is the cross section for interaction of CR with the ISM (Gaisser, 2005). The term in parentheses in the right hand side of the equation above represents losses due to interactions described by the cross sections σ_i and the decay for unstable nuclei with lifetime τ_i (Gaisser, 2005). It is therefore possible to roughly estimate the characteristic diffusion time τ_{esc}, neglecting propagation losses and constraining $Q_S=0$ for secondary nuclei. With these assumptions the diffusion equation can be written as (Gaisser, 2005)

$$n_H \tau_{esc} = \frac{1}{\beta c \sigma_{P \to S}} \frac{N_S}{N_P} \tag{1.32}$$

Let us also assume a particle density in the disk of 1 particle per cm^3, and $\sigma_{P\to S} \sim 10^{-25}$ cm^2; as a result we can derive a characteristic time for the propagation of CR of $\sim 10^7$ years, much longer than the thickness of the Galactic disk (300 pc ∼ 1000 light years) (Gaisser, 2005). Hence, CR diffuse slowly in the galaxy. As we already introduced, the ratio N_S/N_P decreases with increasing E of the primary CR; as a consequence, τ_{esc} also decreases with the energy (e.g. Gaisser, 2005)

$$\tau_{esc} \propto E^{-0.6} \tag{1.33}$$

To see the consequences of this energy dependance on the source spectrum, we consider an abundant primary nucleus like H or He. For these nuclei, the third term of the diffusion equation can be neglected (no important contribution form feed-down of heavier nuclei), and so can be the losses (small cross sections). Accordingly, the diffusion equation can be written as (Gaisser, 2005)

$$Q(E) = N(E)/\tau_{esc} \approx N(E) \times E^{0.6}, \tag{1.34}$$

where N(E) is the local energy density spectrum of CR, related to the measured flux by (Gaisser, 2005)

$$N(E) = \frac{4\pi}{c}\phi(E) \qquad \phi(E)\ (\text{particles/cm}^2\ \text{s sterad GeV}) \approx \mathrm{E}^{-2.7} \quad (\mathrm{E} \lesssim 10^{15}\text{eV}) \tag{1.35}$$

From this calculation (Gaisser, 2005), we see that the CR accelerator must be described by a power law with spectral index α ~2.1; this value is remarkably similar to the spectral index generated via first order acceleration by strong shocks (Fermi first order mechanism). The above calculation is based on the assumption that the sources of CR lie in the disk of the Galaxy. If so, we can integrate the equation for Q(E) over energy and space (being V_G the Galaxy volume) to find the total power P_{CR} required in order to mantain the CR in equilibrium to be (Gaisser, 2005)

$$P_{CR} = \int d^3x \int Q(E)dE = V_G \frac{4\pi}{c} \int \frac{\phi(E)}{\tau_{esc}(E)} dE \tag{1.36}$$

Substituting the value of τ_{esc} found above and the expression for the observed spectrum, one finds P_{CR} ~10^{41}erg s^{-1}. The kinetic energy which can be supplied by a SN explosion is in the order of 10^{51} erg s^{-1}; assuming a rate of explosion of 3 per century, this turns in a power supplied by SN explosions and dissipated into the ISM by shocks of P_{SN} ~10^{42}erg s^{-1} (see Gaisser, 2005). This is one piece of evidence in favour of the hypothesis that Galactic CR with energies up to 10^{15} eV are accelerated by SN, although a definitive proof has not been found yet.

The CR energy spectrum contains much information on the acceleration mechanisms, the sources of primary CR and the intensity of the mean galactic magnetic field. The spectrum of CR with energy higher than 100 MeV (up to more than 10^{20} eV) is shown in the left panel of Fig.1.11 (Cronin, 1999), together with three values of the particle flux for typical energies of 100 GeV (1 particle m^{-2} s^{-1}), 10 PeV (1 particle m^{-2} year^{-1}), and ~10^{18} eV (1 particle km^{-2} year^{-1}); these numbers give the idea of the difficulty to study the most energetic particles, which need a large collecting area in order to be detected, and need to be operative for a long time to obtain enough statistics.

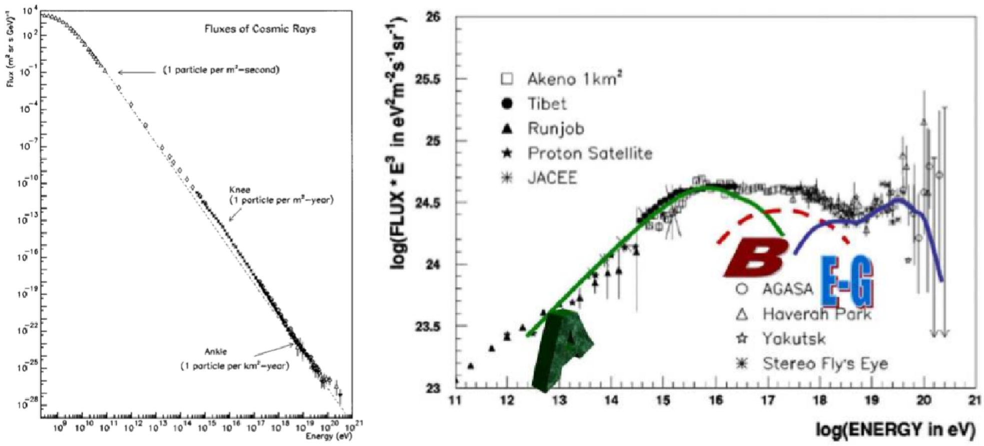

Figure 1.11: *Left*: CR energy spectrum between 1 and 10^{12} GeV (Cronin, 1999). In the plot are also indicated the fluxes of CR measured at Earth at energies of $\sim 10^{15}$ GeV, at the knee ($\sim 10^{15}$ GeV) and at the ankle ($\sim 10^{19}$ GeV). *Right*: CR energy spectrum multiplied for E^3 in order to show the three populations of CR (Nagano & Watson, 2000; Gaisser, 2010); *A* refers to the Galactic component, *E-G* to the extragalactic component and *B* to the higher energetic galactic component whose origin is still under debate.

1.2.3 Spectrum and acceleration of cosmic rays

The differential spectrum of CR is described by a power law of the form

$$dN/dE \propto E^{-\alpha} \tag{1.37}$$

where the spectral index α varies slightly in the three main regions of the spectrum, which are separated by two peculiar structures, the so called *knee* at about 10^{15} eV and the *ankle* at some 10^{18} eV (e.g. Nagano & Watson, 2000). The spectrum has initially a spectral index α=2.7, it then steepens after the knee with α=3.0 between the knee and the ankle, and finally it hardens again at energies above the ankle; the spectral index for the ultra high energy CR (UHECR) is not well defined due to the lack of data (Cronin, 1999). Between the knee and the ankle, there is increasing evidence for a third minor structure, the so called second knee, where the spectrum softens from an index of α=3.0 to α=3.3 (e.g. Gaisser, 2005).

A possible explanation for the nature of the knee is that this structure is associated with the upper limit for the energy that acceleration from shocks in SN explosions can supply to the particles. If this is the case, the knee represents a separation between particles of Galactic origin and the ones coming from the extragalactic universe (Peters, 1960). The relatively smooth behavior of the cutoff is due to the different cutoff energies of different nuclei, depending on the magnetic rigidity of the particle, i.e. R(Z)=Pc/Ze, which provides the scaling relation between the energy of the particle (E=Pc) and its charge (Ze) (Gaisser, 2010). In the scenario where the cutoff of the spectrum occurs at the characteristic rigidity

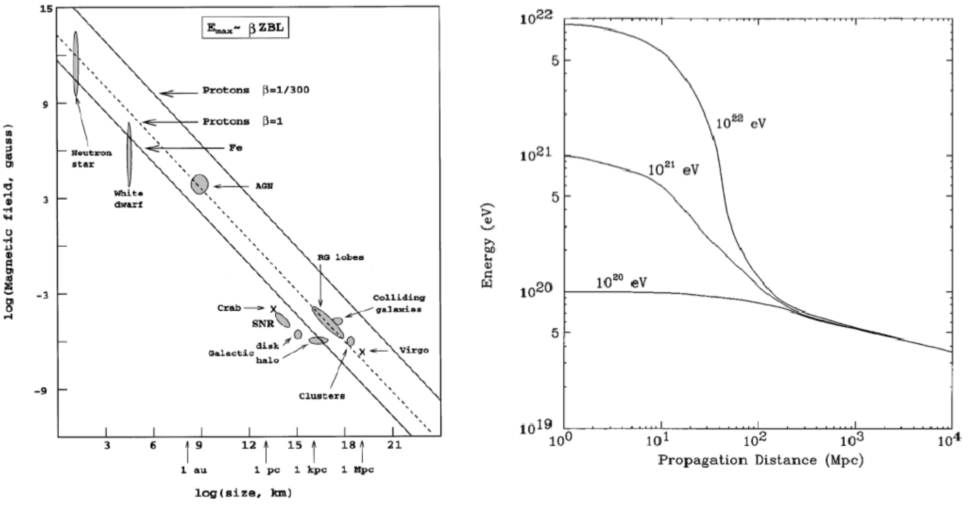

Figure 1.12: *Left*: size versus magnetic field of the possible sites of CR acceleration (Hillas, 1984; Cronin, 1999). Protons cannot be accelerated to energies above 10^{20} eV in sites under the dashed line. *Right*: Proton energy as a function of the propagation distance through the CMB; beyond 100 Mpc, all the three lines tent to an energy lower than 10^{20} eV (Cronin, 1999).

R_c, protons are the first to bend at E_c=eR_c, and then come He nuclei at E_c=2eR_c and so on up to the heavier nuclei; the energy range occupied by this smooth cutoff is a factor of 30 (Gaisser, 2010). In the original idea by Peters, at this energy another component of extragalactic nature, with a harder spectrum, should dominate. In reality, what is shown by the observations is a softening of the spectrum, and a hardening only above the ankle (e.g. Gaisser, 2005). While CR above the ankle are known to have an extragalactic origin (region E-G in the right panel of Fig.1.11), the region between the knee and the ankle is the most controversial. The total power required to fill this region (region B in the right panel of Fig.1.11) can be calculated assuming a spectrum $Q(E) \propto E^{-2}$ and a different energy dependence of the propagation in this energy range, i.e. $\tau_{esc} \propto E^{-0.33}$. The result is a power requirement for the filling of the B region of about 2×10^{39}erg s^{-1}, less than 10% of the total power requirement for all the galactic CR (Gaisser, 2005); the source of these CRs is still unknown.

Particles are not easy to accelerate up to 10^{20} eV. A basic condition for the acceleration of a proton to such a high energy is that the product of the magnetic field B and the size of the acceleration region R is higher than 3×10^{17} Gauss cm (Cronin, 1999). Hillas (1984) presented an illustrative plot which shows the difficulty of accelerating CR to 10^{20} eV. We present his original plot, revised by Nagano & Watson (2000) in the left panel of Fig.1.12.

The upper limit on the energy E can be estimated to be (Cronin, 1999)

$$E_{18} \leq 0.5\beta Z B_{\mu G} L_{kpc}, \tag{1.38}$$

where E_{18} is the maximum energy (in units of 10^{18} eV), Z the nuclear charge of the particle, B the magnetic field of the acceleration source and L its size, and β=v/c is the velocity of the shock wave. The lines plotted in the left panel of Fig.1.12 correspond to a proton with E=10^{20} eV and different β factors. Efficient accelerators should lie above the solid β=1 line (Nagano & Watson, 2000). As seen in the plot, the only objects which can accelerate protons to these high energies are AGN, colliding galaxies and galaxy clusters. Another interesting effect which influences the energetics of the UHECR is their interaction with the CMB. At energies higher than 5×10^{19} eV, the cross section for the interaction of CR with CMB photons is high (Greisen, 1966; Zatsepin & Kuz'min, 1966). The right panel of Fig.1.12 shows the propagation of protons through the CMB; regardless of the initial energy of the proton, after a propagation of 100 Mpc (or longer) the proton kinetic energy will be lower than 10^{20} eV. This distance corresponds to a redshift of 0.025, and it is indeed very small when compared with cosmological distances. As a consequence, any CR proton recorded to have an energy higher than 10^{20} eV must have originated within 100 Mpc distance from the Earth, and there are not many sources in this distance range to satisfy the Hillas' criteria. The authors of the original papers (Greisen, 1966; Zatsepin & Kuz'min, 1966) indeed claimed discovery of an upper limit for the spectrum of CR.

1.2.4 Cosmic rays at the Galactic Centre

To conclude the section on the CR, we here briefly present three outstanding evidences of the presence of CR in the central region of our Galaxy; as discussed above, galactic CR are likely to have energies lower than 10^{15} eV, and therefore will be in the GeV-TeV regime. However, the propagation of such energetic particles cannot be traced directly to the acceleration source, since the interaction with the galactic magnetic fields change the original trajectory. To study the distribution of CR in the Galaxy it is possible to use the radiation that is produced by the interaction of these particles with both the surrounding ISM and the magnetic fields. CR interaction with a magnetic field results in the production of radio photons via synchrotron emission; one of the best and most evident example of synchrotron emission in the GC region can be seen in the non-thermal radio filaments and threads running perpendicular to the Galactic plane. In the left panel of Fig.1.13 we present a 90-cm view of the GC region as observed with the Very Large Array (LaRosa et al., 2000); it is surprising how the GC region is populated by these magnetic structures, the most prominent of which is the giant radio arc that is located at l$\sim$0.2 deg and runs for at least 30 pc. The presence of such unique structures is a peculiar property of the GC region, and it contributes to make the surrounding diffuse emission from radio to the more energetic X-rays and γ-rays particularly difficult to disentangle in its original components.

To infer the energetics of the CR involved in the radio emission at 90 cm (ν=330 MHz) we can write the formula for the characteristic frequency of the synchrotron emission produced by the interaction of an electron of energy E with a magnetic field of intensity B. This is (e.g. Rybicki & Lightman, 1979)

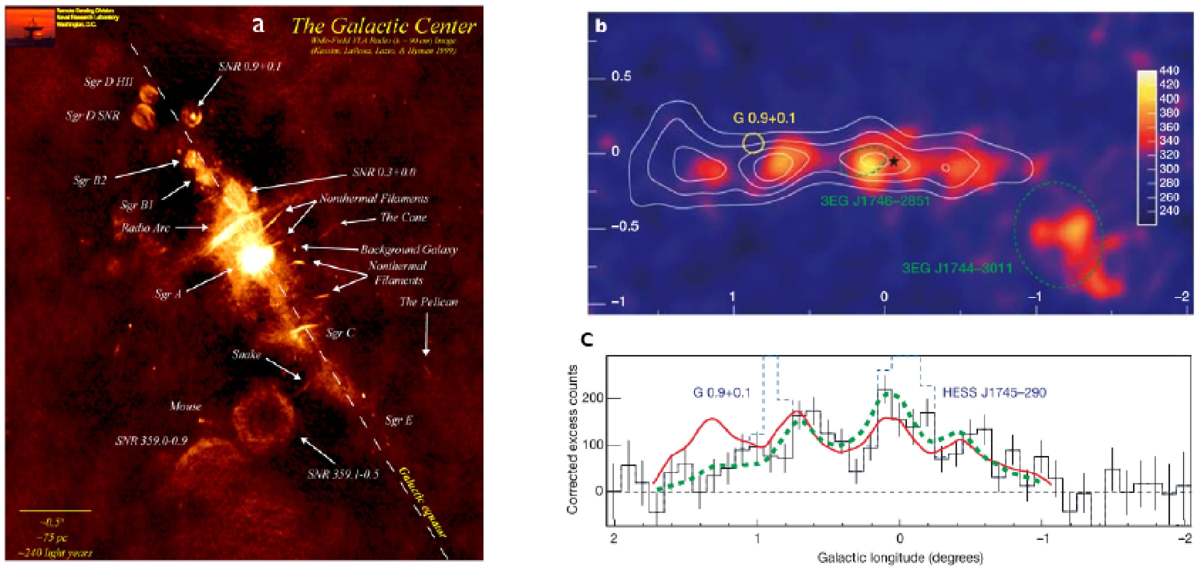

Figure 1.13: *a*: 90 cm view of the innermost GC region as measured with the VLA (LaRosa et al., 2000); in yellow are highlighted the brightest radio structures in the region, especially the giant radio arc. *b*: TeV map of the GC region. The colour map show the intensity of the TeV γ-rays once the brightest point sources have been subtracted. The contours represent the distribution of the CS J=2-1 molecular emission, smoothed in order to match the angular resolution of the HESS instrument (Aharonian et al., 2006). *c*: distribution of the TeV emission in galactic longitude. The red line traces the density of the molecular gas (CS emission), the black points show the TeV emission after point source subtraction, with the best fit model shown by the dashed green curve (Aharonian et al., 2006). To notice the mismatch between the black-green curve and the red one at longitudes higher than $\sim$1.2 deg.

$$\nu_{\rm c} = \frac{3\ {\rm e\ B}\ \gamma^2\ \sin\alpha}{16\pi\ {\rm m}} \approx 1.6\ {\rm GHz}\ \left(\frac{{\rm B}_\perp}{10^{-4}\ {\rm Gauss}}\right)\left(\frac{\rm E}{\rm GeV}\right)^2, \tag{1.39}$$

where e is the electron charge, $\mathrm{B}_\perp$ is the magnetic field perpendicular to the electron motion, γ is the electron Lorenz factor, α is the pitch angle and m is the electron mass. Magnetic fields in the GC non-thermal radio filaments have been measured to be in the order of a few mGauss. Therefore, the electrons to be associated with this radio emission are those with $\sim$GeV energies; for example, assuming B=0.1 mG, the energy of the electron emitting synchrotron emission at 90 cm is $\sim$0.9 GeV.

More generally, the γ-ray satellites EGRET and FERMI have discovered the presence of diffuse emission in the inner region of the Galaxy, due to the interaction of CR with the ISM and the photon field there (e.g. Strong et al., 2007). The main mechanisms which produce γ-ray emission from CR are: inverse Compton from the interaction of energetic CR with a low energy photon field, non-thermal bremsstrahlung due to the Coulomb collisions of e^{+}-e^{-} with the ionised nuclei and pion decay from interaction of CR hadrons with the ISM (Strong et al., 2007).

One of the most outstanding results found in the last decade is the discovery of diffuse TeV emission correlating with the distribution of the most massive complexes in the inner CMZ (Aharonian et al., 2006); these authors, together with mapping the TeV diffuse emission with an unprecedented angular resolution (better than 0.1 deg) using the H.E.S.S. atmospheric Cherenkov telescope, found that the inner ~200 pc of the Galaxy is filled with an extra component of recently accelerated hadronic cosmic rays. In the H.E.S.S. energy range, the dominant component of diffuse γ-ray emission is the pion decay, an electromagnetic process with a lifetime of 8.4×10^{-17} (basically immediate) whose diagram can be written as

$$p_{CR} + p_{ISM} \ \rightarrow \ \pi^0 \ \rightarrow \ \gamma + \gamma \tag{1.40}$$

The probability of decay in 2 γ-ray photons is ~0.988. The π^0 mass, the minimum energy that the decay products can have, is about 135 MeV/c^2; as a result, 2 γ-rays are produced in this electromagnetic process. The right panel of Fig.1.13 shows the results of the TeV study of the inner CMZ. Panel b shows that the TeV diffuse emission is extended for about 2 degrees along the Galactic plane, and well correlates with the contours of the CS molecular emission, which represents the location of the most massive MCs in the region. This emission is not only extended in longitude, but also in latitude, with a characteristic root mean squared width of 0.2 deg, corresponding to about 30 pc, remarkably similar to the height distribution of the molecular target material (Aharonian et al., 2006). The correlation between TeV photons and target material is a strong indication that this emission is due to the interaction of CRs with the MCs. The spectrum of the TeV emission has been measured to be harder than expected, resulting in a CR spectrum with a spectral index α=2.3, significantly lower than the one measured in the solar neighbourhood (α=2.7 see above). This result is readily understood considering that in the GC region the propagation effects are likely to be less pronounced than in the whole Galaxy, and therefore the hardening of the spectrum can be thought to be due to the vicinity of the CR source and accelerators; moreover, the flux of the TeV γ-rays has been measured to be higher than expected from models of ISM and γ-ray distribution (Aharonian et al., 2006). The higher than expected TeV flux, together with the harder than expected CR spectrum, indicates that there is a CR component other than the one filling the Galaxy. In the panel c of Fig.1.13 we present the correlation study between the γ-ray flux and the CS molecular emission; it is noticeable that, whereas the correlation is very good within 1 deg in longitude, at about 1.2-1.3 deg this correlation breaks, indicating that the additional CR component has not yet propagated outwards. The energy required to sustain this additional bunch of CR has been estimated to be about 10^{50} erg, therefore being approximately the 10% of the energy released by a SN explosion (Aharonian et al., 2006). If we represent the diffusion of protons through TeV energies with the diffusion coefficient

$$D = \eta \times 10^{30}\ cm^2 s^{-1}, \tag{1.41}$$

the diffusion timescale can be estimated to be t_{diff}=$R^2/2D$=$3000(\theta/1^{\circ})^2/\eta$ years (Aharonian et al., 2006). Accordingly, a source of age ∼10 kyr could be responsible for the presence of the TeV excess; given the time constraint and the energy required for this additional component, the best candidate is Sgr A East, a SNR whose age has been estimated at about 10 kyr (Maeda et al., 2002).

All the results presented clearly point to the presence of CR in the GC region, with a very wide range of energies and phenomenology. The presence of such an important component besides the classic phases of the ISM must be therefore taken into account in the discussion of the origin and the nature of the diffuse X-ray emission permeating the GC region, especially the 6.4-keV line emission originating from the ionisation of neutral Fe which will be the main subject of this thesis (Chapters 4 and 5).

1.3 The super massive black hole Sgr A*

The GC has been the subject of many years of research including both theoretical investigations and observations throughout the entire electromagnetic spectrum. Nowadays, there is no longer any doubt that the centre of the Milky Way hosts a SMBH with an estimated mass of $\sim 4\times10^6 M_{\odot}$ (Schödel et al., 2002), the radio counterpart of which has been called Sgr A* after its discovery in 1974 by Balick & Brown, published in their paper *Intense Subarcsecond Structure in the Galactic Centre* (Balick & Brown, 1974).

1.3.1 The evidence for an SMBH at the Galactic Centre

The first piece of evidence of the presence of a SMBH at the centre of the Galaxy came from dynamical measurements of the radial velocity of ionised gas which has been measured to increase up to few hundred km s^{-1} in the central parsec of the Galaxy (12.8 μm line of NeII, Wollman et al., 1977); the results of a virial analysis of these data led to the suggestion that the central parsec might be populated by a SMBH with a mass of some $10^6 M_{\odot}$, although the nature of this mass could not be completely substantiated by these measurements alone. In fact, gas motion is sensitive to many forces other than gravity, especially turbulence, which we have shown is acting within the ISM phases in the GC region (see Section 1.1.4). Progress in the study of the nature of the central mass came from the measurements of the motion of the stars within the innermost few parsecs; Genzel et al. (1996) studied the distribution of the nuclear mass, measuring radial velocities of a few hundred late type stars and a few dozen early type stars. These authors inferred a combination of a star cluster with a mass of $10^6 M_{\odot}$ with a core radius of about 0.4 pc and a central mass of $3.0\times10^6 M_{\odot}$, remarkably in agreement with current measurements. The major breakthrough came with the measurement of the proper motion of the fast moving ($\sim 10^3$ km s^{-1}) S-stars which lie in the inner arcsec (0.04 pc), which are characterised by velocity dispersions that can be well described with Kepler's law $\sigma_V \propto R^{-1/2}$ (Genzel et

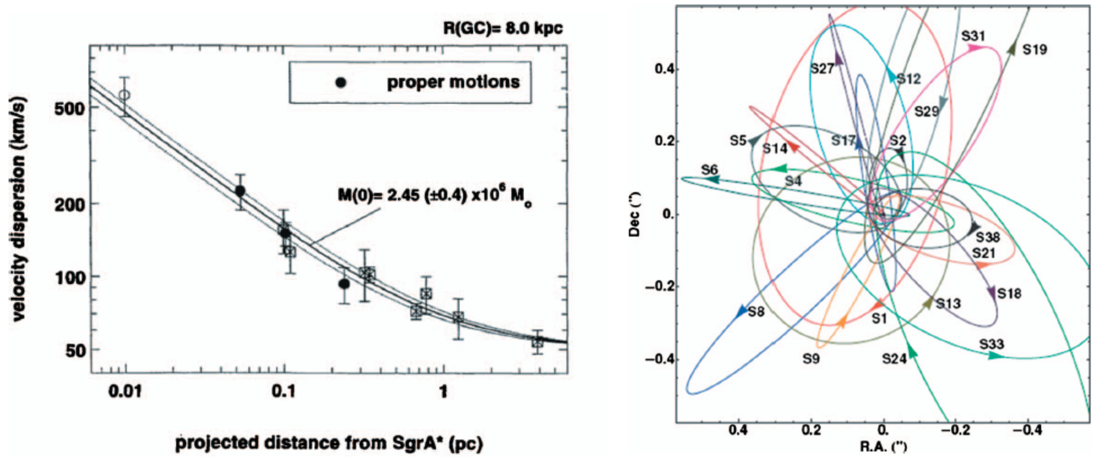

Figure 1.14: *Left*: velocity dispersion of the stars in the inner from Sgr A* (Genzel et al., 1997). *Right*: Stellar orbits of twenty S-stars (over about thirty) around the position of the SMBH Sgr A* as measured in a decade of NIR observations of the GC (Gillessen et al., 2009).

al., 1997; Ghez et al., 1998); as a result, the case for the presence of a central black hole of few millions $M_\odot$ has been well accepted. In the Fig.1.14 we present the stellar velocity dispersion against the separation (projected into the sky) from the position of Sgr A* of the S stars (Genzel et al., 1997).

In the following years, the two leading groups in the field, the infrared group at the Max Planck Institute for Extraterrestrial Physics and another at UCLA, aimed at tracking the orbits of the innermost S stars. The first one for which the entire orbit could be drawn is S2 (see Fig.1.14). This star has a revolution period of 15.8 years, a very high eccentricity e=0.88 (its pericentre distance being 17 light hours) and its orbital measurements indicated a mass for the central SMBH of $4.4{\times}10^6 M_\odot$ (Schödel et al., 2002; Ghez et al., 2003). With the new technologies of adaptive optics, resolution has improved dramatically over the last decade, and this has allowed to follow the orbits of nearly two dozens of S-stars, the orbit of the S2 star now being completely tracked (Gillessen et al., 2009). The results are shown in the right panel of Fig.1.14.

The currently accepted measurements of the distance to the GC and the mass of the SMBH Sgr A* are

$$R_0 = 8.28 \pm 0.15 \pm 0.29 \text{ pc} \qquad \mathrm{M_{SMBH}} = 4.3 \pm 0.2 \pm 0.3 \times 10^6 \ \mathrm{M}_\odot$$

where the first (second) error is a statistical fit (systematic) uncertainty (Gillessen et al., 2009). Sgr A* is nowadays the best evidence for the existence of astrophysical black holes. Very long baseline interferometry also allows us to measure with great precision the size of the radio emitting source Sgr A*. Doeleman et al. (2008) showed that the intrinsic size of Sgr A* decreases towards shorter wavelengths; at the shortest wavelength currently achievable (1.3mm), the source size has been measured to be 37^{+16}_{-10} μarcsec, corresponding to about 3.5 R_S.

To conclude, we can ask whether Sgr A* lies within the M-σ relation which relates the mass of the SMBH at the centre of many galaxies and the velocity dispersion of bulge stars (Gebhardt et al., 2000); Milky Way's measurement of velocity dispersions indicate that the SMBH at the GC lies well (within uncertainties) on the best fit M-σ relation.

1.3.2 Steady emission and flares from Sgr A*

Sgr A* is detectable in the radio, NIR and X-ray regimes of the electromagnetic spectrum; the spectral energy distribution is shown in the left panel of Fig.1.15. The compact radio source is detectable at all times; its spectrum is roughly described by a powerlaw $\nu L_\nu \propto \nu^{1.3}$, which rises up to submm wavelengths (submm peak has a luminosity of about 5×10^{35} erg s^{-1}), whereafter the spectrum suddenly drops down to less than the detection limit in the NIR regime. The other not ambiguous detection of steady emission is in the X-rays, where the steady faint X-ray emission has a luminosity of $\sim10^{33}$ erg s^{-1} in the typical X-ray band 2-10 keV (Baganoff et al., 2003). In the left panel of Fig.1.15 is also shown a model for the quiescent emission; the radio spectrum is well described by optically thick synchrotron emission from relativistic thermal electrons, with a temperature of a few 10^{10}K (Lorentz γ factor $\sim$10) and a density of 10^6cm^{-3}, spiralling around a magnetic field of about 20-50 Gauss.

The quiescent X-ray emission is thought to arise from thermal bremsstrahlung originating from the transition region between the accretion flow and the surrounding ambient medium. The second maximum in the model of the quiescent emission, at a frequency around 10^{16} Hz, is due to inverse Compton scattering of the synchrotron photons by the same population of thermal electrons. As we can see from the SED of Sgr A*, the luminosity of the source over the entire electromagnetic spectrum is very low when compared to the luminosities of SMBHs in other Galaxies. In the X-rays, for example, the measured quiescent state luminosity is 10^{33}erg s^{-1}, about 10^{-11} the Eddington luminosity for a SMBH with the mass of Sgr A*. This low luminosity is not due to the lack of gas to accrete; Cuadra et al. (2006) stated that there is enough gas from stellar winds in the surroundings of Sgr A* which could produce a much enhanced radiative output, up to 10^5 times the measured one. The very low activity is instead due to a radiatively inefficient accretion flow onto the SMBH (for theoretical models see, e.g., Narayan et al., 2002; Quataert, 2003).

The steady emission from Sgr A* shows different polarisation properties within different energy bands. At frequencies higher than 100 GHz (submm) the emission is linearly polarised at a level of about 10%, whereas in the radio regime the linear polarisation is very low and the emission has a circular polarisation on the level of 0.3-1% (Bower et al., 1999). Due to the lack of X-ray polarimeters in space, there is no observation yet of the polarisation of X-ray emission from Sgr A*, as well as from other X-ray sources.

Sgr A* also shows highly variable emission. Many observational campaigns over the last decades in the radio, submm, NIR and X-ray bands have discovered that this peculiar source is variable over the entire observed spectrum, with the degree of variation vary-

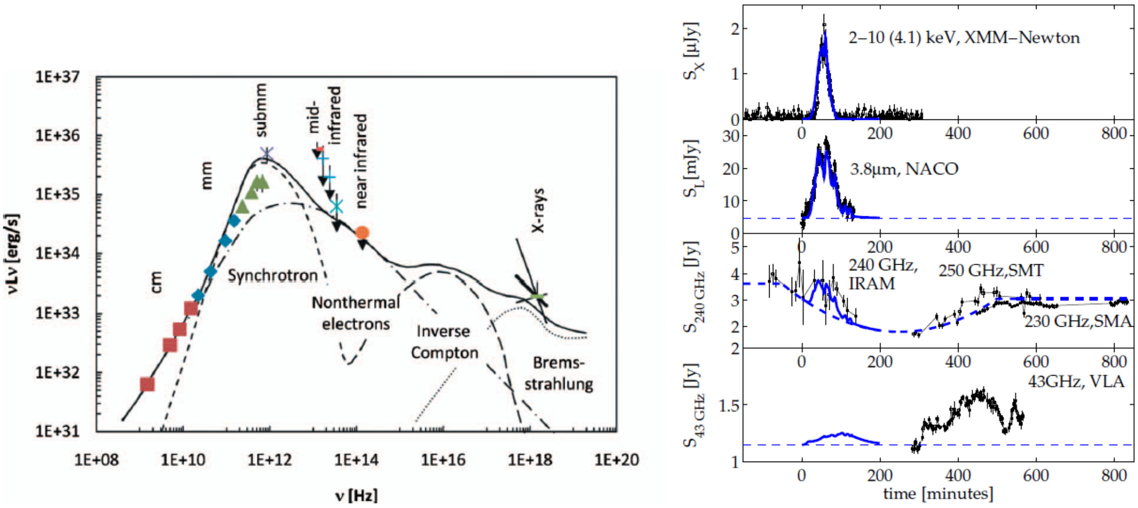

Figure 1.15: *Left*: spectral energy distribution of the steady state of Sgr A* across the electromagnetic spectrum (Genzel et al., 2010). All numbers are given for a galactocentric distance of 8.3 kpc (Gillessen et al., 2009). *Right*: X-ray (top), NIR and submm (middle), and radio (bottom) lightcurve of Sgr A* over the April 4, 2007 flare Dodds-Eden et al. (2010).

ing dramatically between different regimes. At radio wavelengths, the ratio between the maximum and minimum detected fluxes is of the order of one (cm wavelengths) to a few (submm); on the other hand, in the NIR ad X-ray bands, the flux excursion between the quiescent minimum level and the brightest peak is significantly higher and goes from a factor of 20 in the NIR band to a factor of ~160 in the X-rays, where the brightest flare has been measured to have an X-ray luminosity of $3.9{\times}10^{35}$ erg s^{-1} (Porquet et al., 2003). Flares in the NIR occur on average about 4 times per day (Eckart et al., 2006), with a typical duration of ~80 min (Genzel et al., 2010). Contrary to the NIR flares, X-ray ones are detected less frequently, with an average of about 1 per day (Baganoff et al., 2003), with typical duration around 50 min.

In the last decade several models for the flare emission have been developed. The spatial coincidence within few milliarcsec of the NIR flares and the central massive BH and the short timescales of the variability suggest that the flares are generated in the inner region of the accretion flow; this excludes tidal disruption of a star, for example, which would otherwise make the flare much longer than observed. An increase of the accretion rate of the radio-submm source is also unlikely, since the excursion observed in the X-ray luminosity would require a similar excursion in the radio-submm range, which is not seen (Markoff et al., 2001). Baganoff et al. (2001) and Markoff et al. (2001) suggested that the flare might be generated in response to a fast acceleration of electron within the innermost regions of the accretion flow, via magnetic reconnection events and/or accretion instabilities). The accelerated electrons, which can have γ factors up to 10^3, could then upscatter NIR or submm photons to the X-rays via the Inverse Compton effect; besides this, X-ray emission in flares can also be produced by synchrotron emission of highly energetic ($\gamma \sim 10^6$) electrons in a magnetic field of around 5 Gauss (Dodds-Eden et al., 2010).

Whatever the emission mechanism for the NIR and X-ray flares is, the luminosity reached by Sgr A* during these sudden episodes of brightening is still very low compared to normal active galactic nuclei in other galaxies. The question that consequently arises and is a subject of ongoing research is whether Sgr A* might have been much brighter in the past, and is currently in a resting low activity phase. A recent intriguing discovery is that of the so called Fermi bubbles (e.g. Su et al., 2010), two extreme structures about 15 kpc parsec in size with the shape of two giant bubbles extending north-south, symmetrically with respect to the galactic plane; these structures, so far only detected in the γ energy band, might be the remnant of a past catastrophic event related to Sgr A*, although the discovery is very recent and the research on the nature of these gigantic diffuse structures has just begun. On the other hand, for what concerns closely the work presented in this thesis, there is also the hypothesis that Sgr A* could have undergone a period of higher activity, with an X-ray luminosity estimated around 10^{39}erg s^{-1} ($\sim 10^{-5} L_{Edd}$) having occurred some hundreds years ago. We will discuss the origin of this idea and the observations carried out to test it in Chapter 3.

Chapter 2

The physics behind

In this thesis work, we have been mainly dealing with Fe-Kα line emission from neutral Fe in the massive MCs in the GC region. In this chapter, we will briefly review the chemical and physical properties of the element Fe (iron), and then describe the ionisation processes produced by the absorption of (UV-X-rays) photons and by particle bombardment (electrons and ions). To conclude, we are going to describe the phenomenology of the two physical processes involved in the Fe-Kα line emission, discussing the X-ray spectra of an MC either illuminated by X-ray photons or bombarded by low energy CR electrons and protons. However, we must warn the reader that some of the physical processes described in this Chapter are not directly observable (and therefore are not part of our observational doctoral work) with current X-ray observatories because of the insufficient spectral resolution of current instruments; nevertheless, a full theoretical understanding of the Fe ionisation process gives a unique background for future observations of this line emission, whose hyperfine effects (in part described in this Chapter) will be measured by the next generation X-ray detectors (i.e. X-ray calorimeters) in less than a decade from now.

2.1 Why Iron?

Why is Fe special? In the 1-10 keV energy range, the one observed by current operating X-ray satellites like XMM-*Newton*, Chandra and Suzaku, the Fe-Kα lines from different ionisation stages of Fe are the strongest features one can see, and this is because Fe is the element with the highest (by a factor of $\sim$5) product of abundance and fluorescence yield (for the K-shell). The most abundant stable isotope of Fe is ^{56}Fe, whose atomic nucleus is composed of 26 protons (atomic number Z=26) and 30 protons, with an atomic mass measured to be 55.845 atomic mass unit [1].

In Fig.2.1 we show the electronic configuration of the Fe atom, which can also be written as [Ar]3d^{6}4S^2, where [Ar] is the electronic configuration of Argon, i.e. 1S^{2}2S^{2}2P^{6}3S^{2}3P^6. In the right panel of this figure we show the energy levels of the inner shell electrons and the electronic transitions allowed to fill a K-shell vacancy. In this plot, n is the fundamental

---

[1] The atomic mass unit is the mass of the proton, i.e. 1.67×10^{-24} g.

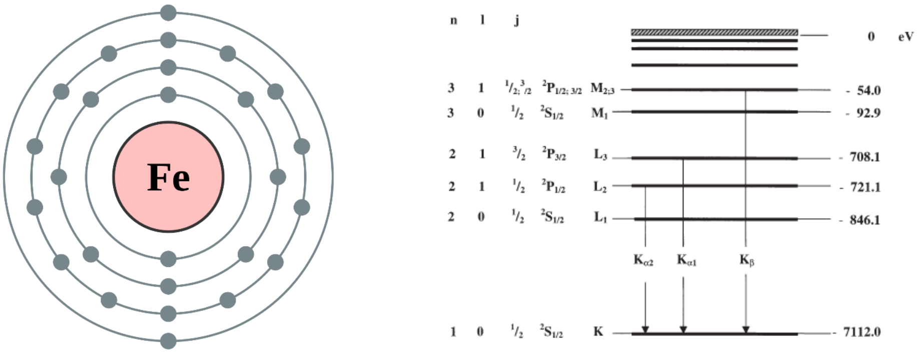

Figure 2.1: Atomic structure (Robson, 2011) and energy levels (Phiwe , 2008) of the K-L-M shells of Iron.

quantum number of the atomic structure, which identifies the zero order energy of an electron bound to the nucleus (and therefore a negative energy). The second quantum number, l, refers to the angular momentum of the electron in a certain shell; as a rule, l can assume n values between 0 and n-1. The last quantum number is j, which is the quantum number which describes the total angular momentum of the electron once the spin orbit coupling has been taken into account; the permitted values of j are $l\pm1/2$. Whenever an inner shell vacancy occurs, the atom is in an excited state, and therefore tends to "relax" by filling this vacancy with an outer shell electron; subsequent to this transition an emission of either a photon or an outer shell electron occurs (see later), because the electron energy is now lower than in the original state (inner shell electrons are more bound to the nucleus). The quantum mechanical selection rules state that the only allowed transitions are those for which $\Delta l=\pm1$ and $\Delta j=0,\pm1$ (see, for example Eisberg & Resnick, 1985). Therefore, the Fe-Kα line from neutral Fe can occur in two separate ways, defined Kα_1 and Kα_2, in which the upper level from where the electron originates is described by l=1 and j=1/2 and j=3/2, respectively. Because of the rule $\Delta l=\pm1$, the transition $L_1 \rightarrow K$ is not observed (see Fig.2.1). The energies of the Fe doublet are 6.391 keV and 6.404 keV, respectively for the Kα_1 and Kα_2 (X-ray data booklet , 2009).

2.2 Photoionisation: theory and phenomenology

Fluorescence is the radiative process which follows the ionisation of an atom by either a photon or a particle. In the former case, the process is called photoionisation and occurs when a photon of energy ν penetrates the atomic structure and kicks the electron out of an atomic shell.

Considering the interaction of a photon with matter, the photoelectric effect is the dominant physical process for photon energies lower than few 10s of keV, therefore at $h\nu \ll m_e c^2$ (=511 keV). At higher energies the dominant effect is Compton scattering, i.e. the inelastic scattering of a photon by a "free" electron; this process dominates up to energies of a few MeV. Finally, the physical process dominating at the highest energies is pair production, i.e. $\gamma \rightarrow e^{+}+e^{-}$, which has a threshold of 1.022 MeV.

If the original energy associated with the electron at rest is -E_i (binding energy), its final energy E_f after the action of the photoelectric effect can be written as the difference between the energy hν of the ionising photon and the initial kinetic energy of the electron E_i, i.e. E_f=hν-E_i. Given a sufficiently energetic photon, a vacancy in a shell is created and an electron is expelled with a kinetic energy given by the energy conservation law. Every atomic shell can be described by its ionisation energy, which represents the minimum energy that a photon (or incident particle) must have in order to ionise it; at higher energies, the cross section for bound-free absorption decreases as $\sigma_{bf} \propto \nu^{-3}$. The calculation of this cross section is a result of the quantum radiation theory; the analytic solution for the K-shell photoionisation in the non-relativistic case (Born approximation), for the energies of the incident photon so that $E_i \ll h\nu \ll m_e c^2$, can be written as

$$\sigma_K = 4\sqrt{2}\sigma_T \alpha^4 Z^5 \left(\frac{m_e c^2}{h\nu}\right)^{7/2} \qquad \alpha = \frac{e^2}{4\pi\epsilon_0 \hbar c}, \tag{2.1}$$

where α is the fine structure constant, σ_T the cross section for Thomson scattering, σ_T=6.65$\times$10^{-25}cm^{-2}. The equation 2.1 is actually the cross section for the removal of both the 1S electrons in the K-shell, since both of them contribute to the element opacity. It is instructive to write the Z (atomic number) and ν dependence of the the cross section for the photoionisation of the K-shell, the one we are most interested in. This is

$$\sigma_K \propto \frac{Z^n}{\nu^m}, \tag{2.2}$$

where $4 \leq n \leq 5$ ($n \sim 4$ for the lighter nuclei, whereas $n \sim 5$ for the heavier elements) and $2.7 \leq m \leq 3.5$ ($m \sim 2.7$ for energies close to the binding energy E_K). Although the heavier elements are much less abundant than H in the ISM, the combination of the ν and Z dependence results in a contribution of metals to the total absorption cross section that becomes dominant at extreme UV and X-ray energies. To summarise and better visualise the previous discussion, we present the plot of the net photoelectric absorption cross section for the different elements in the left panel of Fig.2.2, where also the contribution due to elements in dust phase has been shown. The formula for this cross section, in units of cm^2 per H atom, can be written as (Morrison & McCammon, 1983)

$$\left(c_0 + c_1 E + c_2 E^2\right)\ E^{-3} \times 10^{-24}\ \mathrm{cm}^2, \tag{2.3}$$

where the different c values are constants tabulated in Morrison & McCammon (1983). In the energy range where the bulk of Fe ionisation occurs (E$\sim$8keV), the three constants are c_0=629.0, c_1=30.9 and c_2=0 when the energy is expressed in keV units. To notice in this formula is the E^{-3} dependence, as introduced above.

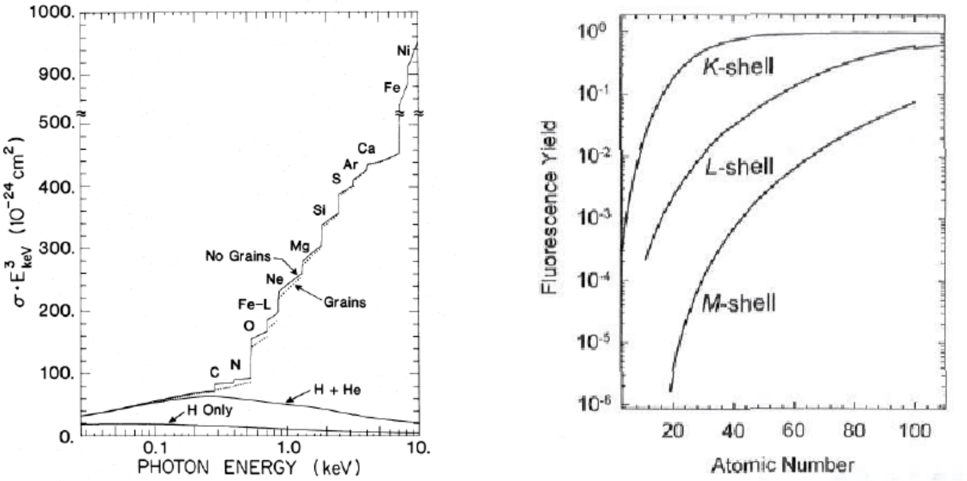

Figure 2.2: *Left*: cross section for photoelectric absorption per H atom in the X-ray energy band (0.1-10 keV). Here, the cross section has been multiplied for E^3 to show deviations from this dependence (from Morrison & McCammon, 1983). *Right*: fluorescence yields as a function of the atomic number of the ionised element for the inner shells ionisation (X-ray data booklet , 2009).

2.2.1 Fluorescence and Auger electrons

As a result of photoionisation, the atom is an excited state; because of the trend of nature to save energy, the atom will certainly relax in order to reach the original ground base configuration. The atomic relaxation can be achieved via two main competing processes, fluorescence (radiative) and the emission of an Auger electron (non radiative). Both these processes follow the filling of the vacancy produced by photoionisation (or particle bombardment) by an electron in the outer shells, which goes to fill the vacancy created in the inner shell; because in this configuration the electron is more bound to the nucleus, its energy being lower, the same amount of energy must be released by the atom. If the atom releases this energy in the form of a photon, the process is called fluorescence and the photon emitted has a characteristic energy which depends of course on the element and on the shells involved in this radiative process (see above). There is however the possibility that this relaxation does not produce a photon, but rather that it releases an electron from the outer shells of the atom; this electron is called an Auger electron, after its discovery by the French physicist Pierre Auger in 1923 (Auger , 1923). As a result of this emission, the number of vacancies in the atom is increased by one unit. The Auger process does not involve the emission of a photon emitted by an atomic electron transiting between upper and lower shell and absorbed by another electron, i.e. it is not an internal photoionisation, but rather an internally stimulated emission.

Fluorescence and the emission of an Auger electron are two competing processes; we can define the fluorescence yield as the ratio between the number of emitted fluorescent photons and the number of photons absorbed (X-ray data booklet , 2009). This quantity strongly depends on the atomic number of the element involved and the shell which was ionised; in the right panel of Fig.2.2 we show the fluorescence yields for the K, L and M shells as a function of the atomic number for the elements with $3 \leq Z \leq 110$. From this plot we can clearly see that the fluorescence yield dramatically varies among different elements; whereas the K shell fluorescence yield is close to 0.1% for the lighter elements, the same quantity is around 100% for elements with $Z \gtrsim 40$, indicating that no Auger electron is emitted in response to the K-shell ionisation of the heaviest metals. Another interesting property of the fluorescence yields is their dependence on the shells which suffer a vacancy; as we can see in the plot, the fluorescence yield decreases for increasing quantum number n of the ionised shell. As a result, an Auger electron will be emitted by each element of the periodic table in response to the ionisation of the M-shell with a probability higher than 90%.

In the second part of this section, we are going to introduce the problem of the illumination of cold material by a cosmic source of X-rays. In Chapters 4 and 5, we have investigated the nature of the Fe-Kα fluorescent emission observed in MCs in the GC region, which arises either from the illumination of a dense MC or from bombardment by CR particles. In particular, since this section is dedicated to the photoionisation, we will introduce the X-ray reflection nebula model and the related theory.

2.2.2 Fe fluorescence

As already written above, the Fe is the element with the highest product of fluorescence yield and abundance in the ISM; these quantities are, respectively, 34% and 3.3×10^{-5} (Bambynek et al., 1972). The energy and depth of the K-shell absorption edge, the energy of the fluorescent photon which results from the inner shell ionisation and the fluorescence yield all depend on the ionisation state of the element; for the case of Fe, the absorption edge for the neutral (or low ionisation) Fe (FeI) is at an energy E_K=7.1 keV, and rises up to E_K=9.3 keV for the H-like Fe ion (FeXXVI) (i.e. Morita & Fujita, 1983). The cross section for photoelectric absorption of Fe decreases from $\sigma_{K,FeI}$=3.8×10^{-20}cm^2 to $\sigma_{K,FeXXVI}$=3.3×10^{-20}cm^2 (the quoted values are per Fe atom). The energy of the fluorescent line also increases from 6.4 keV of the FeI to the 6.96 keV of the FeXXVI; this is clear if we think that the only electron in an H-like Fe ion is more bound to the nucleus because it is no more shielded by the other negative charge carried by the (now missing) 25 electrons. Moreover, also the fluorescence yield depends on the ionisation state of the atom; for Fe, it increases form the 34% of FeI to the 49% of FeII, and then is highly variable for the highest ionisation states, ranging values between 11% and 75% in the four final stages (FeXXIII-FeXXVI) (Bambynek et al., 1972). The branching ratio of the two components (6.404:6.391) of the Fe-Kα doublet is 2:1 (Bambynek et al., 1972); the natural width of the lines is ~3.5 eV, and both this width and the energy difference between the two peaks are negligible for the work we will perform, since the current operating instrumentation is not able to spectrally resolve the doublet. Whereas the Fe-Kα line is produced by a 2p→1s transition, the 3p→1s could also occur; this produces the Fe-Kβ line whose energy is 7.06 keV and its emission can be calculated to theoretically occur at ∼11% that of the Fe-Kα one (Kikoin et al., 1976). These factors are important because in all the spectra of the MCs studied in our work the signal to noise ratio is not high enough to have a good detection/statistics of the Fe-Kβ line; as a consequence, we were forced to fix both the energy of the line peak and its intensity compared with the much better detected Fe-Kα.

Here we want to briefly present the results of the simulations performed by George & Fabian (1991), since they are important for understanding the phenomenology of the X-ray illumination of cold and dense neutral material. These results, together with giving an exhaustive view of the theory and phenomenology of the physical processes involved in the photoionisation, will be important in the near future when X-ray calorimeters will allow us to achieve a better spectral resolution in the studies of the Fe-Kα line from cosmic sources. George & Fabian (1991) simulated the response of a homogeneous semi-infinite slab to X-ray illumination by an X-ray source with a power law spectrum. Moreover, the Fe line has been considered to be a single line peaked at 6.4 keV; the physical processes considered for the study of the opacity of the slab for both continuum and line radiation are photoelectric absorption and electron scattering. The number N_K of fluorescent photons per unit solid angle which could escape from the interacting region is a function of the source spectrum N_0E_0, the Fe abundance Z_{Fe}, the incident angle θ_0 and the final direction of the photon (θ_f,ϕ_f). N_K can be written as (George & Fabian, 1991)

$$N_K(\theta_f, \phi_f, E_f)d\Omega_f = \int_{E_K}^{\infty} N_0(E_0)P_{Fe}(E_0)Y_{Fe}P_{esc}(\theta_f, \phi_f, E_f), \tag{2.4}$$

where $P_{Fe} \propto (\sigma_{Fe}/\sigma_{tot})$ is the absorption probability of the incident photon, and σ_{tot} is the sum of absorption and scattering cross sections, i.e. $\sigma_{tot}=\sigma_{abs} + \sigma_{es}$. In the above formula, Y_{Fe} is the fluorescence yield for the Fe-Kα line production and P_{esc} is the escape probability (into the solid angle $d\Omega_f$) of the fluorescent photon, with an energy $E_f \sim 6.4$ keV. P_{Fe} strongly varies as a function of the energy of the incident photon E_0, since the photoelectric cross section varies as E^{-3}, whereas the scattering cross section is nearly constant up to about 100 keV. The effective fluorescence yield Y_{eff} of the slab can be written as the ratio between N_K and the number of incident continuum photons which can effectively produce inner shell ionisation of Fe, i.e. $E_K \leq E_0 \leq 30$ keV; in formula (George & Fabian, 1991)

$$Y_{eff}(\theta_f, \phi_f, E_f)d\Omega_f = \frac{N_K(\theta_f, \phi_f, E_f)d\Omega_f}{\int_{E_K}^{\infty} N_0(E_0)dE_0} \tag{2.5}$$

The effective fluorescence yield slightly increases towards higher values of the spectral index Γ of the incident spectrum, since a softer spectrum has more photons with energy close to the E_K value (7.1 keV for Fe). Substituting equation 2.4 into 2.5 it is possible to calculate Y_{eff} integrating over E_0; as a result, this quantity lies in the range $10^{-3} \lesssim Y_{eff} \lesssim 10^{-1}$ sr^{-1} (George & Fabian, 1991). In the left panel of Fig.2.3 we show the results of the simulations for the value of Y_{eff} averaged over all the possible final directions (θ_f and ϕ_f) and plotted as a function of the incident angle θ_0, where the incident

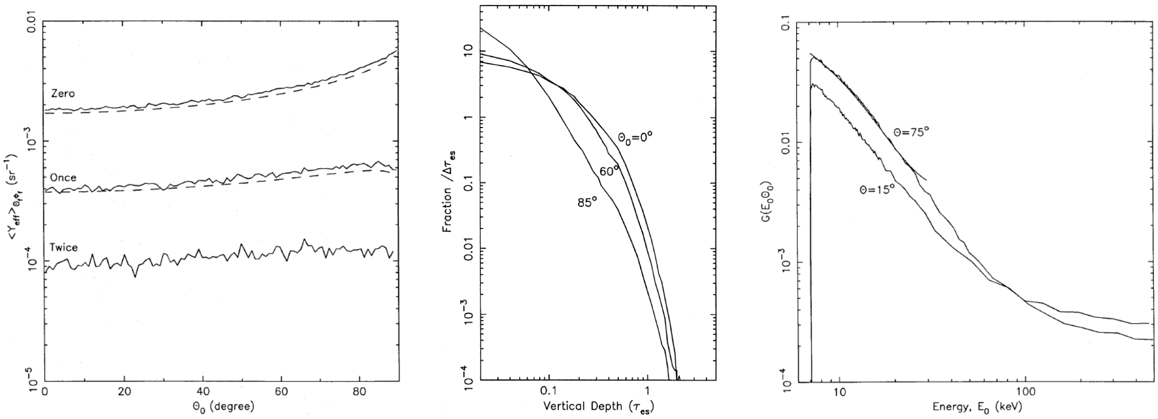

Figure 2.3: *Left*: the effective fluorescence yield of a neutral slab averaged over the solid angle Ω_f=2π, plotted against the incident angle of the ionising photon θ_0. The different curves represent photons which have been scattered zero, one and two times. *Middle*: fraction of the fluorescent photons produced which are able to escape form the slab for unit depth plotted as a function of the Thomson depth for electron scattering in the slab for different incident angle θ_0=0, 60 and 85 degrees. *Right*: the G(E$_0$,θ_0) function as a function of the energy of the incident photon for different values of the angle θ_0=15 and 75 degrees (all the plots are from George & Fabian, 1991).

spectrum has been assumed to be a power law with a spectral index Γ=1.7. The different curves display the effect of Compton scattering (the photon collides with a free electron and transmits some of its energy to the 'rest' particle) on the fluorescent photons, and particularly the ones which suffered no, one and two Compton scatterings on the ambient medium.

In the plot we can see that Y$_{eff}$ slightly increases towards higher values of θ_0 for the unscattered Fe-Kα photons, with its value rising from 1.8×10^{-3} sr^{-1} at θ_0=0 (direction normal to the surface of the slab) up to 5.5×10^{-3} sr^{-1} at θ_0=90 deg (George & Fabian, 1991). This behaviour is a consequence of the P$_{esc}$ dependence on θ_0; for θ_0 values close to 90 degrees the fluorescent photons are produced at a smaller vertical depth within the slab, and therefore have more chances to escape. This behaviour can be seen in the middle panel of Fig.2.3, which shows the number of fluorescent photons per unit Thomson depth which escape the slab as a function of the vertical Thomson depth crossed by these photons; given a certain vertical depth, the fraction of fluorescent photons that can escape is lower towards higher θ_0. Following George & Fabian (1991), it is possible to define the function G(E$_0$,θ_0) as the ratio between the number of photons incident on the slab with an angle θ_0 and energy E$_0$ which produce 6.4-keV photons which are then able to leave the absorption region, and the total number of incident photons with energy E$_0$; this function, which represents the probability of photons at different energies to induce Fe fluorescence which can be observed (the photon leaves the slab), is shown in the right panel of Fig.2.3, plotted for different values of the incident angle θ_0. Defining μ=$\cos\theta_0$, we write (George & Fabian, 1991)

$$G(E_0, \theta_0) = g(E_K, \theta_0) \times f(\epsilon), \tag{2.6}$$

where

$$g(E_K, \theta_0) = 10^{-2} \times (6.5 - 5.6\mu_0 + 2.2\mu_0^2), \tag{2.7}$$

and

$$f(E) = 7.4 \times 10^{-2} + 2.5 \exp -(E - 1.8)/5.7 \tag{2.8}$$

Looking at the plot, we can see that there is a region next to the the threshold energy (7.1 keV) where G is quite hard ($G \propto$ E$^{-1.2}$), whereas for E$\gtrsim$10keV the G function becomes steeper, being proportional to E^{-2}. At higher energies, above ~50 keV, the G function gets flatter because of the Compton down-scattering of high energy photons (photons lose energy), which therefore have a lower energy and increase their probability of being able to photoionise Fe atoms (George & Fabian, 1991).

As shown above, the number of fluorescent photons created (and hence Y$_{eff}$) also varies with the final direction of the emitted photon. The fluorescent emission is isotropic (it emits equally in all directions), so that Y$_{eff}$ does not depend on ϕ_f for a certain θ_f. On the other hand, the fluorescence yield of a semi-infinite absorbing slab strongly depends on the escaping angle of the fluorescent photon. The left panel of Fig.2.4 shows the ϕ_{eff} averaged value of the slab yield Y$_{eff}$ plotted against the emerging angle (θ_{eff}) of the 6.4 keV photon for different incident angles (θ_0) of ionising radiation; the first noticeable effect is the sharp decrease of the fluorescence yield towards high values of θ_f; this behaviour reflects the higher optical depth that the fluorescent photon has to cross in order to leave the absorption region (George & Fabian, 1991). Moreover, the efficiency of Fe-Kα production increases with increasing incident angle of the incoming photons. A further interesting feature of the Fe-Kα line is related to its shape; fluorescent photons which are created inside the slab can suffer Compton scattering with the ambient electrons and be significantly down-scattered; depending on how many times a certain photon is scattered, the final recorded energy associated to this fluorescent radiation will be lower than the unscattered 6.4 keV. As a consequence, a red wing is created in the spectrum, i.e. some line flux is distributed over energies lower than 6.4 keV (see Fig.2.4, right panel); the original 6.4 keV line spreads over two Compton wavelengths, suffering an energy down shifting of ΔE=2E^2/m$_2$c^2 after each scattering (George & Fabian, 1991). The line profile which emerges after these additional electron-photon interactions consists of an unscattered core, which represents the bulk of the emission, and a series of red (lower energy) shoulders; most of the contribution to the first shoulder comes from the photons which undergo one scattering before escaping the interaction region, whereas the second shoulder is dominated by the ones which undergo two scatterings and so on. We also note that the exact shape of this red wing depends on the abundance of elements lighter than Fe, which dominate the photoabsorption cross section at 6.4 keV (George & Fabian, 1991).

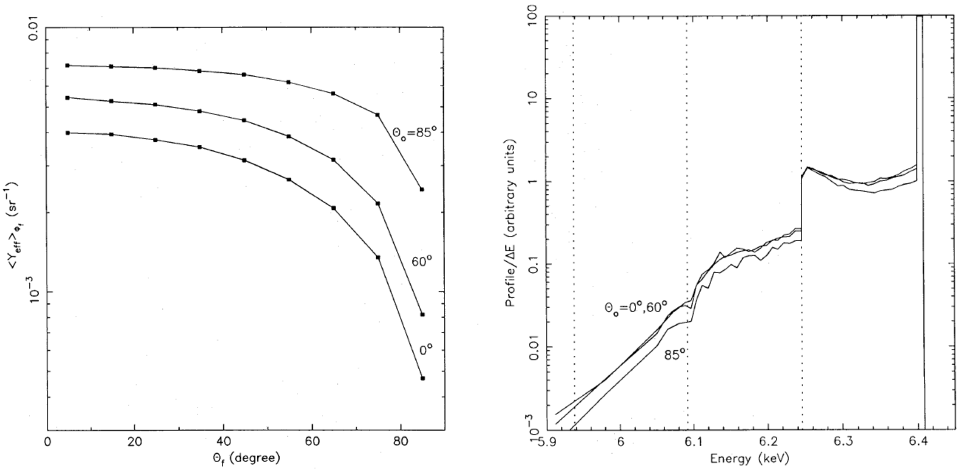

Figure 2.4: *Left*: directionality of the Fe fluorescent line. Here we plot the averaged (over ϕ_f) fluorescent yield as a function of the final direction of the photon for different values of the incident angle θ_0=0, 60 and 85 degrees. *Right*: line profile of the Fe-Kα fluorescent line at 6.4 keV for different illumination angles. The low energy wing/s are created by the scattering of the monoenergetic 6.4 keV photons produced by fluorescence within the slab (all the plots are from George & Fabian, 1991).

So far we have only discussed the 6.4 keV line production and the physics of its interactions with the neutral medium. What happens to the X-ray illuminating continuum? To answer these questions, we write the expression for the albedo A of the slab as the ratio between the number of continuum photons N_c with a certain energy E_f which after interaction with the slab escape in a solid angle $d\Omega_f$ in the direction given by the angles θ_f and ϕ_f, and the number of incident photons with energy E_f. In formula (George & Fabian, 1991)

$$A(\theta_f, \phi_f, E_f) d\Omega_f = \frac{N_c(\theta_f, \phi_f, E_f) d\Omega_f}{N_0 E_f}, \tag{2.9}$$

where N_c also accounts for the contribution by those photons with $E \geq E_f$ which suffered downscattering to E_f within the slab. This albedo, the probability of a continuum photon to survive the passage through the slab, is strongly related to the probability to undergo electron scattering rather than being absorbed, i.e. the relative strenght of these two cross sections. To summarise the results by George & Fabian (1991), the function A averaged over all the possible escaping directions (θ_f and ϕ_f) (1) increases with E_f for a given θ_0, (2) it increases with θ_0 for an assumed E_f and (3) the fractional increase of A between θ_0=0 and θ_0=90 depends on E_f. The first point is clear since towards the higher energies the photoelectric cross section decreases sharply as E^{-3}, and therefore Compton scattering dominates over absorption. If a continuum photon enters the slab with an higher θ_0 (more parallel to the surface), it will cross a lower vertical depth and therefore will have a lower probability of being absorbed (second point). The third point is also a consequence of the decreasing of σ_{abs} with increasing photon energy.

2.2.3 X-ray reflection nebulae

In this section we are going to discuss the physics and phenomenology of what astronomers call an X-ray reflection nebula (XRN); this is the analog of the typical reflection nebulae seen in the optical domain, where a cloud of dust and gas scatters and partially absorbs and re-emits the incident light coming from a nearby star. In the case of an XRN, the source of photons is an X-ray source (AGN, X-ray binary, etc.) and the nebula must have a minimum density in order to be able to absorb and scatter X-rays and make this measurable for astronomers. The spectral and timing features arising from the illumination of a dense MC by a powerful X-ray source have been studied by Sunyaev & Churazov (1998), whose study was performed after the discovery of fluorescent X-ray emission at 6.4 keV from neutral Fe arising from massive MCs in the GC region (Koyama et al., 1996). The goal of this investigation is to derive the features of the Fe-Kα line (flux, equivalent width, shape, morphology, time behaviour) and the reflected continuum in the context of X-ray illumination, in order to be able to differentiate between different mechanisms of excitation which can produce Fe fluorescence as observed in cosmic sources. This treatment of the problem is more focused on the phenomenology of the XRN, and it will be of great utility in the development of this work.

X-ray observations allow us to measure the 6.4 keV line flux from a cloud of neutral material; starting from this measurement, it is possible to infer the luminosity (and/or luminosity history if some variability in the fluorescent signal is detected) of the original putative source of photons. In formula (Sunyaev & Churazov, 1998):

$$F_{6.4} = \frac{\Omega}{4\pi D^2} n_{Fe}\ r\ Y_{Fe} \int_{7.1}^{\infty} I(E)\sigma_{ph}(E)dE \text{ photons s}^{-1}\text{ cm}^{-2}, \tag{2.10}$$

where Ω is the solid angle between the ionising source and the cloud, D is the distance between the cloud and the observer, $n_{Fe}r$ is the Fe column density inside the cloud (in units of cm^{-2}), and I(E) the source photon spectrum intensity (photons s^{-1} keV^{-1}). As we discussed earlier in this Chapter, the σ_{ph} is a steep function of the photon energy; accordingly, the photons which can more efficiently contribute to the Fe ionisation are the ones with energies in the range ~7-9 keV. As a result, it is convenient to write the expression for the 6.4-keV line flux as a function of the photon spectrum intensity at 8 keV. This is (Sunyaev & Churazov, 1998)

$$F_{6.4} = \phi \frac{\Omega}{4\pi D^2} \frac{\delta_{Fe}}{3.3 \times 10^{-5}} \tau_T I(8keV) \text{ photons s}^{-1}\text{ cm}^{-2}, \tag{2.11}$$

where ϕ ~1 is a factor which accounts for the shape of the source spectrum, δ_{Fe} is the Fe abundance with respect to H, and τ_T is the optical depth for Thomson scattering of the cloud. If we convert the intensity of the photon flux at 8 keV into the luminosity of the X-ray source in a 8 keV wide energy band, we can write that $I_8 = L_8/8 \cdot 8 \cdot 1.6 \times 10^{-9} = 10^7 \cdot L_8$.

Substituting this expression in the last formula, we can derive the luminosity that the putative X-ray source must have in order to produce the observed flux. This is (Sunyaev & Churazov, 1998)

$$L_8 = 6\times10^{38}\left(\frac{F_{6.4}}{10^{-4}}\right)\left(\frac{0.1}{\tau_T}\right)\left(\frac{\delta_{Fe}}{3.3\times10^{-5}}\right)^{-1}\left(\frac{d}{100\ \mathrm{pc}}\right)^{2}\ \mathrm{erg\ s^{-1}}, \tag{2.12}$$

where d is the distance between the source and the cloud. As we will se in the Chapters 4 and 5, this formula is a very powerful tool to study the 3D distribution of the MCs radiating in the Fe fluorescent line; indeed, assuming an X-ray luminosity for the source and measuring the 6.4-keV line flux, it is possible to infer the solid angle Ω, and therefore the distance along the line of sight of a certain cloud.

Of course, if the source is located inside the cloud, more photons will interact with it and the corresponding X-ray luminosity needed in order to produce the same Fe-Kα flux significantly decreases; using the same notation as before, the X-ray luminosity of a source embedded in the 6.4-keV emitting MC can be written as (Sunyaev & Churazov, 1998)

$$L_8 = 6\times10^{35}\left(\frac{F_{6.4}}{10^{-4}}\right)\left(\frac{0.1}{\tau_T}\right)\left(\frac{\delta_{Fe}}{3.3\times10^{-5}}\right)^{-1}\ \mathrm{erg\ s^{-1}}, \tag{2.13}$$

a value which is significantly lower than the one required in the external source scenario.

When a cloud is illuminated by an external source, the geometry of the X-ray illumination has been illustrated by Sunyaev & Churazov (1998) and shown in Fig.2.5. The surface of a parabola at a certain time t represents the set of points for which the sum of the distance to the source and the distance to the observer is the same. Therefore, an observer located far away from both the source and the cloud will see fluorescent emission (and the relative reflected continuum) from the regions of the cloud(s) currently (we do not consider the propagation time from the source to the observer) illuminated by the X-ray photons . In the right panel of Fig.2.5 we show the surface brightness distribution of an MC which is illuminated by steady radiation which suddenly turns off, as a function of the relative position of the cloud and the source. The surface brightness was calculated integrating over the sight line the product of the cloud density and the radiation field density (Sunyaev & Churazov, 1998).

The simulations were run for a radius of the cloud of 22.5 pc (comparable to what observed for the Sgr B2 complex at the GC). The position of the cloud with respect to the primary source is indicated by the pairs of numbers at the bottom of the plot. The first number represents the cloud relative shift (in pc) to the left with respect to the source; for example, 0 means that the source and the MC are along the same line of sight of the observer, while -100 means that the cloud is located 100 pc left to the source. The second number represents the location of the cloud along the line of sight; negative (positive) numbers are for a cloud position behind (in front) the plane of the source. Therefore, the first two columns represent a situation where the source is located inside the cloud. On the vertical axis, instead, the temporal evolution of the surface brightness is shown for increasing time (in years). The first noticeable thing is the difference in the surface

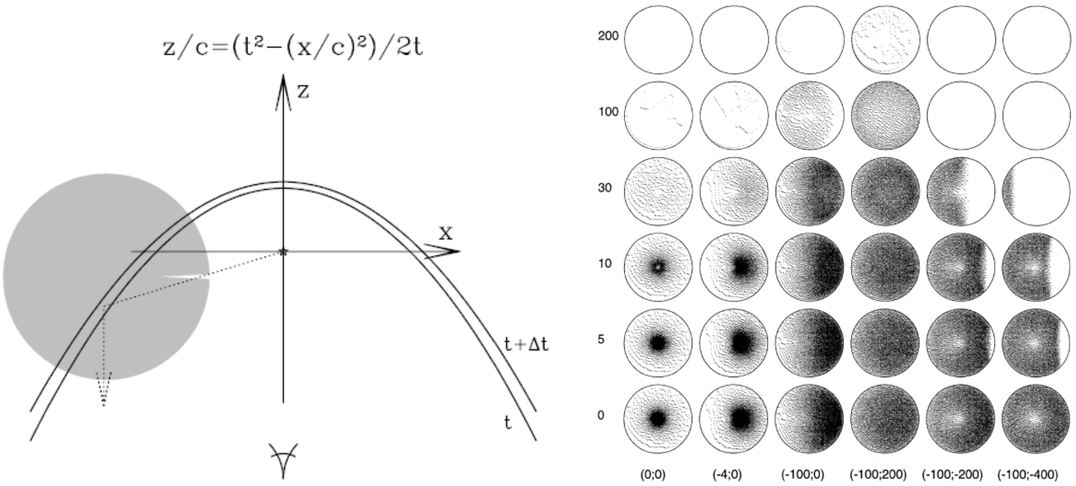

Figure 2.5: *Left*: geometry of the illumination of an MC by a distant source. The points of the parabola, whose equation is also written in the plot, has the same delay time with respect to the primary radiation going directly from the source to the observer, and not scattered by the cloud into the line of sight. The structure of this parabola and its duration in time (Δt) determine the topology and the temporal variability of the 6.4-keV line flux and the associated reflected continuum at high energy. *Right*: distribution of the surface brightness of an MC with a radius of 22.5 pc for different locations of the cloud-source; here the source of radiation is a steady flare which suffer a sudden fading at the time t=0 (see text) (from Sunyaev & Churazov, 1998).

brightness distribution for a source located inside the MCs, compared to a source located outside; when the source is inside the cloud, the surface brightness distribution shows a rather sharp profile, with characteristic peaks which simply reflect the fact that the radiation field is more intense in the immediate vicinity of the source. On the opposite case, when the source is located outside the MC, the surface brightness profile is rather smooth and at first order reflects the Thomson depth of the cloud; moreover, the side of the cloud closer to the source is brighter (Sunyaev & Churazov, 1998).

We want now to discuss the surface brightness profile of an MC which is illuminated by a very short flare (compared to the size of the cloud), in the case of an optically thick and thin cloud (respectively, left and right panel of Fig.2.6). For the optically thin case the distribution of the surface brightness resembles the density of the cloud at the position of the parabolic surface; on the other hand, the optically thick case eliminates these peaks because of the enhanced photoabsorption, i.e. photons produced in the inner cloud do not easily escape the absorbing matter (Sunyaev & Churazov, 1998). This difference between the optically thin and thick case can be seen in the three cases highlighted by red circles in the plots in Fig.2.6; while we see peaks in the emission in the optically thin case (right panel), we do not see them in the optically thick case (left panel).

Besides the shape of the surface brightness distribution within an MC illuminated by a

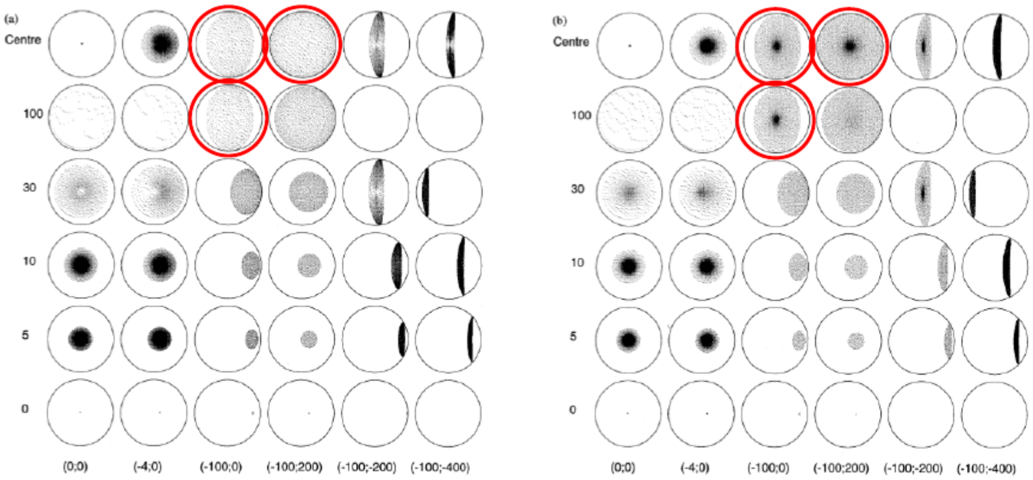

Figure 2.6: *Left*: distribution of the surface brightness of an MC with a radius of 22.5 pc for different illumination geometries; here the source of radiation is a short (compared to the size of the cloud) flare and the cloud has been modelled do be opticaly thick. *Right*: same as in the left panel but for an optically thin case (from Sunyaev & Churazov, 1998).

powerful X-ray source, the spectral parameter that has a primary importance in the study of the possible nature of the primary source is the equivalent width of the Fe-Kα line. This parameter is defined as the number of photons in the line divided by the number of photons at 6.4 keV in the continuum emission; a high value ($\gtrsim$1 keV) of the EW of the 6.4-keV line is always attributed to the illumination of the cloud by an X-ray source. However, the situation in most of the MCs is not so clear and easy to allow us to safely and definitely conclude that an EW larger than 1 keV must be attributed to photoionisation; as we will see in the next sections, bombardment by low energy CR can also produce an large Fe-Kα EW, especially when the Fe abundance in the clouds is high or when protons are the particles responsible for the inner shell ionisation. Therefore, all the spectral parameters of the 6.4-keV line must be taken into account for a safe conclusion about the excitation mechanism. For the case of a source located inside the cloud the EW of the Fe line is $\sim$1 keV$\times\tau_T$, where τ_T is the optical depth for Thomson scattering of the medium surrounding the source. On the other hand, if the source is located outside the cloud, the EW of the 6.4-keV line is expected to be $\sim$1 keV (for solar abundance of Fe) regardless the value of τ_T; this happens because both the Fe-Kα line flux and the continuum at 6.4 keV are proportional to the intensity of the illuminating radiation and the density of the cloud (Sunyaev & Churazov, 1998). As a conclusion, we see that an optically thin cloud located away from the illuminating source will have a large EW of the 6.4-keV line, whereas the same line will have a lower EW if the source is located inside the cloud.

To conclude our discussion about the phenomenology of an X-ray reflection nebula we want here to discuss the other spectral parameter, together with the EW of the Fe fluorescent line, which can help in discerning between different ionisation processes. In the XRN scenario, the intense 6.4-keV line is expected to be accompanied by a significant absorption at the Fe-K edge energy of 7.1 keV. In the case of a source located inside the cloud, the optical depth at the Fe-K edge can be directly associated with the flux of the Fe-Kα line through the fluorescence yield (~34%). However, for the case of an illumination from the side, the situation is much more complex. For example, for low optical depth of the cloud (and therefore very small absorption at 7.1 keV), the EW of the 6.4-keV line can still be higher than 1keV (see Sunyaev & Churazov, 1998). The relation between the depth of the observed edge and the thickness of the cloud also depends on the geometry of the problem. For example, if the source is located inside the cloud, then there is exponential attenuation of the flux at the Fe-K edge. If the source is outside the cloud and we observe the illuminated side of the cloud, then the attenuation is not exponential any more (e.g., for an hypothetical cloud with very large depth the flux near the edge does not go to zero). In the case of negligibly small optical depth the scattered continuum has a shape identical to the incident continuum + fluorescent line (with large equivalent width). In other words, the relation of the flux missing due to the absorption edge and the flux in the 6.4 keV line is not a universal constant, but may vary depending on (i) mutual position of the cloud, illuminating source and observer and (ii) the optical depth of the cloud. For what concerns our work, the clouds that will be studied are neither optically thin nor thick, but somehow in the middle, and moreover there is no clue on the possible position within the CMZ, i.e. the distance along the line of sight. All these elements will contribute to make the discussion of the measurements of the absorption edge more complicated than in the ideal cases discussed above.

To add: some plots for the quantitative analysis. These will also be part of the 3rd paper, so will be added at the end (after response by Prof. Bob Warwick).

2.3 Particle ionisation: theory and phenomenology

Photoionisation is not the only physical process which can ionise an atom; indeed, particles (mainly electrons and protons) can also induce inner shell ionisation followed by the emission of a fluorescent photon. The effective candidates to produce ionisation in atoms are electrons and protons.

The cross section for the ionisation induced by particle bombardment has a completely different behaviour from the one induced by photoionisation. In Fig.2.7 we show the cross section for ionisation of Fe in the case of electron (left, Quarles, 1976) and proton (right Tatischeff et al., 1998) bombardment. The left panel also shows the cross section for photoionisation, which can therefore be easily compared with the other processes. The first thing we note is the different behaviour of the σ_{ph} and the $\sigma_{e,p}$ with energy; while the photoionisation cross section is much higher than the competing processes but for only a very narrow energy band, the cross section for particle bombardment, both via proton and electron interaction, is much wider and involves particles spread over an energy range 4-5 decades wide. The peaks of these two last cross sections are separated by a factor of $\sim m_p/m_e$; while electrons have the highest probability to ionise Fe around an

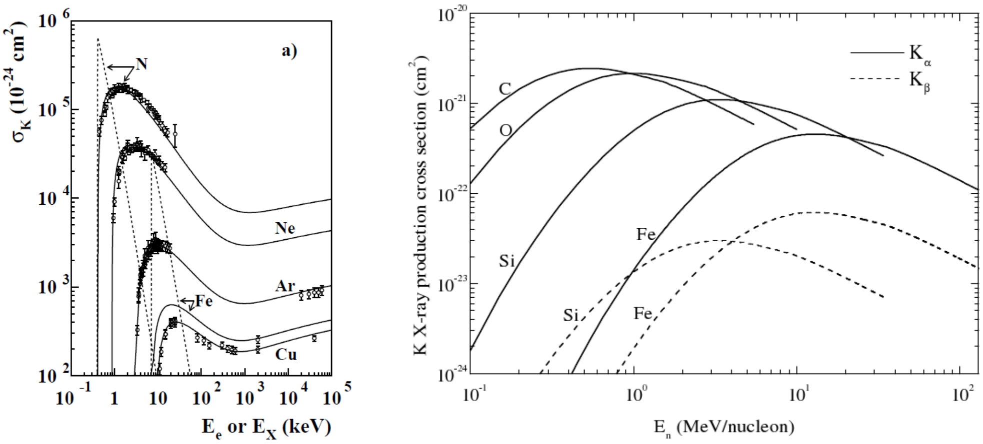

Figure 2.7: *Left*: ionisation cross section for electron collision of different abundant metals (solid lines and data points) as a function of the energy of the incident electron (or photon). For comparison the dotted lines show the photoionisation cross section for N and Fe (Tatischeff et al., 1998). *Right*: proton bombardment cross section for the production of Kα (solid line) and Kβ (dashed line) fluorescent lines from of C, O, Si and Fe as a function of the energy of the incident proton (left, Quarles, 1976).

energy of ∼30 keV, protons can effectively ionise Fe at an energy of about 10 MeV. At these energies, both electrons and protons are non-relativistic, since the Lorentz γ factor is about 1 (β ∼0.1). Here, we always refer to kinetic energy of non-relativistic particles; the electron and proton mass energies are, respectively, $m_e c^2$=511 keV and $m_e c^2$=940 MeV, and therefore are always much higher than the energy involved in the Fe ionisation.

2.3.1 Stopping range for electrons and protons

To understand the ionisation structure of an MC, and to model the X-ray fluorescent emission, it is of unique importance to understand the interactions between incident particles or photons with neutral atoms. The photon atom interaction is based over the relative importance of photoionisation and Compton scattering (see section 2.2). For what concerns CR bombardment, electrons and protons interact with the neutral atoms in a different way; a heavy charged particle exerts electromagnetic forces on atomic electrons and transfers energy to them, being able to ionise or excite the target atom. In these interactions, the maximum energy transfer that a particle can suffer is given by the formula

$$\Delta E_{max} = \frac{4mME}{(M+m)^2} \tag{2.14}$$

where m is the electron mass and M is the mass of a much heavier particle (like protons or CR). If the incident particle is an electron, M=m and the maximum energy transferable in the collision is on the order of the initial energy E. On the other hand, if a proton collides

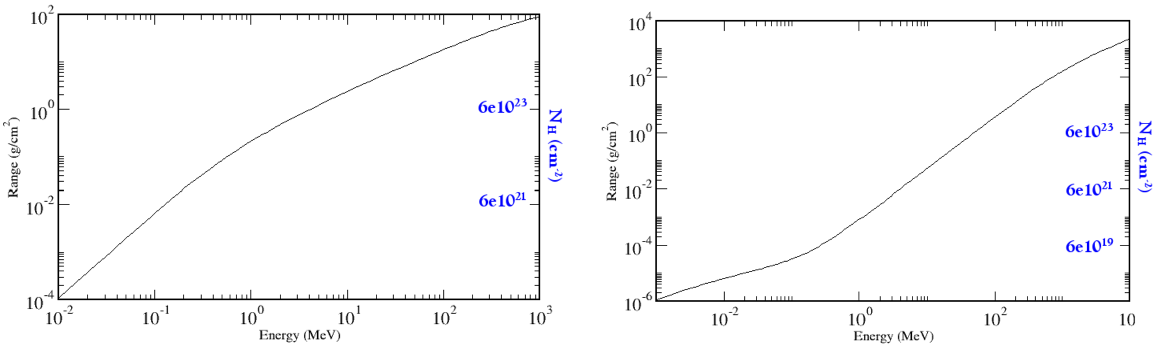

Figure 2.8: *Left*: stopping range in units of g cm^{-2} and of N$_H$ (in units of cm^{-2}) of the absorbing material (pure H) as a function of the energy of the incident electron. *Right*: same for protons (both the plots have been taken from *http://physics.nist.gov/*)

with an electron, the maximum energy it can lose is less than 1% for kinetic energies lower than 1 GeV. As a result, we will see that protons can penetrate much more into the core of a cloud, whereas electrons are stopped almost on the surface. In Fig.2.8 we present the stopping range of electrons (left) and protons (right) in a pure H target as a function of the incident particle energy; the stopping range is a measurement of how long a particle can penetrate a target of a given density, while at the same time an estimation of the column density N$_H$ required to stop a particle with a given initial kinetic energy. Especially the last definition turns out to be very useful for our purposes, since the column density is the most common quantity used to describe the density of a cloud.

In the plots in Fig.2.8 the stopping range is plotted in units of g^2 cm^{-1}; to convert this into a column density for H atoms we must divide the vertical axis for the proton mass m_p=1.67×10^{-24} g. In the right side of each plot we also write the N$_H$ scale, which can be useful for comparison; the MCs radiating in the Fe fluorescent line at 6.4 keV in the GC region have N$_H$ values which typically span in the range 10$^{22-24}$ cm^{-2} (see also Chapter 1). From Fig.2.8 we can see that non-thermal electrons with energies lower than 100 keV are stopped by a column density of about 4×10^{21} cm^{-2}, a value significantly lower than what usually found in a dense MC (see Fig.1.3); moreover, actually the peak of the cross section for Fe ionisation via electron bombardment is at ∼30 keV, which would be stopped in less than 10^{21} cm^{-2}. The consequence of inefficient penetration of a dense cloud by CR electrons have a huge impact on the debate about the source of Fe fluorescence in the GC region; if electrons are responsible for the production of the 6.4-keV line, then this must occur in the outer layers of an MC. It is therefore of great interest to investigate the surface brightness distribution of the Fe-Kα line in order to measure whether the electron bombardment scenario is plausible; in dense clouds like Sgr B2, keV electrons penetrating the cloud from the side could hardly produce Fe ionisation in the core of the cloud (measured to have a size of few parsecs with an N$_H$ $\gtrsim$10^{23}cm^{-2}).

In comparison, for a N$_H$ value of 4×10^{21}cm^{-2} the optical depth for photoelectric absorption is $\tau_{abs} \lesssim 0.01$, so that in the same interacting region where a 100 keV electron is stopped, X-rays with energies higher than the K-edge of Fe (7.1 keV) barely interact with the neutral medium, and therefore can penetrate deeper inside the MC.

On the other hand, protons have a much higher penetrating power than electrons; the cross section for ionisation of Fe atoms via proton bombardment has a high plateau value for proton energies $\gtrsim$20 MeV (Fig.2.7, right panel). Looking at the right panel of Fig.2.8 we can see that the stopping power for protons in the energy interval 10-100 MeV (the ones that most easily ionise Fe atoms) spans the column density interval of 10^{22}-10^{23}cm^{-2}, which are the typical values of column densities found over MCs lying in the CMZ.

Recently, Dogiel et al. (2009a) suggested that a significant portion of the apparently thermal emission from the kT$\sim$10 keV hot plasma in the GC region is due to inverse bremsstrahlung of subrelativistic protons diffusing into interstellar space; these are the same protons which most effectively interact with the MCs and give rise to the Fe fluorescent emission.

2.3.2 Electron bombardment

To understand what kind of spectrum is produced by the interactions of non-thermal electrons with an MC, we want to discuss now the phenomenology of electron bombardment. Let us follow the treatment presented by Tatischeff (2003), where an interaction region composed only of neutral atoms has been considered in order to completely neglect X-ray line emission from collisional ionisation, like the one observed in hot plasmas permeating Galaxy clusters and X-ray coronae. Electrons entering an MC can also suffer Coulomb collisions with the ambient atomic nuclei, and therefore produce bremsstrahlung emission which can subsequently ionise the neutral atoms; accordingly, even without having an external source of X-rays, fluorescent line emission can be produced via both photoionisation and particle bombardment, with relative contributions which depend on the characteristic of the ambient medium and the energy spectrum of the electrons (Tatischeff, 2003). However, in this derivation the N$_H$ of the absorbing medium is assumed to be low enough to neglect the photoionisation of Fe atoms produced by bremsstrahlung photons; electrons are slowed down and emit non thermal bremsstrahlung, but the probability that these photons produce Fe fluorescence is negligible (remembering the difference in the stopping range of electrons and photons). Let us also assume that the averaged properties of the absorbing medium are not modified by the interaction with the flux of non thermal electrons, i.e. the effects of ionisation and heating by electron bombardment are negligible.

For what concerns the continuum emission, the differential rate for production of X-rays in units of photons s^{-1} keV^{-1} can be written as (Tatischeff, 2003)

$$\frac{dQ}{dE_X} = \int_0^{\infty} \frac{dN_e}{dt}(E_e) \times \left[n_H \sum_Z a_Z \int_0^{E_e} \frac{d\sigma_Z}{dE_X}(E_X, E_e') \frac{dE'}{(dE/dl)E_e'} \right] dE_e, \tag{2.15}$$

where dN$_e$/dt is the differential rate of injection of non thermal electrons into the absorbing region (in units of electrons s^{-1} keV^{-1}), n$_H$ is the H density in the medium, a_Z is the Z element abundance (Z is the atomic number), dσ_Z/dE$_X$ is the differential cross section for X-ray production via Coulomb interaction of electrons with the ambient atoms, and dE/dl is the energy loss rate for unit of path travelled by the incident particle (keV cm^{-1}). The terms in square brackets of the equation 2.15 represents the monochromatic (E$_X$) X-ray production by an electron of incident energy E$_e$ till it comes to rest. Since the most abundant elements in the absorbing medium are H and He, we can write the energy loss rate as (Tatischeff, 2003)

$$\left(\frac{dE}{dl}\right) \approx n_H \left[m_H \left(\frac{dE}{dx}\right)_H + a_{He} m_{He} \left(\frac{dE}{dx}\right)_{He}\right], \tag{2.16}$$

where m$_H$ and m$_{He}$ are the atomic masses of H and He respectively, and (dE/dl)$_H$ and (dE/dl)$_{He}$ represent the stopping powers for electrons in a pure H and He ambient medium, measured in units of keV g^{-1} cm^2. The electron stopping power in pure H for E$_e$ in the 10-100 keV energy range is about a factor of 2.0-2.5 higher than the one in pure He. Inserting equation 2.16 into equation 2.15, it is evident that the X-ray production rate does not depend on the density of the material but only on the relative abundances a_Z of the elements which make up the absorbing medium. The elements considered for the production of the Kα (2p$\rightarrow$1s) and Kβ (3p$\rightarrow$1s) fluorescent lines are C, N, O, Ne, Mg, Si, S, Ar, Ca and Fe; the K-shell ionisation cross section by electron bombardment for these elements can be written as (Tatischeff, 2003)

$$\frac{d\sigma_Z^{K_i}}{dE_X}(E_X, E_e) = \delta(E_X - E_{K_i})\ \sigma_Z^I(E_e)\omega_Z^{K_i}, \tag{2.17}$$

where E$_{K_i}$ is the energy correspondent to the Kα or Kβ transitions ($i = \alpha, \beta$), $\delta(E_X - E_{K_i})$ is the Dirac delta function, $\sigma_Z^I(E_e)$ is the cross section for the ionisation of an atom with atomic number Z by an electron with incident energy E$_e$ (Quarles, 1976), and $\omega_Z^{K_i}$ is the K$_i$ fluorescence yield for an atom Z. Because of the electronic structures of atoms with Z$\leq$12, these atoms have $\omega_Z^{K_\beta}$=0. The resulting spectrum from electron bombardment of such medium is shown in the left panel of Fig.2.9, where non-thermal electrons are injected into the absorbing medium at a rate

$$\frac{dN_e}{dt}(E_e) = 2.71 \times 10^8 \ \cdot \ E_e^{-2} \quad \text{electrons s}^{-1}\ \text{keV}^{-1},\ \text{for} \ \ 10 \leq \text{E} \leq 100\ \text{keV}, \tag{2.18}$$

and zero otherwise (Tatischeff, 2003). Notwithstanding this, we cannot completely neglect the effect of photoabsorption since the assumption that the medium is thick enough to stop electrons with energies up to 100 keV, i.e. N$_H$ $\gtrsim$4$\times$10^{21}, tells us that a certain amount of photoabsorption must occur (see also Fig.1.1); the effect of this on the X-ray spectrum of the MC (absorbing region) is shown with a dashed line in the left panel of Fig.2.9. For this spectrum, the normalisation of the electron flux has been chosen in order to constrain the power injected into the neutral medium by the electrons to (Tatischeff, 2003)

$$\dot{W} = \int_0^\infty E_e \frac{dN_e}{dt}(E_e)dE_e = 1 \text{ erg s}^{-1} \tag{2.19}$$

It is interesting to compare this power with the total X-ray luminosity produced and emitted by the interaction region; this is (Tatischeff, 2003)

$$L_X < \int_{0.1\ keV}^{100\ keV} E_X \frac{dQ}{dE_X}(E_X)dE_X = 4.2 \times 10^{-5} \text{ erg s}^{-1} \tag{2.20}$$

We can clearly notice that the ratio $\mathrm{L}_X/\dot{W}$ is very low, therefore the X-ray production via interaction of non-thermal electrons with the ambient medium is inefficient (Tatischeff, 2003). However, where present, the emission of non thermal bremsstrahlung photons must be accompanied by fluorescent emission from the ambient metals; for example, with the parameters assumed above, the EW of the K_α lines from ambient O, Ne, Si and Fe are respectively 355, 107, 73 and 290 eV (Tatischeff, 2003). A significant fluorescent emission from light elements like O and Ne could allow us to distinguish between photoionisation and electron bombardment at the origin of the fluorescence; indeed, for ionisation induced by electron impact, the strong decrease of the fluorescence yields towards the lower Z elements is balanced by the increase of the cross section for K-shell ionisation, whose dependence on the atomic number Z can be approximated by $\mathrm{Z}^{-4/3}$. This is different from what happens in case of photoionisation, where the fluorescence yields increase towards higher Z and so does the cross section for K-shell ionisation. Unfortunately, the column density towards the GC region is so high ($\sim 6\times 10^{22}\mathrm{cm}^{-2}$) that fluorescent lines from O and Ne, both below 1 keV, cannot be detected. In our view, this argument could be however used in other regions which suffer a lower interstellar absorption than the CMZ, in order to discriminate between photoionisation and electron/proton particle bombardment.

2.3.3 Bombardment by protons and heavy nuclei

Let us now turn our attention to the ionisation of a neutral medium induced by proton bombardment. Non relativistic, non thermal protons/ions can induce inner shell ionisation of neutral atoms via quite a few physical processes: inverse bremsstrahlung (IB) radiation of the nuclei within the electron sea, bremsstrahlung emission of the secondary knock-on electrons, molecular-orbital and radiative electron capture, these two last processes playing a dominant role in the impact by heavy ions (Dogiel et al., 1998). To study the phenomenology of the X-ray emission produced by the proton bombardment of a neutral medium, we again follow the example of Tatischeff (2003), which considered accelerated ions injected at a constant rate into an absorbing medium like the one described for the case of electron impact in Section 2.3.2. The differential X-ray production rate can be quantified by an equation very similar to equation 2.15, where two more summations have to be performed; the first over the abundance of the different elements, and the second over the different ionisation states. The particle spectrum is assumed to be the same of Galactic CR, e.g. (Tatischeff, 2003)

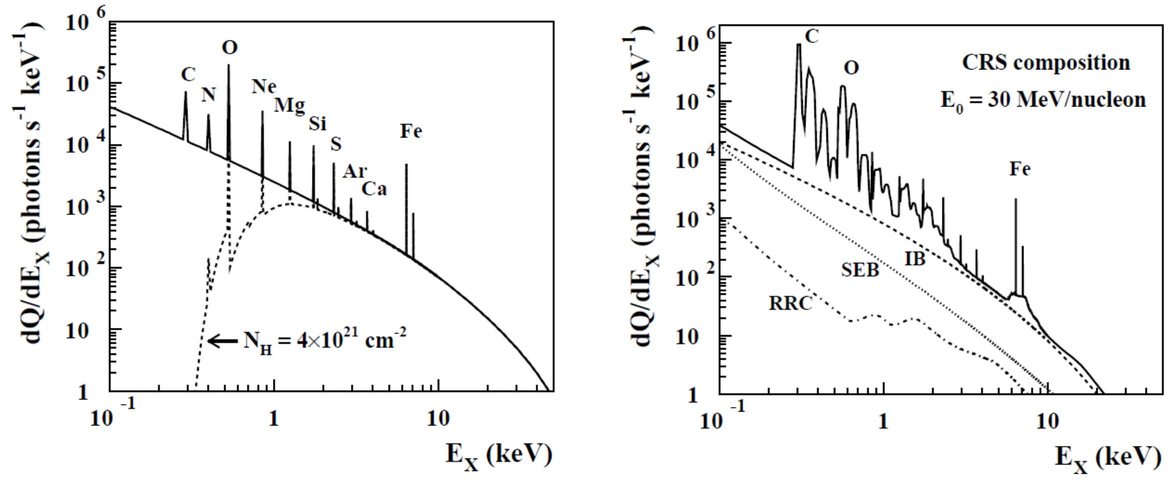

Figure 2.9: *Left*: X-ray spectrum produced by electron bombardment of a neutral MC (interaction region). The solid line traces the contribution by continuum bremsstrahlung emission and fluorescent lines, whereas the dashed line shows the effect of photoabsorption for an N$_H$ value of the medium as high as the stopping range for a 100 keV electron (4×10^{21}cm^{-2}). *Right*: X-ray continuum and fluorescent lines emission produced by protons/ions interaction with neutral material. The dashed, dotted and dashed-dotted lines show contribution to the continuum X-ray emission from different mechanisms (Tatischeff, 2003).

$$\frac{dN_i}{dt}(E_i) \propto E_i^{-1.5} \exp -E_i/E_0, \tag{2.21}$$

a form which can be produced by acceleration of non relativistic particles in shocks (Ramaty et al., 1996). In this spectral form, E$_i$ is the kinetic energy of the incident ion (MeV nucleon^{-1}), and E$_0$ is a parameter introduced to take into account the shock size and the acceleration timescale. The resulting spectrum of the so illuminated interaction region is presented in the right panel of Fig.2.9, where the effect of photoelectric absorption has been neglected for simplicity and for a better visualisation of the shape of the fluorescent lines. The production of continuum X-rays is dominated by IB, the radiation of an electron at rest in the moving electric field of a fast moving ion; this physical process is the kinematical inverse of the normal bremsstrahlung, and therefore the cross sections will be very similar (see also Tatischeff et al., 1998). For example, for non relativistic protons with an initial kinetic energy E$_p$ the cross section for IB is the same as the one for bremsstrahlung emission of electrons with an energy (m_e/m_p)E$_p$ that we already introduced before; for this reason X-rays are efficiently produced by keV electrons and MeV protons (see Fig.2.7). The spectrum in the left panel of Fig.2.9 also shows the continuum X-ray emission produced by radiative recombination of free electrons into the K-shell of ions (RRC) and by the bremsstrahlung emission produced by the secondary knock-on electrons (SEB). The emission lines are due to the ionisation of the neutral material by the bombarding ions; contrary to fluorescent lines produced by electron bombardment, emission lines from ion collision can be shifted by several eV, broadened and split into several component because of multiple simultaneous ionisations (Garcia et al., 1973). For example, the Fe-Kα line produced by the impact of a O ion with an energy of 1.9 MeV nucleon^{-1} is blueshifted of about 50 eV with respect to the one produced by proton impact, having a FWHM of $\sim$100 eV (Garcia et al., 1973).

The broad line features which are visible in the spectrum are produced by atomic de-excitation of the bombarding ions which follow electron capture by charge transfer reactions with ambient medium and collisional excitation Tatischeff (2003). As a result, the fluorescent lines are the superposition of a relatively narrow line due to the ionisation of the neutral medium, and other lines which arise from atomic de-excitation of the bullet particles. The fluorescent lines from different ionisation states of Fe are emitted at $\sim$10 MeV nucleon^{-1} (energy of the bullet particle) and give rise to the characteristic bump in the spectrum, whose width is about 2 keV Tatischeff (2003).

In conclusion, the spectrum produced by the bombardment of an MC by subrelativistic protons/ions is significantly different from the one arising from electron bombardment. As a consequence, it will be interesting in the near future to quantify these spectral differences in order to disentangle the different contribution to the ionisation of the elements (photons, electrons and ions) and constrain much better the physical mechanisms which produce these characteristic spectral lines. Nowadays, X-ray satellites do not provide the spectral capabilities for performing a detailed study of the ionisation structure of an MC; in this sense, a breakthrough will be achieved with the launch of satellites with X-ray calorimeters, capable of reaching a spectral resolution on the order of a few eV (astro-H).

As a final application to the study of the Fe-Kα fluorescence, we want to quantify the difference in the EW of the 6.4 keV line which can be produced by the three ionisation mechanisms which have been studied in this Chapter. Since the EW from photoionisation has already been discussed, we present in Fig.2.10 the cross sections for the 6.4-keV line and continuum emission via the interaction of low energy CR electrons (left) and protons (right).

As we can see from the plots, both the $\mathrm{d}\sigma_B/\mathrm{d}E_X$ functions and the cross sections for the line production display some differences, although the general trend is very well comparable. Besides the fact that these cross sections peak at 10^3 orders of magnitude in energy from each other, the line production by protons impact is more probable than the one produced by electrons: the EW of the Fe-K-α line produced by electron (proton) bombardment can be at the first order quantified as the ratio between the areas subtended by the two curves of the plot in the left (right) panel in Fig.2.10. If this calculation is performed for both electrons and protons, hence for both the plots in Fig.2.10, we notice that the EW given by proton bombardment will be resultingly larger than the electron one. Moreover, the $\mathrm{d}\sigma_B/\mathrm{d}E_X$ for the production of 6.4-keV photons in the continuum slightly differ, with the cross section for electron impact being somewhat higher. These differences have a significant impact on the EW of the Fe-Kα line which can be produced by these two processes. While the EW of the 6.4-keV line is on the order of $0.3{\cdot}\mathrm{Z}_{Fe}$ keV, where the Z_{Fe}

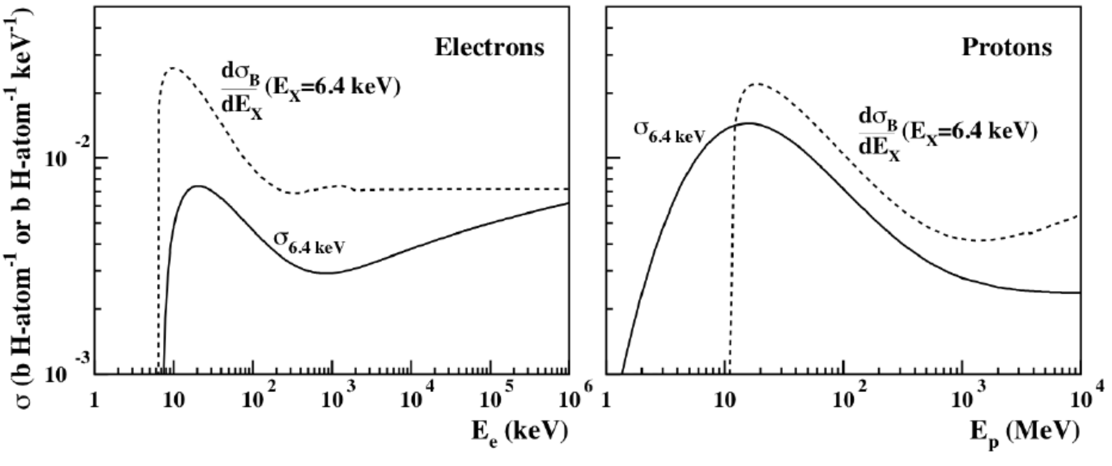

Figure 2.10: *Left*: cross section for continuum (bremsstrahlung) emission of X-rays with an energy of 6.4 keV (dashed), and for Fe-Kα fluorescent photons (solid), produced by electrons bombardment, in units of barn per H atom (1b=10^{-24}cm^2). *Right*: same, but for protons bombardment.

is the Fe abundance with respect to the solar value (i.e. Yusef-Zadeh et al., 2007b), the EW of the FeI fluorescent line produced via proton bombardment can be significantly higher, reaching up to EW∼1keV (Tatischeff et al., 2011). This is an important issue since, for what concerns GC studies and particularly the work done in this thesis, the measurement of the EW of the Fe-Kα line is always used as a marker to distinguish between the illumination scenario and the particle bombardment hypothesis; as we argued here, the measurement of an EW of about 1 keV is not enough, by itself, to safely conclude that the fluorescent emission from neutral Fe is produced by X-ray illumination of an MC.

Chapter 3

Diffuse X-ray emission in the Galactic Centre region

3.1 Three spectral components for the diffuse X-ray emission in the Galactic Centre

Diffuse X-ray emission permeates both the GC region and, on more extended scales, the Galactic plane. The origin of this radiation is still controversial, especially for the GC region, since there are many emission mechanisms which could give rise to the observed amount of X-ray radiation. The X-ray surface brightness distribution in the GC region has been studied in a pioneering paper by Sunyaev et al. (1993), who analysed data from the coded mask telescope *ART-P* onboard the *GRANAT* satellite. These authors mapped the X-ray emission in the inner Galactic plane in the range 2.5-22 keV, showing that soft and hard X-ray emission completely fills the inner GC region. In this Chapter we are going to discuss the nature of this diffuse X-ray emission, disentangling the contribution of three different spectral components to the total emission; (i) a warm plasma with a temperature of ~1 keV, (ii) a hot plasma with a temperature of of ~6-8 keV and (iii) a non-thermal hard X-ray tail which is intimately related with the subject of our thesis, the 6.4-keV line emission from neutral Fe. In my doctoral work I have been dealing with Fe-Kα line emission from MCs in the GC region; since the typical X-ray surface brightness of an MC is very low compared to foreground emission, a complete theoretical and phenomenological understanding of these three spectral components is essential in order to study the net 6.4 keV line signal successfully and to determine the origin of the Fe ionisation process.

In the left panel of Fig.3.1 we show the spectrum of the diffuse emission in the GC region obtained by Warwick et al. (2006) analysing XMM-*Newton* observations performed in the period 2000-2004. The spectral data accumulation was performed over an angular region around the SMBH Sgr A*, with internal and external radii of 4 arcmin and 10 arcmin, respectively; all the point sources and the diffuse sources which could contribute to the total foreground emission (i.e., the bright molecular clouds like the G0.11-0.11 complex) have been removed with a region selection, and so was the instrumental background. From

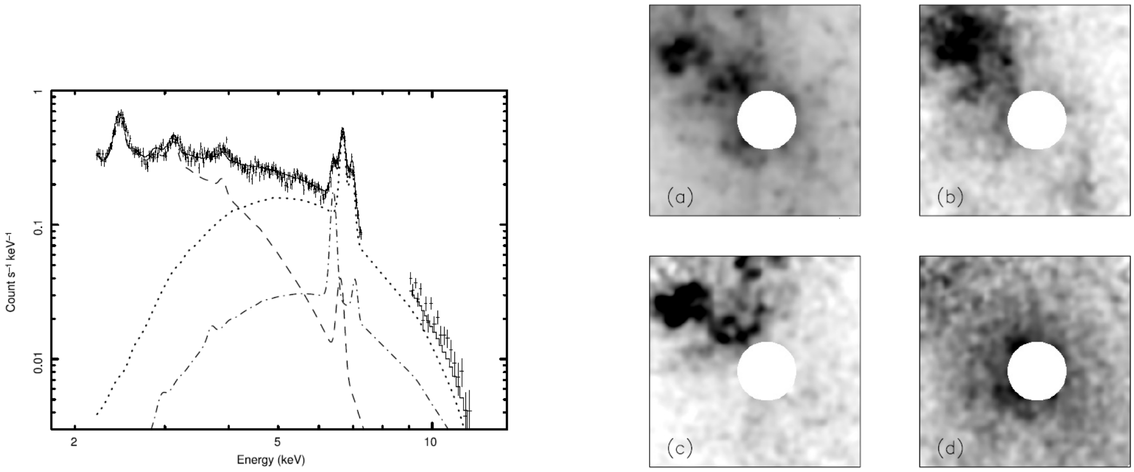

Figure 3.1: *Left*: XMM-*Newton* spectrum of the GC region (spectral model and data points). The curves show the different components of the diffuse emission: the dashed line represents the warm plasma, whereas the dotted and dashed-dotted curves represent the hot thermal component and the non-thermal hard X-rays plus the associated Fe fluorescent emission, respectively (see text). *Right*: narrow band images of the GC region. (a) The 4.5-6 keV continuum band; (b) narrow band image centered at the 2.46 keV sulphur line; (c) map of the Fe-Kα emission at 6.4 keV; (d) a narrow band centred at the FeXXV-Kα energy of 6.7 keV. The grey scale shows in black the brightest regions (all plots are from Warwick et al., 2006).

the plot, we can see that the diffuse emission cannot be fitted with a single spectral model, like a powerlaw or thermal plasma. The spectral model which can describe the data well is composed of four components of a completely different nature and characterised by different spectral features (Warwick et al., 2006). The first of these is photoelectric absorption, which affects all the X-ray sources in the GC region because of the thick layer of ISM along the line of sight. This absorption, however, does not tell us anything about the nature of the diffuse emission, but is rather a side effect. The first spectral component that is important for understanding the nature of the diffuse emission is shown in the plot as a dashed line; this represents a thermal plasma with a temperature of $\sim$1 keV, whose typical spectral feature is the strong emission line from ionised sulfur at 2.46 keV. The dotted line in the X-ray spectrum in the left panel of Fig.3.1 represents a second thermal component which can be well fitted with another plasma at a temperature of 6-8 keV. The spectrum of this second component contains the characteristic fluorescent line from the He-like Fe, FeXXV, at 6.67 keV. Last but not least, the dashed-dotted line in the plot represents a spectral component which has a non-thermal nature and is connected with the 6.4-keV line emission from neutral Fe (and other lines from minor neutral contributors); the nature of this non-thermal radiation has been debated in the last decade, and it seems to be due to a particle component of the foreground emission, specifically CR electrons or protons. This radiation is the dominant contribution to the X-ray spectrum of the foreground emission at energies above 10-15 keV (i.e. Valinia et al., 2000; Dogiel et al., 2009c, respectively); the Fe-Kα line can serve as a tracer of this hard component.

In the right panel of Fig.3.1 we show the map of the GC diffuse X-ray emission in different energy bands, which bracket the differennt spectral components discussed above (Warwick et al., 2006). Panel *a* shows the 4.5-6 keV energy range; at these energies all three the spectral components contribute to the total emission, and the spectrum is relatively devoid of spectral features. As a result, the surface brightness distribution is fairly homogeneously distributed, although some darker spots are present in correspondence with intense X-ray emission from 6.4-keV bright MCs; it is not the 6.4-keV line that contributes here, but the corresponding enhanced underlying continuum. Panel *b* shows the narrow band peaked at the S line energy of 2.46 keV, meaning that the distribution of the thermal warm plasma component is highly asymmetric with respect to the position of Sgr A*. Panel *c* show the Fe-Kα line emission (peaked at 6.4 keV), also irregularly distributed. Finally, panel *d* shows the map of the hot plasma distribution, which is seen to be very evenly distributed about the GC. The study of the surface brightness distribution of the different spectral components is very important in order to constrain their nature.

The origin of the 6.4-keV line emission, its surface brightness distribution and temporal and spectral properties will be studied in the next Chapters and discussed in the next section. In this section we are going to study the features and the physical quantities related to the two other components of the GC X-ray diffuse emission; the warm and hot plasmas. These have been studied in various papers in the last decade; a clear and concise view has been given by Muno et al. (2004), who studied the physical properties of these two ionised plasmas in the GC region as observed by the Chandra X-ray observatory, and whose results we are now going to briefly summarise. The X-ray luminosity (calculated from surface brightness measurements, see the original paper by Muno et al. (2004) for details) of the warm plasma spans the range (6-12)$\times10^{33}$ erg s^{-1}, but can reach $\sim9\times10^{33}$ erg s^{-1} in the brightest regions; the hot component has just about the same luminosity, L$_X$=(5-9)$\times10^{33}$ erg s^{-1}, although it is more evenly distributed along the inner GC region. The density of these two plasmas are on the order of 0.1 cm^{-3}, with a higher value, up to 0.5 cm^{-3}, for the warm plasma in regions where this component is brighter. A second quantity that can be derived from the density of the gas is the energy density, which for the warm and hot plasmas results in 3×10^{-10} erg cm^3 and 10^{-9} erg cm^3, respectively. Supposing that the cooling of the plasma is purely radiative (no expansion), the cooling time for the two components has been calculated to be on the order of (3-6)$\times10^6$ years for the $\sim$1 keV plasma and 10^7 years for the $\sim$6-8 keV plasma (Muno et al., 2004). Another hint towards the origin of these two X-ray emitting components in the GC region comes from the calculation of the speed within the plasma. The escape velocity from the inner (20 pc) GC potential can be estimated to be $\sim$900 km s^{-1} (Muno et al., 2004); calculating the sound speed as

$$c_S = \left(\frac{\gamma kT}{\mu m_p}\right)^{1/2}, \tag{3.1}$$

where γ=5/3 is the ratio between the specific heats of a monotonic adiabatic gas at constant pressure and volume, μ=0.5 for a gas of electron and protons, and k is the Boltzmann constant k=1.38×10^{-16} erg K^{-1}. Considering the values reported above, the sound speed for the warm and hot plasmas is 500 and 1500 km s^{-1} respectively; as a consequence, only the 1 keV plasma is gravitationally bound to the Galaxy, whereas the hot diffuse component is not (for an early paper on this result see, e.g., Yamauchi et al., 1990). Moreover, we saw that the two plasmas have different surface brightness distributions, with the warm component inhomogeneously distributed; any overdensity in the soft plasma should not last very long. Indeed, the tidal disruption timescale from the differential rotation in the inner GC region can be written as (Muno et al., 2004)

$$t_{tide} \approx (R/\Delta R)\ t_{orb}(R) \tag{3.2}$$

where ΔR is the size of the overdensity and t_{orb} is the orbital period at a distance R from the centre. For parsec scale features, like the ones seen in the panel *a* of Fig.3.1, this disruption timescale is on the order of 6×10^5 years, a relatively short time in cosmic scales.

The warm plasma

The last argument presented above suggests that the soft plasma is young; its youth can be understood if we suppose that the gas is heated by SN. The arguments in favour of this hypothesis are the temperature of the diffuse gas in a SNR, which is often measured to be ∼1 keV, and the fact that SN explosions provide enough energy in order to satisfy the energetic requirements. Assuming that this soft component is not expanding, the radiative cooling needs to be sustained with an energy injection of 3×10^{36} erg s^{-1} (Muno et al., 2004); if approximately 1% of the energy released in a SN explosion (10^{51} erg) is going into heating of the warm plasma, this mechanism could provide the required amount of heating with a SN rate of 10^{-5} $year^{-1}$. Considering the galactic SN rate of one in 100 years (10^{-2} $years^{-1}$), and assuming the inner 20 pc to contain about 0.1% of the mass of the entire Galaxy (Launhardt et al., 2002), we can easily estimate the SN rate of 10^{-5} $year^{-1}$ as 10^{-2}×0.1%. Together with the SN, powerful winds from massive stars can also heat the warm ionised plasma; the mass loss rate for a O-B supergiant or a Wolf-Rayet star can reach values of $10^{-5}M_\odot$ $year^{-1}$, with terminal velocities which can be as high as 2000 km s^{-1} (e.g. Stevens & Hartwell, 2003). The kinetic energy of such strong stellar winds is on the order of 10^{37} erg s^{-1}; observations of massive star clusters suggest that about 10% of the kinetic energy of stellar winds is turned into X-rays, via internal shocks within the cluster winds and/or shocks occurring at the boundary region with the ISM (Townsley et al., 2003). As a result, we see that O-WR stars can also participate in producing the heat required to sustain the soft component of the diffuse X-ray emission.

The hot plasma

This is the hard component of the diffuse thermal emission; the most recent measurement of the temperature of this plasma gave a value of 6.5 keV (Koyama et al., 2007a). As we can see in Fig.3.1 (panel *d*), the surface brightness distribution of this plasma is rather uniform across the GC region; this relative homogeneity may result from the higher sound speed ($\sim$1500 km s^{-1}) with respect to the soft component, which would cause overdense regions in the hot plasma to expand and dissolve in a timescale of about 10^4 years, therefore significantly shorter than the analogue timescale for the warm plasma (Muno et al., 2004). However, the temperature measured in this plasma is much too hot when compared to typical temperatures observed in SNR; for this reason, the heating of this thermal component is unlikely to be supplied by SN explosions, and must come instead from other non-thermal emission mechanisms. As we already have seen, the 6.5-keV plasma is not bound to the Galaxy; the energy requirement for the heating of this expanding plasma is on the order of 10^{40} erg s^{-1} (Muno et al., 2004), four order of magnitudes higher than the one needed for the soft plasma, which probably does not cool down by expanding.

The important question related to the nature of this component is whether it is actually diffuse or not. The X-ray diffuse emission from the Galactic ridge has recently been suggested to be due to the superposition of different contributions by unresolved point sources (Revnivtsev et al., 2006); from the analysis of Chandra data, it has been discovered that most ($\sim$88%) of the emission associated with the Galactic ridge can be explained by the superposition of faint and numerous sources, mainly accreting white dwarves and active coronal binaries (Revnivtsev et al., 2006). Indeed, a strong correlation has been found between the distribution of the FeXXV-Kα line flux and the near infrared brightness distribution which is a tracer of stellar mass. In particular, another version of this correlation is also found in the GC region, where the radial profile of the 6.7-keV line surface brightness can be well modelled with a powerlaw with the radial dependance $\propto$ r$^{-0.87}$ (Warwick et al., 2006).

As a result, the ridge emission is now thought to originate from the superposition of many unresolved point sources (Revnivtsev et al., 2009). However, in the GC region the situation might be different; statistical studies of the radial distribution of the point sources show that at most the 20% of the diffuse hot X-ray emission can be ascribed to the contribution of unresolved point sources, leaving the remaining 80% truly diffuse in nature (Muno et al., 2004; Revnivtsev et al., 2007). It is therefore very important to understand which physical processes could heat the plasma to such a high temperature. In the last decade several ideas have been suggested, such as, for example, magnetic reconnection, driven by turbulence in the ISM, and the presence of subrelativistic particles permeating the entire region. In the next secton, we are going to present a recent idea which ascribes the heating of the hard plasma to low energy cosmic ray protons injected in the ISM by stellar accretion onto Sgr A*.

3.1.1 MeV protons from stellar accretion onto Sgr A*?

This idea has been recently proposed in a series of papers by Dogiel V. and collaborators (i.e. Dogiel et al., 2009a). These authors started with the observation that the GC diffuse hard X-ray emission differs from that of the Galactic ridge in a number of ways; the emission in the GC has been found to be a well-separated spherical region with a size of 100-200 pc around Sgr A*, and the temperature associated with this hot plasma is measured to be significantly higher than in the Galactic disk (i.e. Muno et al., 2004). Also, the ratios between the line fluxes $F_{6.9\mathrm{keV}}/F_{6.7\mathrm{keV}}$ (tracer of the plasma temperature) and $F_{6.4\mathrm{keV}}/F_{6.7\mathrm{keV}}$ are higher in the GC than in the ridge (Yamauchi et al., 2009). Moreover, contrary to what is found for the Galactic ridge (Revnivtsev et al., 2006), there is no clear correlation between the 6.7-keV line flux and the distribution of X-ray point sources. These pieces of evidence convinced the above cited authors to consider the GC region as somehow special; that there are some peculiar ongoing processes there, probably related with the activity of the dormant SMBH.

To summarise, they suggested that both the thermal hard X-ray emission and the non-thermal radiation associated with the production of the 6.4-keV line is connected with the injection of subrelativistic protons, produced by stellar accretion onto Sgr A*, into the interstellar medium. Every star which is accreted onto the SMBH can release a huge amount of energy, significantly higher than the one which is achievable with SN explosions; the average rate for the capture of 1M$_\odot$ by SMBHs has been estimated to be in the range 1-10$\times10^{-5}$ year^{-1} (Donley et al., 2002). At the moment of disruption the star is at the pericentre of its orbit and, after suffering tidal disruption, approximately 50-75% of the stellar mass can escape the accretion and become unbound (Dogiel et al., 2009a); this escaping mass receives additional angular momentum and escapes with a velocity that exceeds the original orbital speed and corresponds to an energy of (Dogiel et al., 2009a)

$$E_{esc} \sim \frac{2GM_{BH}m_p}{R_T} \sim 5\times10^7 M_6^{2/3}\ m_*^{1/3}\ r_*^{-1}\ \mathrm{eV}, \tag{3.3}$$

where M$_6$ is the mass of the central black hole in units of 10^{6}M$_\odot$, m$_*$=M$_*$/M$_\odot$ and r$_*$=R$_*$/M$_\odot$ with M$_*$ and R$_*$ the mass and the radius of the star being disrupted, and R$_T$ the capture radius. This can be written as (Dogiel et al., 2009a)

$$R_T \approx 1.4\times10^{13} M_6^{1/3}\ m_*^{-1/3}\ r_*\ \mathrm{cm} \tag{3.4}$$

Assuming the measured black hole mass of 4.3$\times$10^{6}M$_\odot$ the average energy of escaped particles lies in the range 50-100 MeV if a solar mass star is captured. As a result, every stellar capture event can produce about 10^{57} protons with energies of hundreds of MeV (Dogiel et al., 2009a), which can afterwards interact with the surrounding medium and produce X-rays via inverse bremsstrahlung emission and inner shell ionisation (see Chapter 2); surprisingly, the energy of the escaping particles is the one for which the cross sections for X-ray continuum and line production via interaction with low energy protons peak. The energy released in the GC region in the form of CR protons with MeV kinetic energies can efficiently heat the plasma up to ∼6.5 keV; the power required to heat the hard plasma is on the order of 10^{42} erg s^{-1}, a value that is remarkably in agreement with the power that can be supplied by subrelativistic protons. The energy losses of the protons that produce the heating of the hot plasma component are essentially ionisation losses (Dogiel et al., 2009a).

3.1.2 Non thermal emission and the 6.4-keV line

As explained earlier, the X-ray spectrum of the diffuse emission from the GC region also contains a third component, non-thermal in nature, which is the dominant contribution to the X-ray spectrum above 10-15 keV. Together with the thermal emission, low energy CR protons with 100 MeV energies can also produce non-thermal X-ray emission; this is due to inverse bremsstrahlung of protons, which produce X-ray photons with energies of about $E_X \lesssim (m/M) E_p$, where E_p is the kinetic energy of the proton and m and M are the electron and proton mass, respectively. For proton energies lower than 100 MeV, the resulting bremsstrahlung photons have energies lower than 55 keV. The cross section for the production of photons via inverse bremsstrahlung is (Hayakawa, 1969)

$$\frac{d\sigma_{br}}{dE_X} = \frac{8}{3}\frac{Z^2 e^2}{\hbar c}\left(\frac{e^2}{mc^2}\right)^2 \frac{mc^2}{E'}\frac{1}{E_X}\ln\frac{(\sqrt{E'}+\sqrt{E'-E_X})^2}{E_X}, \tag{3.5}$$

where $E'=(m/M)E_p$. From this, the total X-ray flux of inverse bremsstrahlung emission from the GC region can be estimated as (Dogiel et al., 2009a)

$$F_X^{IB}()E_X = 4\pi \int_E dE \int_{V_{GC}} N_p(E,\vec{r},t)\frac{d\sigma_{br}}{dE_X} v_p n(\vec{r}) d^3r, \tag{3.6}$$

where the V_{GC} factor in the integration is the volume of the GC region considered. To see the relative contribution to the X-ray spectrum of the thermal and non-thermal emissions produced by subrelativistic protons, we present in Fig.3.2 the 10-40 keV spectrum as measured by the Hard X-ray Detector onboard the Suzaku satellite (data points); in the plot, the black points show the contribution of the non-thermal IB emission, whereas the dashed line represents the thermal component of the diffuse emission, with a temperature of 6.5 keV. On the top of these two components, the 6.4-keV line from inner shell ionisation of neutral Fe is created (Dogiel et al., 2009a). Recently, it has been shown that the stellar capture by Sgr A* is also able to reproduce the observed 6.4 keV flux from the Sgr B2 molecular cloud (Dogiel et al., 2009c); however, the Fe-Kα line flux from this MC is variable, decreasing from 2000 until now. The level of Fe fluorescence that the stellar capture is able to produce corresponds to the last value measured by the Suzaku spectrometers (Inui et al., 2009); if the decreasing trend of this line emission will stop in the near future, this will be interpreted as a steady contribution to the global Fe-Kα line emission from this molecular complex by particle (in this case proton) bombardment, on top of which X-ray reflection occurred on a limited timescale contrained by the physical properties of the putative primary source of X-ray photons.

Besides models involving subrelativistic protons, Valinia et al. (2000) proposed the interaction of low energy CR electrons (LECRe) with the ISM to be the origin of the non-thermal emission seen in the Galactic ridge. These electrons could also produce inner shell ionisation of Fe and other elements. The total 0.6-9 keV flux produced by the LECRe would account for on the order of 10-20% of the total measured flux. This model has been later applied to the inner GC region, in order to explain the hard X-ray emission and the production of the 6.4-keV line; although the model is generally valid, and it might represent

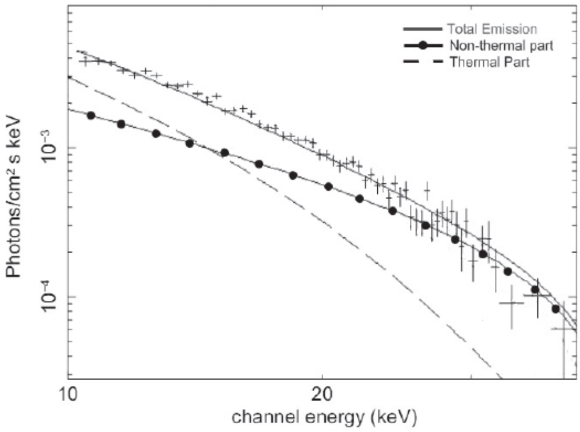

Figure 3.2: 10-40 keV spectrum of the diffuse emission in the GC region as observed by the HXD instrument onboard Suzaku (Dogiel et al., 2009c). The black dots show the inverse bremsstrahlung emission produced by the interaction of MeV protons with the ISM in the GC region, whereas the dashed line represents the thermal X-ray emission with a temperature of 6.4 keV. The best fit model is also shown with the data points, given by the sum of the thermal and non-thermal contributions (see text).

a good model for some nebulosities set in peculiar environments (the Arches cluster and the radio arc region in the GC, for example) the Fe fluorescence in the most massive MCs in the CMZ is problematic because of the low stopping range of electrons in the ISM (see Chapter 2) which would require a far too high Fe abundance and incident particle flux in order to reproduce the Fe-Kα line flux and EW.

3.2 The Fe-K$_\alpha$ line: history and observational background

Where is the Fe fluorescent emission located? Which are the MCs shining in the 6.4-keV line in the inner CMZ? In Fig.3.3 we show the map of the X-ray fluorescent emission from neutral Fe as measured by the Suzaku satellite (Koyama et al., 2006). As expected, the 6.4-keV line emission is strongly correlated with the position of the most massive molecular complexes in the CMZ: the Sgr B (B1 and B2), Sgr C, and the region between Sgr A* and the giant radio arc. Note however that this is the surface brightness distribution measured in 2005, and therefore subject to change since the Fe-K$_\alpha$ line flux from most of the clouds has been observed to be variable. In the next three subsections we are going to briefly summarise the history related to the science of the Fe fluorescence in the GC region.

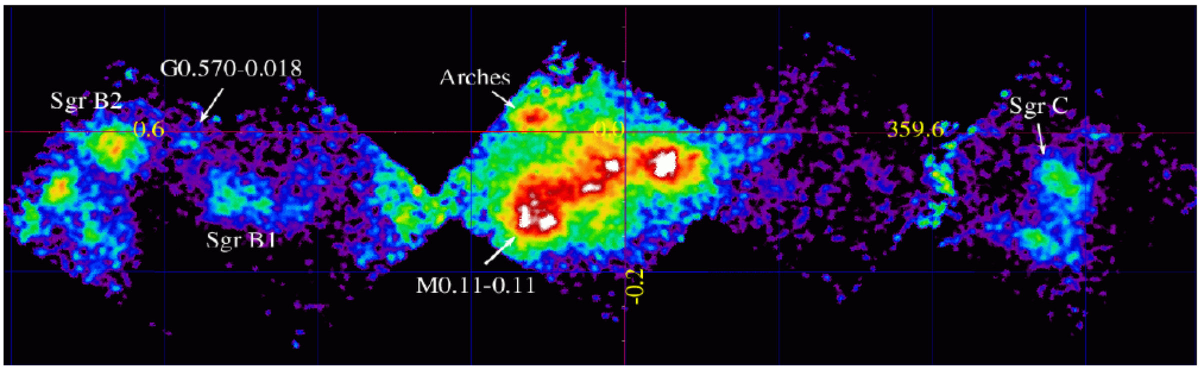

Figure 3.3: Narrow band map of the 6.4-keV line emission in the CMZ; the region shown encloses the Sgr A, Sgr B2 and Sgr C complexes. Other sources bright in the Fe-K$_\alpha$ line are also shown in the map (Koyama et al., 2006).

3.2.1 1993-2004. The dawn: reflection as the most plausible interpretation

It was in 1990 that the ART-P coded mask telescope onboard the *GRANAT* satellite observed the GC region for about 60 ksec; the results of this observation showed that the GC is permeated with diffuse X-ray emission, the hardest component of which is distributed along the inner Galactic plane and strongly correlates with the location of the most massive molecular complexes in the region (Sunyaev et al., 1993). Particularly in the energy range 8.5-19 keV this radiation is elongated parallel to the plane, with a vertical size (in latitude) which is comparable with the size scale of the distribution of MCs; this is the radiation which more efficiently produces inner shell ionisation from Fe atoms and gives rise to the 6.4-keV line. These features led the authors to suggest that the high energy part of this diffuse 2.5-22 keV X-ray emission is due to Thomson scattering of high energy photons from nearby compact sources by the MCs; as a consequence, they suggested that the Fe-K$_\alpha$ line emission should become measurable with proper instrumentation (the ART-P telescope did not have enough spectral resolution to resolve the Fe fluorescent lines from FeI and FeXXV-FeXXVI). However, the total 5-20 keV energy release in the last ~400 years in the region was calculated to be no higher than 10^{48} ergs (Sunyaev et al., 1993); as a consequence, the nucleus could not be brighter than 10^{38-39} erg s^{-1} over the same time period, nor reach the Eddinghton luminosity of $\sim 10^{44}$ erg s^{-1} even for a day, otherwise this would have left a trace in the intensity of the X-ray diffuse emission. This outstanding work gave the first hint to look for the Fe line in the location of the most massive clouds, and already stated that the X-ray luminosity of one or more putative sources could not have exceeded $\sim 10^{39}$ erg s^{-1}.

Almost at the same time as the publication of the *GRANAT* results, the Japanese X-ray satellite ASCA was launched; it was the first to carry onboard X-ray spectrometers capable of resolving the 6.4-keV and 6.7-keV fluorescent lines from Fe. The observation of the GC

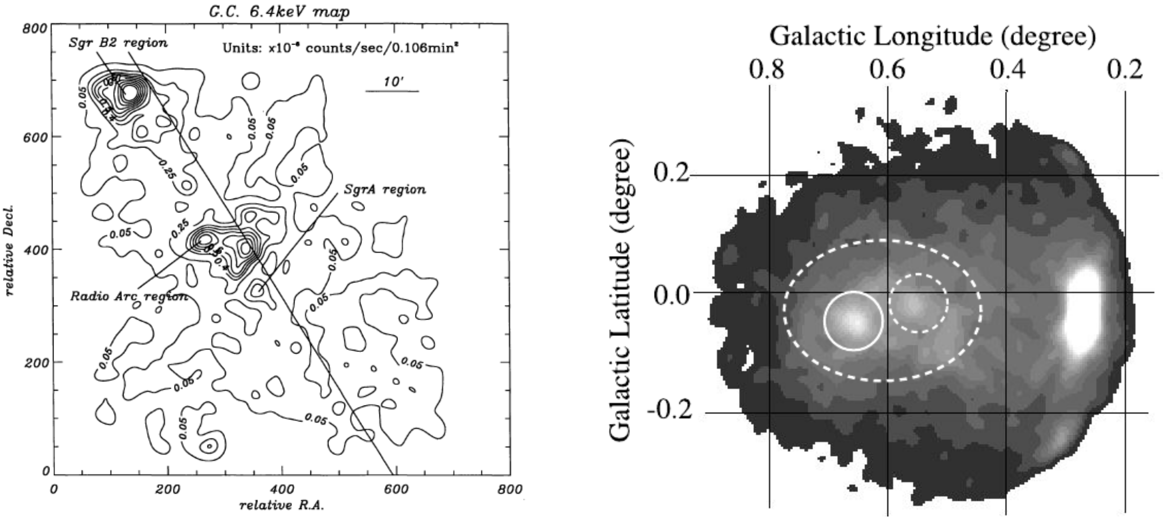

Figure 3.4: *Left*: contours of the surface brightness distribution of the 6.4-keV line in the GC region. The two brightest spots correspond to the Sgr B complex (top-left) and the MCs between the Sgr A* and the radio arc (middle Koyama et al., 1996). *Right*: ASCA GIS image of the Sgr B2 MC. The bright source at the edge of the field of view is the X-ray binary 1E1743.1-2843 (Murakami et al., 2000).

region led to the discovery of 6.4-keV line (Koyama et al., 1996); as previously suggested, the line was found to correspond with the densest molecular complexes in the CMZ, Sgr B2 and Sgr A. The first map of the surface brightness distribution of the fluorescent emission form neutral Fe in the GC region is shown in the left panel of Fig.3.4; the X-ray spectrum of the brightest cloud, Sgr B2, was found to have a large EW ($\sim$1 keV) of the Fe-K_α line, a flat hard X-ray continuum and an absorption feature at the energy of the Fe-K edge (7.1 keV), all ingredients of a typical XRN (see Chapter 2). Given the high 6.4-keV line flux measured from the cloud, $F_{6.4}=1.7\times10^{-4}$photons cm^{-2}s^{-1}, the 2-10 keV X-ray luminosity of the putative source of ionising photons was calculated to be 2×10^{39} erg s^{-1}; at the time of the observation, however, there was no source in the GC with such a high X-ray luminosity, and this led the Japanese group to suggest that the ionising source responsible for the Fe fluorescence was a (recent) past high state activity of Sgr A*. Given the measured 6.4-keV line flux and the distance of the cloud to the GC (approximately 90 pc, $\sim$300 light years), Sgr A* was suggested to have undergone its low AGN activity earlier than 300 years ago, its X-ray luminosity being consistent with the previous constraint ($L_X \lesssim 10^{39}$ erg s^{-1}, Koyama et al., 1996).

Further work has been done subsequently in order to rigorously test the XRN scenario for the Sgr B2 cloud. Together with theoretical papers showing that the spectral parameters and the surface brightness distribution of the Fe-K_α line in the Sgr B2 cloud are just as would be expected in the XRN scenario (Sunyaev & Churazov, 1998), additional observations were performed with the ASCA satellite of the Sgr B2 (right panel of Fig.3.4) and Sgr C clouds (Murakami et al., 2000, 2001); this led to the discovery of 6.4-keV line emission also from the Sgr C complex, located at a projected distance of about 70 pc West to Sgr A*, in the opposite direction with respect to the location of Sgr B2. Only 0.4 degrees from the Sgr C cloud lies the 1E 1740.7-2942 X-ray binary, with a 2-10 keV luminosity of $\sim 3\times10^{36}$ erg s^{-1}; this power is about two orders of magnitude lower than what required to produce the observed flux in the 6.4-keV line in the Sgr C cloud, and therefore it was suggested that the same past activity of Sgr A* illuminated both the Sgr B2 and the Sgr C MC. In only four years, the idea of a past flaring activity in Sgr A* was successfully tested and turned out to be the favoured interpretation for the Fe fluorescence in MCs in the CMZ. To complete the picture, observations of the other Fe-K$_\alpha$ bright clouds in the central region of the Galaxy, i.e. the innermost 20 pc, had to be performed; because of the smaller size of these complexes (parsec scale), the detailed study of the Fe fluorescence in these MCs had to wait for the advent of superior X-ray observatories with improved spectral and imaging capabilities: Chandra, Suzaku and XMM-*Newton*.

3.2.2 2003-2007. The issue is not over: evidence for particle bombardment?

In 2003, P. Predehl and collaborators presented the results of a study of the Fe-K$_\alpha$ line emission from the MCs which lie between Sgr A* and the giant radio arc at l$\sim$2 deg; these clouds are smaller than the large complexes which were studied previously with ASCA. These data, collected with the XMM-*Newton* satellite, showed many randomly distributed filaments bright in the Fe fluorescent line, all oriented perpendicular to the direction towards Sgr A* (see Fig.5 in (Predehl et al., 2003)). The results of the spectral analysis of these molecular filaments showed that although the EW of the 6.4-keV line is $\sim$1 keV, the absorption feature at the Fe-K edge is almost completely absent, or consistent with interstellar absorption alone; this is a significant difference with respect to what was observed in the Sgr B2 and Sgr C clouds, and it can only be explained by assuming a low optical depth in the clouds. The authors studied the averaged spectrum of these MCs both with a reflection model (*pexrav* model in XSPEC), and with a bremsstrahlung model to account for particle bombardment; the reflection model fits the data well only for very low Fe abundances (0.3 times the solar value), which is inconsistent with the high metallicity of the GC region. On the other hand a simple bremsstrahlung model, plus the addition of two Gaussian lines at 6.4 keV and 7.06 keV (Fe-K$_\alpha$ and Fe-K$_\beta$), fits the data well for a plasma temperature of 8.6 keV. Moreover, the 6.4-keV surface brightness of the different filaments in the field did not significantly differ from one another; if these MCs are to be illuminated by a bright X-ray source, the Fe-K$_\alpha$ surface brightness should decrease as the inverse square of the source-cloud distance, but this was not seen in the data. This was the strongest argument for suggesting that particle bombardment is the source of inner shell ionisation in these clouds.

Another important contribution to the case for particle bombardment was made in 2007 by F. Yusef-Zadeh and collaborators. These authors proposed that the 6.4-keV line

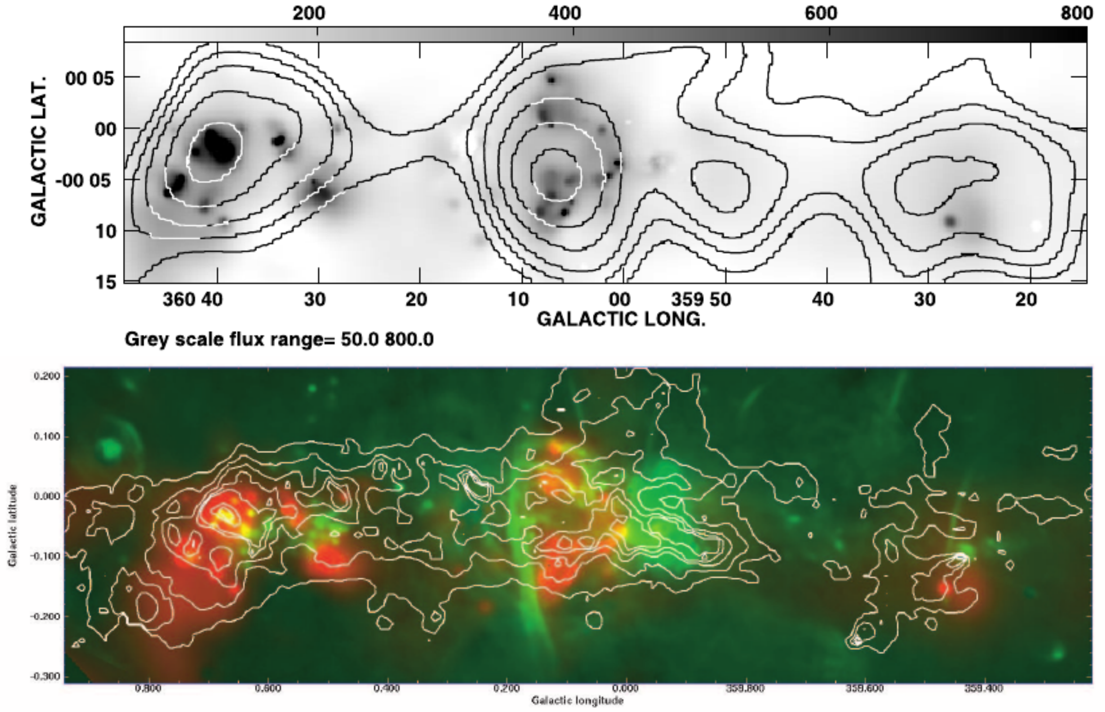

Figure 3.5: *Top*: contours of the TeV emission measured by HESS (Aharonian et al., 2006) superimposed on the Fe-Kα EW map of the inner CMZ. *Bottom*: contours of the submm emission at 850 μm superimposed on the continuum emission at 20 cm (green) and the Fe-Kα EW map (red) (Yusef-Zadeh et al., 2007b).

production must be ascribed to the LECRe bombardment of the MCs; in a certain sense, this is an evolution of the model already proposed for the explanation of the non-thermal emission in the GC ridge as due to the bremsstrahlung emission of keV electrons in the ISM, which also produces the weak Fe-K$_\alpha$ line observed in the spectrum of the ridge. This idea was already tested to be valid on the G0.11-0.11 MC; applying the LECRe model proposed by Valinia et al. (2000), the 6.4-keV line flux could be explained assuming an energy density of the LECRe of about 1-2 eV cm^{-3} (Yusef-Zadeh et al., 2002), which is only a factor of ten higher than the energy density in LECRe required to explain the non-thermal X-ray emission from the Galactic ridge.

The starting point of the new work was the discovery of a strong correlation between the surface brightness distribution of the 6.4-keV line (grey scale in the top panel of Fig.3.5), the distribution of the molecular gas as traced by the submm emission at 850μm (red color in the bottom panel), the 20 cm continuum emission most likely due to synchrotron radiation of low energy electrons spiralling in the GC magnetic fields (green color in the bottom panel of Fig.3.5), and the TeV emission recently discovered by the HESS telescope (Aharonian et al., 2006) (contours in the top panel). A significant feature of these correlations is that they are only found in the GC region; hence, Yusef-Zadeh et al. (2007b) proposed that the emission mechanisms behind these spectral features must be related to one another. Basically, the TeV emission from the MCs in the GC suggests that high energy CR, most likely protons, are interacting with the molecular material (see Chapter 1); hadronic processes would then result in the emission of two γ-ray photons for each two protons encounter. The model requires that, besides high energy protons, a population of low energy electrons also interacts with the clouds in order to create the Fe fluorescence; the energy density of the electrons is inferred assuming the energy equipartition with the magnetic field, and therefore make this argument applicable only to those molecular complexes which show bright 6.4-keV line emission associated with strong synchrotron emission from non-thermal radio filaments (green in Fig.3.5), for which a direct measurement of the magnetic field can be carried out. The resulting Fe-K$_\alpha$ line flux depends on the energy density U in the LECRe population and on the Fe abundance (Z) within the cloud; in formula

$$I_{K_\alpha} \approx 8 \times 10^{-6} \left(\frac{U}{10^3 \text{ eV cm}^{-3}}\right) \times \left(\frac{Z}{2Z_\odot}\right) \quad \text{photons s}^{-1} \text{ cm}^{-2} \text{ arcmin}^2 \tag{3.7}$$

This idea has been demonstrated to reproduce well the 6.4-keV line flux measured in the Sgr C MC; in this cloud, the 6.4-keV line surface brightness arises on top of a non-thermal radio filament for which a magnetic field of 0.22 mG has been estimated. Assuming equipartition of energy with the LECRe, the energy density of these particles results in 1200 eV cm^{-3}, which if inserted in the formula above gives an Fe-K$_\alpha$ line flux of 9.7$\times$10^{-6}photons s^{-1} cm^{-2} arcmin^2, a value that is 1.5 times the one actually observed. This model has been tested also for the MCs in the vicinity of the Arches Cluster, the 45 km s^{-1} and the 30 km s^{-1} MCs and the Sgr B2 complex; while for the other clouds the model can reproduce well the observed 6.4-keV line flux, this cannot be used for the Sgr B2 cloud since there is no evidence of the presence of any radio filament at the location of the Fe fluorescence in this MC. However, although the radio filaments - Fe-K$_\alpha$ line connection seems to work in some MCs, some issues remain open; specifically, if the 6.4-keV line flux is entirely produced by electron bombardment, the high cosmic ray flux would influence the chemistry of the clouds, particularly by heating the gas to higher temperatures and causing them to have a higher infrared luminosity than what is currently observed. We can try to quantify this last statement by writing the heating produced by electron bombardment of a molecular cloud; according to Yusef-Zadeh et al. (2007b), the heating rate per H nucleus can be written as

$$\frac{\Gamma}{n_H} = 4.0 \times 10^{-26} \frac{\xi_H}{10^{-15}\ s^{-1}\ H^{-1}} \qquad erg\ s^{-1}\ H^{-1}, \tag{3.8}$$

where H is the number of H atoms in the cloud and ξ_H the ionisation rate. Assuming typical parameters for giant MCs in the GC region, i.e. R=20 pc and n$_H$=10^{4}cm^{-3}, this heating rate results in a energy injection into the cloud of $\sim$4.5$\times$10^{37} erg s^{-1}. On the other hand, the heating rate per H nucleus required for the MCs which show Fe-Kα line emission in the CMZ in order to explain the total amount of Fe fluorescence observed is about two orders of magnitude higher than previously estimated, about 10^{-24} erg s^{-1} H^{-1} (Yusef-Zadeh et al., 2007a); as a result, if the entire 6.4-keV line flux has to be ascribed to electron bombardment, the cloud temperature should be warmer than about 200K, and the ionisation rate would be about 5×10^{-13} s^{-1}, which is about two order of magnitude higher than the value measured in the MCs between Sgr A* and the radio arc ($\sim10^{-15}$ s^{-1}, Oka et al., 2005) and three order of magnitudes higher than measured in Sgr B2 (4×10^{-16} s^{-1} Crocker et al., 2007).

As a conclusion, after the first years in which it seemed that the XRN scenario was the only plausible explanation for the Fe-K_α line emission from MCs in the CMZ, a more detailed analysis showed that there were some pieces of evidence which suggested that a contribution by particle bombardment was also plausible, at least in some of the clouds where this fluorescent emission has been detected.

3.2.3 2007-2011. The XRN golden age

In 2007, M. Muno and collaborators made a discovery which marked a turning point in the study of the Fe fluorescence feature in the GC region (Muno et al., 2007). Analysing two different Chandra dataset targeted at the GC, these authors discovered that two fluorescent Fe-Kα features varied in morphology and intensity between 2002 and 2005; their projected distance from Sgr A* is about 15 pc. In Fig.3.6 we show the 4-8 keV hard X-ray map of these observations, and the difference between the surface brightness in 2005 and 2002; as indicated by the two ellipses in each panel, thanks to the best angular resolution achieved by Chandra it was possible to measure the variation of both the morphology and the intensity of these two Fe fluorescence features. The timescale of the variability is three years, which requires the illuminating source to vary on a timescale shorter than three years; whenever observed, such a fast variability of the fluorescent emission is a strong argument in favour of the XRN scenario, where the illumination must be supplied by a bright X-ray transient source. Contrary to photons, low energy CR electrons and protons cannot travel the size of the cloud in a few years, and therefore such a fast variability definitely proved that some kind of illumination must be present in these filaments in order to produce the observed spectral and timing features. The authors calculated an X-ray luminosity for the putative source of $\sim10^{38}$ erg s^{-1}; since no such powerful transient has ever been detected in the inner CMZ, the first and best candidate was again the SMBH Sgr A*. The small effective area of Chandra in the Fe-K complex energies did not allow a satisfying quantification of fundamental spectral parameters such as the hardness of the reflected continuum and the depth of the absorption feature at 7.1 keV; for these kind of studies, the best instrument is XMM-*Newton*, whose results were published three years later (Ponti et al., 2010).

After the first discovery that the Fe-Kα line flux in two molecular filaments in the inner 20 pc of the Galaxy is variable, some further work has been performed in order to see if any other variability of the 6.4-keV line flux could be detected in other clouds within the CMZ. As already presented before, the Sgr B2 MC has been subject of detailed studies in the late 1990s and in the early 2000s; the results of these investigations all pointed to the description of Sgr B2 as an XRN illuminated by a past event of high energy activity in

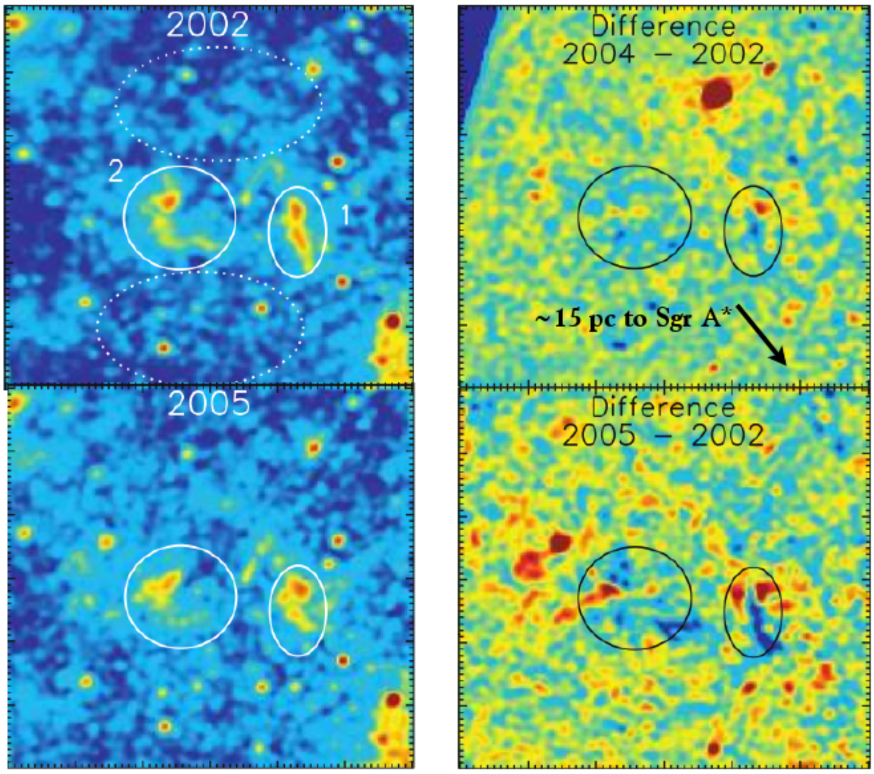

Figure 3.6: *Left column*: Chandra 4-8 keV images of two bright Fe-Kα MCs in the GC region, taken in 2002 and 2005. The clouds which show variable Fe fluorescence are indicated with the two ellipses in each panel. *Left column*: difference in the 4-8 keV surface brightness distribution between the images of 2005 (and 2004) with respect to the one in 2002 (Muno et al., 2007).

Sgr A*. One more piece of evidence was missing, but was achieved in 2009, when the first lightcurve of the Fe-Kα line flux was published (Inui et al., 2009); this shows a constant behaviour till 2000, when it starts to decrease linearly towards the present time. Therefore, the Sgr B2 MC also shows a variable 6.4-keV line flux, with a timescale of a few years, remarkably in agreement with the variability timescale of the other two small filaments previously discovered closer to Sgr A*. After this discovery, the GC community started to be convinced of the past low AGN activity of Sgr A*; since the X-ray luminosity required in order to reproduce the Fe-Kα line flux is about the same for every cloud, and given that the assumption of a past flaring activity of the SMBH is very strong by itself, the next step in the characterisation of this activity was to understand whether a single flare with a given timescale and X-ray luminosity could explain all the 6.4-keV nebulosities observed in the GC region, both the variable and the constant ones. This study was performed by Ponti et al. (2010); these authors collected the whole XMM-*Newton* dataset targeted at Sgr

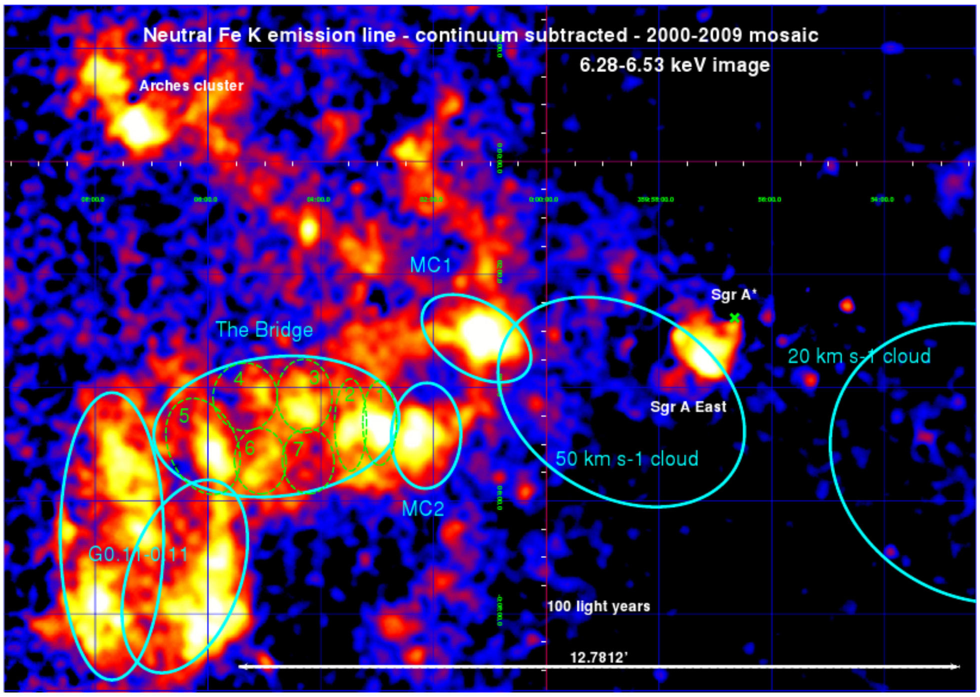

Figure 3.7: XMM-*Newton* map of the 6.4-keV line surface brightness in the innermost 20 pc of the CMZ. The cyan ellipses show the MCs studied in the relative publication (Ponti et al., 2010) and in Chapter 4.

A* and studied the Fe-Kα reverberation in a few MCs located in the innermost 20 pc (in projection) of the Galaxy. Since the XMM-EPIC cameras have a large field of view, these MCs could be studied even though they were not the main target of all the observations; indeed, every pointing done on Sgr A*, which was object of an extensive campaign during the last decade, could be used to study the MCs in the immediate vicinity. The resulting narrow band image of the studied region et al. is shown in Fig.3.7, where the cyan ellipses show the MCs selected on the base of their CS J=1-0 line emission; as discussed in Chapter 1, the l-b and the l-v diagrams help in discerning between different molecular structures distributed along the line of sight, although they might appear next to one another.

The results of this study are surprising, and show that the Fe-Kα line flux has a complex pattern of variability; indeed, some MCs display a rising 6.4-keV line flux, whereas some others, immediately adjacent, show a decrease of the fluorescent signal; the lightcurves of the 6.4-keV line measured in the different clouds in Fig.3.7 are shown in Fig.3.8. In this study, six molecular complexes have been identified: the 50 km s^{-1} and the 20 km s^{-1} MCs, which do not show any Fe-Kα line emission, the two small clouds MC1 and MC2, and the two bigger complexes G0.11-0.11 and the one called the *bridge*, which turned out to be the most interesting structure within this region. In fact, whereas in the other MCs the lightcurve of the 6.4-keV line flux was found to be linearly variable or constant, the different

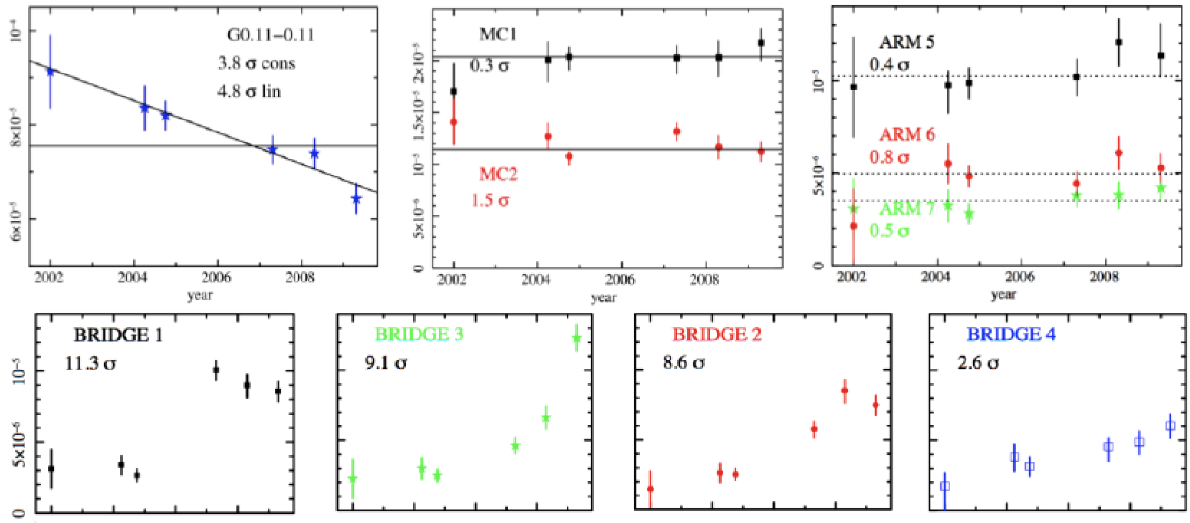

Figure 3.8: Lightcurves of the Fe-Kα line flux (in units of photons cm^{-2} s^{-1}) measured in the different MCs. On the top we show the results for the main molecular complexes, and below the results for the subregions of the *bridge* (see text). The X-axis is the same for every plot and encloses the time window from 2002 to 2009 (Ponti et al., 2010).

subregions within the *bridge* displayed completely different lightcurves (see Fig.3.8); these are consistent with an Fe-Kα flux which is increasing in response an illumination front within the cloud, which is propagating from West to East (exactly the direction which connects Sgr A* to the *bridge*). As a confirmation, in the left panel of Fig.3.9 we show the narrow band image centred at 6.4 keV of the region; looking at the different dashed ellipses within the *bridge*, which represent the subregions which were identified for the timing analysis, we can clearly notice that in November 2004 the regions 1, 2 and 3 within the *bridge* are dark, whereas in 2007 they start to get brighter (see also the lightcurve in Fig.3.8). Later, in 2008 and 2009 the surface brightness of the eastern region *bridge*-3 increases, whereas in the other two ellipses remains constant. Therefore, the ionising flux must have crossed a path of at least 15 light years (∼45 pc) in 5 years, and this is clearly impossible; to resolve this issue, the authors of this discovery put the cloud much further behind the plane of Sgr A*, about 60 pc, in this way solving the paradox of an apparent superluminal motion. The discovery of such a quick variation of the surface brightness within a single cloud was a confirmation that the inner shell ionisation in this cloud is created by photons; the resulting X-ray luminosity of the putative source resulted once again on the order of 10^{39} erg s^{-1}, which suggested that the same high state activity which could explain the Fe fluorescence in the Sgr B2 and Sgr C MCs could have also been responsible for the creation and the variations of all these nebulosities.

Furthermore, these authors tried to build a model of the past activity of Sgr A* collecting all the information available at that time; measuring the N$_H$ of the MCs, and assuming that the same flare with a luminosity of 10^{39} erg s^{-1} has illuminated all the clouds in the

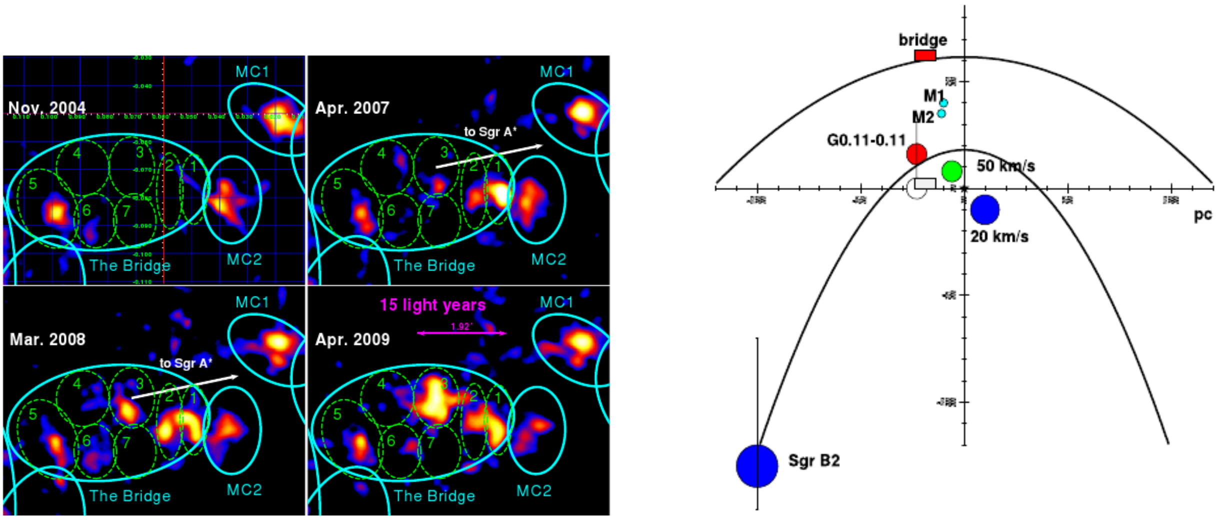

Figure 3.9: *Left*: time resolved images of the bridge region in a narrow band centred at 6.4 keV showing the apparent superluminal propagation of the incident ionising photon flux and the corresponding variability of the Fe-Kα line flux. The direction to the location of Sgr A* is indicated by a white arrow. *Right*: spatial distribution of the MCs into the line of sight. The two parabolas are two isochrones representing the leading and trailing edges of the flare propagating from Sgr A* into the CMZ (Ponti et al., 2010).

CMZ, is possible to infer the distance along the line of sight of each MC. In formula

$$\frac{R^2}{4d^2} = \Omega = \frac{4\pi D^2 \cdot F_{6.4}}{\tau \cdot L_x \cdot 10^7 \cdot Z} = 5.17 \times 10^{-4} \left(\frac{F_{6.4}}{10^{-4}}\right)\left(\frac{0.1}{\tau}\right)\left(\frac{Z_\odot}{Z}\right), \tag{3.9}$$

where D is the distance to the GC (~8 kpc), R is the radius of the cloud, d is the Sgr A*-cloud distance, Ω the solid angle between Sgr A* and the MC (in units of 4π), $F_{6.4}$ is the measured Fe-Kα line flux, L_X is the X-ray luminosity of the flare of Sgr A* (assumed to be 1.4×10^{39} erg s^{-1}, (Ponti et al., 2010)), Z is the Fe abundance within the cloud, and τ is its optical depth for Thomson scattering. Once the flux of the 6.4-keV line and the N_H of the MC are measured, it is possible to measure Ω from which, having the measured radius of the cloud, R, it is possible to derive the cloud-source distance (d). This last parameter is the combination of the cloud projected distance and its location along the line of sight; since the first can be measured, the last can be derived as a final result. The right panel of Fig.3.9 shows the distribution of the MCs in the CMZ along the line of sight, as derived from measurements of the Fe-Kα line flux and variability (Ponti et al., 2010). In this plot, the two parabolas represent the leading and the trailing edges of the flare, propagating in the CMZ at the speed of light; in this scenario, the luminosity of Sgr A* must have been constant at $\sim10^{39}$ erg s^{-1} for more than 100 years. Once the leading and trailing edges have been fixed using the constraints derived from the study of the bridge and G0.11-0.11, which are being crossed by the leading and trailing edges (respectively) in order to explain the increasing and decreasing flux of the Fe fluorescent line, the other clouds were then distributed along the line of sight depending on characteristics of the Fe-Kα flux variability they display. To date, this is the most favoured model for the explanation of all the 6.4-keV features observed the GC.

A further confirmation of this picture came from the measurement of the lightcurve of the hard X-rays Compton scattered by the Sgr B2 MC. As we discussed in Chapter 2, besides the 6.4-keV line from neutral Fe and the absorption feature at the Fe-K edge energy of 7.1 keV, an important feature of an XRN is the Compton scattered radiation at energies higher than $\sim$10 keV; in response to a variable incident photon flux, not only the Fe-Kα line flux will display variability, but the hard scattered continuum X-rays will also display the same variation. As a consequence of illumination by X-ray photons, the lightcurves of these two components of XRN should experience the same temporal variation; this has been found in Sgr B2, for which the INTEGRAL satellite measured a decreasing 20-60 keV flux from 2003 to 2009 (Terrier et al., 2010), which well resembles the same time variability suffered by the 6.4-keV line flux (Inui et al., 2009). This discovery finally proved that Sgr B2 is an XRN; whether the X-ray illumination source is Sgr A* or not, this must still be definitely confirmed by studying the hard X-ray scattered component in other MCs in the CMZ, for which the NuSTAR satellite will be needed (expected launch in late 2012) in order to disentangle the diffuse emission scattered from the (smaller) MCs and nearby X-ray sources.

Although the XRN model well explains the Fe-Kα line flux and variability from most of the MCs in the CMZ, we note that there are some regions where this model does not work and the Fe fluorescence is most probably produced by the bombardment of the clouds by low energy cosmic ray electrons and/or protons; for example, we have demonstrated that the 6.4-keV nebulosities seen in the vicinity of the Arches cluster, about 25 pc in projection North-East to Sgr A*, cannot be explained in the model presented above (see Chapter 5). Indeed, the Fe-Kα line emission from those clouds is most likely to be produced by electrons and/or protons accelerated within the cluster itself, or in the bow shock originating from the relative motion of the cluster with the nearby MCs. Furthermore, a molecular complex, G0.162-0.217, adjacent to the south end of the radio arc, has been found to emit 6.4-keV fluorescent photons with an EW of the Fe-Kα line of 0.2 keV; here the fluorescence is most likely produced by the interaction of low energy electrons, whose presence is confirmed by the intense synchrotron emission from the nearby filamentary structures of the radio arc (Fukuoka et al., 2009).

In this context we developed the main part of my doctoral work. We have also been studying the MCs shown in Fig.3.7, for which we found slightly different results; the main motivation of our studies was that the model presented by Ponti et al. (2010) was only based on the study of the 6.4-keV line variabilty, without considering other important spectral parameters typical of an XRN like the EW of the line and the absorption at the Fe-K edge. We therefore performed a much more detailed spectral study of these clouds, and this is what differentiates our work from the one by Ponti et al. (2010); we will present our results in Chapter 4.

Chapter 4

The X-ray lightcurve of Sgr A* over the past 200 years inferred from Fe-K$_\alpha$ line reverberation in Galactic Centre molecular clouds

Original publication: R. Capelli, R.S. Warwick, D. Porquet, S. Gillessen, P. Predehl, *The X-ray lightcurve of Sgr A* over the past 400 years inferred from Fe-K$_\alpha$ line reverberation in Galactic Centre molecular clouds*. The content of this chapter will be submitted to the International scientific Journal Astronomy & Astrophysics; as first author, my contribution to this work included the data reduction and analysis, as well as the following scientific interpretation of the results. The other authors contributed with the review of the draft and comments and suggestions regarding the scientific interpretation of the results, which helped to improve the work.

Abstract: The spatial distribution and variability of Fe-K$_\alpha$ emission from molecular clouds in the Galactic Center region may provide an important key to the understanding of the history of Sgr A*. A very plausible interpretation is that this variability represents an echo in the reflected radiation from the clouds of a past episode of high activity in Sgr A*. This work examines the Fe-K$_\alpha$ timing and spectral properties within the molecular filaments in the immediate vicinity of Sgr A*, in order to understand and constrain the primary energising source of the Fe fluorescence. We collected all the archival XMM-Newton observations targeted at Sgr A*. We have studied the variability of the 6.4-keV line in specific cloud regions by spectrally fitting the data derived from the EPIC MOS cameras after subtracting a modelled background. We have also studied the reflection imprints (equivalent width and absorption edge) in the time averaged spectra of each cloud. From the measurement of the optical depth of this absorption we estimated the N$_H$ of the MCs, which we further used for estimating the mean Fe abundance and the level of X-ray emission required to produce the measured 6.4-keV line flux. Finally we stacked the MOS spectra of two large regions in order to quantify the East-West asymmetry of this line emission and the probable contribution of cosmic rays to the production of the Fe fluorescence.

The Fe-K$_\alpha$ line has a wide and difficult pattern of variability. The equivalent width of the 6.4-keV line measures ~1 keV in all the clouds, this result being compatible with Fe fluorescence induced by photoionisation of the clouds; all the spectra show an absorption feature at 7.1 keV, also interpreted as due to X-ray absorption and reflection. We found the mean value of the Fe abundance in these clouds to be 1.6±0.2 solar. Finally, we presented the X-ray lightcurve of Sgr A* relative to the past ~200 years; this shows a decreasing trend staggered by sudden episodes of brightening, characterised however by a lower luminosity than the previously suggested 10^{39} erg s^{-1}. The temporal and spectral properties of the MCs are promptly explained in terms of illumination by X-ray transient source/s; in particular we presented a XRN/SgrA* model which accounts for all the results we got from all the single spectra. Given the X-ray luminosity values needed to explain the Fe fluorescence in these clouds, we cannot exclude a powerful transient source to be at the origin of this peculiar phenomenon. To better infer the recent level of X-ray activity of Sgr A* the contribution by particle bombardment to the creation of 6.4-keV photons will have to be carefully measured.

4.1 Introduction

The Galactic Centre (hereafter GC) region is a unique environment within the local Universe, which provides many tests of our understanding of fundamental issues in astrophysics. The region hosts the nearest Super Massive Black Hole (SMBH), Sgr A*, with a mass of 4×10^6M$_\odot$ (Schödel et al., 2002; Ghez et al., 2008). It is also a region in which high energy phenomena abound. For example, in X-rays the Sgr B2 and Sgr C molecular complexes, located at projected distances of 90 pc and 70 pc from Sgr A*, shine brightly through 6.4-keV Fe-K$_\alpha$ line emission (Koyama et al., 1996; Murakami et al., 2000; Nakajima et al., 2009), consistent with the prediction of Sunyaev et al. (1993).

The physical mechanism responsible for the Fe-K$_\alpha$ emission from these molecular clouds near the GC is the fluorescence of cold, neutral or near-neutral matter irradiated by high energy particles or X-ray photons. So far several hypotheses have been proposed as to the nature and origin of the primary source of this irradition. The possibilities include: the X-ray reflection nebulae model (XRN, Sunyaev & Churazov, 1998), heating by low-energy cosmic-rays (Yusef-Zadeh et al., 2002), shock mechanisms (Yusef-Zadeh et al., 1997), and electron bombardments (Predehl et al., 2003).

A recent suggestion is that subrelativistic protons can be created via accretion of stellar debris onto the central black hole, thus explaining both the observed X-ray continuum and the 6.4 keV line emission from the GC (Dogiel et al., 2009c). Other particle-like candidates can be cosmic-ray electrons originating in supernova events (Valinia et al., 2000). If the fluorescence observed in molecular complexes is the result of irradiation by X-ray photons, a luminous localised source of X-rays must be invoked to power the observed emission, since the diffuse hot plasma which permeates the central regions of the Galactic plane produces a factor ten less photons than is required to account for the observed Fe-K$_\alpha$ flux. It has been estimated that depending on its position relatively to the Sgr B2 and Sgr C molecular clouds, this source should have a 2-10 keV luminosity of the order of 10^{38}-10^{39}erg s^{-1}.

Presently no persistent sources in the GC region have such a high luminosity; however a past transient outburst in a source, which has now returned to a relatively quiescent state, might well match the requirement. Sgr A* itself is arguably the best candidate, since although its activity is currently rather weak (the brightest flare measured with XMM-Newton has a luminosity of the order of a few 10^{35}erg s^{-1}, Porquet et al., 2003), the SMBH could have undergone a period of high-state activity in the past (Koyama et al., 1996). In fact, the projected light travel time to Sgr B2 implies an outburst roughly 75-150 years ago, according to a recent estimate (Terrier et al., 2010). Since there are a number of filaments nearer to Sgr A* which emit at 6.4-keV, the same argument would require Sgr A* to also have flared more recently, say within the last 100 years, depending on the relative position of the clouds along the line of sight.

One method of distinguishing between the point source and the particle hypothesis is to investigate the lightcurve of the filaments which emit the 6.4-keV line. If we are dealing with a transient source as an engine of the fluorescent emission, one might expect some temporal evolution of the observed line flux corresponding to the light curve of the outburst blurred by any inherent spread in light-travel delays imposed by the source to cloud geometry. Such effects have been found in the Sgr B2 molecular cloud, where the brightest peak of the Fe-K$_\alpha$ emission, first measured in 2000 by Asca (Murakami et al., 2000), was 40% weaker in 2005 when re-observed with Suzaku (Inui et al., 2009). Similarly, Nakajima et al. (2009) discovered variability of the Fe-K$_\alpha$ flux from Sgr C on the basis of recent Sukaku observations. Moreover, Muno et al. (2007) have reported the evolution in intensity and morphology of the 4-8 keV continuum emission in two filamentary regions located close to Sgr A*. The latter changes occurred on parsec scales (in projection), which requires a brightening/fading of the illuminating source over a 2-3 year period, with an inferred 2–8 keV luminosity of at least 10^{37} erg s^{-1}. Recently, Ponti et al. (2010) showed that the 6.4 keV line flux from the molecular filaments with 15 arcmin of Sgr A* exhibit a complex pattern of variability. If these molecular clouds/knots have a particular distribution along the line of sight, then it is possible to argue that they were all energised by the same outburst on Sgr A*, consistent with the XRN scenario (Ponti et al. 2010). However, given the observational complexities, it is very possible that this is not the complete story; indeed, very recently Capelli et al. (2011b) studied the Fe-K$_\alpha$ line emission from the MCs in the Arches cluster region (about 20 pc in projection from Sgr A*), showing that the XRN/Sgr A* scenario can hardly describe the spectral and temporal properties of those clouds.

The above results open once more the question whether Sgr A* has exhibited AGN activity in the past and, if so, what is the exact nature of that activity. It is in this context that we reassess in this paper, the morphology, variability and spectral properties of the 6.4-keV emitting clouds within 15 arcmin the GC, using the extensive set of XMM-Newton observations targeted at this region. Our goal is to investigate both the past role of Sgr A* (or other transient sources) in illuminating the GC molecular clouds and also to seek evidence for a contribution from alternative mechanisms, such as CR bombardment, in the excitation of the Fe fluorescence which characterises the GC environment. Throughout this work, the distance to the GC has been taken to be 8 kpc (Gillessen et al., 2009).

Table 4.1: Specifications for the selected OBSIDs: MODE/FILTER combination used for each of the pointings, and GTI compared to the total exposure for each instrument. F=Full Frame MODE; E=Extended Full Frame MODE; T=Thick filter; M=Medium Filter.

OBSID	Obs Date yyyy-mm-dd	PN mode/filter-GTI/exp	MOS1 mode/filter-GTI/exp	MOS2 mode/filter-GTI/exp
0111350101	2002-02-26	F/T-38.590/40.030	F/M-42.262/52.105	F/M-41.700/52.120
0202670501	2004-03-28	E/M-13.320/101.170	F/M-33.070/107.784	F/M-30.049/108.572
0202670601	2004-03-30	E/M- 25.680/112.204	F/M-32.841/120.863	F/M-35.390/122.521
0202670701	2004-08-31	F/M-59.400/127.470	F/M-80.640/132.469	F/M-84.180/132.502
0202670801	2004-09-02	F/M-69.360/130.951	F/M-94.774/132.997	F/M-98.757/133.036
0402430301	2007-04-01	F/M-61.465/101.319	F/M-61.002/93.947	F/M-62.987/94.022
0402430401	2007-04-03	F/M-48.862/93.594	F/M-40.372/97.566	F/M-41.317/96.461
0402430701	2007-03-30	F/M-32.337/32.338	F/M-26.720/33.912	F/M-27.685/33.917
0505670101	2008-03-23	F/M-74.216/96.601	F/M-73.662/97.787	F/M-74.027/97.787
0554750401	2009-04-01	F/M-30.114/38.034	F/M-32.567/39.614	F/M-33.802/39.619
0554750501	2009-04-03	F/M-36.374/42.434	F/M-41.376/44.016	F/M-41.318/44.018
0554750601	2009-04-05	F/M-28.697/32.837	F/M-37.076/38.816	F/M-36.840/38.818

4.2 Observations and Data Reduction

We checked in the HEASARC archive for XMM-Newton observations of the GC region and selected observations with a nominal pointing position within 15' from Sgr A* (R.A.=17^h 45^{m}40.045^s, DEC.=-29°0'27.9"). Data from the EPIC cameras, consisting of one PN back illuminated CCD detector (Strüder et al., 2001) and two MOS front illuminated CCD detectors (Turner et al., 2001), have been reprocessed using the tasks EMPROC and EPPROC in the Science Analysis Software SAS version 9.0. For our purposes it is necessary to rigorously select the Good Time Intervals (GTI), representing the periods in which the internal background of the cameras was relatively quiescent. For this reason we used the SAS task ESPFILT to screen data with a high particle-induced background. This task was originally developed inside the Extended Sources Analysis Software (ESAS, Snowden et al. 2004) and then converted into a proper SAS task; it fits a Gaussian peak to the distribution of count rates, and creates a GTI for those time intervals with count rates within the thresholds, defined to be $\pm 1.5\sigma$ from the mean count rate. The GTI filtering has been done separately for all the three EPIC cameras. Figure 4.1 shows the results for the screening done on the MOS1 data of OBSID 0202670701, and how the task operates. The upper panel shows the histogram for the full Field Of View (FOV) lightcurve in the 2.5-12 keV band, while in the middle and the lower panels are, respectively, the 2.5-8.5 keV lightcurve of the IN FOV region and the corner data. The green time intervals are those selected by the filtering process and used for the further analysis. The results of the screenings done on all the selected data sets together with the specifics of each observation are reported in Table 4.1.

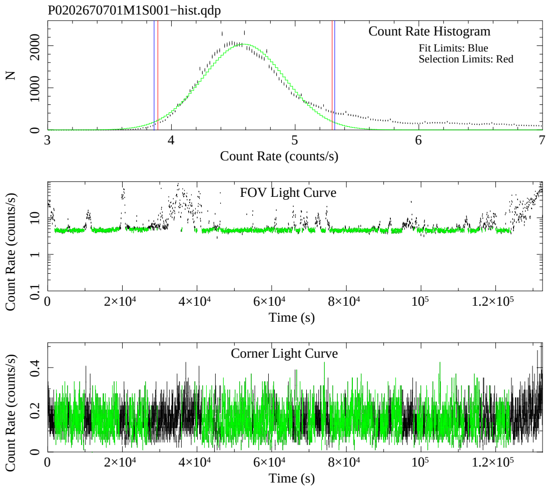

Figure 4.1: Soft proton flare filtering of the MOS1 dataset from OBSID 0202670701. *Upper panel*: 2.5-12 keV count rate histogram. The blue lines mark the region used in the Gaussian fit, the green line represents the best fit Gaussian and the red lines show the bounds used to filter the data. *Mid panel*: 2.5-8.5 keV lightcurve of the IN FOV region. *Lower panel*: 2.5-8.5 keV lightcurve of the corner data. In both the Mid and the Lower panels, the points coloured green in the light-curves correspond to the selected GTI intervals (see text).

Only for OBSIDs 0402430301, 0402430401 and 0505670101, contaminated by a very high radiation level at the end of these observations, we performed a different GTI selection. Indeed, the method selecting the count rate inside $\pm1.5\sigma$ from the mean count rate can lead to a bias in the case of a very strong flare during an observation (especially for the PN camera; this does not influence the MOS cameras). Moreover when removing the count rates below the mean count rate-1.5σ (see Fig.4.1) all the genuine low background exposure times in the observation are removed. The ESPFILT filtered PN event files for OBSIDs 0402430301, 0402430401 and 0505670101 have a GTI exposure of 0.3, 4.3 and 9.2 ks, respectively. We then built the 10-12 keV lightcurve of the full FOV for these OBSIDs, and selected those intervals with a count rate lower than 1.5 counts s^{-1} (for OBSIDs 0402430301 and 0402430401) and 1.25 counts s^{-1} (OBSID 0505670101). The total exposures in the PN cameras of these OBSIDs with the new filtering process are 61.5, 48.9 and 74.2 ks, respectively.

Throughout our analysis we have only selected single and double events (PATTERN$\leq$4) for PN and up to quadruple events for MOS1 and MOS2 (PATTERN$\leq$12) cameras. For all the instruments a further screening for good events was done selecting only events marked as real X-rays (FLAG==0).

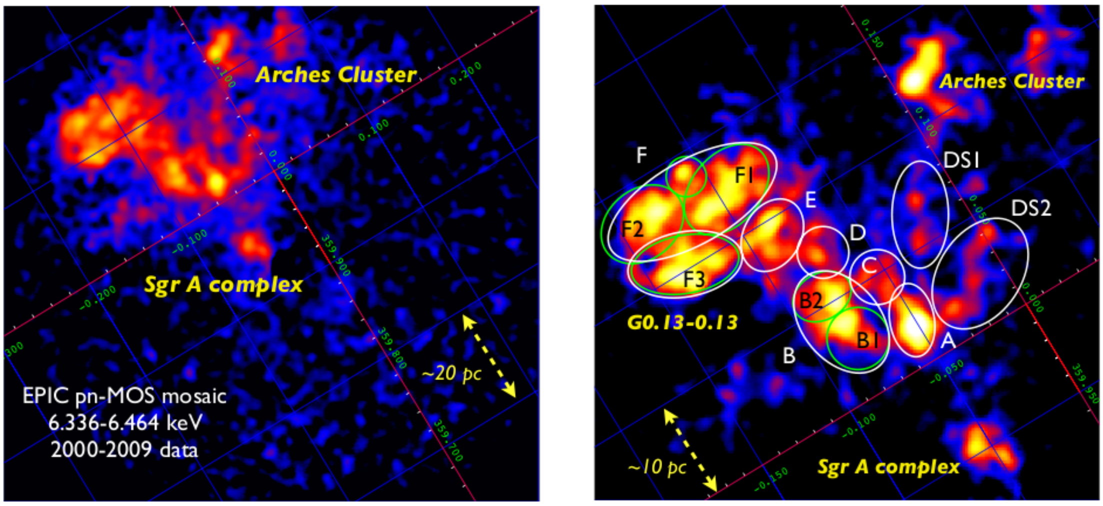

Figure 4.2: *Left panel*: Fluence map (6.336-6.464 keV) of the Fe-K$_\alpha$ emission from the filaments in the GC. The image has been smoothed with a 8-pixel diameter top-hat filter. The grid lines define the Galactic Coordinate frame. *Right panel*: A zoom-in on the region of the bright filaments. The white (green) ellipses show the regions (sub-regions) selected for the spectral analysis (see Table 4.2); region B has been divided into two subregions B1 and B2; region F (G0.11-0.11) into three subregions, F1 (ellipse plus small circle), F2 and F3.

4.3 Data analysis and results

4.3.1 Imaging

Method

First we built a fluence (integrated flux over time) map for the Fe-K$_\alpha$ line in a very narrow energy window in order to identify and locate the brightest Fe fluorescence regions. We proceeded by merging all the GTI filtered event files for the three EPIC cameras (where available) for every OBSID selected (see Table 4.1), using the SAS task EMOSAIC. In building the image of the Fe-K$_\alpha$ emission, we assumed a value of $E/\Delta E=50$ for the spectral resolution (FWHM) of both PN and MOS1&2 at 6.4 keV, corresponding to a bandpass for the Fe fluorescence signal of 6336-6464 eV.

An important issue for our analysis is the subtraction of instrument background and, where appropriate, the continuum underlying the line emission. To quantify the percentage of counts in the narrow band 6336-6464 eV due to both components, we selected the energy range 3904-6208 eV in the total event file and produced 18 adjacent images of the whole FOV, each 128 eV broad. The spectral window thereby encompassed is free of contamination by strong emissions lines, including both the Fe-K$_\alpha$ emission from neutral or near-neutral ions and the Fe-K emission from high ionisation lines which characterise the

GC high-energy thermal components. We then fit the distribution of counts as a function of the energy, and further used this best fit to infer the number of counts in the continuum for the images in the ranges 6208-6336 eV and 6336-6464 eV, where the counts due to Fe fluorescent emission are. Finally, we used the 6272 eV centered image properly scaled as background for the Fe Ka map.

Results

The background- and continuum-subtracted narrow-band (6336-6464 eV) image produced by the method outlined in the previous section, in effect, represents a Fe-K_α line fluence map (with the provision that the effective exposure varies somewhat over the field). This image is shown in Fig.4.2. The morphology of the Fe K_α emission evident in this image is consistent with that reported earlier by other X-ray satellites including ASCA (Koyama et al., 1996), Chandra (Yusef-Zadeh et al., 2007a), and Suzaku (Koyama et al., 2006). The main differences arise because of instrumental effects (different angular resolution and sensitivity in the hard X-ray domain) or different exposure times. Our results are also in good agreement with those reported recently by Ponti et al. (2010), based on an independent analysis of a broadly similar set of XMM-Newton observations.

All the maps clearly show an asymmetry in the distribution of the Fe-K_α emission with respect to the position of Sgr A*. All the filaments are located east from Sgr A* at negative Galactic latitudes. On the western side of the GC region, the closest molecular complex bright in Fe fluorescent lines is Sgr C, located at a projected distance from Sgr A* of approximately 70 pc. Looking at the radio maps of the GC region in CO (Oka et al., 1998) and CS (Tsuboi et al., 1999) rotational lines, an asymmetry in the distribution of molecular matter is very noticeable, with more concentrated to the east of Sgr A*. Nevertheless, a certain amount of cold matter not shining in the 6.4-keV line is present along the whole plane of the Galaxy, and this should be taken into account in explaining the origin of the Fe-K_α emission in the filaments between Sgr A* and the GC feature known as the Radio Arc. Looking at the left panel in Fig.4.2, the presence of low surface brightness 6.4-keV line emission is evident across the whole region between the Radio Arc ($l \approx 0.2°$) and Sgr A* (coded as diffuse blue in Fig.4.2). In contrast, this low-level emission is totally absent at negative longitudes. We emphasise that this is not an image artifact. In fact, the 6.4-keV spatial distribution at faint levels coincides remarkably well with the contours of TeV γ-ray emission measured by HESS (Aharonian et al., 2006), a connection first noted by Yusef-Zadeh et al. (2007a) using the 6.4-keV line equivalent-width image measured by Chandra. Thanks to the much higher effective area of XMM-Newton, we are now able to establish that this strong correlation apparently extends to regions outside of those occupied by very dense molecular clouds (see Section 4.3.7).

The bright region in Fig.4.2 located at $l \sim 0.12°$, $b \sim 0.05°$ is the Arches Cluster; for the study of the 6.4-keV line emission from the MCs in this region we cross refer to the recent work by Capelli et al. (2011b). We have excluded from our study the bright feature at $l \sim -0.05°$. This is the Sgr A complex, containing both Sgr A* itself and the Sgr A East Supernova Remnant (SNR). In Table 4.2 we report the coordinates and the sizes of the

Table 4.2: Coordinates (J2000) of the center, sizes (radius or semi-axis) and projected distance from Sgr A* of the regions selected for the spectral analysis (see Fig.4.2). Regions F (G0.11-0.11) and F1 are made up of two selections. The clouds marked with a star are subregions of the *bridge* cloud as identified by Ponti et al. (2010).

Region	Ponti	R.A.(J2000)	DEC.(J2000)	size (arcmin)	d_{proj} (pc)
The 9 clouds					
A	MC1	17:45:52.398	-28:56:38.15	0.65x1.08	10.9
B1	MC2	17:45:59.592	-28:57:10.09	0.91x0.91	12.6
B2	1&2*	17:46:04.394	-28:55:56.74	0.90x0.68	16.3
C	new	17:45:57.026	-28:55:22.91	0.8x0.8	14.7
D	3&4*	17:46:04.252	-28:54:39.64	0.75x0.75	18.3
E	5*	17:46:10.997	-28:54:09.50	1.12x0.83	21.6
F	G0.11-0.11	17:46:21.627	-28:53:11.36	2.75x1.22	27.2
		17:46:22.615	-28:55:00.14	1.68x0.95	
DS1	new	17:45:51.294	-28:53:35.76	0.77x1.52	17.0
DS2	new	17:45:43.377	-28:55:14.99	1.78x1.16	12.3
The 3 F subregions					
F1		17:46:17.084	-28:52:49.45	1.49x1.01	
		17:46:22.443	-28:52:26.99	0.59x0.59	
F2		17:46:28.297	-28:53:50.10	1.32x1.01	
F3		17:46:22.615	-28:55:00.14	1.68x0.95	
Large regions					
EDE		17:45:53.128	-28:52:26.19	10.95x7.09	
EDW		17:45:13.233	-29:06:46.85	10.95x7.09	

selected regions of elliptical shape upon which our spectral analysis is based. We selected these sky regions solely on the basis of Fe-K$_\alpha$ morphology without reference to potential radio molecular counterparts (that could help to identify spatially and physically connected regions). In doing so, we neglected the possibility that some of the filaments which are bright in the Fe-K$_\alpha$ line could be part of a single, more extended, molecular complex. This issue will be addressed in Section 4.4.1.

4.3.2 Spectroscopy: studying the Fe-K$_\alpha$ variability

Method

We carried out a spectroscopic analysis of the Fe-K$_\alpha$ bright filaments shown in Fig.4.2, with the objective of measuring the photon flux in the 6.4 keV line and searching for any variations in this quantity over an eight-year timeframe. The molecular complexes bright in

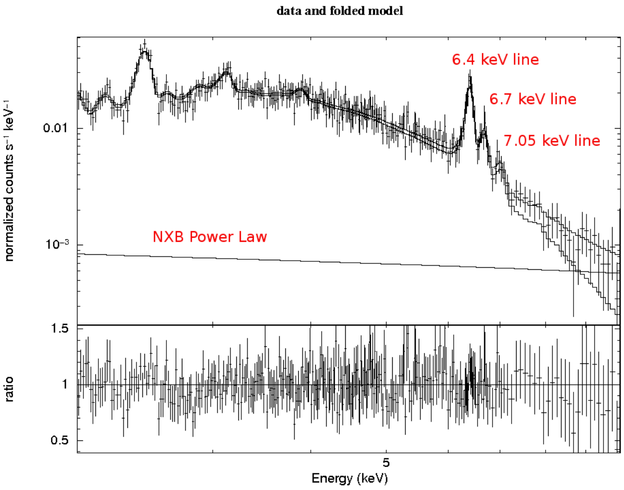

Figure 4.3: *Upper panel*: The spectrum derived for Region B from the September 2004 MOS1 dataset together with the best-fitting spectral model. The lower solid line shows the NXB power law component. The two curves show the net X-ray source spectrum and the source plus NXB best fit model (top curve). Three Fe lines are labelled; neutral Fe-K_α and K_β lines at 6.4 and 7.05 keV, and the Fe XXV K_α line at 6.7 keV. *Lower panel*: Ratio between the spectral points and the best fit model.

the Fe fluorescent line are embedded in strong X-ray emission due to the presence along the line of sight of unresolved thermal X-ray emission. This thermal emission, which permeates the whole GC region can be characterised as a two-temperature plasma with typically $kT_1 \approx 1$ keV and $kT_2 \approx 6.5$ keV (Koyama et al., 2007a). For our purposes, everything but the 6.4-keV line emission is considered as background radiation. Unfortunately due to the relatively low surface brightness of the fluorescent emission and the spatial variations inherent in the foreground emission, the subtraction of a "local background" introduces many systematics in the resultant spectrum. Therefore, we adopted the approach of modelling the Non X-ray Background (NXB) rather than subtracting it. In Appendix A we describe the different ways of dealing with NXB in an XMM-Newton dataset, and specify the methodolgy we actually employed. One consequence of the use of the background modelling technique was that for this part of analysis we were restricted to the use of the MOS data only.

We built response and ancillary files with the SAS tasks RMFGEN v1.55.1 and ARFGEN v1.76.4. No point source excision has been applied. The need for a systematic analysis with spectra encompassing very different exposure times and net counts, led us to use the Cash statistic (Cash, 1979) rather than χ^2. We grouped the channels in each spectrum with the GRPPHA tool to ensure at least 1 count/bin.

We fitted all the spectra with a model which accounts for all of the source and instrumental components. The former includes the two thermal components noted above, a power-law continuum plus an associated 6.4-keV Fe line (representing reflection and fluo-

Region	Feb02	Mar04	Sep04	Apr07	Mar08	Apr09
A	2.5±0.3	2.2±0.2	2.1±0.1	2.2±0.2	2.2±0.2	2.2±0.2
B1	2.3±0.3	1.7±0.2	1.5±0.1	1.6±0.1	1.3±0.2	1.2±0.1
B2	0.9±0.2	0.7±0.2	1.1±0.1	2.1±0.2	2.1±0.2	2.1±0.2
C	0.8±0.3	0.7±0.2	0.9±0.2	1.2±0.2	1.1±0.3	1.2±0.2
D	0.5±0.2	0.7±0.2	0.8±0.1	1.0±0.1	1.1±0.2	2.1±0.2
E	2.4±0.4	2.2±0.3	1.8±0.2	2.1±0.2	2.2±0.3	2.1±0.2
F	13.1±1.0	11.2±0.8	11.4±0.5	10.0±0.5	9.4±0.7	9.1±0.5
F1	4.4±0.6	4.0±0.5	4.4±0.3	3.4±0.3	3.0±0.4	3.4±0.3
F2	4.1±0.6	3.1±0.4	3.6±0.3	3.7±0.3	3.3±0.4	2.6±0.3
F3	5.2±0.6	4.2±0.5	3.8±0.3	3.5±0.3	3.4±0.4	3.4±0.3
DS1	1.5±0.3	1.5±0.3	1.4±0.1	1.4±0.1	1.4±0.2	1.4±0.2
DS2	2.8±0.4	2.3±0.3	2.4±0.2	2.1±0.2	2.4±0.2	2.5±0.2

Table 4.3: Fluxes of the Fe-K$_\alpha$ line in units of 10^{-5}photons cm^{-2} s^{-1}. The values are the weighted mean of the MOS1&2 measured fluxes. The different columns refer to different datasets (see text). The Apr07, Mar08 and Apr 09 fluxes for the regions D, DS1 and DS2 are based on MOS 2 data only, as a consequence of the damaged sustained by CCD6 in MOS 1 on 9 March 2005 (Abbey et al., 2006).

rescence in the clouds) and a second power-law component modelling a defined contribution from teh cosmic X-ray background. For a more detailed description of these spectral components see Capelli et al. (2011b). Note that in this analysis we fixed the temperature of the hot plasma in every spectrum to 6.5 keV (Koyama et al., 2007a) since this is critical in obtaining a consistent measurement of the Fe-K$_\alpha$ line flux across all the spectra (different instruments/epoques).

Throughout our spectral analysis we have considered only observations with an exposure longer than 30 ks. If different datasets were part of a set of observations carried out over a couple of days, the associated spectra were added together with the ftool MATHPHA, with the same done for the response files using the ftools ADDARF and ADDRMF. Errors have been considered at the 90% confidence level. The resulting temporal sampling was as follows: the OBSIDs 0111350101 (Feb02), 0202670501 + 0202670601 (Mar04), 0202670701 + 0202670801 (Sep04), 0402430301 + 402430401 + 402430701 (Apr07), 0505670101 (Mar08), 054750401 + 0554750501 + 0554750601 (Apr09). A typical result from this spectral modelling process is illustrated in Fig.4.3.

Results

Our goal is to study the temporal behaviour of the Fe fluorescence in the filaments with a view to constraining the nature and location of the energising source. For example, a clear spatial pattern to the variations might, in principle, help us identify a preferred direction for the incoming photons/particles. The 6.4-keV line fluxes derived from our spectral analysis for the selected regions in the different observing periods are presented in Table 4.3. Here the measurements are calculated as the weighted mean of the MOS1&2 values with the errors representing the 90% confidence range. Fig.4.4 shows the resulting Fe-K$_\alpha$ flux lightcurves for the different regions covering the period 2002-2009. In each of the selected regions the surface brightness of the 6.4-keV line lies in the range 5-10$\times10^{-6}$ photons cm^{-2} s^{-1} arcmin^{-2}, comparable with that measured in Sgr C molecular cloud (Murakami et al. (2001)). From the lightcurves it is clear that some regions show evidence of substantial variability, while some others appear to remain roughly constant. To quantify this, we fitted the 6.4-keV line fluxes as a linear function of time t:

$$\mathrm{f_{6.4-keV} = A + B \cdot t},$$

where B>0 indicates an increasing Fe-K$_\alpha$ flux ($\mathrm{f_{6.4-keV}}$). Table 4.4 reports the results for the selected regions and in Fig.4.4 we show the best fit linear functions overplotted on the lightcurves. From this it is clear that the temporal behavior of the Fe-K$_\alpha$ flux differs markedly from filament to filament. In brief, the different regions exhibit the following behavior:

Region A: the Fe-K$_\alpha$ flux measured in this molecular complex does not show any variability on a timescale of 8 years; the value of the χ^2_{red} for the linear fit (χ^2_{red}=0.55) makes us confident of this result. The weighted mean flux across the full set of observations is 2.16±0.07$\times10^{-5}$ photons cm^{-2} s^{-1}, which translates to a surface brightness of 9.9±0.03$\times10^{-6}$ photons cm^{-2} s^{-1} arcmin^{-2}.

Region B1: we have measured a decrease of the 6.4-keV flux from the sub-region B1 at a confidence of 2.6σ; the confidence with the linear decrease is acceptable, given by a χ^2_{red} value of the best fit function of 1.46 (see Table 4.4). The rate of decrease of the Fe-K$_\alpha$ line flux in this cloud is 8.1±3.1$\times10^{-7}$ photons cm^{-2} s^{-1} year^{-1}.

Region B2: we have measured a strong increase of the Fe K$_\alpha$ flux from the region B2 with a 7.2σ confidence, although the high value of the χ^2_{red} (2.85) for the fit suggests that this rise may not be truly linear. The measured rate of increase of the Fe-K$_\alpha$ line flux is 2.4±0.3$\times10^{-6}$ photons cm^{-2} s^{-1} year^{-1}.

Region C: the Fe-K$_\alpha$ flux from region C has been measured to have an increase at 2σ confidence with the overall χ^2_{red} for the best fit linear function being 0.23. The rate of increase of the Fe-K$_\alpha$ line flux is 7±4$\times10^{-7}$ photons cm^{-2} s^{-1} year^{-1}. Looking at the lightcurve in greater detail, we notice that there is a step-wise change at the approximately mid-way point, the weighted means being respectively 0.8±0.1 and 1.2±0.1$\times10^{-5}$ photons cm^{-2} s^{-1}. Region C encompasses the position of a known X-ray transient, XMMU J174554.4-285456, (Porquet et al., 2005b), located at the north-west edge of the circle region. This spatial coincidence and the possibility that the transient is the illumunation source for the Region C cloud will be discussed later (§4.2.1).

Region D: we have measured a rapid increase of the 6.4-keV flux from region D with a confidence of 5.6 σ. The rate of growth of the Fe-K$_\alpha$ line flux in this region is 1.6±0.3$\times10^{-6}$ photons cm^{-2} s^{-1} year^{-1}. In the lightcurve of region D three of the six points are not fitted

Region	B (10^{-6})	σ_B (10^{-6})	$\#_\sigma$ (B/σ_B)	χ^2_{red}
A	-0.03	0.35	0.09	0.55
B1	-0.81	0.31	2.61	1.46
B2	2.37	0.33	7.24	2.85
C	0.77	0.40	1.95	0.23
D	1.67	0.30	5.62	3.24
E	0.22	0.45	0.49	0.91
F	-5.14	1.16	4.45	0.12
F1	-2.05	0.69	2.95	0.61
F2	-1.47	0.71	2.07	1.29
F3	-1.70	0.67	2.54	0.56
DS1	-0.11	0.35	0.33	0.10
DS2	-0.19	0.42	0.46	0.80

Table 4.4: Results for the study of the Fe-K$_\alpha$ variability in the selected regions and sub-regions (first column). The second and third columns give the value of the gradient obtained for the best-fit linear function together with its uncertainty (in units of 10^{-6} photons cm^{-2} s^{-1} year^{-1}). The fourth and the fifth columns report, respectively, the number of sigma for the deviation from the constant behavior of the best-fit function and the reduced χ^2 for the linear fit.

by the best fit function (see Fig.4.4, fourth panel); this translates into a high χ^2_{red} value (3.24, Table 4.4) suggesting the behavior is not well represented by a simple linear increase.

Region E: the Fe-K$_\alpha$ flux measured in this molecular complex is constant over a period of 8 years; we are very confident of this result because of the value of the low χ^2_{red} of the best fit for the lightcurve of this region (χ^2_{red}=0.91). The weighted mean flux over the set of observations is $2.1\pm0.1\times10^{-5}$ photons cm^{-2} s^{-1}, which translates to a surface brightness of $7.24\pm0.03\times10^{-6}$ photons cm^{-2} s^{-1} arcmin^{-2}.

Region F: this is the region for which the measurements are most precise. The Fe-K$_\alpha$ flux shows a clear decrease with a 4.5 σ confidence; the χ^2_{red} value of the best fit function is 0.12, strongly confirming the measured decrease and constraining the functional shape of this decrease to be linear. The rate of decrease of the Fe-K$_\alpha$ line flux is $5.1\pm1.2\times10^{-6}$ photons cm^{-2} s^{-1} year^{-1}. To improve the spatial resolution, we have divided this region into three sub-regions and studied these separately.

Sub-regions F1-F2-F3: we have measured a decrease of the 6.4-keV line flux from all three sub-regions with a confidence of 3.0, 2.1 and 2.5 σ respectively. The corresponding rates of decrease are 2.1 ± 0.7, 1.5 ± 0.7 and $1.7\pm0.7\times10^{-6}$ photons cm^{-2} s^{-1} year^{-1}. The χ^2_{red} values of the best fit linear functions are, respectively, 0.61, 1.29 and 0.56; confirming the decrease is a linear function of time. Moreover we point out that the rates of decrease from the three sub-regions are compatible with each other. The agreement between the temporal behavior of both the whole complex and the individual subregions suggests a

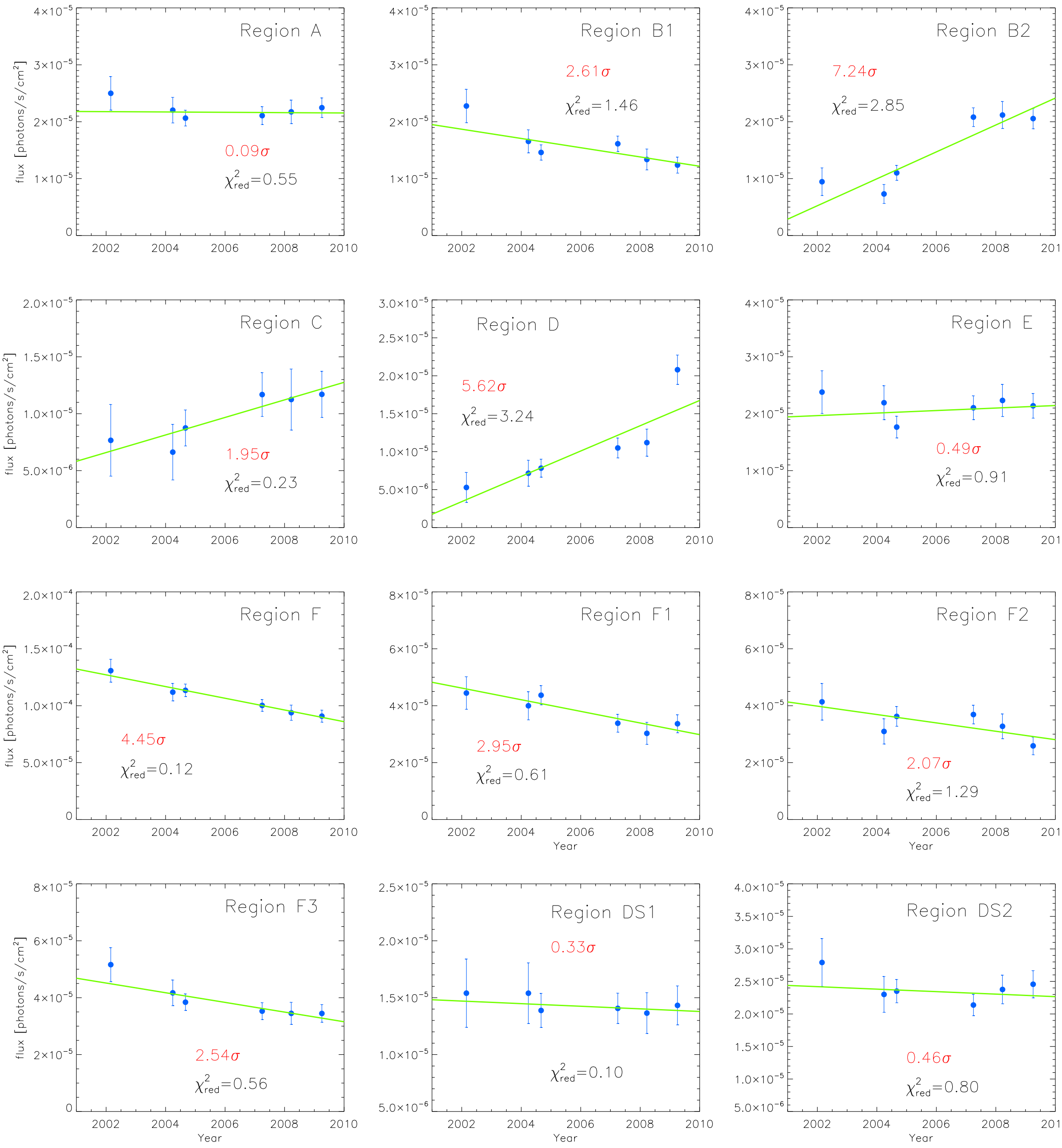

Figure 4.4: Lightcurves of the Fe-K$_\alpha$ flux from the filaments in the GC. The flux is plotted in units of 10^{-5}photons cm^{-2} s^{-1}. The green line represents the best fit linear function to the data, whose parameters are reported in Table 4.4. In each panel we present the significance of the measured gradient (B/σ_B) together with the χ^2_{red} for the best fit linear function.

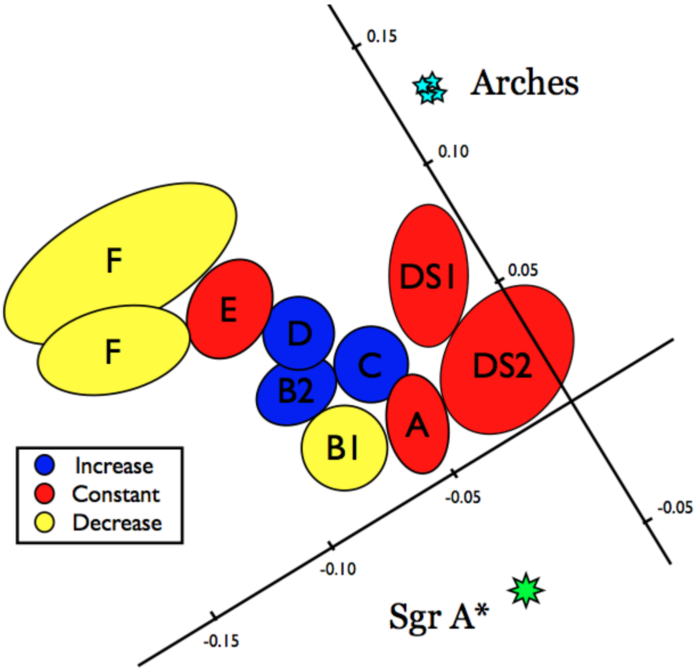

Figure 4.5: Colour-coded sketch of the molecular clouds and Fe-K$_\alpha$ line flux variability studied in this work. The circles and ellipses represent the regions selected for the timing and spectral studies (see also the right panel of Fig.4.2). The colors are blue (increase of the 6.4-keV line flux), red (constant) and yellow (decrease). A Galactic coordinate grid, and the positions of Sgr A* (green star) and the Arches cluster (cyan stars) are also indicated.

common origin for the Fe-K$_\alpha$ emission within a single large molecular structure, *i.e.* the G0.11-0.11 molecular cloud (Yusef-Zadeh et al. 2002). Tsuboi et al. (1997) have show that this molecular complex has a shell-like structure that may be interacting with the western vertical filaments of the Radio Arc. Thus, G0.11-0.11 could host an extended high energy particles accelerator/decelerator.

Regions DS1 and DS2: both the low surface brightness regions DS1 and DS2 show a constant 6.4-keV line signal over a period of 8 years. The weighted mean flux within this set of observations is 1.42±0.07 and 2.33±0.09×10^{-5} photons cm^{-2} s^{-1} respectively, which translates into a surface brightness of 3.8±0.2 and 3.6±0.1×10^{-6} photons cm^{-2} s^{-1} arcmin^{-2}. The χ^2_{red} values make us confident of the constant nature of the light curves.

To summarize, we have independently established a pattern of Fe-K$_\alpha$ variability similar to what already found by Ponti et al. (2010) for the clouds A, B2, D, E and F. For cloud B1, our analysis implies a decrease of the line flux at a confidence level of 2.6σ whereas Ponti et al. (2010) report a constant line flux for this cloud (designated MC2 in their study), which have implications on the location of the cloud relative to the leading and trailing edges of ionizing wavefront. We have also studied three lower-surface brightness regions (C, DS1 and DS2), the first of which shows an interesting step-wise increase in its fluorescent line flux, with the latter two having constant light curves.

In order to investigate the spatial dependency of the observed Fe-K_α variability, and show the complexity of its pattern across the inner CMZ, we sketched the distribution of the MCs studied in this paper, with a colour-coding which identifies the type of variability measured in the 6.4-keV line flux (see Fig.4.5). The most noticeable variation in the Fe-K_α flux comes from the zone bounded by $0.05° < l < 0.1°$ and $-0.1° < b < -0.05°$ (l and b are, respectively, galactic longitude and latitude), which encompasses the regions B2 and D. Indeed, these molecular filaments show the clearest evidence for Fe-K_α variability across the selected regions. Besides these complexes, region C also shows a noticeable increase in the Fe-K_α surface brightness, whereas the G0.11-0.11 cloud shows fading 6.4-keV line emission. Ponti et al. (2010) have suggested that this complex pattern of variability can be largely explained in terms of a single flare from Sgr A* illuminating molecular clouds at differing positions along the line of sight. However, as we show below, detailed consideration of the spectral properties of the various MCs lead us to conclude that this is not the complete story.

4.3.3 Spectroscopy: looking for the reflection imprints

Method

In order to study the spectral features typical of an XRN, we have considered the PN camera spectra of the regions highlighted in Fig.4.5 (see also Table 4.2). For this analysis we selected only PN spectra because of the much higher effective area in the hard X-ray band ($\gtrsim$6 keV). Building the PN spectra for the Fe-K_α bright filaments, we used the same GTI filtered event files as employed to build the fluence map in Section 4.2. We stacked all the spectra (of both the source and the background) and the response files using the ftools MATHPHA, ADDARF and ADDRMF, without caring about the 6.4-keV line variability. The background region was centred on R.A.=17:45:42.289, DEC.=-29:07:53.39 (circle 1 arcmin in radius), at the same Galactic latitude as the filaments in order to avoid any systematics due to the different intensity of the Galactic Ridge emission at different Galactic latitudes. The spectral model used in the fitting comprises two thermal plasmas (APEC; Smith et al. 2001) with a metallicity fixed at 2 times solar, two gaussian emission lines (GAUSS) which account for the Fe-K_α and K_β lines, and a non-thermal continuum (POWER LAW). All of these components are subject to photoelectric absorption in the line-of-sight column density (WABS; Morrison & McCammon 1983, common to all the spectral components). The ratio between the Fe K_β and Fe-K_α line fluxes has been fixed at 0.11 (Koyama et al., 2009). Moreover, to quantify the presence of a putative Fe-K edge, we multiplied the hard power-law continuum by an EDGE component at a fixed energy of 7.1 keV. We note that, although we have applied the background subtraction technique in this study, all the spectra still exhibit a residual contribution from the *hot* APEC component (kT$\sim$6.5 keV). We have therefore retained this spectral component in the fitted model, a different approach to the one we adopted in our study of the MCs in the

Arches cluster region (Capelli et al., 2011b). Although the temperature of this hot plasma is approximately the same all over the inner CMZ, its intensity can significantly change; the best evidence of the substructures of this spectral component is the relative contribution of the Fe XXV K$_\alpha$ line at 6.7 keV in the spectra shown in Fig.4.6; the MCs A, B1, DS1 and DS2 show the significant presence of the 6.7 keV line, while in the spectra of the other regions the contribution from this fluorescent line is lower. To avoid high residuals in the spectral domain of the Fe fluorescent lines (6-7 keV), we therefore accounted for this spectral component in the fitting model of all the MCs. In the spectral fitting procedure we used again the Cash statistic because of the low signal-to-noise ratio in the spectral channels.

The specific goal of this analysis is to quantify the depth (τ) of the K edge at 7.1 keV and also to establish the equivalent width (EW) of the 6.4-keV line with respect to the underlying ionising continuum (POWER LAW). Our investigation of the spectral characteristics of the various regions and sub-regions is more detailed than that recently reported by Ponti et al. (2010).

Results

Sunyaev & Churazov (1998) have shown that in the XRN model, the 6.4-keV line emission has to be accompanied by strong absorption above 7.1 keV, the minimum energy that a photon must have in order to be able to produce a K-shell vacancy in neutral Fe via the photoelectric effect. Moreover, because the primary source of ionisation is not seen by the observer, the EW of the line is expected to be very high, i.e. of the order of 1 keV. On the other hand, the depth of the Fe absorption edge at 7.1 keV is strongly related to the intrinsic N$_H$ of the MC, with cloud column densities in excess of 10^{23}cm^{-2} imprinting edge features with optical depth of about 0.1-0.2 at 7.1 keV on the emergent reflected (*i.e.,* electron-scattered) continuum. In Fig.4.6 and Table 4.5, we present the results of our search for the imprints of reflection on the time averaged spectra of the selected GC molecular filaments. We measured a very high value of the EW of the 6.4-keV line in all the MCs we studied; the largest values have been measured in the MCs B2 and F, where we also see a variable the Fe-K$_\alpha$ line flux (respectively a decreasing and increasing flux).

We first note that the N$_H$ values for the clouds reported Ponti et al. (2010), as inferred from radio CS measurements, are always lower than 10^{23}cm^{-2}. Specifically, we measured the strongest absorption edge in the spectrum of region A (called MC1 in Ponti et al., 2010), where the Fe optical depth has been measured to be 0.6±0.1. This is rather peculiar since this cloud has one among the lowest values of N$_H$ (4×10^{22}cm^{-2} as inferred from the CS measurements) among the MCs considered. On the other hand, MCs with higher reported column densities show no Fe-K edge at 7.1 keV. For example, the regions B2 and D (subregions of the larger complex referred to by Ponti et al. (2010) as the *bridge*) have (9×10^{22}cm^{-2}, see Table 2 in Ponti et al., 2010), but we could only measure an upper limit to the Fe absorption edge.

In Section 4.3.5 we present a prescription to calculate the N$_H$ of the MCs from the measurement of the optical depth of the absorption at the Fe-K edge. This method will

Table 4.5: Results from the analysis of the PN time averaged spectra of the Fe-K_α bright filaments. The spectral parameters reported in the table are the column density (in units of 10^{22} cm^{-2}), the temperatures of the warm and the hot plasma components (in keV), the normalizations of the warm and hot plasmas (in units of 10^{-17} and $10^{-18} \int n_e n_H dV/4\pi D^2$, respectively), the slope of the powerlaw with its normalization (in units of 10^{-5} photons keV^{-1} cm^{-2} s^{-1} at 1 keV), the peak energy and the σ of the Fe-K_α line (in keV), the 6.4-keV line flux (in units of 10^{-5} photons cm^{-2} s^{-1}), the EW of the 6.4-keV line (in keV), the optical depth at the Fe-K edge and the C-stat value for the best fit model.

	A	B1	B2	C	D
N_H	$6.7^{+5.3}_{-0.4}$	$7.7^{+0.6}_{-0.4}$	7.6 ± 0.4	7.9 ± 0.5	6.4 ± 0.4
kT $_{warm}$	0.7 ± 0.1	0.9 ± 0.1	0.9 ± 0.1	0.8 ± 0.1	1.0 ± 0.1
norm	$3.7^{+6.1}_{-0.9}$	$4.4^{+1.9}_{-0.7}$	$3.2^{+0.9}_{-0.6}$	$4.5^{+1.2}_{-1.0}$	$2.1^{0.4}_{-0.5}$
kT $_{hot}$	6.7 ± 1.2	$6.4^{+1.5}_{-1.6}$	$5.1^{+1.8}_{-1.9}$	$6.6^{+2.0}_{-2.2}$	6.5 fix
norm	$2.2^{+0.4}_{-0.5}$	$2.0^{+0.2}_{-0.4}$	$1.1^{+0.4}_{-0.3}$	1.4 ± 0.3	0.6 ± 0.3
Γ	$0.62^{+0.24}_{-0.05}$	$1.21^{+0.12}_{-0.09}$	1.1 ± 0.1	$1.3^{+0.2}_{-0.1}$	$1.0^{+0.2}_{-0.3}$
norm	$6.8^{+3.8}_{-1.1}$	$14.2^{+5.5}_{-2.1}$	$7.4^{+2.7}_{-1.4}$	$12.0^{+5.9}_{-2.3}$	$4.0^{+2.0}_{-1.7}$
E $_{6.4}$	$6.420^{+0.007}_{-0.004}$	$6.416^{+0.007}_{-0.006}$	$6.415^{+0.003}_{-0.004}$	$6.421^{+0.006}_{-0.013}$	$6.417^{+0.011}_{-0.007}$
σ	0.03 ± 0.01	0.05 ± 0.01	$0.039^{+0.005}_{-0.008}$	$0.042^{+0.015}_{-0.011}$	$0.043^{+0.012}_{-0.020}$
F $_{6.4}$	$1.86^{+0.8}_{-0.7}$	$1.42^{+0.07}_{-0.06}$	1.61 ± 0.06	$0.98^{+0.06}_{-0.05}$	0.87 ± 0.05
EW	$0.86^{+0.21}_{-0.32}$	$0.94^{+0.23}_{-0.29}$	$1.64^{+0.46}_{-0.40}$	$0.98^{+0.31}_{-0.36}$	$1.36^{+1.11}_{-0.51}$
τ	0.6 ± 0.1	0.2 ± 0.1	≤ 0.07	$0.23^{+0.15}_{-0.19}$	≤ 0.4
C-stat	1842.62	1742.87	1568.51	1731.63	1691.50

	E	F	DS1	DS2
N_H	$6.5^{+0.4}_{-0.3}$	7.8 ± 0.2	$8.1^{+0.9}_{-1.0}$	$9.2^{+1.6}_{-1.1}$
kT $_{warm}$	1.0 ± 0.1	$1.08^{+0.02}_{-0.03}$	0.6 ± 0.1	0.4 ± 0.1
norm	$4.1^{+0.8}_{-0.7}$	$22.5^{+1.9}_{-1.8}$	$8.6^{+5.7}_{-4.4}$	$42.2^{+3.4}_{-8.2}$
kT $_{hot}$	6.5 fix	–	$7.1^{+2.0}_{-1.0}$	$6.6^{+1.2}_{-0.9}$
norm	0.9 ± 0.5	–	$3.1^{+0.7}_{-0.6}$	$5.4^{+1.0}_{-0.6}$
Γ	1.0 ± 0.2	1.1 ± 0.2	0.8 ± 0.3	$1.0^{+0.3}_{-0.2}$
norm	$9.0^{+3.9}_{-2.9}$	$39.7^{+18.0}_{-12.7}$	$6.4^{+3.6}_{-2.9}$	$18.6^{+13.7}_{-6.1}$
E $_{6.4}$	6.417 ± 0.008	6.411 ± 0.005	$6.414^{+0.010}_{-0.009}$	6.412 ± 0.007
σ	$0.030^{+0.018}_{-0.014}$	$0.029^{+0.009}_{-0.012}$	$0.041^{+0.014}_{-0.019}$	$0.053^{+0.009}_{-0.012}$
F $_{6.4}$	1.62 ± 0.08	7.5 ± 0.3	$1.17^{+0.08}_{-0.07}$	2.1 ± 0.1
EW	$1.23^{+0.66}_{-0.41}$	$1.54^{+0.80}_{-0.52}$	$0.84^{+0.81}_{-0.34}$	$0.77^{+0.43}_{-0.35}$
τ	$0.22^{+0.21}_{-0.20}$	$0.34^{+0.25}_{-0.24}$	0.4 ± 0.2	$0.53^{+0.14}_{-0.18}$
C-stat	1751.11	1843.80	1653.91	1761.42

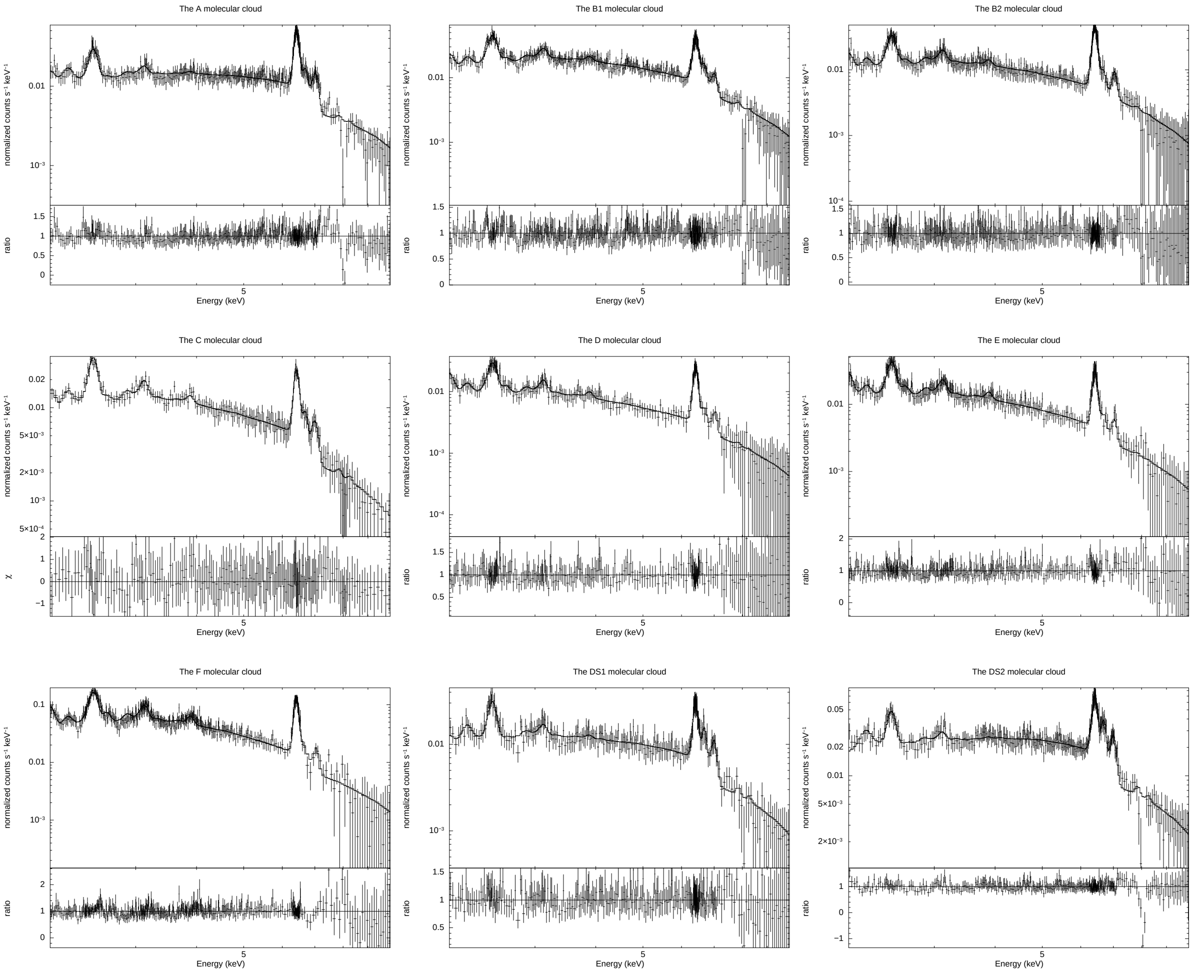
The A molecular cloud
The B1 molecular cloud
The B2 molecular cloud
The C molecular cloud
The D molecular cloud
The E molecular cloud
The F molecular cloud
The DS1 molecular cloud
The DS2 molecular cloud

Figure 4.6: Time-averaged PN spectra of the set of MCs in the present study. Each panel shows the measured data along with the best fitting spectral model and (in the lower section) the ratio of these two quantities . The residuals which can be seen in the spectra of the regions A, B1 and DS2 are due to the inhomogeneous pattern of the Cu fluorescent line at 8.05 keV in the XMM PN detector. This are systematics due to the background subtraction, which however do not influence the measurements of the other spectral parameters, namely the optical depth at the Fe-K absorption edge and the slope of the non-thermal power law.

generally give us higher column densities for the MCs than the ones assumed by Ponti et al. (2010).

A very important result is the identification of a hard non-thermal component associated with the 6.4-keV line, which in the XRN model represents the fraction of incident reflected (*i.e.* Thomson scattered) by the molecular material. In all the observed spectra we were able to discern underlying rather hard continuum modelled as a power-law with a photon index in the range Γ=0.6-1.3. The different determinations of Γ are not consistent with a single value within the 90% uncertainties but this may be result of the impact of varying effective N_H values for the clouds (see Section 4.3.5).

The value Γ=1.3 determined for cloud C is the highest amongst the set of measurements. Interestingly in March 2004 region C also contained the X-ray transient XMMU J174554.4-285456, whose best fit model during the outburst activity was found to be an absorbed power law (N_H=1.41×10^{23}cm^{-2} and Γ=1.86, Porquet et al., 2005b). It is certainly plausible that reflection by Cloud C of the light from the transient accounts for the upward biasing of the slope of the hard continuum in the time-averaged measurement.

We have also investigated the characteristics of the Fe-K_α line, in terms of its energy and width. For this purpose we built a time-averaged spectrum for the whole region, stacking all the spectra across all the observations. In this stacked spectrum, the intrinsic width of the line is 36±3 eV, while its peak is at 6414±2 eV, slightly higher than the nominal value of 6403 eV for neutral iron[1]. The results from the individual spectra (see Table 4.5) show the same trend, with the measured Fe-K_α line energy in all cases exceeding the theoretical value. Although the EPIC calibration is known to be better than 10 eV, the presence of soft protons in the FOV might slightly change the energy and the width of the lines (Ponti et al., 2010). To check whether these are instrumental effects or real features, we measured the same quantities for the Cu instrumental line at 8.04 keV. The centroid of the Cu K_α line is at 8047^{+4}_{-2} eV, while its width is 34^{+6}_{-4} eV. The line peak is in good agreement with its nominal value of 8048 eV. Although a relative shifting between the two lines is present (the Cu K_α peak perfectly matches the theoretical expectation, whereas the Fe-K_α is noticeably higher), taking into account the systematics and the statistical uncertainties, we conclude that no statistically significant line blueshift and broadening have been measured and that our results are consistent with emission from neutral, or close-to-neutral, Fe atoms embedded in the material of the cold molecular clouds. We also note that Suzaku measured the Fe-K_α line energy in the molecular filaments to be 6409±1 eV with a line width of 33^{+2}_{-4} eV, the latter being marginally higher than the expected systematics (≈30 eV) (Koyama et al., 2007a).

4.3.4 The Fe abundance within the MCs

In this Section we make use of the measurements of the EW of the Fe-K_α line from the spectral analysis of the stacked PN spectra (written in 4.5) to infer the mean Fe abundance across the MCs under study. To proceed towards this, we first derive an expression for Fe-line equivalent width. As discussed in Sunyaev & Churazov (1998), the Fe-K_α line flux (F_{64}) induced by ionisation of a MC by a powerful X-ray source can be written as

$$F_{64} = \frac{\Omega}{4\pi D^2}\, Z_{\rm Fe}\, \tau_{\rm T}\, I_{\rm 8keV} \text{ photons cm}^{-2}\text{s}^{-1}, \tag{4.1}$$

where Ω is the solid angle (in units 4π) subtended by the diffuse cloud from the perspective of the radiation source, D the distance to the GC, Z_{Fe} the Fe abundance within

---

[1] The nominal values for the energy peak of the Fe-K_α and Cu K_α lines have been taken from *http://physics.nist.gov*

the MC, and τ_T is the optical depth for Thomson scattering (based on the angular averaged Thomson cross section). Here $\mathrm{I_{8keV}}$ is the photon output of the source at 8 keV in units of photon $\mathrm{s^{-1}}$ keV-1.

If we assume we are dealing with a small element of the cloud, then the scattered signal at 6.4 keV at an angle θ is

$$\mathrm{S_{64}} = \frac{\Omega}{4\pi \mathrm{D}^2}\ \tau_\mathrm{T}(\theta)\ \mathrm{I_{8keV}}(6.4/8)^{-\Gamma_\mathrm{in}}\ \text{photons cm}^{-2}\text{s}^{-1}\text{keV}^{-1}, \tag{4.2}$$

where Γ_{in} is the photon index of incident continuum. Therefore we can write the EW of the Fe-K$_\alpha$ line with respect to the reflected continuum as:

$$\mathrm{EW_{Fe-K_\alpha}} = \frac{\mathrm{Z_{Fe}}\ \tau_\mathrm{T}}{\tau_\mathrm{T}(\theta)}\left(\frac{6.4}{8.0}\right)^{\Gamma_\mathrm{in}} \sim \frac{644\ \mathrm{Z_{Fe}}}{[0.75\times(1+\cos^2(\theta))]}\ \text{eV} \tag{4.3}$$

The same factor applies to all the cloud elements provided the cloud is not optically thick, and hence to the cloud as a whole. The equivalent width is thus independent of L_X, but it does depend on the spectral slope of the incident (and hence reflected) continuum *i.e.,* harder spectra produce relatively more 6.4 keV photons.

Using this last formula we have attempted to calculate the average Fe abundance, making the reasonable assumption that Z_{Fe} is constant across the nine clouds. The weighted mean of the EW of the Fe-K$_\alpha$ inferred from the spectral analysis of the nine clouds is 1.01±0.12 keV, where we used the inverse of the squared error to assign a weight to the different measurements. Moreover, we assume the clouds to be uniformly distributed in the region $25^\circ \lesssim \theta \lesssim 155^\circ$, i.e. we assume the distance along the line of sight of the clouds to be lower than twice the projected distance. From this assumption we can calculate the mean value for the geometrical function in formula 4.3 to be

$$\overline{1+\cos^2(\theta)} = 1.33.$$

Substituting the weighted mean for the EW and the geometrical factor value into equation 4.3, we obtain the mean value for the Fe abundance to be Z_{Fe}=1.56±0.19 $\mathrm{Z}_\odot$. This important result confirms a higher than solar metallicity for MCs and (presumably) the interstellar medium generally found in the GC region.

Another interesting application of equation 4.3 is the study of the geometry of the illumination process. These calculations might indeed turn to be a powerful tool for inferring the distribution of the MCs Fe-K$_\alpha$ bright MCs in the CMZ. In Fig.4.7 we show both the EW dependence on the geometry (for different Fe abundances) and the Z_{Fe} dependence on the scattering angle for different values of the EW of the 6.4-keV line. Both panels in Fig.4.7 can help us in estimating the line of sight distance of the clouds relative to the plane including Sgr A*. The Z_{Fe}=1.56 $\mathrm{Z}_\odot$ curve in the left panel of Fig.4.7 (plotted in red) is intersected by the blue lines corresponding to the clouds with lower values of the EW in correspondence of θ values of 0.6-0.9 and 2.2-2.5; this might give the line of sight of the C, B1, A, DS1 and DS2 clouds to be about the same of the projected one (scattering angles around 45 and/or 135 degrees). The highest EW values also intersect the Z_{Fe}=1.56

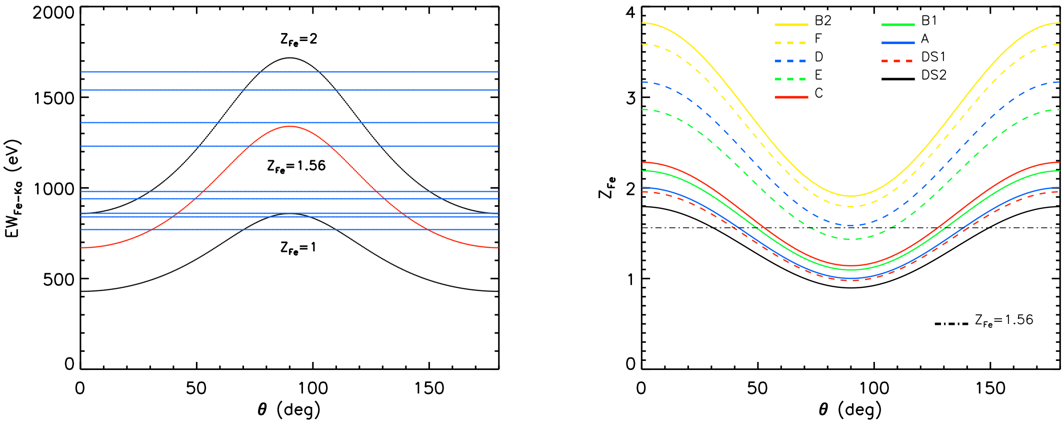

Figure 4.7: *Left panel*: The predicted EW (from equation 3) plotted against the scattering angle (θ) measured between the direction of incident radiation on the cloud and the line of sight, for different values of the Fe abundance (the red curve is for Z=1.56, see text). The blue horizontal lines show the EW measurements for the nine MCs in our data set - ordered from top to the bottom as follows: B2, F, D, E, C, B1, A, DS1 and DS2 MCs. For clarity, here we plot only the value of the EW, without the error bars. *Right panel*: The Fe abundance inferred for the different MCs using equation (3) as a function of the scattering angle. The different curves show the Z_{Fe}-θ dependance for each value of the EW measured in the MCs. The dashed-dotted black line represents the averaged metallicity value (Z_{Fe}=1.56) found across our set of MCs.

red curve if the error bars on these quantities are taken into account, giving these clouds a scattering angle close to 90 deg, therefore resulting in a limited line of sight distribution. The same applies for the plot in the right panel of Fig.4.7; considering the error bars (90% confidence levels), the MCs with the highest EW of the 6.4-keV line meet the Z_{Fe}=1.56 line at angles close to 90 degrees (short line of sight distance).

In all of these calculations, we assumed that the MCs are illuminated by the same powerful X-ray source, in a pure XRN scenario. However, we note that these clouds, especially the ones located (in projection) in the vicinity of the Radio Arc (i.e. those in the bridge subregions and in G0.11-0.11), could be subject to intense cosmic-ray particle bombardment, a process which would result in a boosting of the EW of the Fe-K_α line. Any adjustment of the 6.4-keV line flux arising from photoionisation would of course impact on estimates of line of sight distance derived from the above methodology. We will discuss this issue further in the Section 4.3.7.

4.3.5 The optical depth of the MCs

For optically thin clouds, the Fe K_α brightness is proportional to the column density of Fe atoms through the cloud. In practice, we measure the optical depth at the iron K-edge

τ_{Fe}; theoretically, this parameter can be written as

$$\tau_{\mathrm{Fe}} = \mathrm{N}_{\mathrm{Fe}}\ \sigma_{\mathrm{Fe}} = 3 \times 10^{-5}\ \mathrm{Z}_{\mathrm{Fe}}\ \mathrm{N}_{\mathrm{H}}\ \sigma_{\mathrm{Fe}}, \tag{4.4}$$

where N_{Fe} is the column density of Fe atoms inside the MC and σ_{Fe} is the cross section for photoabsorption of Fe at the K-edge (σ_{Fe}=4.03×10^{-20} per Fe atom). The N_{Fe} value can be further written in terms of the H column density (N_H) using the standard solar Fe:H ratio and assuming that the Fe abundance relative to solar within the cloud is Z_{Fe}.

In the XRN scenario, both τ_{Fe} and the distance of the cloud from the illuminating source are the crucial parameters when estimating the X-ray luminosity required to produce a given Fe-K$_\alpha$ flux. Previous studies have often relied upon estimates of N_H combined with assumptions of Z_{Fe} in such calculations, where the former is inferred from intensity maps of CO, CS or other molecular tracers of high density material in the inner Galaxy. However, the estimation of the cloud N_H is often a very difficult measurement. For example, the G0.11-0.11 cloud (our region F) has been the subject of numerous studies in the last decade. Adopting two different ways of measuring the N_H of this MC, respectively using the intensity of the CS and the H^{13}CO$^+$ emission lines, Amo-Baladrón et al. (2009) and Handa et al. (2006) measured two extreme values for the N_H of this MC: 2×10^{22} and 10^{24} cm^{-2}, respectively.

Here, we suggest that a much more direct approach is to use the measured optical depth of the absorption at the Fe-K edge directly. In the spectral analysis of the stacked spectra in Section 4.3.3, we were able to determine the Fe-K edge optical depth (the EDGE component in XSPEC) with reasonable precision, as is evident from the results reported in the second last row of Table 4.5. Taking the G0.11-0.11 cloud as an example, if we assume the average Fe abundance determined earlier (Z_{Fe}=1.56), we estimate the N_H to be 1.8×10^{23} cm^{-2}, a value between the two extreme numbers cited in the literature.

Technically the X-ray spectrum does not give a direct measure of the column density of neutral Fe atoms through the cloud, but instead records the Fe-K edge imprinted on the reflected continuum by absorption. However, our simulations (see later) show that for optically thin clouds and simple cloud geometries, these two quantities are of very similar magnitude. In the limit when the cloud becomes optically thick, the depth of the edge will reach a maximum value (i.e. the value predicted by reflection models such as *pexrav*).

In order to test whether the value of N_H that we measured are a good set, we run some simulations in order to describe the relation between the spectral shape of the scattered high energy continuum (power law in the stacked spectra) and the column density of the cloud. In a Thomson scattering process, the incident spectrum and the reflected one have the same slope; but two caveats are to be considered. Theoretically high energy photons escape from the absorption zone (the cloud) more easily than low energy ones. Moreover, a 30 keV photon will suffer less scattering than a 10 keV photon in crossing a certain amount of cold matter (e.g. George & Fabian, 1991). For these reasons, the spectrum reflected by a MC has a different shape from the incident one; it will be harder than the incident spectrum and this hardness is a function of N_H (or τ_{Fe}) within the MC.

We have made an estimation of the effective power law slope of the reflected continuum

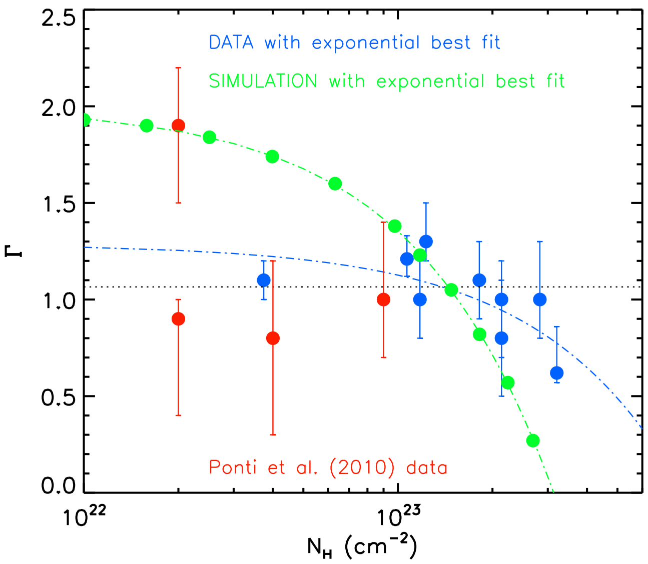

Figure 4.8: The spectral slope of the reflected spectrum as a function of the measured column density (derived from the Fe-K edge and the average value for Z_{Fe}). The green points show the results of our simulations (see text), with the best fit exponential function overplotted in green. The blue points relate to the nine clouds studied in this work, where the blue line represents the best fit exponential function to the data. The red points are based on the data from Ponti et al. (2010). The dotted black line shows the best fit constant function to the blue data (see text).

emergent from the cloud assuming an incident Γ=2.0, Z_{Fe}=1.5 and θ=90 deg. The results of this simulation are plotted as green points in Fig.4.8; as earlier explained, the spectrum of the reflected continuum flattens towards higher column densities, because of the absorption occurring in the cloud both up to the scattering point and as the scattered photons emerge from the MC. In order to model the flattening of the reflected continuum, we fitted the green points with an exponential function of the form Γ=A$\cdot$ exp($-B \cdot N_H$)+C; we are aware of the fact that the exponential fit does not have any physical basis, *apart from the functional dependance of the absorption (i.e.* exp($-\tau$)*)*, we however chose it because it better fits the data points, whereas a linear decrease or a power law does not fit the data as well. The best fit function is described by A=41.4 and B=1.8×10^{-25} cm^2 and C=-39.0, and it is shown as a green dashed-dotted line in Fig.4.8.

The blue points in Fig.4.8 show the Γ-N_H combinations measured in the MCs studied in this work. For comparison, we also plotted in red the points which refer to the same clouds as studied in Ponti et al. (2010), where different values of the N_H were assumed and the relative slopes Γ of the reflected spectrum measured (Table 4 in this reference). As a general comment, we can see that in our measurements show a general decrease

Table 4.6: Values for the Fe-K edge optical depth at 7.1 keV (as measured from the time averaged X-ray spectra, see Table 4.5), listed together with the N$_H$ values measured form the optical depth of the Fe K edge absorption (assuming Z=1.56, see text) and the ones assumed in (Ponti et al., 2010, N$_{H,old}$ in units of 10^{22} cm^{-2}).

MC	τ_{Fe}	N$_H$	N$_{H,old}$
A	0.6	32.1	4.0
B1	0.2	10.7	$\leq$2.0
B2	$\leq$0.07	3.7	9.0
C	0.23	12.3	-
D	$\leq$0.4	21.4	9.0
E	0.22	11.8	9.0
F	0.34	18.2	2.0
DS1	0.4	21.4	-
DS2	0.53	28.3	-

of the power law slope (an hardening of the reflected spectrum) towards higher N$_H$, as expected. To quantify the flattening of the reflected continuum as seen in our data, we fitted the measured Γ-N$_H$ points (blue data in Fig.4.8) with an exponential form as the one used before. The resulting best fit function is shown in Fig.4.8 as a blue dashed-dotted line, whose parameters have been measured to be A=90.3, B=1.6$\times10^{-25}$ cm^2 and C=-89.0 (χ^2_{red}=0.96). Moreover, when fitted with a constant function (i.e. Γ=constant, black dotted line in Fig.4.8), the reduced χ^2 for the blue data results 1.87, too large to consider the constant behaviour as a good model for our data. We can therefore safely conclude that also in our data we see a significant flattening of the reflected spectra towards higher absorptions.

On the other hand, the Γ-N$_H$ points measured in Ponti et al. (2010, red points in Fig.4.8) are randomly distributed in the plot area and no decreasing trend is evident. We also notice that the error bars of the blue points are much smaller than the red respective measurements; this is due to the use of the Cash statistics (instead of the standard χ^2 statistics), which better measures the spectral parameters and therefore allow us to place a better constrain on the spectral shape of the non thermal reflected continuum.

We remind the reader that the simulations were performed for a fixed geometry of the MCs, i.e. all the clouds projected into the plane of Sgr A* (θ=90 deg); this is very unlikely to be the case for the actual distribution of the clouds studied in this work, which are more likely distributed along the line of sight as previously discussed (see Sections 4.3.4 and 4.3.6). Because of this dislocation, and since the effective slope of the reflected continuum depends on the geometry of the illumination, the decreasing trend for the actual data could be slightly smeared with respect to simulated ones (i.e. the green points in Fig.4.8), resulting in a more spread distribution of the data points into the Γ-N$_H$ plot, like we effectively measured. As a confirmation of this, we notice that the three points that more significantly differ from the simulated exponential decay are the ones for the B2, DS2 and A clouds, which we will find to likely have a significant distribution behind the plane of Sgr A* (see Section 4.3.6). More generally, the spread measured in the Γ-N_H distribution with respect to a simulated decay will also depend on all the clouds parameters, i.e. N_H and Z_{Fe}.

To conclude, we are confident that the N_H values inferred from the measurement of the optical depth of the absorption at the Fe-K edge through equation 4.4 (see third column in Table 4.6) are more suitable for the calculations of all the other MCs properties we will develop in this paper.

4.3.6 An X-ray lightcurve for Sgr A* over the last 200 years

The line of sight distribution of the MCs

If the intrinsic N_H of a particular MC is known, it is possible to use its Fe-K_α flux to investigate its position relative to the photon illumination source. This issue has been recently discussed by Ponti et al. (2010), assuming that the MCs in their study are all illuminated by a past outburst on Sgr A* reaching an X-ray luminosity of $\sim 10^{39}$ erg s^{-1}. In the previous section (§4.3.5) we noted that the N_H values assumed by these authors are much lower than our own determinations implying significant revisions to the cloud-source geometry. Using equation 4.1, we can derive an expression which relates the separation of a MC from the illuminating source to the optical depth at the Fe-K edge as measured in its X-ray spectrum; this is

$$\tau_{\rm Fe} = \frac{16\pi\ {\rm D}^2\ {\rm F}_{6.4}}{10^7\ {\rm L_X}\ {\rm R}^2}\ {\rm d}^2, \tag{4.5}$$

where τ_{Fe} is the optical depth at 7.1 keV, D is the distance to the GC, $F_{6.4}$ is the Fe-Kα line flux (Table 4.5), d is the distance of the MC from the ionising X-ray source (whose X-ray luminosity is L_X), and R is the radius of the cloud. If we also assume $L_X \sim 10^{39}$ erg s^{-1} (e.g. Terrier et al., 2010), we can calculate the total distance of the clouds *d*, and from this, assuming the projected distances written in Table 4.2, the line of sight distribution $d_{\rm los}$. We underline that the line of sight measurement through equation 4.5 does not depend on the Fe abundance; indeed, the Z_{Fe} dependence in equation 4.5 is cancelled by its dependence on τ_T in equation 4.1, i.e. $\tau_T \sim 0.55\ \tau_{Fe}\ Z_{Fe}^{-1}$.

Employing the method and the assumptions described above, we derived the localization of the MCs studied in this paper as shown in Fig.4.9; this plot also shows the region influenced by the propagating Sgr A* outburst in the modelling reported by Ponti et al. (2010). Clearly the assumption of a single outburst with L_X=10^{39} erg s^{-1} results in a spread along the line of sight of the MCs which is not compatible with the spread in projected distances (see Table 4.2); hence we conclude that this scenario is oversimplistic.

To reduce the distance of a MC with respect to the position of Sgr A*, the only physical parameter we can tune (i.e. decrease) is the outburst L_X. Therefore, we conclude that

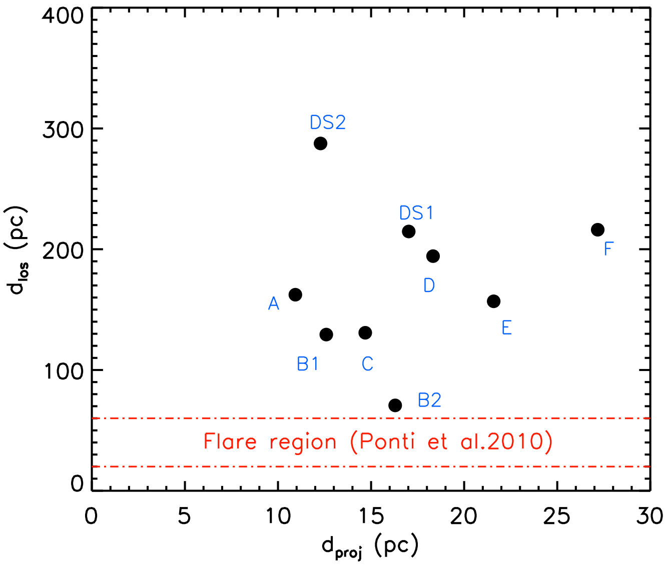

Figure 4.9: Distribution along the line of sight of the MCs bright in the Fe-K$_\alpha$ line, plotted against the projected distance, calculated with the new values of N$_H$ found in Section 4.3.5. The area between the two red dashed-dotted lines represents the flare region in Ponti et al. (2010) (here plotted as straight lines instead of branch of parabolas).

while an X-ray luminosity of the Sgr A* flare of about 10^{39} erg s^{-1} is needed to explain the Fe-K$_\alpha$ measured in the Sgr B2 cloud (e.g. Murakami et al., 2000; Terrier et al., 2010), a significantly lower L$_X$ is needed in order to account for all the timing and spectral properties of the MCs studied in this paper, which lie within a 30 pc of Sgr A*.

Building a lightcurve for Sgr A*

Ideally, rather than assuming a particular outburst L$_X$, we would now build a model for the X-ray activity of Sgr A* over the last few hundreds years (within a pure XRN/Sgr A* scenario), which accounts for all the Fe-K$_\alpha$ variations seen in all the MCs in our study. Unfortunately our lack of knowledge of the position of the clouds along the line of sight relative to Sgr A* hampers this endeavour.

In principle, one can attempt to reconstruct the light curve of Sgr A* by first projecting all the clouds in the plane of Sgr A*, i.e. by assuming the scattering angle θ to be 90 degrees so that d=d$_{\rm proj}$ for all the MCs (for a definition of these geometrical quantities, see Fig.4.10). We can approximate the Fe-K$_\alpha$ light curve of each cloud as a simple linear trend (also based on our fits in Section 4.3.2), considering the 6.4-keV line flux value to be F$_{6.4,t}$, where t can assume all the values within our lightcurves (basically, for our purposes we will only use the values at the beginning and the end of the temporal window under examination, i.e. 2002 and 2009). In this configuration, we can easily calculate the delay of the reflected signal from the cloud relative to the direct signal from the primary source. The observed 6.4-keV light curves then transform directly into a Sgr A* L_X variation (the "90-deg" points in Fig.4.4).

In practice both the scaling of 6.4-keV flux to ionizing source luminosity and the inferred time delay of the reflected signal from the cloud depend on the actual scattering angle θ (*i.e.,* the actual observer-MC-Sgr A* geometry). The dependencies are:

$$\mathrm{L_{X,t}} = \frac{\mathrm{F_{6.4,t}}\ \mathrm{d}^2(\theta)}{1.9 \times 10^{-40}\ \mathrm{R}^2\ \tau_{\mathrm{Fe}}}, \tag{4.6}$$

and

$$\Delta \mathrm{t} = \frac{1}{\mathrm{c}}\ \mathrm{d_{proj}}\ \left[\sqrt{1+\cot^2\theta} - \cot\theta\right], \tag{4.7}$$

where c is the speed of light (3×10^{10} cm s^{-1}). We therefore calculated $L_{X,2002}$ and $L_{X,2009}$ assuming θ=90 degrees and plotted this points shifted forwards into a light curve correcting for the relative delay; we performed this calculation for every cloud. We then relaxed the constraints on the geometry, allowing the angle θ to span the range 45-135 degrees, and shifted the variation of L_X in time as in equation 4.7, scaled as for the following:

$$\mathrm{L_X} = \mathrm{L_X}(\mathrm{d_{proj}})\ \left[1 + \cot^2\theta\right] \tag{4.8}$$

By repeating the above calculations for each of the nine clouds our aim is to see whether any Sgr A* variability pattern can match all the MCs constraints. The results of this "astro-archeology" study are shown in Fig.4.11, where we consider three different geometric assumptions (*i.e.¡* θ=45, 90 and 135 degrees). In this figure we have split the clouds into subgroups depending on the pattern of variability that they exhibit; B1 and F (decreasing flux, top panel), B2, C and D (increasing flux, middle panel) and A, E, DS1 and DS2 (constant flux, bottom panel). In each of the three panels in Fig.4.11 different colours refer to different clouds; The main idea is to see if there are any L_X-delay combination where these sub-groups of MCs cluster, for a certain scattering angle θ which can be different from cloud to cloud. This could give us the trace of the sought Sgr A* variability and the more general view of the distribution along the line of sight of these MCs; in doing this, we assume that the simplest solution has to be preferred to a more complicated one. However, we must admit that our view might not be the unique solution to the requisite convolution.

The B1 and F clouds:

In the top panel of Fig.4.11 we can see that the light curve segments for the B1 and F clouds cluster around an X-ray luminosity of $\sim3\times10^{37}$ and a time delay of 100 years. If these clouds are responding to the same decrease in the incident L_X, then we might infer that the scattering angle for cloud F is $\sim$ 90 deg and that of cloud B1 nearer to 135 deg. This places cloud F on the same plane as Sgr A* and cloud B1 12.6 pc behind the Sgr A* plane. The inferred excursion of the L_X is from $\sim$4 to 2×10^{37} erg s^{-1} over 7 years. However, we must not forget that the uncertainties in the τ_{Fe} and the $F_{6.4}$ measurements

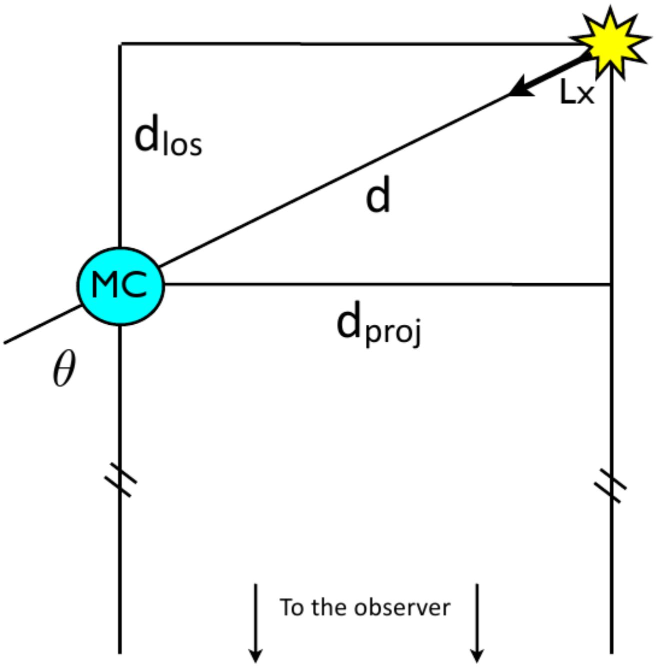

Figure 4.10: Geometry of the illumination scenario. Highlighted in the plot are the total distance from the cloud to the source (d), the projected distance onto the Sgr A* plane (d$_{\rm proj}$), and the distance along the line of sight (d$_{\rm los}$) as a function of the scattering angle θ.

translate to an equivalent L$_X$ scaling error bar. We also notice that the geometry inferred for these two MCs very well agrees with the results plotted in the left panel of Fig.4.7, once the uncertainties on the measurements of the EW are taken into account. In conclusion, a drop in the ionising X-ray luminosity by a factor of two (4 to 2×10^{37} erg s^{-1}) around 100 years ago might be responsible for the decaying Fe-K$_\alpha$ line flux currently observed from the B1 and F MCs.

The B2, C and D clouds: in the same way we can try to put together a scenario which explains the steady increase in the Fe-K$_\alpha$ flux seen from clouds B2, C and D clouds. (middle panel of Fig.4.11). Here the situation is more complex, since for each assumed angle the light curves inferred from the clouds cluster together in a fairly tight fashion. In order to restrict the possibilities we need to bring in extra information as follows. For example, we can perhaps safely assume that these the clouds are not in front of the Sgr A* plane, and therefore exclude the points clustering at $\sim$ 30 years ago; indeed, this would mean that X-ray activity in Sgr A*, likely associated with emission in other longer wavelength, could have been observed by the first X-ray satellites in the 1980s. Another good argument which reinforces this assumption is the level of 6.4-keV line emission measured in the 50 km s^{-1} and 20 km s^{-1} MCs; these clouds are closer to Sgr A* than the ones studied in this

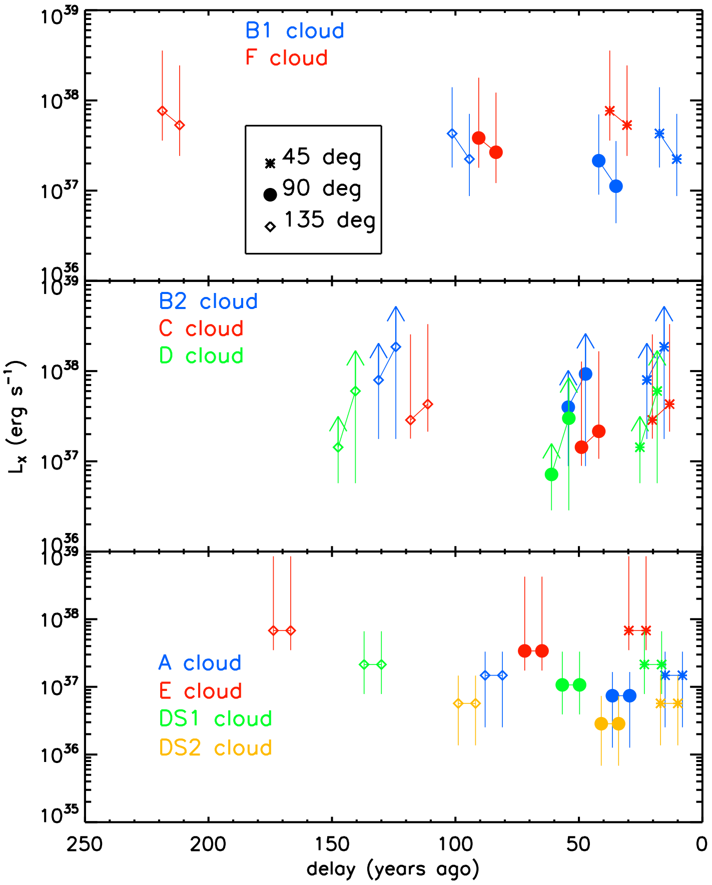

Figure 4.11: Light curves segments derived for the X-ray luminosity of Sgr A* as a function of the time delay for the different MCs. We have divided the MCs into subgroups depending on the type of Fe-K$_\alpha$ line variability observed. The different colours show the L$_X$-delay dependence for the different clouds (see text). The box in the top panel shows the angle correspondence of the symbols we have drawn. (Also plotted are the 90% confidence ranges on the L$_X$ calculation). The arrows in the middle panel indicate that the measurement for the B2 and D clouds do not have upper limits.

paper, and should nowadays show a significant Fe-K$_\alpha$ line flux if illuminated by an L$_X$ in the order of 10^{37-38} erg s^{-1} during the last 30 years.

We now examine the 90 degrees case, i.e. the points marked with a circle in the middle panel of Fig.4.11. We notice that two of these regions, B2 and D, are subregions of the larger molecular complex called *bridge* in Ponti et al. (2010); here, these authors claimed to have discovered a superluminal echo of X-ray reflection, due to the propagation of the ionising front within the MC placed about 60 pc behind the plane of Sgr A*. If we assume the B2 and D clouds are part of the same larger complex, then to explain the superluminal Fe-K$_\alpha$ line variability we have to locate the cloud behind Sgr A*; accordingly, we do not consider the 90 degrees case to satisfactorily describe the Fe fluorescence in this subgroup of MCs.

We focus here on the θ=135 degrees case (diamonds in the middle panel of Fig.4.11). We first notice that the measurement of the optical depth at the Fe-K edge for both the B2 and D clouds is only an upper limit; this is likely due to the fact that these two regions are the smallest in our sample, and therefore the signal to noise ratio is not high enough to have a smaller error on this parameter. This translates in a lower limit for the X-ray luminosity of Sgr A* as calculated in the equations 4.6. However, we can see that the green segment is shifted forwards with respect to the other two measurements; hence, we need to slightly relax the constraint on the geometry relative to the D cloud, assuming a scattering angle around 130 degrees. The line of sight distances of these clouds can be calculated as 16.3, 14.5 and 15.4 pc; the inferred separation of the B2 and D clouds can still explain the apparent superluminal motion of the ionising front, since the minimal dislocation behind Sgr A* of these complexes must be of the order of 2-3 times the apparent displacement (about 15 light years). Therefore we can assume the same variation in L$_X$ from 10^{37} to 10^{38} erg s^{-1} (again, with actual latitude due to the error bars) to be the origin of the rise of the Fe-K$_\alpha$ line flux observed in these three clouds, with this rise of the X-ray luminosity from Sgr A* happening around 130 years ago. Of course, dealing with X-ray luminosities of the order of 10^{37} to 10^{38} erg s^{-1}, we cannot exclude a powerful X-ray binary to be at the origin of the Fe fluorescence in these clouds.

Comparing our findings with the left panel in Fig.4.7 we can see that the curves for B2 and D clouds are higher than the averaged Fe abundance line at Z$_{Fe}$=1.56. In fact, they neither intersect this line; this picture is in contrast with the geometry for these two clouds we inferred in this section. However, if we take into account the large error bars on the measurement of the EW of the Fe-K$_\alpha$ line from the spectra of these two clouds, the agreement between the two results becomes clear. In fact, assuming the lower limit on the EW for the D cloud of 0.85 keV (Table 4.5) the dashed blue line would be dragged down to reach the dashed red line (DS1 region, EW=0.84 keV), which meet the Z$_{Fe}$=1.56 line at angles higher than 120 degrees. The same goes for the B2 cloud; considering the lower limit value of the EW (1.24 keV), the solid yellow curve in the left panel in Fig.4.7 would be superposed to the dashed green line correspondent to the E cloud (EW=1.23 keV); this, together with the reasonable assumption of an EW slightly higher than average (up to twice solar) within the B2 cloud would explain all the results we got for the B2 and D clouds in the XRN/Sgr A* scenario, making once again the agreement between the two results clear. Regarding the C cloud, the θ ∼135 deg result found above well agrees with the solid red curve in the right panel of Fig.4.7.

The A, E, DS1 and DS2 clouds: the bottom panel of Fig.4.11 shows the light curves for these clouds for the three angular assumptions. We can clearly see that the different segments are spread over a large area of the plot and it is not straightforward to infer a pattern for the X-ray activity in Sgr A* which easily explains all the observed 6.4-keV line emission. We can start assuming that the E cloud is located on the same plane of Sgr A*, i.e. considering the L$_X$ found for a scattering angle θ of 90 deg; We assume the lowest value for the E cloud (i.e. 90 deg) and move the other three clouds (changing their position along the line of sight, i.e. θ) until they reach a delay of about 70-80 years ago, which is the delay coordinates for the red circles in the bottom panel of Fig.4.11. As a result we found that the location of the clouds A, DS1 and DS2 must be described by θ angles of about 125, 105 and 120 deg, respectively. Accordingly, the distances of these clouds behind the plane of Sgr A* are 7.6, 4.6 and 7.1 pc, respectively, while the distance for the E cloud is close to null, being the θ angle of this cloud assumed to be 90 deg. Comparing these geometrical results with the geometry which can be inferred from the left panel in Fig.4.3, we can see that there is a very good general agreement between the two set of results, consistent with the average Fe abundance Z_{Fe}=1.56±0.19 $Z_{\odot}$ found in Section 4.3.4.

When considering the 90% errors plotted in Fig.4.11, we found that the lower limit for the L_X at θ=90 deg for the region E is 1.7×10^{37} erg s^{-1}, a value which is not consistent with the upper limit of the same measurement for the region DS2 at θ=120 deg of 9.8×10^{36} erg s^{-1}. The reasons for such a discrepancy might be found in the possible contribution to the 6.4-keV photons production by other mechanisms, mainly cosmic ray bombardment. The effect of a contribution by particle ionisation within all these MCs is the boosting of the Fe-K_{α} line flux and EW. We calculated that the lower limit on the $F_{6.4}$ parameter from region E needed to reconcile the L_X ranges for the E and DS2 clouds is 1.2×10^{-5} photons cm^{-2} s^{-1}, rather than the 2.0×10^{-5} found in Section 4.3.3. This would mean that 0.8/2.0=40% of the 6.4-keV line flux could be due to particle bombardment. We will discuss the possible explanation for the presence of this additional ionisation component in Sections 4.3.7 and 4.4.3.

As a result of this section, we found that a constant X-ray luminosity of 10^{39} erg s^{-1} for the Sgr A* past activity can explain neither the intensity of the Fe-K_{α} line flux nor the variability we measured in the studied MCs. Specifically, we found that the clouds closer to Sgr A* need a lower X-ray ionising flux in order to account for all the spectral and timing properties; moreover, we discovered that a certain amount of variability must be invoked within a more general lower level of emission needed to explain the Fe fluorescence phenomenon in the inner 30 pc.

As a natural step forward, we attempt to build a long term light curve of the X-ray activity of Sgr A*, considering the new results we got in this paper. The final result is shown in Fig.4.12. The first measurement from which we started is the X-ray luminosity required to explain the strong 6.4-keV line emission in the Sgr B2 MC; since its discovery (Koyama et al., 1996), there has been a general agreement that the total amount of Fe-K_{α} fluorescent photons produced in this giant MC have been generated by a powerful X-ray flare on Sgr A*, which reached a luminosity of a few $\times10^{39}$ erg s^{-1} a few hundred years ago. The end of this low luminosity AGN activity by Sgr A* has been recently dated back to 100^{+55}_{-25} years ago (Terrier et al., 2010); this time interval is drawn as a orange area on the top of Fig.4.12, where the vertical extent is given by the uncertainty on the L_X reported by Terrier et al. (2010, 2-5$\times10^{39}$ erg s^{-1}). Accordingly to Inui et al. (2009), the 6.4-keV line flux from Sgr B2 has been constant for at least six years (time of the ASCA first measurement) before the onset of the decrease trend occurred in 2000; this constant

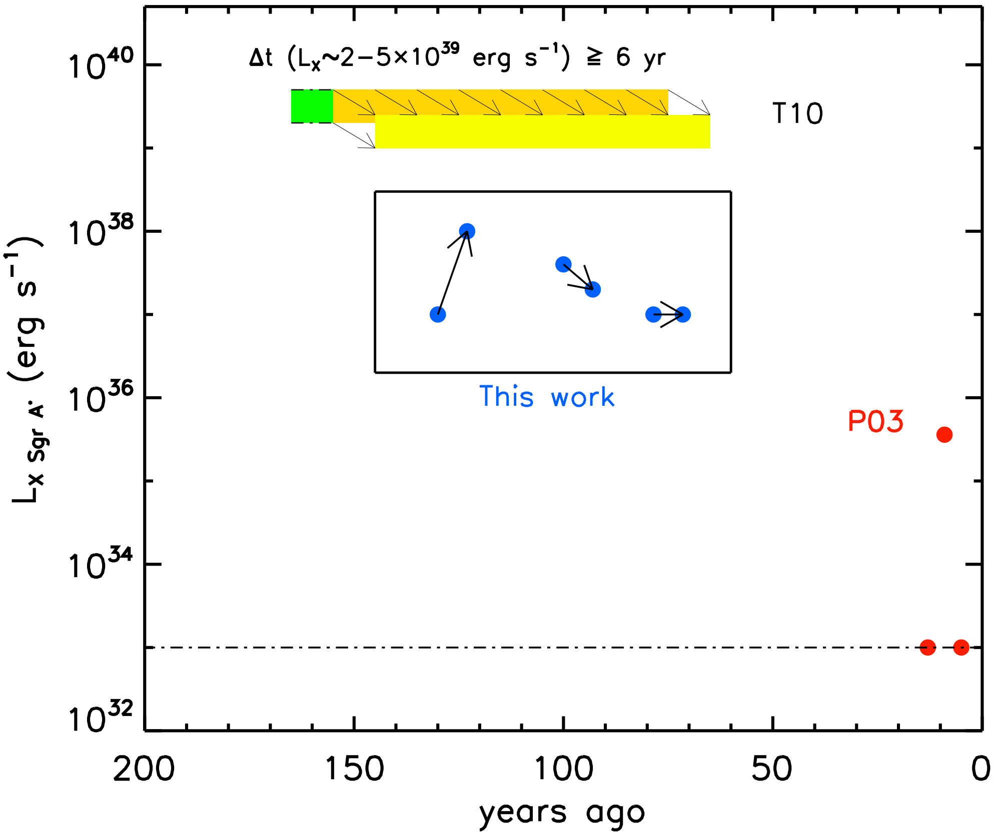

Figure 4.12: X-ray light curve of Sgr A* over the past 200 years. The green area at L$_X$ ∼10^{39} erg s^{-1} show the constraints on the Sgr A* activity inferred from the Fe-K$_\alpha$ measurements in the Sgr B2 cloud (see text, Terrier et al., 2010, T10). The red points show the current quiescence level of Sgr A*, together with the brightest flare ever measured (Porquet et al., 2003, P03). The blue points in the box show the results of this work, with the connecting black arrows displaying the time direction of the variable incident X-ray luminosity.

emission put a strong constrain on the lightcurve of Sgr A*, which must have been constant too, with the same luminosity estimated in the 2-5×10^{39} erg s^{-1} range for at least six years. This constant phase of X-ray activity is drawn as a green area in Fig.4.12. After 2000, the Fe-K$_\alpha$ within Sgr B2 has been continuously decreasing, suffering a drop of about 50% in a 10 years timescale (Terrier et al., 2010). The yellow area in Fig.4.12 shows the linear decrease in the Sgr A* luminosity inferred from the lightcurve of Sgr B2, where the Sgr A* L$_X$ lies in the range 1-2.5×10^{39} erg s^{-1} (i.e. 50% of the constant value before 2000).

Between the end of this high energy activity and the current quiescence state at a L$_X$ of 10^{33} erg s^{-1}, we plotted the results/constraints derived by the study of the clouds shown in Fig.4.2. From the study of the MCs showing an increase of the 6.4-keV line flux, we calculated that Sgr A* should have experienced a rise of the X-ray luminosity of about one order of magnitude about 130 years ago, between 10^{37} up to 10^{38} erg s^{-1}. Moreover, we showed that the variability of the Fe-K_α line flux measured in the clouds F and B1 suggests that Sgr A* has undergone a declining phase around 100 years ago, with a drop in the X-ray luminosity of about a factor of two, i.e. from 4 to 2×10^{37} erg s^{-1}. This short declining phase, must have been followed by a period of slightly constant luminosity at 10^{37} erg s^{-1}, which must have lasted for no more than about 30-40 years. A useful constrain in this time region is the current flux measured from the 50 km s^{-1} MC. Given the short distance to the GC, about 10 pc, Ponti et al. (2010) calculated the mean X-ray luminosity of Sgr A* in the past 60 years to be lower than 8×10^{35} erg s^{-1}; this ties in with the end of the "constant level" of emission at $\sim10^{37}$ about 70 years ago which we inferred from the study of the MCs that show a constant 6.4-keV line flux.

For comparison and completeness we plotted in Fig.4.12 (red points) the present level of X-ray emission from the SMBH ($\sim10^{33}$ erg s^{-1}) and the brightest flare ever detected (L_X=3.5×10^{35} erg s^{-1}, Porquet et al., 2003).

To conclude, in the framework of an XRN/Sgr A* scenario, we have found that the X-ray light curve of Sgr A* shows a clear decreasing trend over the last two hundred years This is not a completely smooth trend, with evidence for flaring or, more precisely, for periods of relative brightening, counter to the long-term trend, by factors of several when averaged over a few years. Given that the light-curve is not monotonic, a much more comprehensive study of the Fe-K_α properties of the MC within say $\sim$ 100 pc will be needed to piece together the full recent history of the Sgr A*

4.3.7 The low surface brightness Fe-K_α diffuse emission

Method

We have measured the 6.4-keV line flux from two extended regions to the East and West (EDE and EDW) of Sgr A*, in order to quantify the difference between the low surface brightness emission at positive and negative galactic longitudes. For this purpose we considered the two elliptical regions shown in Fig.4.14, the central coordinates and sizes of which can be found in the last two rows of Table 4.2. In the case of the EDE region, all the sky regions coincident with the MCs previously studied have been excised, as have the 6.4-keV bright knots in the Arches cluster region (already studied in Capelli et al., 2011b), and the Arches cluster itself (see Capelli et al., 2011a).

We have constructed MOS1&2 spectra for both the non-excised EDE area and the EDW region by stacking all the observational data available. Here we apply a background modelling technique in fitting the four resultant spectra using the same method as described in Section 4.3.2.

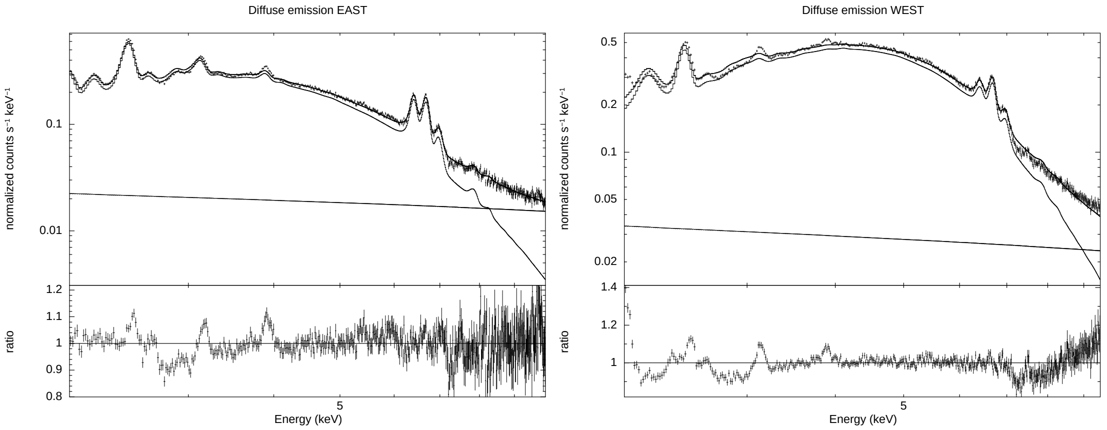

Figure 4.13: *Left panel*: MOS2 spectrum of the EDE region, with the residuals in the bottom panel. The data have been collected stacking all the MOS2 spectra of the region from all the observations. *Right panel*: same for the EDW region.

Results

The results of this investigation are summarised in Table 4.7 and the MOS2 spectra of the EDE and EDW regions are shown in Fig.4.13. The latter shows significant residuals near the high ionisation Si, S, Ar and Ca lines in the 2–4 keV region; these residuals may be due to a range of temperatures and/or metallicities and/or temperatures within the extended plasma which are not well matched by the simple two-temperatuure model which has been applied. The Fe-K$_\alpha$ line flux is, however, very well determined in all these spectra. The 6.4-keV line fluxes for the EDE and EDW regions are 3.44±0.06 and $1.91\pm0.06\times10^{-4}$ photons cm^{-2} s^{-1} respectively. The surface brightness calculated from these values are therefore $1.71\pm0.03\times10^{-6}$ and $7.8\pm0.3\times10^{-7}$ photons cm^{-2} s^{-1} arcmin^{-2}, respectively. The substantial higher level of the *underlying surface brightness* to the east of Sgr A*, compared to the situation to the west, is also apparent in Fig.4.14.

The fact that the underlying diffuse Fe-K$_\alpha$ emission at positive Galactic longitudes is roughly 120% more intense than than that seen at the corresponding negative longitudes is an interesting result. In particular it can be directly compared with the very-high energy γ-ray map of the GC region obtained with the HESS telescope (Aharonian et al., 2006). The TeV emission (see also Yusef-Zadeh et al., 2007b) also shows a strong enhancement to the East of Sgr A* which peaks close to the centre of our EDE region.

Since the TeV emission is most likely the result of the interaction of CRs with the molecular material in the CMZ, this prompts the question as to whether the high underlying level of the 6.4-keV emission to the east of the GC, and perhaps the non-varying emission pedestals seen in some of the 6.4-keV bright MCs, might also be the result of cosmic-ray bombardment (albeit by CR particles of very different energy to those giving rise to the TeV signal). Consider, in this context, the B2 and D regions (see Fig.4.2), which apparently compose the Western side of the region referrred to by (Ponti et al., 2010) as the *the bridge.*

Table 4.7: Results for the spectral analysis of the regions EDE and EDW. The values are the MOS1 and MOS2 weighted means. The N_H is in units of 10^{22}cm^{-2}, the kT of the two plasmas in keV, the normalization of the non-thermal component is in photons cm^{-2} s^{-1} keV^{-1} at 1 keV. The Fe-K$_\alpha$ line flux is in units of photons cm^{-2} s^{-1}.

	EDE	EDW
N_H	7.5±0.1	9.4±0.1
kT_{warm}	0.91 ±0.01	0.356±0.002
kT_{hot}	6.4±0.1	6.1±0.2
Γ	0.78±0.04	1.0±0.1
norm	$5.5\pm0.1\times10^{-3}$	$1.61\pm0.01\times10^{-2}$
$f_{6.4_{keV}}$	$3.44\pm0.06\times10^{-4}$	$1.91\pm0.06\times10^{-4}$

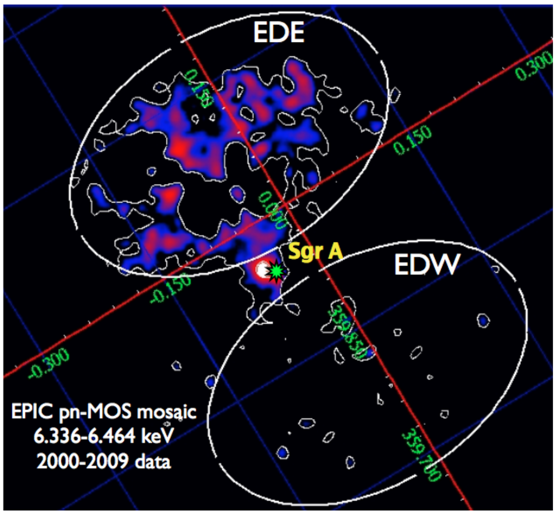

Figure 4.14: A colour-coded and contoured map of the 6.4-keV line emission in GC region. The contours levels are scaled in arbitrary units. The position of Sgr A* is marked with the green star in the centre of the image, whereas the bright spot close to it is the Sgr A EAST SNR complex. The regions selected for the spectral analysis lie within the two ellipses marked as EDE and EDW. For the regions within the EDE ellipse corresponding to the MCs studied in this paper and in Capelli et al. (2011b) have been blanked out.

The first three data points (covering the period 2002-2004) in their 6.4-keV light curves (see Table 4.3 and Fig.4.4) are consistent with constant levels of 1.1±0.1 and $0.8\pm0.1\times10^{-5}$ photons cm^{-2} s^{-1} respectively. These measurements translate to surface brightnesses of 5.2±0.5 and $4.5\pm0.6\times10^{-6}$ photons cm^{-2} s^{-1} arcmin^{-2}, which are compatible with each other, we can see that both are higher than the mean 6.4-keV diffuse surface brightness calculated from the region EDE and EDW. If one then compares the 6.4-keV surface brightness of the B2/D pedestals, the EDE region (after excluding bright MCs) and the EDW region one obtains the ratio 6.4/2.2/1.0. On the other hand, if we look at the contours of the TeV emission map (fig.12a in Yusef-Zadeh et al., 2007b) we can see that there is a remarkable agreement between the 6.4-keV surface brightness scaling found in this Section and that seen in the TeV emission; the brightest TeV emission is detected in a region which well describes the physical extent of the B2 and D clouds (innermost contour of Fig.12a in Yusef-Zadeh et al., 2007b), whereas the EDE region is well delimited by the third contour of the TeV surface brightness distribution, and the EDW one by the two following.

We interpret this agreement in terms of cosmic ray bombardment of the MCs producing a ground level of 6.4-keV emission in all the variable bright clouds, as well as a strong contribution (locally dependent on the CR density and the N$_H$ of the MCS) for all the other clouds include the unresolved "diffuse" emission (see also Capelli et al., 2011b).

4.4 Discussion

In this section we first discuss the dynamical properties of the molecular filaments identified in this paper as strong Fe-K$_\alpha$ emitters. We next consider the characteristic velocity of the molecules inside such entities and the implications for the likely disposition of such filaments within larger scale structures. We then go on to interpret the results of our spectral analysis in the context of the two main scenarios suggested for the Fe-K$_\alpha$ fluorescence effect, namely the XRN and the particle bombardment models.

4.4.1 Molecular clouds in the GC environment

The MCs in the GC region have a typical particle density in the range 10^4-10^5 cm^{-3}; the typical mass is about 10^5-$10^{6.5}$ M$_\odot$ for the giant molecular complexes (like Sgr B2 and Sgr C) and 10^2-10^4 M$_\odot$ for the smaller condensations. The sizes of these molecular clouds span a range from the 10-60 pc for the larger clouds down to 0.1-1 pc for the smaller knots. Oka et al. (1998) pointed out that molecular clouds in the GC have velocity widths of the order of 30-80 km s^{-1}. For a spherical, pure H$_2$ molecular cloud, the escape velocity is:

$$\mathrm{v_{escape}} \approx 1.4 \times 10^2 \left[\frac{\mathrm{n_{H_2}}}{10^4\mathrm{cm^{-3}}}\right]^{1/2} \left[\frac{\mathrm{R}}{35\mathrm{pc}}\right] \ \frac{\mathrm{km}}{\mathrm{s}}, \tag{4.9}$$

where n$_{H_2}$ is the particle density of molecular hydrogen and R is the radius of the spherical cloud. For a large cloud like Sgr B2, describing it as a uniform sphere of radius 35 pc with an internal density of 10^4 cm^{-3}, the escape velocity is about 140 km s^{-1}, higher than the largest velocity width measured in the GC region. Since the escape velocity is higher than the typical turbulent velocities inside the cloud, one can infer that these molecular complexes remain gravitationally bound. On the other hand, if we consider a cloud with the same density as above but only 1 pc in radius, like the Fe-K$_\alpha$ emitting knots we are studying in the region between Sgr A* and the GC Radio Arc, then the formula above yields 4 km s^{-1} for the escape velocity. This value is smaller than the velocity width we see in molecular lines measured in the radio band, as noted above. A third velocity we might consider is the thermal velocity given by:

$$\mathrm{v_{thermal}} = \sqrt{\frac{3\mathrm{K_B T}}{\mathrm{m_{H_2}}}} \approx \left[\frac{\mathrm{T}}{100\mathrm{K}}\right]^{1/2} \frac{\mathrm{km}}{\mathrm{s}} \tag{4.10}$$

where T is the mean temperature of the cloud. However, this velocity is always lower than the turbulent velocity implying that the dynamics inside molecular clouds in the GC region is dominated by turbulence. To study the stability of a certain cloud we must compare the velocity dispersion due to turbulence inside the cloud with the escape velocity. More specifically if the internal turbulence is stronger than the self gravity, one should expect such clouds to evaporate.

A further consideration relates to the potential pressure confinement of the clouds. The energy density associated with the two thermal components (at $\mathrm{kT_1}$≈1 keV and $\mathrm{kT_2}$≈6.5 keV) of the diffuse emission in the GC region has been measured to be 3×10^{-10} erg/cm^3 and 2×10^{-9} erg/cm^3, respectively (Muno et al., 2008). At the same time, for the thermal pressure within the cloud we can write

$$\mathrm{P_{th}} \approx 10^{-7}\left[\frac{\mathrm{n_{H_2}}}{10^4\mathrm{cm^{-3}}}\right]\left[\frac{\mathrm{v}}{3\times10^6\mathrm{cm\ s^{-1}}}\right]^2 \ \mathrm{erg/cm^3}, \tag{4.11}$$

where n_{H_2} is the density of H_2 molecules and v the highest turbulent velocity of the particles. Comparison of the last expression with the pressure produced by the GC diffuse emission shows that a plasma with density and temperature typical of the GC region could not produce a pressure high enough to effectively confine the internal turbulence in molecular complexes. The conclusion of the above argument is that filaments of dimension ≈ 1 pc must have internal velocity dispersion no higher than ≈ 1 km s^{-1} in order to avoid a rapid disassociation. Given the wide velocity range typically seen in radio maps the implication is that the small scale features (≈ 1 pc) are likely to be overdensities in a much larger molecular structure rather than truly isolated clouds.

On the other hand, many studies (*i.e.* Tsuboi et al. (1997) and Oka et al. (2010)) showed that some molecular clouds in the GC region show a peculiar high turbulent velocity, likely connected with high energy phenomena (SN explosion and interaction with high energy particles) taking place in the inner Galaxy. So, the presence of small high velocity molecular clouds confirms the interaction with candidate sources of ionisation.

4.4.2 X-ray Reflection Nebulae

This idea was first suggested by Sunyaev et al. (1993) and later developed by Koyama et al. (1996), Sunyaev & Churazov (1998) and Murakami et al. (2000). In this scenario, a powerful transient X-ray source supplies the primary photons needed to produce the fluorescence observed from the GC molecular clouds. The whole phenomenology, both the line flux and the topology of Fe-K$_\alpha$ line emission, of Sgr B2 giant molecular cloud is well explained in this scenario. In this context Sgr A* must have been bright roughly 100 years ago (based on the projected separation of Sgr B2 and Sgr A*) and remained so for a number of years, given the timescale of the measured variability, reaching an X-ray luminosity of 2-5$\times10^{39}$ erg s^{-1} (Terrier et al., 2010). This latter luminosity is about 10^5 times lower than the Eddington luminosity for a SMBH with the mass of Sgr A*, and so is entirely plausible.

If Sgr A* is indeed the primary source of the ionising photons for Sgr B2 then, by implication, the Fe-K$_\alpha$ emission observed in the more immediate vicinity of Sgr A* might similarly serve as tracer of past outbursts in this same source. Again a test of the validity of this idea might be evident in the pattern of variability in the Fe-K$_\alpha$ signal. Recently Ponti et al. (2010) have reported the complex nature of the variability seen in the 6.4-keV bright filaments close to Sgr A* and have suggested a scenario in which all the observations might be explained in terms of a single outburst from Sgr A*, the same one invoked to explain the 6.4-keV line emission form the Sgr B2 giant complex. In this scenario, a single outburst with a constant luminosity of about 10^{39} erg s^{-1} over about 100 years has been proposed to be the source of the primary photons producing the Fe fluorescence observed in the whole CMZ. Other even faster 4-8 keV continuum variability has been found within regions A and B1 (Muno et al., 2007). In these Fe-K$_\alpha$ bright knots, as noted above, we do measure an absorption feature at the Fe-K edge energy of 7.1 keV (τ_A=0.6 and τ_{B1}=0.2) and an high EW of the 6.4-keV line (EW$_A$=0.84 and EW$_{B1}$=0.96 keV), typical features of an XRN.

In broad terms our study serves also as a confirmation of many of the observational details reported by Ponti et al. (2010), although our conclusion is quite different, namely that the luminosity required to ionise the MCs studied in this paper must be at least one order of magnitude lower than the outburst which is currently illuminating Sgr B2. Furthermore Sgr A* appears to exhibit relatively short-term (*i.e.,* timescales of a few years) episodes of brightening superimposed on a general decreasing trend.

As discussed earlier in this paper, the pattern of the Fe-K$_\alpha$ variability exhibited by the GC filaments is complex. The central 6.4-keV bright knots show a strong increase, while at the western (*i.e.* knots A and B1) and the eastern (region F, the G0.11-0.11 MC) extremes the Fe-K$_\alpha$ line flux is either constant or slightly decreasing. This topology does not allow all the filaments to be part of the same molecular structure, but forces them to be independent complexes distributed along the line of sight.

Comparing the Fe K$_\alpha$ topology and CO and CS line maps, Ponti et al. (2010) argued that the molecular filaments we designate as B2, D and E, are all part of a bigger molecular complex. The Fe-K$_\alpha$ variability measured from these filaments is too fast to be explained in terms of a primary radiation flux crossing the entire molecular cloud from West to East, since this apparent superluminal motion covers a path about 15 light-years long in less than 8 years. These authors solve this issue by moving the entire molecular cloud to a distance of about 60 pc behind Sgr A*. In contrast, we find that the 6.4-keV line lightcurve of the region E (the eastern part of the complex called *the bridge* by Ponti et al., 2010) does not show any very distinct variability pattern. This is difficult to understand within the setting of an apparent superluminal motion of the incident photon flux propagating eastwards from B2. The knot E should get bright in 6.4-keV line well after knots B2 and D; moreover, it should show a pattern of variability, compatible with the one measured in the western components of this molecular cloud. Moreover, the simulations performed by Sunyaev & Churazov (1998) and Murakami et al. (2000) indicate that the fluorescence should face towards the primary source direction. This does not appear to happen in the putative molecular structure formed by the B2, D and E bright knots. Interestingly, the same happens in the Sgr C cloud, where the Fe-K$_\alpha$ line has been detected primarily on the west side of the molecular complex (Yusef-Zadeh et al., 2007a). Our results suggest that the B2 and D clouds lie about 20 pc behind the plane of Sgr A*, whereas the E cloud has a rather small line of sight distance, i.e. is located in the plane of the ionising source.

Radio observations show that the 50 km s^{-1} molecular cloud lies between the eastern filaments A and B1 and Sgr A*, although its location along the line of sight is not yet well defined. It seems likely that the presence of this molecular cloud will produce a shadow which would prevent any molecular filaments eastwards of it, appearing as bright as the directly illuminated molecular complexes (i.e. Sgr B2). We measure the surface brightness of the selected molecular complexes to be of the same order of magnitude (5-10$\times$10^{-6} photons/cm^{-2} s^{-1}/arcmin^{-2}). The measured variability only involves a factor of two; in a pure reflection scenario where Sgr A* supplies the primary photons at constant luminosity, we should see a factor of 20-50 higher 6.4-keV surface brightness in these MCs. This observational evidence seems to rule the possibility that Sgr A* has held a relatively constantly level of output over the duration of its recent AGN activity, since an approximate inverse square fall-off of the Fe-K$_\alpha$ surface brightness might be expected in such a case.

In this paper we have also carried out a detailed spectral analysis with the objective of better defining the physical properties of the MCs under consideration. In particular we started with a more careful determination of the local N$_H$ inside the MCs; in Section 4.3.5 we showed that the N$_H$ values we assumed for the MCs well agrees with the theoretical expectation of a spectral hardening of the reflected spectrum towards higher clouds column densities. On the other hand, we showed that this is not seen in the data reported in Ponti et al. (2010), where the N$_H$ was inferred from CS (J=1-0) intensity measurements, on the assumption of a rather low temperature for the molecular gas (T$\sim$ 20K). Within a theoretical framework, we also used our measurements of the EW of the 6.4-keV line in order to calculate the averaged Fe abundance within the selected MCs (see Section 4.3.4), and to infer the geometry of the MCs distribution within the inner CMZ which turned out to be a powerful and independent test for the light curve we have built in Fig. 4.12. Our results show that the mean metallicity of the MCs in our study is supersolar, with Z$_{Fe}$=1.56 Z$_\odot$ value in good agreement with previous estimates (e.g. Nobukawa et al., 2010).

With the new estimations of the N$_H$, we have calculated the X-ray luminosity required to explain the Fe-K$_\alpha$ emission features observed in each cloud. Here the important result is that the primary source has, at least for some protracted intervals over the last 70-150 years, varied within a much lower band of L$_X$ than has previously been invoked.

As we discussed in Section 4.3.7, the Fe-K$_\alpha$ line flux measured from the *bridge* shows a constant, non-zero, level before the onset of the variability. We have calculated the pre-variability surface brightness of the two complexes B2 and D and found them to be consistent. The comparison between ratio of the 6.4-keV emissivity in the *bridge* subregions B2 and D, the region EDE and EDW and the TeV contour map, suggests that there might be a fluorescence component induced by CR bombardment. The location of these clouds between the Radio Arc and the GC, together with the general enhancement of synchrotron radiation observed in this region (e.g. Nord et al., 2004), is at least circumstantial evidence for the possible presence of such a component. To support this hypothesis, we note that Capelli et al. (2011b) recently showed that there are MCs in the Arches cluster region (about 20 pc in projection from Sgr A*) which show Fe-K$_\alpha$ line emission best explained in terms of bombardment, where the candidate particles are non-relativistic electrons and/or protons). We want to stress that to model the true level of the X-ray variable activity of the primary ionising source, a careful qualitative and quantitative characterization of the possible contribution by CR bombardment must be carried out, since the presence of particle ionisation could result in a boosting of the EW Fe-K$_\alpha$ line and therefore alter our results, which are based on a pure reflection model.

A further issue is represented by the hardness of the continuum non-thermal emission associated with the production of the Fe-K$_\alpha$ fluorescence. In all our spectra we measured a spectral index of the power-law component close to Γ=1. As discussed by Capelli et al. (2011b), a harder spectrum might be the signature of the particle bombardment contribution, since in this scenario the spectra shape is harder, with $\Gamma\sim$1.3-1.4 (Valinia et al., 2000). However, as we discussed in the text, due to absorption, the spectrum of the reflected continuum may well appear harder than the intrinsic (incident) form (Revnivtsev et al., 2004; Terrier et al., 2010). As a result, the reflection/scattering mechanisms at work in these MCS are not well constrained by the measurements of the spectral shape of the reflected continuum.

In summary, we think that the XRN/Sgr A* scenario proposed by Ponti et al. (2010) has significant difficulties in explaining all aspects of the Fe-K$_\alpha$ line emission observed from the MCs in the inner CMZ. The observed variability and measured line equivalent widths values point unequivocally towards the photoionisation of the MCs by X-ray transient source/s as the excitation mechanism. We calculate the X-ray luminosity of this putative source to vary between 10^{37} and 10^{38} erg s^{-1} on a timescale of several years; a significantly lower estimate than the 10^{39} erg s^{-1} required to explain the Fe fluorescence phenomenon associated with the Sgr B2 cloud (i.e. Terrier et al., 2010). Whereas low AGN activity in Sgr A* is a very plausible scenario largely in agreement with the observations, we cannot exclude that the activity at the the level of 10^{37-38} erg s^{-1} can be due to other X-ray transient sources in the GC, which might have also played a role in creating the observed fluorescence distribution.

Association of the X-ray transient XMMU J174554.4-285456 with region C

The X-ray transient source XMMU J174554.4-285456 was first detected with XMM-Newton during an outburst on 2002 October 3rd (Porquet et al., 2005b). Repeated observations of the GC region performed with Chandra later revealed this source to be bright in June-July 2004 (Muno et al., 2005; Wang et al., 2006). A closer inspection to the XMM-Newton

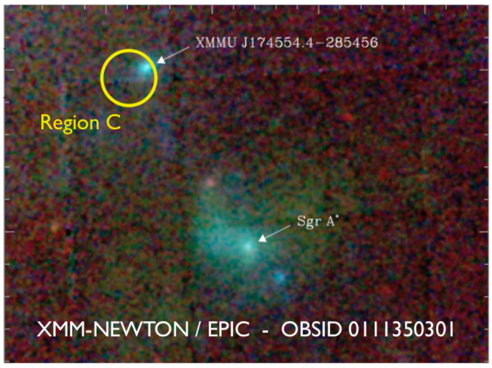

Figure 4.15: XMM Newton / EPIC color image of the X-ray transient XMMU J174554.4-285456 (Porquet et al., 2005b). The colors are red (0.2-2 keV), green (2-5 keV) and blue (5-10 keV). The yellow circle on the top of the image shows region C.

dataset employed in this work revealed the presence of this source also in the March 2004 data. So far, the nature of this peculiar X-ray binary has not been yet identified. The ratio between the X-ray luminosity at the outburst and in the quiescence state is about 10^4. For this reason, we decided to investigate whether the measured fluxes of the 6.4-keV line from the region C could be due (in part) to the flaring activity of this X-ray binary.

The resulting 6.4-keV line flux lightcurve from the region C shows a step behavior (see Fig.4.4). Dividing the six epochs into two, we obtain weighted means of 0.8±0.1 and $1.2\pm0.1\times10^{-5}$ photons cm^{-2} s^{-1}, respectively. A closer inspection to the full band X-ray image fromobservations 0202670501 and 0202670601 shows the presence of the X-ray transient source XMMU J174554.4-285456 within the circle representing region C (Porquet et al., 2005b). The best spectral model has been found to be an absorbed powerlaw, with a Γ=1.7±0.2 and a very high column density (N_H) of $14.1^{+1.0}_{-1.4}\mathrm{cm}^{-2}$. The flaring X-ray luminosity of this source was 1.5×10^{35}erg s^{-1} in the 0.5-10 keV band (Porquet et al., 2005b).

Assuming the non-zero constant level of 6.4-keV line emission measured with the first three data points in the lightcurve due to CR bombardment, we considered the enhancement in the Fe-K_α line flux to be $12-8=4\times10^{-6}$ photons cm^{-2} s^{-1} and calculate the requisite distance of the binary to be 2 pc. Given the high N_H value measured towards this source, we favor the geometry in which the MC lies in the line of sight between us and XMMU J174554.4-285456. In this case there is a significant agreement between the variability timescale and the distances assumed in this scenario, where the size of the cloud is about 3.7 pc (12 light years); the time delay between the first reported flare (October 2002) and the first observed enhanced 6.4-keV flux is about 4.5 years, and this perfectly matches with the distance inferred for the X-ray source of about 2 pc. In conclusion, we found that the Fe fluorescence in the region C can be well described as the superposition of a constant particle bombardment induced 6.4-keV line emission, plus a component due to X-ray irradiation from the close transient source XMMU J174554.4-285456. Potentially this is the second XRN positively associated with an X-ray transient source in the GC region (Capelli et al., 2011b). A deeper inspection with the Chandra satellite would be of great interest to confirm this scenario; indeed, the angular resolution achieved by the satellite would allow us to measure the ionising front/s due to different flares expanding within the MC.

4.4.3 Particle bombardment

This model has been proposed and discussed by Valinia et al. (2000), Predehl et al. (2003), Yusef-Zadeh et al. (2007a) and Dogiel et al. (2009c). In this context, the primary source of the Fe fluorescence are cosmic-rays (CRs), potentially with a variety of compositions, origins and energies. While the photoionisation cross section is a steep function of the energy of the primary photon, the cross section for collisional ionisation is a relatively smooth function of the energy of the incident particle; for electrons with energies in the range 10-100 keV and protons with energy between 10 and 100 MeV, the cross section for collisional ionisation of Fe reaches the maximum values, i.e. these are the energy ranges over which the particle bombardment most likely takes place.

Although electrons have been historically favoured as source of ionisation of MCs in the CMZ, we notice that electrons with a kinetic energy of some tens of keV, i.e. where the cross section for Fe ionisation is higher, can only penetrate a small amount of the target clouds; these particles are stopped by a column density of about 10^{21}cm^{-2}, a value which is significantly lower than what usually found in dense MCS in the GC region. As a consequence, fluorescent emission via electron bombardment most likely takes place within the outermost edges of a cloud, and cannot propagate through the densest layers of the target because of its intrinsic inefficiency. On the other hand, protons have a much larger penetrating power than electrons; a 100 MeV proton is stopped by a column density of about 4×10^{23}cm^{-2}, a value which well resembles the highest column densities found in the GC region. Accordingly, we think that protons are generally to be preferred to electrons as a source of ionisation of MCs, although peculiar locations (radio arc, Arches cluster) might reveal different mechanisms at work.

Very recently, Capelli et al. (2011b) showed that in the Arches cluster region there are MCs similar to those studied in this paper in terms of their density and size, which shine in the 6.4-keV line with a surface brightness comparable to the typical value found in clouds closer to Sgr A* (about 10^{-6} photons cm^{-2} s^{-1} arcmin^{-2}). There, the XRN/Sgr A* model proposed by (Ponti et al., 2010) fails to explain in a self consistent picture the topology and the temporal/spectral variability of the bright knots. The EW and the variability of the 6.4-keV line seem to indicate an origin in the photoionisation of the MCs by nearby X-ray transient sources, although the most likely source of this fluorescent emission is particle bombardment, where the estimated CR energy density is about 50-100 eV/cm^3, about two orders of magnitude higher than the one estimated for the larger Galactic plane (see Capelli et al., 2011b); of course, the AC is the best candidate to produce and accelerate these CR particles.

For what concerns the MCs studied in this paper, our results point towards a major contribution to the Fe-K$_\alpha$ line emission to be due to photoionisation. The measured EWs of the 6.4-keV line are always very high (EW$\gtrsim$1keV), especially in the B2, D, E and F regions; such high values of the EW are a clear indication of reflection. Only in the MCs A, DS1 and DS2, the EW value is also consistent with illumination by interaction of the MC with low-energy CR electrons and or protons (EW$\lesssim$1keV). On the other hand, the highest values for the optical depth at the Fe-K edge have been measured here, suggesting that the MCs A, DS1 and DS2 host XRNs.

Moreover, the fast variability measured in some clouds is difficult to explain in the context of a pure particle bombardment scenario; in this case, for the 6.4-keV line flux to vary, we need to tune the primary energy entering the molecular cloud. The physical quantities which might be subject to change over the timescale of a few years are the magnetic field and the CRs flux. Thus, together with the measurement of the EW of the 6.4-keV line, the variability is a key factor; to understand whether at least part of the Fe-K$_\alpha$ flux variability can be also explained in the context of a particle bombardment scenario, we suggest that radio continuum observations could reveal a similar variability in the flux of the radio filaments correlating with the Fe fluorescence topology. This is expected both from a variable CRs flux or a rapidly (some years) changing magnetic field. In this context the Fe-K$_\alpha$ variability together with studies in the GeV, TeV and radio bands, can help to discern between different families of CRs as source of the Fe fluorescence in molecular clouds in the GC region.

The strong correlation between the Fe-K$_\alpha$ line emission and the high energy diffuse γ-rays (E$\approx$TeV) found in the GC region might be an argument supporting a significant contribution to the Fe fluorescence by particle bombardment. There, diffuse γ-rays are produced in hadronic collisions of CRs with the target material (i.e. molecular clouds). Aharonian et al. (2006) showed that the strongest diffuse γ-ray emission is seen towards the Sgr B, Sgr C and the Radio Arc molecular complexes; these are exactly the GC molecular clouds also shining in Fe-K$_\alpha$ fluorescent line. In this paper, thanks to the large effective area of XMM-Newton, we have shown that in the region between Sgr A* and the Radio Arc there is also a remarkable correlation between the enhancement of the diffuse low surface brightness Fe-K$_\alpha$ emission (measured only at positive longitudes) and the contours of the TeV emission. This result fits in well with the particle bombardment scenario; indeed the ratio between the low surface brightness 6.4-keV emission at the base of the MCs studied in this paper, in the East of Sgr A* and to its West (region EDE and EDW in Section 4.3.7), are the same as the ratio between the TeV surface brightness within the same regions. The intensity of 6.4-keV line emission is proportional to the density of the target material; besides the production of the brightest Fe-K$_\alpha$ emission in the dense molecular filaments, CRs also ionise the cold diffuse interstellar medium.

Oka et al. (2010) discovered high velocity compact clouds in the GC region which show a CO J=3-2/J=1-0 intensity ratio higher than that typically found in the Galactic disc. These features are likely to be knots of shocked molecular gas, heated by energetic events such as supernovae explosions. The distribution of these clumpy structures correlates well with the location of the molecular filaments we have studied in this work; the same is true for the Sgr C molecular cloud (Oka et al., 2010). This correlation suggests a close relation between these shocked molecular complexes and the Fe-K$_\alpha$ line emission, since shocks internal to the clouds act as particles accelerators. Moreover, Muno et al. (2008) showed that there are many physical processes active in the GC region which appear to produce diffuse X-ray features. For example, these authors discovered $\approx$ 20 candidate pulsar wind nebulae within 20 pc of Sgr A*, which are among the best established sites of CRs acceleration. The particle bombardment hypothesis places few contraints on the geometry of the Fe-K$_\alpha$ line emission since Fe fluorescence can also take place on the farside of the cloud with respect to the position of Sgr A* (as observed, for example, in Sgr C (Yusef-Zadeh et al. 2007a). All these correlations seem to suggest that the ground level of the Fe-K$_\alpha$ line flux measured in the lightcurves of all the variable MCs may be due to bombardment by CR particles.

SN ejecta fragments have also been proposed as sources of the Fe-K$_\alpha$ emission (Bykov, 2002). The 6.4 keV line surface brightness produced by a fast SN fragment 0.01 pc in size interacting with a molecular cloud lies in the range [9-400]$\times 10^{-5}$ photons cm^{-2} s^{-1} arcmin^{-2} for propagation velocities of the fragment respectively of 1080 and 2700 km s^{-1} (Bykov, 2002). These estimates are over a factor 10 higher than the values we actually measured in the GC filaments. However, in this scenario we cannot account for the variability exhibited by at least some of the selected Fe-K$_\alpha$ bright knots, since fragments moving at 1000 km s^{-1} would need at least 100 years to cross a small molecular structure 0.1 pc in size.

Chapter 5

Fe-K$_\alpha$ line emission in the Arches cluster region: evidence for ongoing particle bombardment?

Original publication: R. Capelli, R.S. Warwick, D. Porquet, S. Gillessen, P. Predehl, *Fe-K$_\alpha$ line emission in the Arches cluster region: evidence for ongoing particle bombardment?*. The content of this chapter was published by the International scientific Journal Astronomy & Astrophysics (Capelli et al. 2011, A&A, 530, A38); as first author, my contribution to this work included the data reduction and analysis, as well as the following scientific interpretation of the results. The other authors contributed with the review of the draft and comments and suggestions regarding the scientific interpretation of the results, which helped to improve the work.

Abstract: Bright Fe-K$_\alpha$ line emission at 6.4 keV is a unique characteristic of some of the dense molecular complexes present in the Galactic Center region. Whether this X-ray fluorescence is due largely to the irradiation of the clouds by X-ray photons or is, at least in part, the result of cosmic-ray particle bombardment, remains an interesting open question. We present the results of XMM-Newton observations performed over the last eight years of the region surrounding the Arches cluster in the Galactic Center. We study the spatial distribution and temporal behaviour of the Fe-K$_\alpha$ emission with the objective of identifying the likely source of the excitation. We have constructed an Fe-K$_\alpha$ fluence map in a narrow energy band of width 128 eV centered on 6.4 keV. We use this to localize the brightest fluorescence features in the vicinity of the Arches cluster. We have investigated the variability of the 6.4-keV line emission of several clouds through spectral fitting of the EPIC MOS data with the use of a modelled background, which avoids many of the systematics inherent in local background subtraction. We also employ spectral stacking of both EPIC PN and MOS data to search for evidence of an Fe-K edge feature imprinted on the underlying X-ray continuum. The lightcurves of the Fe-K$_\alpha$ line emission from three bright molecular knots close to the Arches cluster were found to be constant over the 8-year observation window. However, West of the cluster, we found a bright cloud which shows the fastest Fe-K$_\alpha$ variability yet seen in a molecular cloud in the Galactic Center region. The time averaged spectra

of the molecular clouds revealed no convincing evidence of the 7.1-keV edge feature, albeit with only weak constraints. The EW of the 6.4-keV line emitted by the clouds near to the cluster was found to be ~ 1.0 keV. The observed Fe-K$_\alpha$ line flux and the high value of the EW suggest an origin of the fluorescence in the photoionization of the MCs by X-ray photons, although excitation by cosmic-ray particles is not specifically excluded. For the three clouds nearest to the Arches cluster, the identification of the source of these X-rays as an earlier outburst on Sgr A* is at best tentative, although not entirely ruled out by the observations. On the other hand, the hardness of the nonthermal component associated with the 6.4-keV line emission might be best explained in terms of the bombardment of the clouds by cosmic-ray particles emanating from the Arches cluster itself. The relatively short-timescale variability seen in the 6.4-keV line emission from the cloud to the west of the cluster is most likely the result of its X-ray illumination by a nearby transient X-ray source.

5.1 Introduction

The Galactic Center (GC) is a bright source of diffuse 6.4-keV fluorescent line emission corresponding to the K$_\alpha$ transition in neutral iron (Fe) atoms (or low-ionization Fe ions). The spatial distribution of the line emission is clumpy, but at the same time widespread across the whole region, and shows a good correlation with that of molecular clouds (MCs) (Yusef-Zadeh et al., 2007a). The three regions which have the most prominent 6.4-keV line emission are Sgr B2 (Inui et al., 2009), Sgr C (Nakajima et al., 2009) and the molecular filaments between Sgr A* and the Radio Arc (Koyama et al., 2009). However, more than a decade after the discovery of this fluorescent emission (Koyama et al., 1996), the mechanism of its excitation remains a puzzle. The fluorescence may be the result of the irradiation of cold gaseous matter by hard X-rays photons with energies above 7.1 keV (the K-edge of neutral iron). Alternatively, the excitation might be through the bombardment of the gas by cosmic-ray (CR) particles with energies above this same threshold. In both cases the removal of a K-shell electron, is rapidly followed by recombination and the emission of a fluorescent K$_\alpha$ photon. In X-ray binaries and active galactic nuclei (AGNs), the observed 6.4-keV line is generally interpreted as the reprocessing of X-rays from the central X-ray continuum source at the surface of surrounding dense media, such as an accretion disc and/or a molecular torus (e.g., Fabian et al., 1989; Nandra et al., 1997). However, in the case of the fluorescencing structures seen in the GC region, there is no obvious persistent source bright enough to explain the observed line fluxes. One possible solution to this paradox is that the X-ray illuminating source, from our offset perspective, is highly obscured. Alternatively, such a source may possibly have been bright in the past, but is currently faint.

The first observations of 6.4-keV emission from the GC (Koyama et al., 1996) prompted the suggestion that the required X-ray illumination might be associated with the past activity of Sgr A* (Sunyaev & Churazov, 1998). In particular, Murakami et al. (2000) suggested, based on their X-ray study of the molecular cloud with the brightest 6.4-keV emission, Sgr B2, that Sgr A* had been in an active phase roughly three hundred years

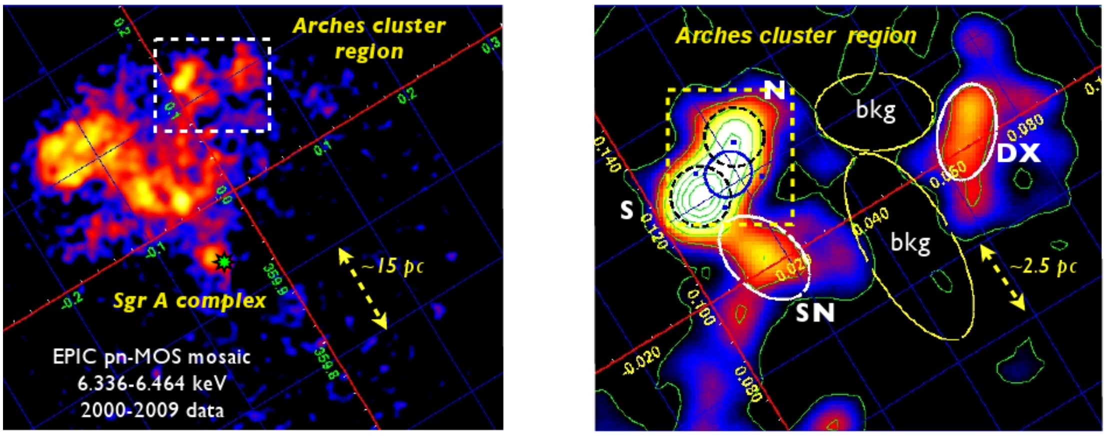

Figure 5.1: *Left panel*: Fe-K$_\alpha$ emission line map of the GC region. The data have been background subtracted and vignetting corrected. The position of Sgr A* is marked by a green star. The dashed white ellipse shows the AC region. *Right panel*: A zoom into the AC region. The position of the AC is indicated by the blue ellipse at l∼0.12°, b∼0.02°. Bright 6.4-keV knots are highlighted by dashed black circles (labelled N and S) and white ellipses (labelled SN at b∼0.015° and DX at b∼0.07°). The region used for background accumulation is shown by the two yellow ellipses (bkg). The dashed yellow box shows the sky region studied in Wang et al. (2006, Fig.14). The galactic coordinate grid is shown in red.

earlier. This interpretation has remained in favour; for example, Terrier et al. (2010) have recently measured the decay of the lightcurve of the scattered X-ray continuum emanating from Sgr B2 and argue that this requires the period of intense activity of Sgr A* to have ended between 75 and 155 years ago. In this setting a key observational fact is that Sgr A* is currently some six orders of magnitude fainter than required (Baganoff et al., 2001). Even the brightest X-ray flares detected so far (amplitude 100-160; Porquet et al., 2003; Porquet et al., 2008) are still 4 orders of magnitude fainter than required and have too short a duration (∼1 hour). The X-ray photon irradiation scenario is often referred to as the X-ray Reflection Nebulae (XRN) model, irrespective of whether Sgr A* is the actual source of the X-ray photon illumination.

An alternative to the XRN model is to invoke the incidence of CR electrons and/or protons as the excitation source (e.g. Predehl et al., 2003; Yusef-Zadeh et al., 2007a; Dogiel et al., 2009c). Although low-energy (E$\lesssim$100 keV) CR electrons are favoured over highly energetic particles (Yusef-Zadeh et al., 2002), we note that the cross section for the production of inner shell ionization of Fe atoms by ultra-relativistic (Lorenz factor $\gtrsim$100) electrons is not negligible; in fact, it amounts to about 1% of the Fe-K photoionization cross section (see Tatischeff, 2003). In the case of protons, the cross section for the ionization process is highest for subrelativistic particles (Dogiel et al., 2009c).

One main way to distinguish between the two proposed scenarios is to investigate the

Table 5.1: Specifications for the selected OBSIDs. In each of the instrument related columns we report the threshold used for the Good Time Interval (GTI) selection in the 10-12 keV lightcurve (in units of counts/s), the total GTI exposure and the nominal duration of each observation.

OBSID	Obs Date yyyy-mm-dd	PN cut/GTI/exp	MOS1 cut/GTI/exp	MOS2 cut/GTI/exp
0111350101	2002-02-26	0.8/38.590/40.030	0.5/42.262/52.105	0.5/41.700/52.120
0202670501	2004-03-28	2.0/13.320/101.170	1.0/33.070/107.784	1.0/30.049/108.572
0202670601	2004-03-30	2.0/25.680/112.204	1.0/32.841/120.863	1.0/35.390/122.521
0202670701	2004-08-31	1.0/59.400/127.470	0.5/80.640/132.469	0.5/84.180/132.502
0202670801	2004-09-02	1.0/69.360/130.951	0.5/94.774/132.997	0.5/98.757/133.036
0402430301	2007-04-01	1.5/61.465/101.319	0.8/61.002/93.947	0.8/62.987/94.022
0402430401	2007-04-03	1.5/48.862/93.594	0.8/40.372/97.566	0.8/41.317/96.461
0402430701	2007-03-30	1.5/32.337/32.338	0.8/26.720/33.912	0.8/27.685/33.917
0505670101	2008-03-23	1.25/74.216/96.601	0.5/73.662/97.787	0.5/74.027/97.787
0554750401	2009-04-01	1.0/30.114/38.034	0.5/32.567/39.614	0.5/33.802/39.619
0554750501	2009-04-03	1.0/36.374/42.434	0.5/41.376/44.016	0.5/41.318/44.018
0554750601	2009-04-05	1.0/28.697/32.837	0.5/37.076/38.816	0.5/36.840/38.818

temporal variability of the 6.4-keV line emitted from the GC MCs, since fast variability (typically on a timescale of a few years) in which reflection echos appear to propagate at roughly the speed of light, favours illumination by X-ray photons rather than by non-relativistic CR particles. Ponti et al. (2010) argued that the XRN model coupled with the hypothesised past activity of Sgr A*, provided a consistent explanation for the complex pattern of variability seen in the molecular filaments located between Sgr A* and the Radio Arc. However, it remains unclear whether or not CR particle bombardment also plays a role in the excitation of the X-ray fluorescence from at least some of these peculiar MCs. For example, the non-zero level of the Fe-K$_\alpha$ lightcurve prior to the onset of an episode of enhanced emission in the molecular complex known as the "Bridge" (Ponti et al., 2010), could be due to an underlying CR-induced line flux.

Here, we report an X-ray study of the MCs in the surroundings of the Arches cluster (AC) based on observations carried out by XMM-Newton. This region was not studied in detailed in the recent Chandra and XMM-Newton compilations of 6.4-keV cloud properties (Muno et al., 2007; Ponti et al., 2010), although earlier Chandra results for the AC have been reported by Yusef-Zadeh et al. (2002), Law & Yusef-Zadeh (2004), and Wang et al. (2006)

Throughout this paper, we assume the distance to the GC to be 8 kpc (Gillessen et al., 2009). In Section 5.2 of this paper we present the XMM-Newton observations and describe the data reduction techniques we have employed. In Section 5.3, we investigate the spatial distribution of the Fe-K$_\alpha$ line emission in the vicinity of the AC and select four bright regions for further temporal and spectral analysis. The study of the Fe-K$_\alpha$ line variability has been performed using background modelling, while for the spectral analysis of the time averaged spectra we employed a standard background subtraction technique. We then go on to discuss our results in the context of the two main scenarios proposed to explain the Fe fluorescent-line emission, namely the XRN model and the CR particle bombardment model (Chapter 2). Finally, in Chapter 7 summarises the main results of this study.

5.2 Observations and data reduction

We selected archival XMM-Newton data of the GC region largely targeted at Sgr A*. We reprocessed the data from both the PN and MOS cameras (Strüder et al. (2001), Turner et al. (2001)) with the tasks EPPROC and EMPROC in the Science Analysis Software version 9.0. In order to mitigate the effects of occasional high particle background rates in the detectors, induced by bursts of soft protons incident on the satellite, we constructed the 10-12 keV lightcurve of the data from the whole field of view (FOV). A threshold was then set so as to cut all the peaks in the background rate, thereby defining the Good Time Intervals (GTIs) for the time filtering of the observation. Since the selected observations were performed in varying conditions of internal/particle background and orbital phase, we investigated all the lightcurves independently and selected a threshold count rate separately for each observation/camera combination (see also Capelli et al., 2011a). The specifics of the XMM-Newton observations employed in the present work are reported in Table 5.1. Throughout our analysis we have only selected single and double events (PATTERN$\leq$4) for the PN and up to quadruple events (PATTERN$\leq$12) for the MOS1 and MOS2 cameras. For all the instruments a further screening involved selecting only events marked as real X-rays (FLAG==0).

5.3 Analysis and Results

5.3.1 The spatial distribution of the 6.4-keV line and its association with MCs

A first task was to construct a fluence (integrated flux over time) map for the Fe-K$_\alpha$ line in a narrow spectral window from which we might hope to identify and locate the brightest fluorescence regions. We merged the GTI-filtered event files for the three EPIC cameras (where available) for each observation, using the SAS task EMOSAIC. In building the image of the Fe-K$_\alpha$ emission, we assumed a value of E/ΔE=50 at 6.4 keV for the spectral resolution (FWHM) of both the PN and MOS1/2 cameras, corresponding to a bandpass for the Fe fluorescence signal of 6336-6464 eV. The resulting map of the 6.4-keV line emission is shown in the left panel of Fig.5.1; the AC is located at the edge of the XMM-Newton FOV at the position R.A.=17^{h}45^{m}40.045^s, DEC.=-29°0'27.9". The general distribution of the Fe fluorescent emission evident in this figure is very similar to that previously reported from both XMM-Newton (Predehl et al., 2003) and Suzaku (Koyama et al., 2009) observations.

Yusef-Zadeh et al. (2003) studied the non-thermal emission in the locality of the AC and showed that the giant non-thermal filament of the Radio Arc (l$\sim$0.2°) runs to the East

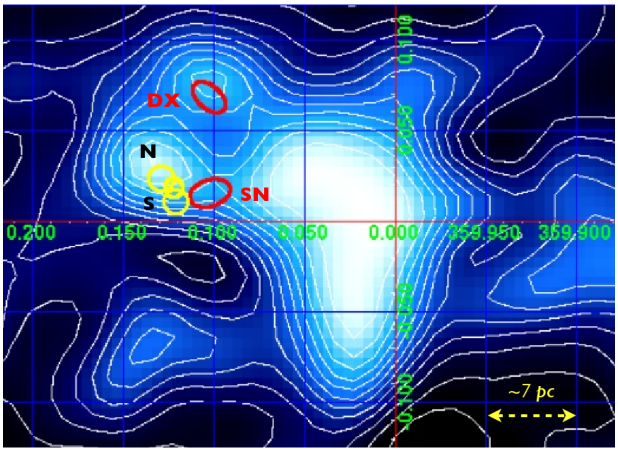

Figure 5.2: Intensity map in galactic coordinates of the CS J=1-0 line (Tsuboi et al., 1999) integrated over the velocity range -40 km/s - 0 km/s. The locations of the four bright knots identified in the XMM-Newton Fe-K$_\alpha$ image are also indicated.

of the AC with smaller thermal filaments lying to the north. The non-thermal emission originates in synchrotron radiation emitted by relativistic electrons in the strong magnetic fields within the Radio Arc structure. Examination of a broadband (2–10 keV) version of Fig.5.1 shows that the general profile and extent of the AC inferred from the XMM-Newton data is in good agreement with previous Chandra measurements (Yusef-Zadeh et al., 2002; Law & Yusef-Zadeh, 2004; Wang et al., 2006). The AC morphology consists of a northern core component (designated as A1 and A2 in Yusef-Zadeh et al., 2002) and a southern extended component (A3 in Yusef-Zadeh et al., 2002). XMM-Newton separates these north and south continuum components but is unable to resolve structures within them. The right panel of Fig.5.1 shows that there are three regions relatively close to the AC which can be identified as distinct sources of 6.4-keV fluorescence. Two of these regions coincide with the north (N) and south (S) continuum components defined above. The third is located to the South-West of the S component (labelled as region SN). Moreover, the XMM-Newton observations also reveal a 6.4-keV bright knot further to the West of the N component (labeled as region DX).

There are some notable differences between the Fe-K$_\alpha$ line emission map obtained with XMM-Newton (Fig.5.1, right panel) and the one measured by Chandra (Wang et al., 2006). First, XMM-Newton detected a northern 6.4-keV feature (knot N) close to the AC itself, which was not seen in the equivalent Chandra line image. With the higher statistics and the larger effective area of EPIC cameras, we also discovered a prominent tapered feature (knot SN) that seems to be connected to the knot S region.

To identify possible molecular counterparts to the Fe-K$_\alpha$ bright knots we used data from the CS J=1-0 (48.99 GHz) survey of the Central Molecular Zone (CMZ) (Tsuboi et al., 1999). The results are shown in Fig.5.2, where the blue colour scale and the contours represent the CS J=1-0 line emission intensity integrated over the -40 km/s to 0 km/s velocity range. The locations of the bright 6.4-keV knots are also indicated. A CS enhancement at l∼0.13°, b∼0.03° coincides positionally with knot N. This molecular feature has a velocity of -30 km/s. Lower surface brightness molecular structures are also seen close to the SN and DX knots. We note that the CS emission at the four knot locations spans a spread of velocities which, although narrow enough to likely rule out the possibility that the molecular material is widely distributed along the line of sight, is sufficiently broad to suggest that the dynamics of the MCs in this region are dominated by turbulence.

Table 5.2: Physical properties of the 6.4-keV emitting clouds. Here, we report the cloud size in parsecs (in radius or semi-axis), the equivalent H column density through the cloud, the estimated total number of H atoms inside the cloud and the optical depth of the cloud to Thomson scattering.

cloud	size (pc)	N_H(cm^{-2})	#H (10^{59})	τ_T
N	0.92	4×10^{22}	9.6	0.0266
S	0.92	2×10^{22}	4.8	0.0133
SN	1.6×1.0	2×10^{22}	9.0	0.0133
DX	1.5×0.9	2×10^{22}	7.6	0.0133

Hereafter, we take the view that the four 6.4-keV knots represent coherent molecular structures in the vicinity of the AC. On this basis, Table 5.2 details the physical parameters of each MC. The angular size of the clouds have been estimated by eye and then converted to a linear size. For the hydrogen column density through the N and S clouds, N_H, we use the values reported by Amo-Baladrón et al. (2009) which in turn were derived from CS molecular emission. Because these authors did not report the equivalent H column densities for the other two knots, we assumed these to be the same as the region S (since the emission contours of the CS J=1-0 line, at the locations of these knots are similar to those in the S region). We caution that the estimate of the N_H of a MC in the GC is strongly dependent on the method used to measure it. For example, for the large G0.13-0.13 molecular complex, two extreme values have been inferred for N_H, namely 4×10^{22} cm^{-2} (Amo-Baladrón et al., 2009, using CS J=1-0 line) and a much higher value of 10^{24} cm^{-2} (Handa et al., 2006, based on the H^{13}CO^{+} J=1-0 line). Finally, we calculated the number of H atoms in the MCs and the value of the optical depth for Thomson scattering (τ_T). The estimates in Table 5.2 will be used in Section 5.4 to investigate the origin of the Fe-K$_\alpha$ line emission.

5.3.2 Fe-K$_\alpha$ line flux and variability - background modeling

We are interested in determining both the absolute photon flux in the Fe-K$_\alpha$ line and in searching for temporal variability in this signal. To this end, we extracted the spectra for each of the four bright 6.4-keV knots for each observation and then, for observations separated by only a few days, combined the data to give a sampling at six epochs as follows:

February 2002 (1 observation), March 2004 (2 observations), August/September 2004 (2 observations), March/April 2007 (3 observations), March 2008 (1 observation), and April 2009 (3 observations).

The 6.4-keV emitting knots are not visible in the full band (2–10 keV) X-ray image, since their continuum signal is hard to distinguish against the strong diffuse X-ray emission which permeates the GC region. Indeed, the main contribution to the 2–10 keV spectrum of these extended sources is the thermal emission from the GC region. The best choice in performing a self-consistent spectral analysis of these low surface brightness features is to model the background as a component within the spectral fitting rather than subtracting it prior to the fitting. This technique avoids many systematic errors due to the contamination by foreground emission (De Luca & Molendi, 2004; Leccardi & Molendi, 2008), but has the disadvantage that we are forced to exclude PN data (since at present, no detailed study of the instrumental background for the PN EPIC-camera has been provided).

The model used in the spectral fitting accounts for:

- Photoelectric absorption (WABS, Morrison & McCammon, 1983). All the emission components are subject to soft X-ray absorption so as to account for the high column density along the line of sight to the GC region.

- Galactic thermal diffuse emission (2 × APEC, Smith et al., 2001). Two thermal components are needed to explain the spectral shape of the GC thermal emission: one *warm* with a temperature of ≈ 1 keV (Ryu et al., 2009) and one *hot* with a temperature in the range 5-7 keV (Koyama et al., 2007a). The higher temperature plasma is needed to constrain the fit in the region of Fe-line complex. The metallicities of the two thermal plasmas have been fixed to twice solar. Tanaka (2002) showed that the equivalent width of the S and Fe lines in the spectrum of the Galactic Ridge decrease as one moves away from the GC, with higher than solar metallicities required for elements such as Si, S and Fe in the diffuse plasma permeating the GC region. Recently, Nobukawa et al. (2010) also measured a supersolar metallicity for the hot plasma in the GC region. The twice solar constraint results in a broadly satisfactory fit to all our spectra, whereas use of a solar metallicity produces high residuals in all the soft X-ray (i.e., $\lesssim$ 3-4 keV) emission lines.

- The Cosmic X-ray Background (POWER-LAW). The spectral shape of this component is modelled as a power-law continuum with a photon index fixed at Γ=1.4 (Hickox & Markevitch, 2007). The normalization of this component was set to 10.9 photon cm^{-2} s^{-1} sterad^{-1} keV^{-1} (Hickox & Markevitch, 2007).

- A non-thermal hard X-ray component (POWER-LAW). The non-thermal continuum emission directly linked to the Fe-line fluorescence. We fixed the slope of the power-law component associated with the source of fluorescence to Γ=1 in order to give consistency in the measurement of the 6.4-keV flux across the different datasets[1].

---

[1] The value of Γ was chosen after studying the stacked spectrum of region S (see §3.3), which shows the

Table 5.3: Fluxes of the Fe-K_α line. The values reported in the Table are the weighted means of the MOS1&2 measured fluxes, in units of 10^{-6} photons/cm^2/s. The different columns refer to different datasets (see text). The Apr07, Mar08 and Apr09 fluxes for region D are based on MOS 2 data only, as a consequence of the damaged sustained by CCD6 in MOS 1 on 9 March 2005 (Abbey et al., 2006).

region	Feb02	Mar04	Sep04	Apr07	Mar08	Apr09	Wtd Mean	χ^2_{red}
N	3.4±1.7	4.0±1.0	4.8±1.0	3.4±1.0	3.4±1.1	4.4±1.1	3.9±0.4	0.4
S	4.9±1.9	7.2±1.3	7.8±1.2	6.5±1.0	6.6±1.4	7.4±1.3	6.9±0.5	0.4
SN	4.7±1.6	3.9±1.0	5.3±0.9	4.5±0.8	6.3±1.2	3.5±0.9	4.6±0.4	0.9
DX	1.2±1.1	3.1±0.9	4.7±0.9	3.3±0.7	1.9±0.8	1.7±0.7	2.7±0.3	2.1

- Fe fluorescent lines (2 GAUSS). The two spectral lines with gaussian profiles were used to represent the Fe-K_α and Fe-K_β fluorescent lines at 6.4 keV and 7.05 keV. The flux of the Fe-K_β line was fixed at 0.11 times that of the K_α component (Koyama et al., 2009).

- The particle background (POWER-LAW). We used the values reported in Leccardi & Molendi (2008) for the slopes of the particle component in the MOS1 and MOS2 spectra, respectively Γ=0.24 and Γ=0.23. Since this instrumental background is not focused in the detector, it does not need to be convolved with the instrument response.

The statistics of each spectrum (per region, per epoch) differ markedly from one another. Since the construction of the lightcurves of the 6.4-keV line flux must be done in a consistent way, we decided to fix the temperature of the hot plasma component at 6.5 keV (Koyama et al., 2007a), given that variations in the temperature of this component have the potential to unduly influence the measured Fe K_α line flux. Note, however, that the temperature of the warm thermal emission was taken to be a free parameter, as were the normalizations of the two thermal plasma components. The warm component temperature ranges inferred for the N, S and SN clouds are 0.5-2 keV, 0.7-1.3 keV and $\sim$ 1 keV respectively, values which are in good agreement with those obtained in Section 5.3.3 from the analysis of the stacked spectra. These temperatures are marginally lower than the value of 1.7 keV measured for the core of the AC, (Capelli et al., 2011a), hinting at a decrease in the warm plasma temperature as one moves away from the cluster until an "ambient" medium with kT $\approx$ 1 keV is reached. Because of the reduced signal to noise ratio, all the spectra of the DX region were fitted with the warm plasma temperature fixed at the ambient value, (i.e. kT=1 keV).

---

most intense 6.4-keV line emission, and therefore has the best statistics. This analysis gave $\Gamma = 1.0^{+0.1}_{-0.2}$ consistent with earlier estimates from Chandra (Γ=$1.3^{+1.4}_{-1.1}$) and Suzaku (Γ=$0.72^{+0.68}_{-0.72}$) (respectively, Wang et al., 2006; Tsujimoto et al., 2007).

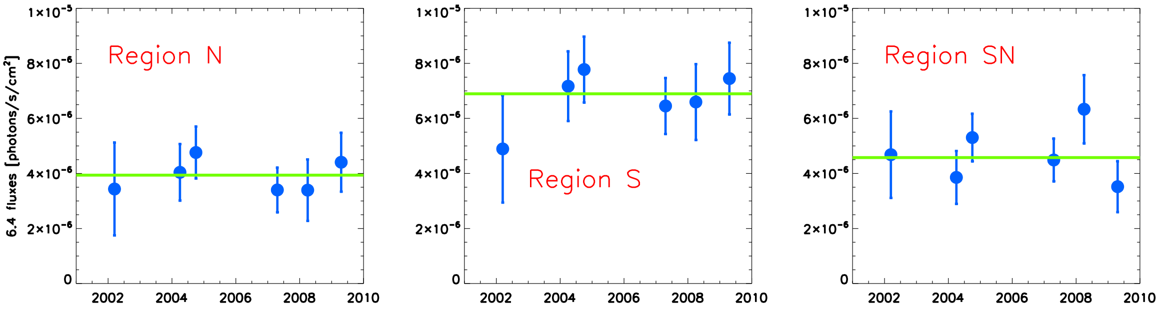

Figure 5.3: Lightcurves of the Fe-K$_\alpha$ line flux from the MCs in the vicinity of the AC. The flux values are in units of 10^{-6} photons/cm^2/s. The green horizontal lines show the weighted means of the data points.

Because of the different slopes of the particle component in the MOS cameras, the MOS1 and MOS2 spectra were kept separate, giving two spectral datasets for each of the four regions (N, S, SN, DX) for each of the six epochs. Given the restricted photon statistics, we used the Cash statistic rather than the χ^2. Prior to spectral fitting we grouped the channels in each spectrum with the GRPPHA tool in order to have a minimum of 1 count/bin (De Luca & Molendi, 2004). The photon fluxes in the 6.4-keV line determined from this analysis are reported in Table 5.3. In the last two columns of this table we also report the weighted mean across the six measurement epochs and the reduced χ^2 for the constant flux hypothesis. Fig.5.3 shows the lightcurves of the 6.4-keV line for the three MCs in the immediate vicinity of the AC, together with the weighted mean flux. We find that the 6.4-keV line fluxes from all of these knots (regions N, S and SN) are constant with time.

The DX cloud is $\sim$ 3 arcmin (about 7 pc in projection) to the West of the AC, in a region which appears to be disconnected from the cluster itself and from the other 6.4-keV bright knots studied in this paper. The lightcurve of the Fe K$_\alpha$ emission from the DX cloud shows clear evidence for time variability (Fig.5.4), which is supported by the high value of χ^2_{red} for these data with respect to the constant flux hypothesis (Table 5.3). Clearly, the temporal behavior of this particular cloud is very different to that of the three bright knots closer (in projection) to the AC. Its temporal behaviour is also different to that reported for all the other MCs in the GC (Inui et al., 2009; Ponti et al., 2010). In the DX knot we clearly see both an increase and decrease in the Fe fluorescent flux rather than solely an increasing (or decreasing) trend over the monitoring period. The Fe-K$_\alpha$ flux from this cloud appears to have increased by a factor of three over a period of about 2.5 years with a peak in September 2004 after which, over a timescale of a few years, it faded back to its pre-outburst level. Interestingly the average of the first and last points in the lightcurve is not zero, suggesting that the outburst was superimposed on a base level. The variability exhibited by this cloud is the *fastest* yet reported for the GC region.

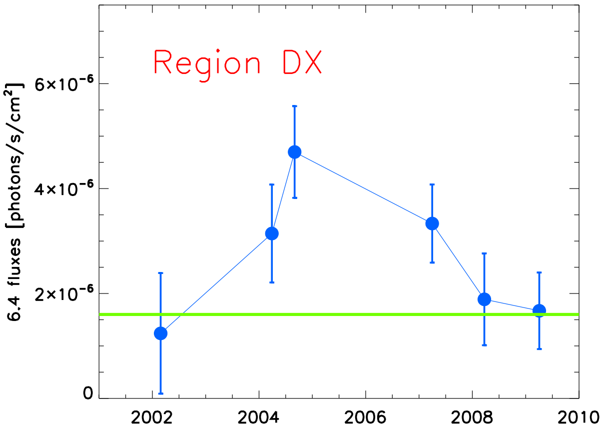

Figure 5.4: Lightcurve of the 6.4-keV line for the DX cloud. The weighted mean ($1.6\pm0.5\times10^{-6}$photons/cm^2/s) of the first and last data points is shown as the horizontal green line. The emission reaches a maximum in September 2004 with a line flux roughly three times the base level.

5.3.3 Analysis of the time averaged spectra - stacking + background subtraction

We have also carried out an analysis of the stacked PN and MOS spectra of the four 6.4-keV knots with the objective of determining the equivalent width (EW) of the Fe-K$_\alpha$ fluorescent line with respect to the associated continuum. A second objective was to check for an Fe-K absorption edge at 7.1 keV imprinted on the same continuum (Sunyaev & Churazov, 1998; Murakami et al., 2000). Because of the stacking of the data (i.e. the addition of all the spectra across the set of observations), the photon statistics were much improved, which allowed us to employ a more standard background subtraction technique and therefore include the EPIC-PN data in the study. We again used the C-statistics because of the low number of counts per bin in the spectra; indeed, when fitting with the χ^2 statistics the χ^2_{red} values are always too small (about 0.2-0.3) to be confident with the best fit results. Moreover, for what concerns the spectral analysis of the MCs in the vicinity of the AC, we notice that the C-statistics give always tighter constraints on the spectral parameters.

The background spectra for the PN and MOS channels were built by stacking all the background spectra collected for the different datasets. The region selected for the background accumulation corresponds to the two ellipses with semi-axes 0.8×0.5 arcmin and 1.4×0.6 arcmin shown in the right panel of Fig.5.1. The spectral model used to fit the data comprises a collisional ionized *warm* plasma (APEC, with temperature and normalization free parameters) and a power-law continuum with associated Fe-K$_\alpha$ and Fe-K$_\beta$ lines at 6.4 and 7.05 keV (K$_\beta$/K$_\alpha$=0.11). All the emission components were then subject to absorption in the ISM along the line of sight (WABS, common to both the APEC and the power law).

Table 5.4: Results for the spectral analysis of the stacked spectra. Here we report the total column density (N$_H$, in 10^{22} cm^{-2}) inferred from the X-ray measurements, the temperature and the normalization of the APEC thermal plasma (in units of $10^{-18}\int n_e n_H dV/4\pi D^2$, where n$_e$ and n$_H$ are the electron and H densities in cm^{-3}, and D the distance to the source in cm), the flux of the Fe K$_\alpha$ line (in units of 10^{-6} photons/cm^{-2}/s), the normalization of the powerlaw component (10^{-5} photons/keV/cm^{-2}/s at 1 keV), the EW of the Fe-K$_\alpha$ line (in keV) with respect to the powerlaw component, the upper limit to the optical depth of the Fe-K edge, and the C-stat values for the best fit model (the degrees of freedom are 2119 for the regions N, S and SN, 397 for the region DX).

	N	S	SN	DX
N$_H$	9.5±1.5	10.1±0.7	$8.5^{+4.0}_{-3.4}$	6.0 (fixed)
kT (keV)	1.8±0.3	1.6±0.1	$1.0^{+1.0}_{-0.5}$	-
norm$_{kT}$	$4.7^{+2.4}_{-1.5}$	$9.2^{+2.5}_{-2.4}$	$2.8^{+17.7}_{-2.4}$	-
F$_{6.4}$	3.2±0.5	6.2±0.6	3.2±1.0	1.9±0.5
norm$_{POW}$	2.0±0.3	4.4±0.4	$1.8^{+0.4}_{-0.2}$	0.5±0.1
τ	≤ 0.4	≤ 0.6	≤ 1.8	-
EW$_{6.4}$	1.0±0.4	0.9±0.2	1.1±0.4	$2.6^{+2.1}_{-1.1}$
C-stat	2337.60	2280.52	2335.05	453.92

For this analysis the slope of the non-thermal continuum radiation associated with the fluorescence was again fixed at Γ=1. The use of a local background removes the requirement for two of the spectral components included previously, namely the hot thermal component and the cosmic X-ray background, both of which can be assumed to have constant surface brightness across the AC region.

The results are summarised in Fig.5.5 and Table 5.4[2]. Regions N and S have rather similar spectra, in which contamination by residual thermal emission (not removed by the background subtraction) is clearly present in the form of the helium-like Fe line at 6.7 keV and other helium-like lines of other elements (S, Ar, Ca) at lower energies. In these regions, close to the AC core, we derive a temperature of the *warm* plasma consistent with that previously measured in the core (Wang et al., 2006; Tsujimoto et al., 2007; Capelli et al., 2011a). The X-ray spectra of both complexes exhibit high line-of-sight absorption and a relatively high EW for the neutral iron Fe K$_\alpha$ line ($\sim$ 1.0 keV). The high value of the EW might be interpreted as evidence for X-ray irradiation as the origin of this

---

[2] The values quoted here are based on the MOS data only. We do not consider the PN values here because of likely systematic errors in the background subtraction. The fluxes of the 6.4-keV line in the background-subtracted PN spectra are generally lower than those determined from the equivalent MOS spectra such that, if the PN measurements are included, then the line fluxes based on the stacked spectra are not consistent with the MOS-only values derived in Section 5.3.2. We tried also to fit the stacked PN spectra modeling the background with a simple powerlaw component (Γ=0), and got consistent results, both between PN and MOS cameras, and with the fluxes measured in Section 5.3.2. Therefore, we associate these systematics in PN measurements of the 6.4-keV emission to the background subtraction.

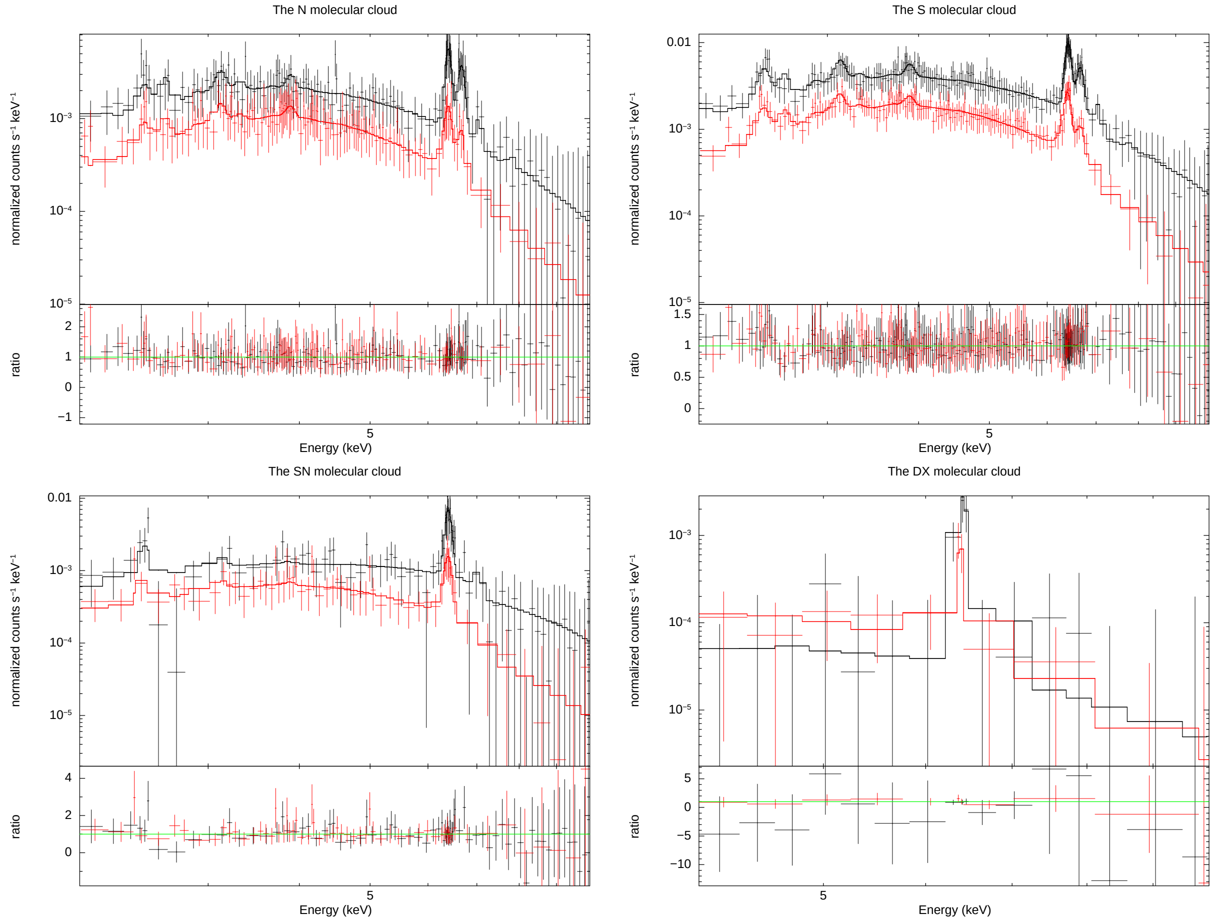

Figure 5.5: PN (black) and MOS (red) stacked spectra of the four selected MCs in the 2-10 keV (4-10 keV for the DX cloud) energy range, together with the ratio between the data points and the best fit model. The top panels show the spectra of the N and S molecular complexes, with the bottom panels similarly presenting the spectra of SN and DX clouds.

fluorescence. For this reason, we also investigated whether there is any evidence for the Fe-K absorption edge, by applying a multiplicative EDGE model (with a fixed energy of 7.1 keV) to the power-law continuum component; however, on the basis of the spectral fitting there was no requirement for such a feature. We could only measure an upper limit to the optical depth of this absorption edge (see Table 5.4). However, the detection of an optical depth of about 0.1-0.2 (equivalent to $N_H \sim 10^{23} \mathrm{cm}^{-2}$) at the Fe-K absorption edge energy (7.1 keV) is challenging when the statistics are limited and the spectrum above 7 keV is potentially contaminated by systematic errors in the subtraction of the instrumental background (which has a non-uniform pattern in the detector).

The spectral parameters inferred for the SN region are similar to those obtained for the N and S clouds, except for the marginally lower temperature inferred for the warm plasma (kT $\sim$ 1 keV) which, as noted earlier, may plausibly be a consequence of the increased distance from the AC core. A high value for the EW of the 6.4 keV line (EW $\sim$ 1.1 keV) is again evident, with no requirement for an absorption edge at 7.1 keV.

In the case of the DX cloud the derived spectrum, which is shown in the lower right panel of Fig.5, is very strongly photon limited. In fact the statistics are so poor that no net signal was detected below 4 keV and no warm plasma component was required in the fit. The inferred 2-10 keV photon flux based on the spectral fitting was $5.9 \pm 3.5 \times 10^{-6}$ photons/cm^2/s, that is almost an order of magnitude lower than the continuum fluxes inferred for the other knots. The measurement of an Fe-K absorption edge could not be done.

5.3.4 Summary of the results

The results of Section 5.3 can be summarized in five main points:

- Fe-K$_\alpha$ line variability (N-S-SN): the lightcurve of the 6.4-keV line flux has been found to be constant in the regions N, S and SN.
- Fe-K$_\alpha$ line variability (DX): we measured a fast variability of the Fe fluorescent line in the DX cloud, with a timescale of about 2-3 years.
- EW of the 6.4-keV line: All four MCs studied have high values ($\sim$ 1 keV) for EW of the Fe fluorescent line, although the errors, particularly for the DX cloud, are relatively large. Unfortunately, the 90% confidence range for the EW is too wide to place tight constraints on the excitation mechanism of Fe fluorescence.
- Fe-K edge at 7.1 keV: we failed to detect an absorption edge imprinted on the power-law component in any of the MCs - much better statistics would be required to properly constrain the optical depth of such a feature.
- Hardness of the non-thermal emission: we measured a hard spectral slope for the non-thermal emission for the region S (i.e. $\Gamma=1.0^{+0.1}_{-0.2}$) with the spectra of the other clouds compatible with the presence of such a component.

5.4 Discussion

The CMZ contains approximately 10% of the molecular gas of the entire Galaxy largely in the form of dense clouds (Morris & Serabyn, 1996). The bright Fe-K$_\alpha$ line emission at 6.4 keV is a peculiar feature of the MCs located within this region. The 6.4-keV line is produced by the fluorescence of neutral (or near-neutral) Fe atoms subject to irradiation by hard X-rays (with energies above the Fe-K edge at 7.1 keV) and/or bombardment by CR particles with energies in the range from 7.1 keV up to, potentially, many 100's of keV. More than a decade after its first detection, the combination of circumstances which give rise to the bright Fe-K$_\alpha$ emission in the GC remains a matter of discussion (e.g. Yusef-Zadeh et al., 2007a; Koyama et al., 2009; Dogiel et al., 2009c). In a recent development, Muno et al. (2007) and Ponti et al. (2010) have studied the variability of the 6.4-keV line flux seen in several MCs lying between Sgr A* and the GC Radio Arc. These authors interpret their results in terms of the photoionization of molecular material by hard X-rays produced in a past (∼100 years ago) bright (L_{2-10} $\sim 10^{39}$ erg/s) flare on the SMBH at the center of the Galaxy. On the other hand, some authors are not fully convinced by the Sgr A* outburst model (e.g., Predehl et al., 2003; Yusef-Zadeh et al., 2007a; Dogiel et al., 2009c).

Here, we interpret the results of our study of four 6.4-keV bright knots located within ∼ 3 arcmin of the AC. Projected onto the plane of the sky the separation of these knots from the AC is no more than ∼ 7 pc; however, we have limited information on the relative line-of-sight locations, so the association of these structures with the AC is only tentative.

5.4.1 The XRN hypothesis

The three knots closest (in projection) to the AC exhibit a constant Fe-K_α line flux and it is tempting to imagine that the AC itself might be the source of the excitation, whether via photons or particles. However, in the case of the former the average X-ray luminosity of the AC is nowhere near sufficient to produce the total amount of fluorescence observed. On the other hand, if the AC entered a putative high activity state in which its X-ray luminosity exceeded 10^{37} erg/s, then it would be possible to explain the observed 6.4-keV fluxes of the nearby clouds in the context of the XRN model. Capelli et al. (2011a) recently reported X-ray flaring activity within the AC, most likely originating from stellar winds interactions in one or more massive binary systems, but even at its peak the measured luminosity remains three order of magnitude lower than that cited above. An alternative is to consider the temporary brightening of an X-ray binary source close to or even within the AC. Then the requirement is for the bright state to have lasted for more than 8 years at or above $L_x \sim 10^{37}$erg/s; this is much longer than the typical flaring timescales of X-ray transient sources (e.g., Degenaar & Wijnands, 2010).

Fe-K_α variability

In the XRN scenario, it has been conjectured that the most plausible source of hard X-ray photons is Sgr A*. On the basis of this assumption, we have investigated the possible distribution along the line of sight of the 6.4-keV clouds in the AC vicinity. In the following calculations, we assumed the X-ray luminosity of the Sgr A* giant flare to have been 1.4×10^{39} erg/s (Ponti et al., 2010). We then infer the physical separation between the clouds and Sgr A* using the formula reported in Sunyaev & Churazov (1998) which, to better fit our purposes, can be written in the form

$$\frac{\mathrm{R}^2}{4\mathrm{d}^2} = \Omega = \frac{4\pi \mathrm{D}^2 \cdot \mathrm{F}_{6.4}}{\tau \cdot \mathrm{L_x} \cdot 10^7 \cdot \mathrm{Z}} \; = \; 5.17 \times 10^{-4} \left(\frac{\mathrm{F}_{6.4}}{10^{-4}}\right) \left(\frac{0.1}{\tau}\right) \left(\frac{\mathrm{Z}_\odot}{\mathrm{Z}}\right).$$

In this equation D is the distance to the GC (assumed to be 8 kpc), $F_{6.4}$ is the Fe-K_α line flux (in photons/cm^2/s), τ the optical depth to Thomson scattering of the cloud, and

Table 5.5: Cloud parameters and distances inferred in the XRN/Sgr A* outburst model. Here, Z is the metallicity assumed for the MC, R the radius of the cloud as seen from Sgr A* (pc), $F_{6.4}$ the flux measured in the Fe-K$_\alpha$ line (photons/cm^2/s), Ω the solid angle (scaled to the whole sky, in units of 10^{-5}) subtended by the MC from the perspective of Sgr A*, d(pc) the distance of the MC from Sgr A*, d_p(pc) and $d_{l.o.s.}$(pc) the distance projected onto the plane of the sky and along the line of sight, respectively.

cloud	Z	R	$F_{6.4}$	Ω	d	d_p	$d_{l.o.s.}$
N	$Z_\odot$	0.92	3.9	7.6	52.8	27.6	45.0
-	1.25 $Z_\odot$	0.92	3.9	6.1	58.9	27.6	52.0
-	1.5 $Z_\odot$	0.92	3.9	5.1	64.4	27.6	58.2
-	2 $Z_\odot$	0.92	3.9	3.8	74.6	27.6	69.3
S	$Z_\odot$	0.92	6.9	26.8	28.1	26.3	9.9
-	1.25 $Z_\odot$	0.92	6.9	21.4	31.4	26.3	17.2
-	1.5 $Z_\odot$	0.92	6.9	17.9	34.4	26.3	22.2
-	2 $Z_\odot$	0.92	6.9	13.4	39.7	26.3	22.2
SN	$Z_\odot$	1.27	4.6	17.9	47.5	23.3	41.4
-	1.25 $Z_\odot$	1.27	4.6	14.3	53.1	23.3	47.7
-	1.5 $Z_\odot$	1.27	4.6	11.9	58.2	23.3	53.3
-	2 $Z_\odot$	1.27	4.6	8.9	67.3	23.3	63.1
DX	$Z_\odot$	0.9	4.7	18.0	33.5	27.5	19.2
-	1.25 $Z_\odot$	0.9	4.7	14.4	37.5	27.5	25.5
-	1.5 $Z_\odot$	0.9	4.7	12.0	41.1	27.5	30.5
-	2 $Z_\odot$	0.9	4.7	9.0	47.4	27.5	38.6

L_x the X-ray luminosity of the Sgr A* flare. The solid angle Ω is defined as $\Omega = R^2/4d^2$, where R is the radius of the cloud as seen from Sgr A* (basically, the minor axis for the cloud DX and a combination of major and minor axis for the region SN, as measured on the sky) and d is the distance of the cloud from Sgr A* (Ω is scaled to be the fraction of the whole sky subtended by the MC from the perspective of Sgr A*).

By first determining Ω, we are then able to estimate d from the cloud dimension (assuming spherical symmetry). By comparison of d with the projected distance of the cloud from Sgr A* on the plane of the sky (d_p), we can then derive the position of the clouds along the line of sight relative to Sgr A* ($d_{l.o.s}$).

Our calculations are, of course, highly dependent on the assumed past lumininosity of Sgr A*. However, since we use the best estimate available based on the XRN modelling of other GC clouds (Ponti et al., 2010), we are in effect testing this model for internal self-consistency. However, the inferred line of sight location of the clouds ($d_{l.o.s}$) will depend on the assumed metallicity (Z) of the molecular material (more specifically on the iron abundance) and also on the optical depths of the MCs. In the literature, there is not yet a consensus on the typical values of these parameters for MCs in the CMZ. In the case of the metal abundance, the best estimate is for supersolar values, closer to Z=2 than Z=1 (Morris & Serabyn, 1996).

All the assumptions and the results of our calculations are detailed in Table 5.5. The

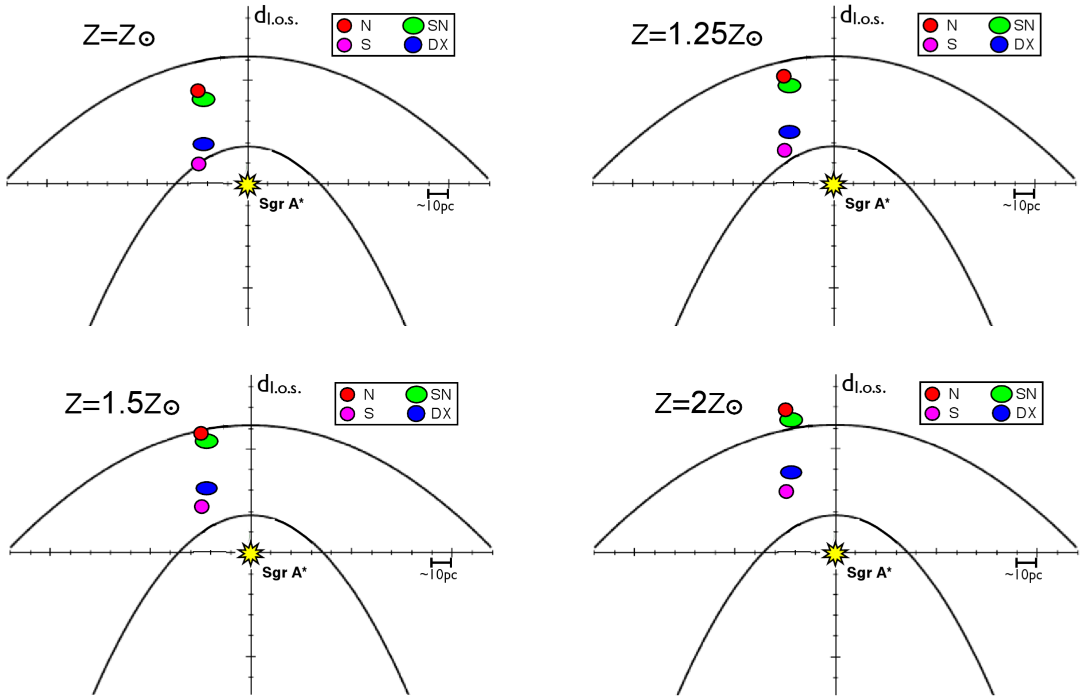

Figure 5.6: The relative locations of the four MCs as inferred from the XRN/Sgr A* outburst model suggested by Ponti et al. (2010). This is the view of the Galactic plane as seen from above (i.e. the clouds positions are shown projected onto the plane). The two parabolas in each sketch represent curves of constant path length for a burst of ionizing flux propagating outwards from Sgr A*. The size of each cloud has been enlarged by a factor of 3.5 to aid the visualisation. The distance (in parsecs) along the line of sight (relative to Sgr A*) is plotted along the Y axis (see also Table 5.5). The SMBH Sgr A* is located at the origin of the axes and marked by a yellow star. The four panels represent the situation for an assumed metallicity of 1, 1.25, 1.5 and 2 times the solar value.

Fe-K_α line fluxes for the different clouds are assumed as in the weighted mean column of Table 5.3; because of the measured variability, only for the DX cloud we assumed the peak flux measured in September 2004 (see Table 5.3) of 4.7×10^{-6}photons/cm^2/s. The inferred geometry of the clouds distribution is shown in Fig.5.6. Here, the cloud locations relative to Sgr A* are shown projected onto the Galactic plane with the y-axis representing the direction along the line of sight. The two parabolas correspond to curves of constant light path, representative of the leading and trail edge of the inferred outburst on Sgr A*, as discussed by Ponti et al. (2010). The panels in Fig.5.6 illustrate the impact of different assumptions with respect to the metallicity of the MCs.

We first consider the three clouds close to the AC (in projection), namely the N, S and SN clouds. Assuming a solar metallicity for the MCs, we infer line of sight displacements relative to Sgr A* ($d_{l.o.s}$) of 45, 9.9 and 41.4 pc for the N, S and SN knots (Fig.5.6, upper left panel). In this scenario we have the N and SN clouds placed in the region between the two parabolas and therefore currently illuminated by the Sgr A* outburst. A relatively constant 6.4-keV line flux is consistent with this model (assuming that Sgr A* remained in a relatively constant high state for the duration of the outburst). On the other hand, the cloud S is being crossed by the trailing edge of the irradiation burst. Therefore, one might expect that its Fe-K$_\alpha$ line flux to exhibit similar behaviour to that seen in the Sgr B2 and G0.11-0.11 MCs (Inui et al., 2009; Ponti et al., 2010, respectively), i.e., a steady decrease with time. Since such a decrease is not observed, there is clearly some inconsistency in the model based on the solar metallicity assumption. Moreover, we notice that the molecular complexes N and S are probably dense regions within the same larger MC (the -30 km/s MC, see Fig.14 in Wang et al., 2006): therefore, the relative separation of these two complexes by about 30-40 pc along the line of sight seems unlikely.

We therefore repeated the calculations assuming different Fe abundances; the values we considered are 1.25, 1.5 and 2 times solar ($d \propto Z^{0.5}$). The results of these calculations are detailed in Table 5.5, and illustrated in Fig.5.6. We find that for a metallicity higher than 1.5, the XRN model again has problems in explaining the constancy of the Fe-K$_\alpha$ lightcurves of all the clouds. In the case of Z=1.5, while the clouds S and SN lay well within the outburst region, the N cloud is at its leading edge (lower left panel), implying an increasing fluorescence signal (a behavior similar to the one measured from the *bridge* in Ponti et al., 2010). When Z=2 (lower right panel) although the S region lies within the outburst region, the incident ionizing front propagating from Sgr A* has not yet reached the N and SN knots.

For Z=1.25, the N, S and SN clouds all lie in the outburst region. In this case, and more generally for a metallicity range of 1.2-1.4 times solar, the XRN/Sgr A* outburst model can, in principle, explain the observed fluorescence both in terms of the observed line flux and the lack of strong variability. Within this framework, the separation of the N and S clouds is inferred to be between 30-40 pc which seems to be a highly unlikely scenario (as noted previously). However, given the uncertainty in measuring the optical depths of the individual clouds based on the available N$_H$ measurements, it is at least plausible that this unlikely cloud separation is a consequence of the limited precision of the optical depth estimates.

An alternative to the Sgr A* outburst hypothesis is that the energising photons are supplied by other nearby sources; indeed the GC region hosts numerous X-ray transient sources (Muno et al., 2005, 2006; Porquet et al., 2005a,b). We note that Koyama et al. (2003) have studied the diffuse Fe-K features from the MCs in the AC surroundings using Chandra which, through its sharp angular resolution, is better able to delineate the shape of the 6.4- keV bright regions. These authors first suggested that the line emission is probably due to sources other than a past intense flare on Sgr A*. Particularly for the N and S MCs, the different surface brightness of two different regions within the same MC (the -30 km/s MC, Wang et al., 2006) would need to be explained in terms of varying optical depths if the irradiation is from a single (relatively distant) bright source. Given the proximity of these clouds to the AC, the alternative scenario of bombardment by low-energy CR electrons certainly merits consideration (see below).

The peculiar case of the DX cloud

We now consider the DX cloud, which is *unique* amongst the GC MC that are 6.4-keV bright in that it has exhibited both an increase and decrease in its Fe-K_α flux. The variability measured in the DX MC is too fast to have been produced by the same Sgr A* flare which has been proposed to have illuminated the other XRN in the CMZ, since the inferred flare duration for the latter is greater than ten years. Notwithstanding this constraint, we have determined the location along line of sight of the DX cloud using the same method as employed above (see Table 5.5 for the detailed results). As we can see in all the panels of Fig.5.6, the $d_{l.o.s}$ value for this cloud spans the range 20-40 pc, putting it squarely within the outburst region for any of the metallicity assumptions. Clearly, a simple XRN/Sgr A* picture as the one proposed by Ponti et al. (2010) is not consistent with our results on the DX cloud; on the other hand, we note that there is a source of potential errors introduced by the uncertain measurement of the distance along the line of sight. However, the fast variability measured for the Fe-K_α line flux points to an origin other than Sgr A*, whose flare luminosity is supposed to be constant over the whole flaring period. In this cloud, the non detection of the Fe-K edge is due to the poor statistics.

In the XRN hypothesis, the energising source could also be a transient source, most likely an X-ray binary (XRB) system. The typical 2-10 keV luminosities reached by these X-ray point sources are of the order of 10^{36} and 10^{38} erg/s for a high-mass and a low-mass system respectively. Assuming an XRB embedded in the DX cloud (Ω=1 in the formula above), the required X-ray luminosity is $\sim 2\times 10^{35}$erg/s, compatible with a transient source hypothesis. On the other hand, if we consider the possibility that the primary source might have been a low-mass XRB lying in a region of high obscuration immediately behind the cloud, then it could be up to ∼10 pc from the cloud assuming a typical X-ray luminosity of 10^{38} erg/s. Given the X-ray luminosity requirements, we favor the scenario where a high-mass XRB is located inside, or closely behind, the cloud. Among such systems, transients sources can have orbital periods of years, with a flare timescale of some months. Of course, given the very limited information we have to date, we cannot exclude the contributions of more than one X-ray source or even perhaps a more exotic contribution to the fluorescence excitation from a short-lived particle bombardment episode.

EW of the Fe-K_α line

The relatively high values of the line EW measured in the three MCs closest to the AC are readily explained in terms of photoionization of the clouds by X-ray photons. In the context of the XRN model, the EW of the Fe-K_α line is expected to be high (about 1 keV), since the direct source of photoionization is not seen by the observer (e.g., Sunyaev & Churazov, 1998). Therefore, our results seem to confirm that some kind of X-ray reflection is working in the MCs close to the AC; however, the lack of a strong present-day X-ray source leaves open the discussion about the identity of the putative energizing source. Although the EW of the 6.4-keV line measured in the three MCs is about 1 keV, we notice that the error ranges (90% confidence level) are always consistent with an EW value of 0.6-0.7 keV; this is what expected from fluorescence to be induced by particle bombardment (subrelativistic electrons) in a MC with an Fe abundance of about twice the solar value. We therefore cannot exclude a priori one of the two ionization mechanisms only based on the present measurements of the EW.

Fe K absorption edge

We did not measure any Fe-K absorption edge at 7.1 keV; although the detection of such a spectral feature is challenging for N$_H$ values of the clouds in the range 10^{22}-10^{23}cm^{-2}, we notice that in other GC clouds with similar density an Fe-K edge has been measured (Ponti et al., 2010). We could only find upper limits to the optical depth of the absorption edge, listed in Table 5.4.

Spectral hardness

The shape of the non-thermal continuum associated with the production of the 6.4-keV line can also, in principle, provide a clue as to the nature of the excitation mechanism. Our analysis suggests that this non-thermal continuum has a very hard spectrum with a power-law photon index Γ=$1.0^{+0.1}_{-0.2}$. In the particle bombardment scenario, Γ=1.3-1.4 is expected for CR electron spectra typical of the GC region (e.g. Yusef-Zadeh et al., 2002), although a somewhat harder spectrum might be indicative of an unusual particle environment in the vicinity of the AC. Therefore, the hardness of the power law component might be best explained in terms of the bombardment of the clouds by cosmic ray particles emanating from the AC itself. Of course, the pure reflection scenario also predicts a reflected X-ray continuum significantly harder than that characteristic of the illuminating X-ray source (Revnivtsev et al., 2004; Terrier et al., 2010).

5.4.2 The CR particle bombardment hypothesis

An alternative explanation of the Fe fluorescence involves the interaction of CR particles (electrons and/or protons) with cold molecular matter. In this context the cross section for collisional ionization of Fe has its highest value in the energy range extending from the energy of the Fe-K edge (at 7.1 keV) up to a few MeV. Recently, two main ideas have been developed in order to explain the Fe fluorescent emission, namely bombardment by either electrons (Yusef-Zadeh et al., 2007a) or protons (Dogiel et al., 2009c). Valinia et al. (2000) first suggested that a distribution of low-energy CR electrons (LECRe) might be responsible for the Galactic Ridge X-ray emission. In their model, the hard X-ray continuum associated with the Ridge is produced by non-thermal bremsstrahlung as the LECRe interact with the material of the ISM. The low-ionization line emission from Fe and other metals is similarly produced through LECRe collisions with the neutral medium. The energies of the LECRe involved in this mechanism span the range 7.1 keV to ∼100 keV. In this setting, the flux of the 6.4-keV line is directly proportional to the density of the target material (in our case the MCs), and the in situ kinetic energy density of the LECRe, while the resulting EW of the Fe-K$_\alpha$ line spans the range 0.3-0.7 keV for metallicities from solar to twice the solar value.

The 6.4-keV photon production rate inferred from the results of Valinia et al. (2000) is

$$\mathrm{F}_{6.4} = \frac{4.8 \times 10^{-22}\mathrm{H}}{4\pi \mathrm{D}^2} \left(\frac{\mathrm{U}}{\mathrm{eV/cm^3}} \right) \ \mathrm{photons/cm^2/s},$$

where F$_{6.4}$ is the 6.4-keV line flux in units of photons/cm^2/s, D is the distance to emitting cloud (8 kpc for the GC clouds), U is the kinetic energy density of LECRe (in eV/cm^3) and H is the number of H atoms in the MC (see fourth column of Table 5.2).

Using the estimates of the number of H atoms given in Table 5.2, we have calculated the LECRe energy density required to explain the observed 6.4-keV fluxes (Table 5.3). We find that the energy density required in the N, S and SN knots is 61, 216 and 77 eV/cm^3. For the DX cloud, assuming the Fe-line flux to be 1.6$\times$10^{-6}photons/cm^2/s (i.e. the minimum in the lightcurve), the required energy density is 32 eV/cm^3. All these four values have to be divided by two in case the Fe abundance we assume is twice the solar value (as discussed above). For comparison, Valinia et al. (2000) found that the mean LECRe energy density required to explain the Galactic Ridge was 0.2 eV/cm^3; moreover, using the same model, Yusef-Zadeh et al. (2002) found that the Fe-K$_\alpha$ line flux measured from the G0.13-0.13 MC requires a LECRe energy density of 150 eV/cm^3, a value very similar to what found for the AC MCs.

A significant enhancement of the CR flux in the GC region compared to the Galactic plane is perhaps to be expected. Also energetic particles might well be accelerated in the shocked stellar winds which characterise the core region of the AC (White, 1985; Yusef-Zadeh et al., 2003), potentially resulting in a greatly enhanced energy density in the vicinity of the cluster. The fact that the 6.4-keV line flux measured from region S is significantly higher than that from knot N could be a consequence of the stellar distribution within the cluster. As shown first by Yusef-Zadeh et al. (2002) and later by Law & Yusef-Zadeh (2004), the southern component of the cluster is populated by strong stellar-wind sources, which are also detectable at radio wavelengths (Lang et al., 2001). These massive early-type stars could also be present in binary systems, and be the origin of the X-ray flaring activity recently discovered by Capelli et al. (2011a). Massive interacting binaries are efficient in producing X-ray emission in the shock fronts within the winds and also in accelerating CRs.

In a variation on this theme, Wang et al. (2006) proposed the interaction of the -30 km/s MC with the AC to be the origin of the Fe fluorescent emission. These authors found that the -30km/s molecular complex is moving towards the AC with a relative velocity of ∼120 km/s. In this picture, particles are accelerated in reversed shocks through efficient Fermi first order mechanism, and gain enough energy to be able to ionize Fe atoms within the cloud.

In the case of the DX cloud, we discovered the *fastest* variability ever found for a GC MC. Given that the timescale of the variability is comparable to the size of the cloud, this would seem to completely rule out bombardment by sub-relativistic particles as the origin of the increase in the Fe-K$_\alpha$ line flux measured from this complex. However, it is at least plausible that the underlying base level of the 6.4-keV lightcurve could represent a relatively constant particle contribution to the fluorescence budget. The presence of high energy particles in this cloud may be inferred from radio continuum observations at 20 cm (see Fig.1b in Yusef-Zadeh et al., 2002) in which non-thermal filaments propagate westwards from the Radio Arc into the general region of this cloud.

The nature of the non-thermal radio filaments in the GC region is still under debate. The concentration of these strong radio features in the inner Galaxy may well be related to the peculiar high energy activity of this unique region (Yusef-Zadeh, 2003). Many attempts have been made to explain the formation of such structures, involving all the likely high energy sources connected with the GC region, that is the SMBH Sgr A*, massive wind binaries, Galactic winds and gas clouds. A recent suggestion is that the origin of these filaments might be due to the presence of many young and massive stellar clusters in the central region of the Galaxy (Yusef-Zadeh, 2003). Whatever the origin of the radio filaments, their presence in the region suggests that cloud fluorescence induced by particle bombardment must be present at some level (i.e. Fukuoka et al., 2009). Potentially, X-ray flaring events of the sort recently discovered in the AC (Capelli et al., 2011a), might also induce some variablity in the local LECRE energy density, which could in turn impart variability in the fluorescence signal, albeit delayed and smeared out relative to the activity in the primary source.

Recently, Dogiel et al. (2009c) have suggested that at least some of the Fe-K$_\alpha$ line emission from MCs in the CMZ can be produced by the interaction of high energy protons (with energies in the range of several hundred MeV) with the molecular target. This model naturally explains the presence of both the non-thermal components in the spectrum of the GC hard X-ray emission (Koyama et al., 2009). As in the LECRe model, this scenario has some difficulties in accounting for the rapid variability of the 6.4-keV line found in some MCs in the inner GC region, including the DX cloud.

LECRe with E$\sim$100 keV can be stopped by matter with column densities of about 10^{22} H atoms/cm^2 (Tatischeff, 2003). Considering the sizes and column densities of the MCs quoted in Table 5.2, we can calculate that LECRe loose their energy within depths that are at most half the cloud size. Similarly, (Dogiel et al., 2009c) estimate that high energy protons in the GC region typically travel for 0.1-0.3 pc before being stopped through interactions with the ISM. These estimates imply that particle-induced fluorescence and other interactions will occur only in the outer shell of a dense cloud. Both LECRe and high energy protons lose most of their energy in heating the ISM rather than in producing non-thermal continuum emission or fluorescence photons. Yusef-Zadeh et al. (2007b) argue that the reason the temperature of the MCs in the CMZ is higher (T$\sim$100-200 K) than that measured for MCs in the Galactic plane (about 20 K) is due to CR particle heating. In fact, the ionization rates modelled for LECRe and high energy proton bombardment of MCs are in good agreement with the temperature enhancements which are actually measured (Yusef-Zadeh et al., 2002; Dogiel et al., 2009c). Furthermore, both Huettemeister et al. (1993) and Rodríguez-Fernández et al. (2001) measured temperature gradients in most of the MCs in the GC region; this is a natural consequence of the interaction of subrelativistic electrons and protons largely with the surface layers of the MCs.

Chapter 6

Discovery of X-ray flaring activity in the Arches cluster

Original publication: R. Capelli, R.S. Warwick, N. Cappelluti, S. Gillessen, P. Predehl, D. Porquet, S. Czesla, *Discovery of X-ray flaring activity in the Arches cluster.* The content of this chapter was published by the International scientific Journal Astronomy & Astrophysics (Capelli et al. 2011, A&A, 525, L2); as first author, my contribution to this work included the data reduction and analysis, as well as the following scientific interpretation of the results. The other authors contributed with the review of the draft and comments and suggestions regarding the scientific interpretation of the results, which helped to improve the work.

Abstract: We present a study of the Arches cluster based on XMM-Newton observations performed over the past 8 years. Unexpectedly, we find that the X-ray emission associated with the cluster experienced a marked brightening in March/April 2007. We investigate the origin of both the X-ray continuum emission emanating from the star cluster and the flare. To study the time variability of the total X-ray flux, we stacked the PN and MOS data of observations performed within a time interval of a few days leading to the detection of the flaring episode. We then constructed two spectral datasets, one corresponding to the flare interval (March/April 2007) and another to the normal quiescent state of the source. The X-ray light curve of the Arches cluster shows, with high significance (4σ), a 70% increase in the X-ray emission in the March/April 2007 timeframe followed by a decline over the following year to the pre-flare level; the short-term duration of the flare is constrained to be longer than four days. The temperature and the line-of-sight column density inferred from the flare spectrum do not differ from those measured in the normal activity state of the cluster, suggesting that the flux enhancement is thermal in origin. We attribute the X-ray variability to in situ stellar activity: early-type stars may be responsible for the flare via wind collisions, whereas late-type stars may contribute by means of magnetic reconnection. These two possibilities are discussed.

6.1 Introduction

Three massive star clusters are located at the Galactic center (hereafter GC) region: the central (IRS 16) star cluster, the Arches cluster (hereafter AC), and the Quintuplet cluster (e.g., Morris & Serabyn, 1996). Whereas all three are very bright in the infrared band (e.g. Becklin & Neugebauer, 1975; Nagata et al., 1995), their X-ray properties differ markedly. Both IRS16 and the Quintuplet cluster are not particularly bright in X-rays with $L_X \sim 10^{33}$erg/s (Baganoff et al., 2003; Law & Yusef-Zadeh, 2004). In constrast, the AC has a relatively high X-ray luminosity ($L_X \sim 10^{34}$erg/s)(e.g. Yusef-Zadeh et al., 2002). Although the total mass of each of these clusters is similar at about 10^4 $M_\odot$ (Figer, 2004), the size of the clusters are different, with the AC being the most compact. The X-ray diffuse emission from the AC has been investigated in a number of published papers over the last decade (i.e. Yusef-Zadeh et al., 2002; Wang et al., 2006; Tsujimoto et al., 2007). All these studies confirm the co-existence in the cluster of both thermal and non-thermal radiation. The former is thought to be due largely to multiple interactions between the strong winds from massive stars, with the high stellar concentration in the AC providing an explanation of why its X-ray luminosity is enhanced (e.g. Cantó et al., 2000; Raga et al., 2001). Irrefutably, the AC, which is the densest cluster in the Galaxy with a core density of 10^5 $M_\odot/pc^3$, provides an excellent opportunity to study stellar processes, within the environment of a massive star cluster, that lead to particle acceleration and X-ray emission. The study of these massive star clusters is of particular interest in the context of the chemical enrichment of the GC region and their overall contribution to the high energy activity that characterises the innermost zone of the Galaxy.

6.2 Observations and data reduction

We selected archival XMM-Newton observations of the Galactic center region targeted at Sgr A*. We reprocessed data from both the PN and MOS cameras (Strüder et al. (2001), Turner et al. (2001)) with the tasks EPPROC and EMPROC in the Science Analysis Software version 9.0. The main properties of the XMM-Newton observations employed in the present work are reported in Table 6.1. We selected good time intervals (GTI) corresponding to periods of relatively low internal background. For this purpose, we compiled the 10–12 keV lightcurve of the full field of view and selected the time intervals for which the count rate was lower than a certain threshold. Since the selected observations were performed in different conditions of internal/particle background and orbital phase, we investigated all the lightcurves independently and selected an appropriate threshold count rate for each. The thresholds used in screening the data are reported in Table 6.1; in practice, these thresholds were selected so as to exclude all the peaks in the 10–12 keV full-field lightcurve. Throughout our analysis, we have only selected single and double events (PATTERN$\leq$4) for the PN and up to quadruple events for the MOS1 and MOS2 (PATTERN$\leq$12) cameras. Similarly, only events tagged as real X-rays (FLAG==0) were utilised.

Table 6.1: The selected datasets identified by means of both the OBSID and the observation date. For each instrument, we report the threshold in the 10-12 keV lightcurve (counts/s) used for GTI selection, the total GTI exposure (ks), and the nominal observation duration (ks).

OBSID	Obs Date yyyy-mm-dd	PN cut/GTI/exp	MOS1 cut/GTI/exp	MOS2 cut/GTI/exp
0111350101	2002-02-26	0.8/38.590/40.030	0.5/42.262/52.105	0.5/41.700/52.120
0202670501	2004-03-28	2.0/13.320/101.170	1.0/33.070/107.784	1.0/30.049/108.572
0202670601	2004-03-30	2.0/25.680/112.204	1.0/32.841/120.863	1.0/35.390/122.521
0202670701	2004-08-31	1.0/59.400/127.470	0.5/80.640/132.469	0.5/84.180/132.502
0202670801	2004-09-02	1.0/69.360/130.951	0.5/94.774/132.997	0.5/98.757/133.036
0402430301	2007-04-01	1.5/61.465/101.319	0.8/61.002/93.947	0.8/62.987/94.022
0402430401	2007-04-03	1.5/48.862/93.594	0.8/40.372/97.566	0.8/41.317/96.461
0402430701	2007-03-30	1.5/32.337/32.338	0.8/26.720/33.912	0.8/27.685/33.917
0505670101	2008-03-23	1.25/74.216/96.601	0.5/73.662/97.787	0.5/74.027/97.787
0554750401	2009-04-01	1.0/30.114/38.034	0.5/32.567/39.614	0.5/33.802/39.619
0554750501	2009-04-03	1.0/36.374/42.434	0.5/41.376/44.016	0.5/41.318/44.018
0554750601	2009-04-05	1.0/28.697/32.837	0.5/37.076/38.816	0.5/36.840/38.818

It was evident that the source was seen in an anomalous state in the three 2007 observations (separated by four days). For this reason, we considered the March/April 2007 observations (i.e., the flare dataset) separately from the other observations. The region considered for the accumulation of the count rate spectrum of the source is an ellipse centered at R.A.=17:45:50.358 DEC=-28:49:20.08, with axes of 0.32'x0.30'. We chose an elliptical region in order to enclose most of the X-ray diffuse emission in the AC (see contours in Fig.2 in Yusef-Zadeh et al., 2002). Similarly a circular region of radius 0.4', centered on R.A.=17:45:44.081 DEC=-28:49:25.72 was used to determine the background. Spectra corresponding to multiple observations were produced by stacking the data, using the tools MATHPHA, ADDRMF and ADDARF. The channels in each spectrum were grouped with the GRPPHA tool in order to have a minimum of 20 counts/bin, validating the use of the χ^2 statistic.

6.3 Results

6.3.1 The X-ray lightcurve

To search for evidence of temporal variability in the X-ray emission from the AC, we constructed a "long-term" X-ray lightcurve based on six observation epochs, which in the majority of cases encompassed more than one individual observation. These were February 2002 (1 obs), March 2004 (2 obs), August/September 2004 (2 obs), March/April 2007 (3 obs), March 2008 (1 obs), and April 2009 (3 obs) - see Table 6.1.

The resulting 2–10 keV lightcurve is shown in Fig.6.1. Here the flux values are derived from model fits to the stacked spectra for each epoch using the average spectrum for the normal state (see below); more specifically, the points are the weighted mean of the PN and MOS values, corrected for absorption. A high state or flaring episode is evident in the 2007 measurements. As a check, we also considered the net source count rates measured in the individual cameras, which confirmed that this flaring is very likely a feature of the lightcurves. To quantify the statistical significance of this flare, we compared the weighted mean of the other five measurements in Fig.6.1 of 1.53±0.07×10^{-12} erg/cm^2/s with the flux measured in March/April 2007 of 2.4±0.2 ×10^{-12} erg/cm^2/s; the variability is significant at the level of 4σ.

To check whether the observed flare was produced by systematics in the background, we also built the lightcurve of the flux measured from the region used for the background (the red points in Fig.6.1). For these data, the χ^2_{red} with respect to the weighted mean of the measurements (3.4±0.4×10^{-13}erg/cm^2/s) is 0.7, fully consistent with a constant background.

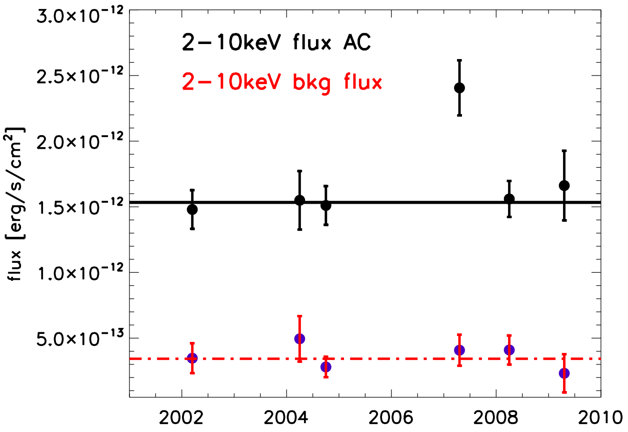

Figure 6.1: The 2–10 keV X-ray lightcurve of the AC extending over an eight year period. The horizontal line is the weighted mean excluding the March/April 2007 flare. The red points show the lightcurve for the background, where the weighted mean is shown with a dashed red line.

We have also studied the 2–10 keV lightcurve of the individual March-April 2007 observations to look for evidence of short-term variability during the episode of enhanced activity. The result of this investigation is shown in Fig.6.2. There is no clear evidence of a trend in this full lightcurve; a constant fit to the data gives a mean count rate of 0.059±0.001 cts/s, with a χ^2_{red}=1.1. Although there are some low-level short-term features apparent in the individual observations, we conclude that these are most likely due to background-subtraction errors, since similar effects are apparent in the lightcurves of other sources in the field of view. We conclude that the duration of the high state activity is longer than ∼4 days.

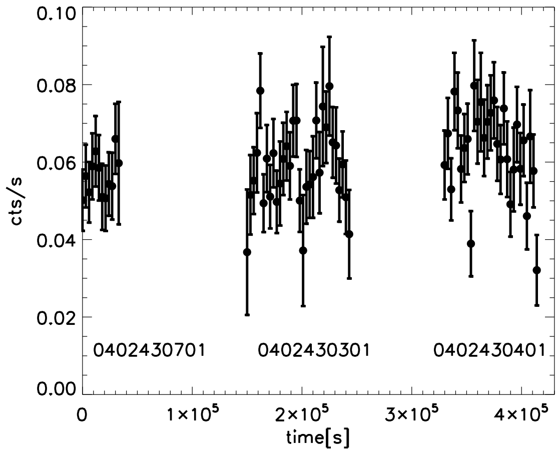

Figure 6.2: The lightcurve from the March-April 2007 observations. The energy range is 2–10 keV and the time binning is set to 3 ks.

6.3.2 X-ray spectral analysis

We first performed an analysis of the stacked PN and MOS X-ray spectra pertaining to the normal state of the AC. The spectral model comprised a collisionally ionized plasma (APEC, Smith et al., 2001) plus a non-thermal hard tail modeled by a power-law continuum with a photon index Γ. In the present investigation, we found it advantageous to fix Γ to a value of 1, thereby avoiding potential biases in the spectral modeling of multiple datasets with a different balance between the thermal and non-thermal contributions. This approach is consistent with earlier studies that generally found Γ to be in the range 1-1.5 (e.g., Wang et al., 2006; Tsujimoto et al., 2007) and consistent with the power-law slope characterising bright 6.4 keV fluorescent line-emitting regions in the vicinity of the AC (which will be the subject of a later study). In the analysis, we also fixed the metallicity of the thermal plasma at 2 $Z_\odot$ (e.g., Wang et al., 2006), since the spectral fitting of both the stacked and the single datasets did not usefully constrain this parameter. In this context, we note that there is strong evidence that the diffuse plasma in the GC region has a super-solar metallicity (e.g., Tanaka, 2002; Koyama et al., 2007a). Two gaussian lines were included to account for the neutral (or near-neutral) Fe K_α and Fe K_β lines, at 6.4 and 7.05 keV respectively, the K_β/K_α flux ratio being tied to 0.11. Finally, all the components were subject to interstellar absorption (WABS model in XSPEC, Morrison & McCammon, 1983).

The results of the joint fitting of the PN and MOS spectra for the normal state of the source are reported in the second column of Table 6.2 and the corresponding spectra are shown in Fig.6.3 (left panel). The best-fit temperature of the cluster was found to be kT $=1.7\pm0.1$ keV, in good agreement with that previously measured with Suzaku (Tsujimoto et al., 2007) and Chandra (Wang et al., 2006). Moreover, the resulting total 2–10 keV flux is $5.3\pm0.5\times10^{-13}$ erg/cm^2/s ($1.5\pm0.1\times10^{-12}$ erg/cm^2/s absorption corrected), which translates into a luminosity of 3.8±0.4×10^{33}erg/s. To quantify the respective contributions of the thermal and non-thermal emission to the spectrum, we measured the fluxes associated with the different continuum components in the best fit model. For the 2–10 keV band, the division was into an 85% contribution by the thermal emission and a 15% one by the hard non-thermal tail. Both the thermal and non-thermal components are very likely to be manifestations of in situ activity within the AC. More specifically, shocks produced by strong colliding stellar winds can both heat the plasma and supply high energy particles. Law & Yusef-Zadeh (2004) proposed that energetic electrons within the cluster might be able to upscatter IR radiation from stars via the inverse Compton effect; in this case, the power-law component should contribute about a sixth of the total flux, in excellent agreement with the measurements.

Table 6.2: Results of the spectral fitting for the normal state and the net flare spectrum of the AC. The values are the weighted mean of the PN and MOS measurements. The fluxes (2–10 keV) are in photons cm^{-2} s^{-1}.

	NORMAL	FLARE
$N_H(10^{22}cm^{-2})$	10.4±0.9	10.2±2.1
$kT_{APEC}(keV)$	1.7±0.1	1.8±0.3
$flux_{APEC}(10^{-5})$	5.4±0.4	5.2±0.9
Γ_{POW}	1.0	1.0
$flux_{POW}(10^{-5})$	1.3±0.1	-
$f_{Fe_I K_\alpha}(10^{-6})$	1.4±0.7	-
$flux(10^{-5})$	7.0±0.5	5.2±0.9
χ^2/dof	234/1144	246.5/852

Given the discovery of significant variability in the X-ray flux from the AC, the next step was to investigate the spectrum of the enhancement. For this, we used the stacked 2007 dataset as the source event file, with the background taken to be the source spectrum of the AC during its normal state. The PN and MOS spectra corresponding to the flare (net flare spectra) are presented in the Fig.6.3 (right panel), in comparison to the normal state spectrum (left panel). The main difference between the spectra of the two states of the AC is in the 6.4 keV fluorescent line from neutral (or near-neutral) Fe; the flare spectrum does not show significant emission at this energy. This clearly indicates that the 6.4 keV Fe K_α line has a different origin to the higher ionization 6.7 keV iron line. This observational evidence points to a thermal origin for the flare. This was confirmed when we attempted to fit the flare spectra with the same model as applied to the normal state data. For the flare, we found that the nonthermal power-law and the low-ionization state lines of Fe (at 6.4 and 7.05 keV) were then no longer required. The flare spectrum is described well by a thermal plasma with kT=1.8±0.3 keV and a total flux of 3.7±0.6×10^{-13} erg/cm^2/s; in terms of 2–10 keV X-ray flux, the flare represents an increase over the normal state activity of about 70±13%.

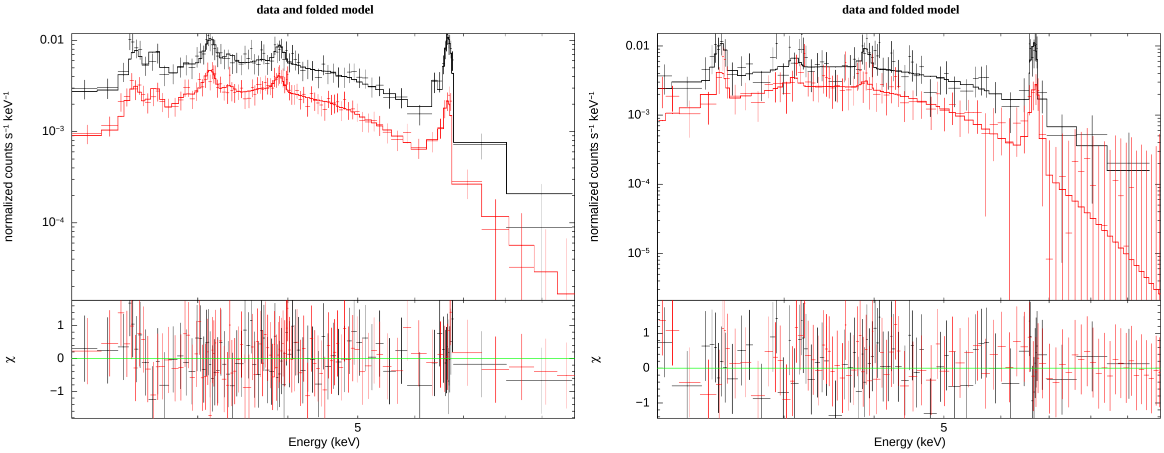

Figure 6.3: The 2–10 keV X-ray spectra of the AC as measured in the PN (black) and MOS (red) cameras. *Left panel:* The spectrum measured in the normal state. *Right panel:* The net flare spectrum measured during the flaring episode. In both cases, the best fitting spectral model and the corresponding residuals are also shown.

We highlight that the temperature and the N_H values inferred for the flare spectra are in excellent agreement with the values derived from the normal state spectrum (see Fig.6.3 and Table 6.2). It would seem that the variability in the cluster is produced by an increase in the intensity of the thermal emission, while the other physical observables, namely the temperature and N_H, remain unchanged. The emission measure (EM) of this X-ray activity (the flare component) was estimated from the normalization of the APEC component to be some 1.2×10^{57}cm^{-3}.

6.4 Discussion

We have investigated the X-ray properties of the AC and reported the first detection of significant variability in its hot thermal emission. The bulk of this component is thought to arise from the thermalization of the strong winds expelled by massive stars. Cantó et al. (2000) calculated the expected temperature of such a cluster wind to be

$$\mathrm{kT_{cluster}} = 1.3\left(\frac{\mathrm{v_w}}{10^3\ \mathrm{km}\cdot\mathrm{s}^{-1}}\right)^2 \mathrm{keV},$$

where v_w is the terminal velocity for the stellar wind, which is assumed to be the same for all the stars within the cluster. The temperature we measured in the AC is 1.7±0.4 keV, which requires a terminal velocity of 1100-1200 km/s, in good agreement with the actual wind velocities reported by Cotera et al. (1996). In the normal state of the AC, the EM of this plasma is $1.4\pm0.3\times10^{57}$cm^{-3}. If we model the AC as a sphere of 0.7 pc radius and set $n_e \sim n_H$, the inferred electron density is 1-10 cm^{-3}. This value again compares very well to theoretical estimates obtained by modeling the X-ray emission of dense clusters of massive stars (see middle panel of Fig.3 in Cantó et al., 2000). Using the superior spatial resolution of the Chandra telescope, Yusef-Zadeh et al. (2002) identified three distinct spatial components in the AC; components A1 and A2 were found to have strong thermal emission, whereas A3 component was found to be extended and more elongated towards the south-west of the cluster core. Overall the diffuse emission is characterized by a highly significant Fe K_α line at 6.4 keV corresponding to neutral or low ionization gas. Because of the lower angular resolution of XMM-Newton, we could not resolve these three components and study them separately but simply analyzed a composite spectrum. In a similar way, Tsujimoto et al. (2007) used Suzaku data to study a 1.4 arcmin wide region centred on the cluster and derive spectral parameters very similar to those reported here.

The non-thermal radiation associated with the AC is most likely attributed to the presence of a sea of cosmic rays permeating the whole region within the cluster and the surroundings; Valinia et al. (2000) showed that the diffuse emission from the Galactic ridge can be explained in terms of low energy cosmic rays (LECRs) producing both the continuum and the low ionization lines from the different elements. However, the slope of the non-thermal continuum emission found by these authors is about 1.3-1.4, somewhat steeper than the value we adopt. This difference may reflect the extreme conditions in the vicinity of the AC itself. The collisions between powerful stellar winds with terminal velocities at or in excess of 1200 km/s can create shocks that accelerate CRs up to keV energies, thereby leading to a flattening of the spectrum in the high energy domain via either bremsstrahlung or inverse Compton emission.

Here we report an unexpectedly high state of activity in the AC, although the XMM-Newton off-axis PSF does not allow us to directly locate the flare emission within the spatial substructure observed in the AC with Chandra (Yusef-Zadeh et al., 2002). The spectrum of the AC in this flaring state is well modeled as a hot plasma with $kT=1.8\pm0.3$ keV. This, and the presence in the spectrum of the high ionization lines of elements such as S, Ar, Ca, and Fe implies a stellar origin for the observed flux increase. The longest detected stellar coronal flares to date had a duration of nine days. For the AC, we can set a lower limit to the duration of the enhanced luminosity of $\sim$4 days. This is consistent with a coronal origin for the flare. On the other hand, we note that if the flare duration were a few months, its origin would be very unlikely to be coronal. Assuming a distance to the GC of 8 kpc (Gillessen et al., 2009), the estimated EM for the AC flare is 1.2×10^{57} cm^{-3}, very significantly higher than the values typically measured in stellar X-ray flares ($\sim10^{55}$ cm^{-3}) associated with late-type stars (e.g., Güdel, 2004; Güdel & Nazé, 2009). The X-ray flares from late-type stars observed to date exhibit a strong correlation between the peak temperature and the EM. Aschwanden et al. (2008) found that the EM in a stellar flare is proportional to $T^{4.5}$; according to this relation, an EM of 1.2×10^{57} cm^{-3} yields a temperature well above 10^8K (8.6 keV), and well beyond the value measured in the AC flare (1.8 keV corresponding to $\sim2\times10^7$K). We therefore dismiss the late-type star hypothesis for the origin of the flare.

An alternative scenario that could account for the detected variability entails early-type stars, possibly in binary configurations. Either an orbital modulation of the system or a sudden eruption by one star might produce the observed high state activity. In both cases, the density and the velocities of the colliding stellar winds might change, thus producing an enhancement in the X-ray flux. The X-ray emission arising from equally strong colliding winds is inversely proportional to the binary separation (D^{-1}); for stellar parameters such as those found in the AC ($\dot{M}$ $\sim10^{-5}M_\odot$/yr and $v_\infty\sim1200$ km/s) the X-ray luminosity created by colliding winds is about 10^{32-33}erg/s, for $D\gtrsim10$-500AU. In this context, it is plausible that the enhanced X-ray activity might mark the periastron passage of a system with an eccentric orbit. Mauerhan et al. (2010) reported X-ray emission from massive stars in the GC region. Among the sources studied in their sample, four are located in the AC, two of them being inside the XMM PSF and good candidates for the location of the flaring event. Another example of variability involving early-type stars can be found in the binary system η Carinae; this has been measured to be variable with an increase in the X-ray luminosity of about 80%. In this supermassive colliding wind binary, the X-ray luminosity reaches 10^{34} erg/s and the flare timescales range between a few days and about 100 days (Moffat & Corcoran, 2009). A likely explanation of this variability is the interaction of clumpy winds; this process has been observed to produce an X-ray luminosity 1.8 times brighter than the normal level, with a spread in the duration of the high state activity between $\sim$3 and 50 days, characteristics that might equally well describe the AC flare.

Here we propose that the colliding wind binary hypothesis provides the most plausible explanation of the AC flare. On the basis of the lightcurve, the upper limit to the duration of the measured flare is about four years. Assuming a wind velocity of 1200 km/s, the linear size of the region intersected by a propagating density enhancement over a four year period is about 0.005 pc, whereas the mean distance between stars in a dense environment such as the AC core can be estimated to be $\sim$ 0.1 pc. This argument lends further support to the stellar origin of this X-ray activity. Presumably, these interactions are quite probable in a dense cluster such as the AC, especially in the southern component, where the highest concentration of massive colliding wind binaries has been reported (Yusef-Zadeh et al., 2002).

Chapter 7

Conclusions and Outlook

This thesis work reports on the research carried out by the author in his Ph.D., and presents its main scientific results. We have investigated the features of the Fe-K$_\alpha$ line emission at 6.4 keV arising from dense MCs in the GC region, discussing them in the context of the two physical mechanisms which can produce this fluorescent line: illumination by a bright X-ray source and cosmic ray bombardment. Moreover, a temporal and spectral study of the properties of the Arches cluster has been performed. Here following, we write the conclusions to each of the three Chapters, discussing the importance of the studies we have been pursuing in the context of the Galactic Centre science and Galactic Astronomy in general, suggesting some important guidelines for future work on these topics.

7.1 The recent low AGN activity of Sgr A*

In Chapter 4 we examined the Fe-Kα topology and variability in the molecular clouds close to Sgr A* in order to understand and constrain the primary energising source of the Fe fluorescence. We collected and analized all the archival XMM-Newton observations of the Fe-Kα bright filaments within ∼15 arcminutes of the Galactic Centre (∼8-30 pc), and performed a temporal and spectral study of these MCs. Our results can be summarised as follows:

- *Clouds identity*: we found that most of the filaments studied in this paper are unlikely to be independent structures dislocated along the line of sight. The only certain molecular counterpart to the bright Fe-K$_\alpha$ knots is G0.11-0.11. Presuming that regions B2, D and E belong to the same molecular complex, the observed variability pattern is difficult to be explained in a pure XRN/Sgr A* scenario.

- *Fe-K$_\alpha$ topology*: the diffuse and filamentary structure of the Fe-K$_\alpha$ line emitting regions has been confirmed. We have studied the temporal and spectral properties of several MCs; three of these are newly studied (regions C, DS1 and DS2).

- *Fe-K$_\alpha$ variability*: significant variability is seen from the selected molecular clouds, although the pattern is not a simple one. The Fe-K$_\alpha$ flux from G0.11-0.11 is declining.

On the other hand filaments in the region 0.05°<l<0.1° and -0.1°<b<-0.05°, show an increasing 6.4-keV line flux measured with a confidence higher than 7σ. The overall pattern of variability well agrees with previous works. Only in the MC B1 we measured a decrease of the Fe-K$_\alpha$ line flux, in contrast with what found previously in other works.

- *Fe-K$_\alpha$ surface brightness*: we measured the surface brightness of the 6.4-keV line to be of the same order of magnitude in all the molecular filaments we have studied. The variability only involves a factor of two. This result is difficult to interpret in the XRN/Sgr A* scenario, since the surface brightness of the filaments might be expected to decline with distance from the putative source, Sgr A*. This issue is solved in case the X-ray luminosity of the illuminating source is not the same for all the clouds we have considered; indeed, our results for the X-ray light curve of Sgr A* go in this direction.
- *Fe-K$_\alpha$ EW and Fe-K edge*: we measured a high value of the EW of the 6.4-keV line from all the MCs considered in this study. Our results suggest that the Fe fluorescence is mainly produced by photoionisation of the MCs. Moreover, almost all the clouds show an absorption feature at the Fe-K edge energy of 7.1 keV, some of them very high, inconsistent with an Fe fluorescence to be due to a pure particle ionization.
- *Spectral hardness*: the slope of the underlying continuum is always measured to be very hard; moreover, the values for this spectral parameter among the different clouds are not consistent with one another. All our results well fit in a reflection scenario, where the shape of the reflected continuum strongly depends on the local N$_H$ of each MC.
- *The N$_H$ in the MCs*: in Chapter 4 we showed a new method for calculating the local N$_H$ inside the MCs. This is based on the measurement of the optical depth of the absorption feature at 7.1 keV. Our results better conciliate the theory with the observations of the Γ-N$_H$ relation; the column densities so calculated result in most of the cases significantly higher than the one inferred in previous works, which made use of different measurement techniques.
- *Fe abundances*: by measuring the EW of the Fe-K$_\alpha$ line we calculated the mean Fe abundance within the MCs we studied to be 1.56 ± 0.19 times the solar value. This result very well agrees with the general agreement of an higher metallicity of all the ISM phases in the GC region.
- *The role of Sgr A**: studying the 6.4-keV line emission properties in the MCs of the inner 30 pc of the GC region, we proposed a model for the X-ray emission of Sgr A* in the last ~200 years. Our results show a decreasing trend which might be staggered by sudden hiccups described by a lower X-ray luminosity, and/or a proper multiflare scenario, with a decreasing peak luminosity of these sudden flaring events in time, from $\sim10^{39}$ erg s^{-1} of 150 years ago to 10^{37-38} of 130-70 years ago.

- *Low surface brightness 6.4-keV line emission*: thanks to the large effective area of XMM-Newton, we found that the correlation between the TeV emission and the Fe K_α line emission observed in the inner CMZ involves regions more extended than the size of the most dense MCs. We measured a diffuse, low surface brightness emission to the East of Sgr A*, which seems to permeate the whole region between the Sgr A East SNR and the giant radio arc; this fluorescence component might be common to all the lightcurves which show an increase of the measured Fe-K_α line flux. We have also shown that this diffuse low surface brightness 6.4-keV line emission correlates quite well with the contours of the brightest features seen in TeV γ-rays. This fact makes reasonable to suggest that CRs might play an important role in the ionisation of both the bright K_α filaments and the low surface brightness diffuse emission at 6.4-keV within the studied region. The further investigation of this component is essential to better calculate the level of X-ray emission needed from the primary source of ionising photons.

- *The C cloud - a different XRN?*: we found that the 6.4-keV line flux variability measured from the region C could also be associated with the transient X-ray source XMMU J174554.4-285456. In this scenario, the Fe fluorescence in this complex is composed of a steady non-zero level produced by the interaction of subrelativistic CR with the ambient gas, and an X-ray irradiation on the top. This would be the second XRN found in the GC region where an identification with a transient source has been found (Capelli et al., 2011b).

- *Cosmic ray variability*: the variabilities found in the molecular filaments studied in this paper are very difficult to explain in pure particle bombardment scenario. However, the lightcurves of the 6.4-keV line flux are all compatible with a variable incident CR flux. In the case of the region B2, D and E the CR pipes should move perpendicular to the direction of the apparent superluminal propagation. The open issues related to this theory are the high metallicity that the molecular cloud must have in order to produce the observed high equivalent width of the 6.4-keV line and the energetics of the electrons hitting the molecular matter. Further temporal studies of the non-thermal radio filaments/threads which populate the inner CMZ are needed to completely rule out the CR bombardment as a contributor to the Fe-K_α line flux variability.

- *Supernovae products*: we exclude the interaction of supernovae fragments embedded within a molecular cloud as the energising source of Fe fluorescence, since the variability timescales are too short to be produced by heavy, slowly moving fragments.

The importance of this study is clear; the SMBH at the Galactic Centre is known to be a dormant nucleus, which only shows some short faint flares due to the magnetic instabilities in the accreted gas stream (however very small compared to the hypotesised AGN life). The discovery of a relatively recent AGN activity opens the question on the nature of the quiescent nature of our SMBH, on the whole history of the Galaxy and, more specifically, the nature and the origin of structures like the gigantic bubbles recently discovered with the Fermi γ-ray satellite and the peculiar state of magnetic streams and highly shocked ISM in the inner few hundred parsecs of the Milky Way. However, with our dataset we cannot completely uncover the mistery. It will be of great importance in the near future to further monitor the Fe-K_α line emission from the MCs in the CMZ to better characterise (or even exclude) the past activity of Sgr A*, carrying out complementary studies in different energy domains, from the radio band (continuum and lines) up to the TeV regime, in order to model the recent past activity of Sgr A* and to fully chart the influence of cosmic rays on the Fe fluorescence phenomenon. Unlike other issues in modern astrophysics, we expect that the possibility of a recent low AGN activity at the GC will be successfully clarified in the next few years, thanks to the new X-ray observatories which will be launched between 2012 and 2014 by the NASA and JAXA agencies, i.e. NuSTAR and ASTRO-H; specifically, NuSTAR will finally put into focus the hard X-ray universe, with unprecedented spectral coverage (5-80 keV) joint to a spatial resolution of about 10 arcsec. A part of the NuSTAR core program is a survey of the GC region, with several hundreds of ksec observations of the CMZ planned for every year of the mission; this dataset will provide a unique monitoring of the Fe-Kα line from the most massive molecular clouds in the GC region together with the flux of the hard X-ray continuum reflected the same clouds. These two features, as explained in Chapter 4, are the tracers of the past activity of the SMBH at the GC; if NuSTAR will observe the same temporal behaviour of the Fe fluorescent line and the reflected continuum, and this will be compatible with the 3D distribution of the MCs in the CMZ and the X-ray lightcurve suggested for the Sgr A* activity (like the one we suggested in Chapter 4), this will be the definitive proof that the Milky Way hosts at its centre a dormant nucleus, which has been active in the recent past and just turned off shortly before the dawning of X-ray Astronomy. The other very important contribution to the science of the GC region, and especially on the XRNs as traces of X-ray activity of the SMBH, will come from ASTRO-H satellite; in fact, this space observatory will have onboard the first X-ray calorimeters, which can achieve a spectral resolution of about 3-5 eV. When compared with the best spectral resolution currently achievable, about 130-150 eV, this is an enormous improvement, and this will give huge benefits to the physical studies which will be performed with ASTRO-H observations. For what concerns the topics discussed in this thesis, ASTRO-H will be able to definitely proof the existence of a contribution to the total Fe-Kα fluorescent signal given by bombardment of low energy cosmic rays. This aim will be achieved in basically two ways: i. if the 6.4-keV line is produced by collision of a subrelativistic particle with an Fe atom, the intrinsic width of this line will be broaden because of multiple simultaneous ionisations. ii. If a significant contribution to the fluorescent signal is produced by protons, this will be seen in XRN spectra collected by ASTRO-H in the form of broad fluorescent lines (other than Fe) as the ones showed in the right panel of Fig.2.9, which are produced by the atomic de-excitation of the bullet ions.

To conclude, the question whether our own Galactic Centre has been hosting an active nucleus in the last few hundreds years will find a definitive answer in the next few years. In the meantime, we contributed to clarify the physical constraints on this suggested activity, arising the doubt that, given the peculiarity of the GC environment, the real situation might be XRN and particle bombardment working in tandem. Future studies will also clarify this issue.

7.2 Fe-Kα line emission in the Arches cluster region: ongoing particle bombardment

In Chapter 5 we have used data from XMM-Newton to study the diffuse Fe-K$_\alpha$ fluorescent line emission emanating from the region surrounding the Arches Cluster. Our results can be summarized as follows:

- We detected four Fe-K$_\alpha$ bright MCs in the vicinity of the AC. Two of these are new detections (referred to herein as knots SN and DX).
- The Fe-K$_\alpha$ line flux measured from the three clouds nearest to the AC (knots N, S and SN) has remained constant over an interval of eight years. The EW of the 6.4-keV line in the spectra of these clouds is measured to be about 1 keV. This is consistent with the origin of the Fe fluorescence being the irradiation of the MCs by X-rays. The XRN/Sgr A* outburst scenario, which has been recently suggested as the explanation for all the Fe-K fluorescence seen in the GC region, in broad terms fits the observations, although with some reservations. Other X-ray sources, in particular nearby X-ray binaries and transients, might well have contributed to the 6.4 keV line production. Within the errors, the Fe-K$_\alpha$ line EWs are also compatible with the CR bombardment scenario, with the AC itself being a likely location of the requisite particle acceleration. In this context, the required particle kinetic energy density is roughly a hundred times higher than that previously estimated as a possible explanation of the hard X-ray Galactic Ridge emission, but such an enhancement might well arise from in situ acceleration of particles in the AC. The particle candidates are subrelativisitc electrons and/or protons.
- We have discovered variability on a timescale of a few years in the Fe-K$_\alpha$ line emission from the DX cloud. Because of the highly variable emission, this is unlikely to be the product of past high-state activity in Sgr A*. We propose an X-ray binary to be the energising source of this fluorescence. Moreover, on the top of the variability, this molecular complex shows a non-zero underlying level of the fluorescent line flux, suggesting the possibility that both the reflection and CR bombardment processes may be working in tandem. The variability seen in the DX cloud is the *fastest* yet recorded in the GC region and, to date, it is the only example of a MC exhibiting both an increase and subsequent decrease in its Fe fluorescent emission.

The fundamental importance of this study for the GC community is the awareness that not all 6.4-keV nebulosities in the GC are to be produced by Sgr A*; this study will also have a strong impact on the modelling of the 3D distribution of the molecular clouds in the CMZ. Moreover, the discovery of the XRN which displays the quickest Fe-K$_\alpha$ line variability so far detected broadens the phenomenology of the XRN phenomenon in the CMZ; in fact, to date this is only XRN in the GC region with a confirmed X-ray primary source of ionisation, which adds to the XRN produced by illumination from a past activity of Sgr A* and the ones where the Fe line is produced by particle bombardment.

The available data for the AC region does not allow the precise measurement of the spectral parameters relating to the Fe fluorescence phenomenon, namely the EW of the Fe-K$_\alpha$ line and the absorption edge at 7.1 keV. However, with deeper observations there is the prospect of fully characterising the emission spectrum and dispelling any ambiguity concerning the underlying excitation process. This would be an important further step in the on-going investigation of whether Sgr A* has exhibited AGN-like activity in the recent past.

7.3 Flaring activity within the Arches cluster

In the Chapter 6 of this thesis, we have also studied the X-ray properties of the Arches cluster, located at about 20 pc in projection from the SMBH Sgr A*. Although this was not the main topic of our doctoral studies, we have included in this thesis because of the importance of accounting for all the high energy processes which interplay with one another in this peculiar region. We have collected all the XMM-Newton data targeted at the Arches cluster and performed a study of its temporal and spectral properties in order to understand the origin of the intense X-ray emission generated within the cluster itself and characterise the nature of the flaring activity. Our results can be summarised as follows:

- *X-ray lightcurve:* we built the 7 years long term lightcurve stacking the data from observations taken within a few days, from which we discovered an unexpected high state of X-ray activity in the cluster (flare), with a 2-10 keV flux measured to be 2.4×10^{-12} erg cm^{-2} s^{-1}, about 70% higher than the normal state flux. The flare was detected with a statistical significance of about 4σ. The only noticeable difference between the spectra of the two states of the AC is the lack of non-thermal emission (and the associated Fe K? line at 6.4 keV) in the flare spectrum, suggesting a thermal stellar origin for this high state activity. The analysis of XMM-Newton data allowed us to place a lower limit to the duration of the flare of $\sim$4 days, with an emission measure of 1.2×10^{57} cm^{-3}, significantly higher than that usually detected in stellar flares.

- *Spectral properties of the cluster quiescence:* the enhanced X-ray luminosity of the Arches cluster, in the order of 10^{34} erg s^{-1}, is given by the high stellar concentration; in this configuration, thermal X-ray emission has been suggested to be due to multiple interactions between strong winds from massive stars. As a result, the 2-10 keV X-ray spectrum of the cluster in the quiescent state is well described by a thermal plasma with a temperature of 1.7±0.1 keV. In addiction to this thermal component, a non-thermal continuum is detected, with associated Fe-Kα line emission at 6.4 keV, which we suggested to be the signature of the particle bombardment ongoing in the surrounding molecular clouds. The flux associated with the non-thermal component is about 15% of the total 2-10 keV flux, a number which is in agreement with theoretical predictions which describe this emission in terms of upscattering of IR radiation from stars by energetic electrons: these particles are accelerated by shocks produced by strong colliding stellar winds.

- *Spectral properties of the flare:* the X-ray spectrum of the flare is well described by a thermal plasma with a temperature of 1.8±0.3 keV. The main difference between the spectra of the two states of the Arches cluster is the presence of the 6.4-keV line and the relative underlying non-thermal continuum; in the flare spectrum, this component is no longer required to properly fit the data.

- *Origin of the flare:* In the context of an enhanced coronal activity, the high value for the EM would result in a temperature higher than 10^8 K for the flare. This value is higher than what ever found in stellar flares, and therefore we consider the early-type star scenario to be more likely. The origin of the flaring activity must be attributed to a massive colliding wind binary, where the increase in the ux might be due to the collision of clumps within the winds and/or to an orbital modulation (are in periastron due to the 1/D dependance of the X-ray luminosity, with D distance between the stars) of the X-ray emission from supersonic colliding winds.

In the future it will be of great importance to characterise more precisely the temporal variability exhibited by massive star clusters such as the AC, both from the perspective of the underlying processes and in the context of the contribution of these events to the high-energy budget of the whole GC region; in fact, the fundamental importance of this discovery, besides the characterisation of the flaring mechanism itself, is the triggering of further studies on the connection between the Arches cluster and the other peculiar structure of the region, the giant radio arc, which could be performed in the near future connecting the sinergies of X-ray observatories and radio telescope and interferometers. More generally, the discovery of a time variability in the cluster could be the pathfinder that drives time variability studies of the radio filaments (within the radio arc and elsewhere) in order to understand the physical relation between these two structures, and more in general, of massive star formation regions, young clusters and highly shocked MCs with magnetic structures such as radio filaments and threads, which are only observed in the GC region. Moreover, an hypothetical discovery of a variable radio flux from the bright filaments in the GC region would once again open the question whether, at least in part, particle bombardment can also contribute to the variability of the Fe-Kα flux observed in the MCs all over the CMZ.

Appendix A

Dealing with the XMM-*Newton* non X-ray background

Within an XMM-Newton observation dataset, two main background components can be defined namely, particle-induced events and photon-induced events. Solar-flare particles and cosmic rays are responsible for the continuum element of the Non X-ray Background (NXB), as well as for the strong instrumental lines (Leccardi & Molendi, 2008). A further minor component within the particle-induced background is due to Quiescent Soft Protons (QSP). These are particles which enter the optics and are focused on the detector; they are mostly filtered during the GTI selection, but is likely that there is a low-level residual component in the screened event file. In the case of the photon background from the sky, the main components are the hard X-ray emission along the plane of the Galaxy (the Galactic Ridge emission) both in the foreground and extending beyond the GC, and also the extragalactic Cosmic X-ray Background (CXB). We did not take into account the Galactic Halo since its emission is negligible above 2.0 keV (Leccardi & Molendi, 2008). The difficulty of carrying out a systematic analysis with a careful characterization of the background is that the particle-induced background, which is the dominant component in the hard X-ray band, changes both spatially on the detector and in time throughout the duration of the mission. Given the focus of our investigation, there was a clear requirement that all the datasets should be analysed in a very systematic fashion. This led us to consider the advantages and disadvantages of the standard methods of dealing with the background in XMM-Newton observations.

Local Background subtraction: this procedure consists of selecting a region in the same image/dataset close to the source of interest; it is certainly the best choice for the analysis of a bright point source. The fact that we are dealing with extended sources, which are close to each other, forces us to select a region well separated from the position of the filaments under study; this may, potentially, produce a large discrepancy between the intensity of the instrumental lines in the source and in the background spectra, especially in the PN camera (Cu line at 8.05 keV), generating strong systematic errors which are difficult to deal with. As a further difficulty, the presence of the Galactic Ridge Emission throughtout the whole FOV prevents us from selecting a region for the background with a low surface brightness.

Blank Sky Fields: Blank sky files are constructed using a superposition of pointed observations of regions of the sky without contamination by bright sources (Carter & Read, 2007). They contain most of the background components listed above, like the particle induced NXB and the CXB. To study an extended source, we tried to cast the blank event file onto the sky at the position of our observations using the *skycast* script. In doing so, we are able to select the same detector region for the production of both the source and the background spectra. This method has the great advantage of completely avoiding the possibility of having different instrumental lines intensities, but the various components of the background can all vary in different ways over long time periods. So far, the blank sky files available are for observations done before revolution ≈1200, that is early 2007 (private communication, A. Read). We tested the public blank fields in our spectral analysis; while for revolutions earlier than 1200 the instrumental background subtraction was feasible, the spectra obtained with later data still show strong contamination, which is easily noticeable in the intense Cu K_α line at 8.05 keV in the PN camera. Since we are using XMM-Newton observations taken over a period of ≈10 years, the blank sky event files technique cannot be used for our purposes.

Background modeling: this technique requires a careful characterization of all the background components. The strong advantage of modelling the background rather than subtracting it, is that many of the systematics may thereby be avoided. De Luca & Molendi (2004) and Leccardi & Molendi (2008) studied in detail the properties of the particle-induced background for the MOS cameras, giving a spectral shape to both the continuum and the line emission. Modeling the background, instrumental and cosmic components we can, in principle, account for all the photons collected by the instrumentation and make every photon count.

On the basis of the above, we decided to follow the background modelling technique for the temporal studies of the 6.4-keV line from the molecular clouds in the GC region. With this choice we could not consider the EPIC-PN data for the seeking of Fe-Kα variability, but worked only with MOS cameras. Up to the present, a self-consistent and exhaustive characterization of the background for EPIC-PN camera has not been developed, mainly because the fraction of out-of-time events in the PN CCDs is not negligible and the Out FOV region is much smaller compared to the one in the MOS detectors. Moreover, MOS cameras are better suited to the study of extended sources because of the lower level of the instrumental background (which is most likely a consequence of the different CCD structure).

Bibliography

Abbey, T., Carpenter, J., Read, A., et al. 2006, in ESA Special Publication, Vol. 604, The X-ray Universe 2005, ed. A. Wilson, 943–+

Aharonian, F., Akhperjanian, A. G., Bazer-Bachi, A. R., et al. 2006,Nature, 439, 695

Amo-Baladrón, M. A., Martín-Pintado, J., Morris, M. R.,Muno, M. P., & Rodríguez-Fernández, N. J. 2009, ApJ, 694,943

Aschwanden, M. J.,Stern, R. A., G&uumldel, M. 2008, ApJ, 672, 659

Auger P., Sur les rayons secondaires produits dans un gaz par des rayons X, C.R.A.S. 177 (1923) 169-171.

Baganoff, F. K., et al. 2001, Nature, 413, 45

Baganoff, F. K., et al. 2003, ApJ, 591, 891

Balick, B., & Brown, R. L. 1974, ApJ, 194, 265

Bambynek, W., Crasemann, B., Fink, R. W., Freund, H.-U., Mark, H., Swift, C. D., Price, R. E., & Rao, P. V. 1972, Reviews of Modern Physics, 44, 716

Becklin, E. E., & Neugebauer, G. 1975, ApJ, 200, L71

Bertoldi, F., & McKee, C. F. 1992, ApJ, 395, 140

Binney, J., Gerhard, O. E., Stark, A. A., Bally, J., & Uchida, K. I. 1991, MNRAS, 252, 210

Black, J. H. 1987, Interstellar Processes, 134, 731

Boehringer, H., & Werner, N. 2009, arXiv:0907.4277

Bower, G. C., Wright, M. C. H., Backer, D. C., & Falcke, H. 1999, ApJ, 527, 851

Bykov, A. M. 2002, A&A, 390, 327

Burton, W. B., Gordon, M. A., Bania, T. M., & Lockman, F. J. 1975, ApJ, 202, 30

Cantó, J., Raga, A. C., & Rodríguez, L. F. 2000, ApJ, 536, 896

Capelli, R., Warwick, R. S., Cappelluti, N., et al. 2011a, A&A, 525, L2+

Capelli, R., Warwick, R. S., Porquet, D., Gillessen, S., & Predehl, P. 2011b, A&A, 530, A38+

Carruthers, G. R. 1970, ApJ, 161, L81

Carter, J. A. & Read, A. M. 2007, A&A, 464, 1155

Cash, W. 1979, ApJ, 228, 939

Condon J.J. & Ransom S.M., National Radio Astronomy Observatory 2010, Radio astronomy course

Cotera, A. S., Erickson, E. F., Colgan, S. W. J., Simpson, J. P., Allen, D. A., & Burton, M. G. 1996, ApJ, 461, 750

Crocker, R. M., Jones, D., Protheroe, R. J., Ott, J., Ekers, R., Melia, F., Stanev, T., & Green, A. 2007, ApJ, 666, 934

Cronin, J. W. 1999, Reviews of Modern Physics Supplement, 71, 165

Cuadra, J., Nayakshin, S., Springel, V., & Di Matteo, T. 2006, MNRAS, 366, 358

Dalgarno, A., Yan, M., & Liu, W. 1999, ApJS, 125, 237

Dame, T. M., Elmegreen, B. G., Cohen, R. S., & Thaddeus, P. 1986, ApJ, 305, 892

Degenaar, N., & Wijnands, R. 2010, A&A, 524, A69

De Luca, A. & Molendi, S. 2004, A&A, 419, 837

Diplas, A., & Savage, B. D. 1991, ApJ, 377, 126

Dodds-Eden, K., Sharma, P., Quataert, E., Genzel, R., Gillessen, S., Eisenhauer, F., & Porquet, D. 2010, ApJ, 725, 450

Doeleman, S. S., et al. 2008, Nature, 455, 78

Dogiel, V. A., Ichimura, A., Inoue, H., & Masai, K. 1998, PASJ, 50, 567

Dogiel, V., et al. 2009, PASJ, 61, 901

Dogiel, V. A., et al. 2009, PASJ, 61, 1099

Donley, J. L., Brandt, W. N., Eracleous, M., & Boller, T. 2002, AJ, 124, 1308

Draine, B. T. 2003, ARA&A, 41, 241

Draine, B. T. 2011, Physics of the Interstellar and Intergalactic Medium by Bruce T. Draine. Princeton University Press, 2011. ISBN: 978-0-691-12214-4,

Dubner, G., Giacani, E., Reynoso, E., & Parón, S. 2004, A&A, 426, 201

Eckart, A., et al. 2006, A&A, 450, 535

Eidelman, S., 2004, & PDG collaboration, Physics Letters B592

Eisenhauer, F., Schödel, R., Genzel, R., Ott, T., Tecza, M., Abuter, R., Eckart, A., & Alexander, T. 2003, ApJ, 597, L121

Eisenhauer, F., et al. 2005, ApJ, 628, 246

Elmegreen, B. G., & Falgarone, E. 1996, ApJ, 471, 816

Ewen, H. I., & Purcell, E. M. 1951, Nature, 168, 356

Fabian, A. C., Rees, M. J., Stella, L., & White, N. E. 1989, MNRAS, 238, 729

Ferrière, K. M. 2001, Reviews of Modern Physics, 73, 1031

Figer, D. F. 2004, The Formation and Evolution of Massive Young Star Clusters, 322, 49

Fryer, C. L., Rockefeller, G., Hungerford, A., & Melia, F. 2006, ApJ, 638, 786

Fukuoka, R., Koyama, K., Ryu, S. G., & Tsuru, T. G. 2009, PASJ, 61, 593

Gaetz, T. J., & Salpeter, E. E. 1983, ApJS, 52, 155

Gaisser, T. K. 2005, Neutrinos and Explosive Events in the Universe, 3

Gaisser, T. K. 2010, arXiv:1010.5996

Garcia, J. D., Fortner, R. J., & Kavanagh, T. M. 1973, Reviews of Modern Physics, 45, 111

Gebhardt, K., et al. 2000, ApJ, 539, L13

Genzel, R., Thatte, N., Krabbe, A., Kroker, H., & Tacconi-Garman, L. E. 1996, ApJ, 472, 153

Genzel, R., Eckart, A., Ott, T., & Eisenhauer, F. 1997, MNRAS, 291, 219

Genzel, R., Eisenhauer, F., & Gillessen, S. 2010, Reviews of Modern Physics, 82, 3121

George, I. M., & Fabian, A. C. 1991, MNRAS, 249, 352

Ghez, A. M., Klein, B. L., Morris, M., & Becklin, E. E. 1998, ApJ, 509, 678

Ghez, A. M., et al. 2003, ApJ, 586, L127

Ghez, A. M., Salim, S., Hornstein, S. D., Tanner, A., Lu, J. R., Morris, M., Becklin, E. E., & Duchêne, G. 2005, ApJ, 620, 744

Ghez, A. M., Salim, S., Weinberg, N. N., et al. 2008, ApJ, 689, 1044

Gillessen, S., Eisenhauer, F., Trippe, S., et al. 2009, ApJ, 692, 1075

Gilli, R., Comastri, A., & Hasinger, G. 2007, A&A, 463, 79

Goldsmith, P. F. 1987, Interstellar Processes, 134, 51

Goldsmith, P. F., & Langer, W. D. 1978, ApJ, 222, 881

Goldwurm, A. 2006, Journal of Physics Conference Series, 54, 86

Greisen, K. 1966, Physical Review Letters, 16, 748

Güdel, M. 2004, A&A Rev., 12, 71

Güdel, M., & Nazé, Y. 2009, A&A Rev., 17, 309

Güsten, R., & Philipp, S. D. 2004, The Dense Interstellar Medium in Galaxies, 253

Habart, E., Walmsley, M., Verstraete, L., et al. 2005, Space Sci. Rev., 119, 71

Handa, T., Sakano, M., Naito, S., Hiramatsu, M., & Tsuboi, M. 2006, ApJ, 636, 261

Hayakawa, S. 1969, Interscience Monographs and Texts in Physics and Astronomy, New York: Wiley-Interscience, 1969,

Hickox, R. C., & Markevitch, M. 2007, ApJ, 671, 1523

Hillas, A. M. 1984, ARA&A, 22, 425

Huettemeister, S., Wilson, T. L., Bania, T. M., & Martin-Pintado, J. 1993, A&A, 280, 255

Inui, T., Koyama, K., Matsumoto, H., & Tsuru, T. G. 2009, PASJ, 61, 241

Kaneda, H., Makishima, K., Yamauchi, S., Koyama, K., Matsuzaki, K., & Yamasaki, N. Y. 1997, ApJ, 491, 638

Kikoin, I. K., Kikoin, L. I., & Lasarev, S. D. 1976, Physics Letters A, 59, 47

Kim, S.-H., Martin, P. G., & Hendry, P. D. 1994, ApJ, 422, 164

Koyama, K., Murakami, H., & Takagi, S. 2003, Astronomische Nachrichten Supplement, 324, 117

Koyama, K., Maeda, Y., Sonobe, T., et al. 1996, PASJ, 48, 249

Koyama, K., Hyodo, Y., & Inui, T. 2006, Journal of Physics Conference Series, 54, 95

Koyama, K., Hyodo, Y., Inui, T., et al. 2007a, PASJ, 59, 245

Koyama, K., Inui, T., Hyodo, Y., et al. 2007b, PASJ, 59, 221

Koyama, K., Takikawa, Y., Hyodo, Y., et al. 2009, PASJ, 61, 255

Lang, C. C., Goss, W. M., & Rodríguez, L. F. 2001, ApJ, 551, L143

LaRosa, T. N., Kassim, N. E., Lazio, T. J. W., & Hyman, S. D. 2000, AJ, 119, 207

Larson, R. B. 1981, MNRAS, 194, 809

Launhardt, R., Zylka, R., & Mezger, P. G. 2002, A&A, 384, 112

Law, C., & Yusef-Zadeh, F. 2004, ApJ, 611, 858

Leccardi, A. & Molendi, S. 2008, A&A, 486, 359

Maeda, Y., et al. 2002, ApJ, 570, 671

Markoff, S., Falcke, H., Yuan, F., & Biermann, P. L. 2001, A&A, 379, L13

Martín-Pintado, J., de Vicente, P., Rodríguez-Fernández, N. J., Fuente, A., & Planesas, P. 2000, A&A, 356, L5

Martín-Pintado, J., Rizzo, J. R., de Vicente, P., Rodríguez-Fernández, N. J., & Fuente, A. 2001, ApJ, 548, L65

Mathis, J. S., Rumpl, W., & Nordsieck, K. H. 1977, ApJ, 217, 425

Mauerhan, J. C., Muno, M. P., Morris, M. R., Stolovy, S. R., & Cotera, A. 2010, ApJ, 710, 706

Miyazaki, A., & Tsuboi, M. 2000, ApJ, 536, 357

Moffat, A. F. J., & Corcoran, M. F. 2009, ApJ, 707, 693

Morita, S., & Fujita, J. 1983, Journal of the Physical Society of Japan, 52, 1957

Morris, M., & Serabyn, E. 1996, ARA&A, 34, 645

Morrison, R. & McCammon, D. 1983, ApJ, 270, 119

Muno, M. P., et al. 2004, ApJ, 613, 326

Muno, M. P., Pfahl, E., Baganoff, F. K., et al. 2005, ApJ, 622, L113

Muno, M. P., Bauer, F. E., Bandyopadhyay, R. M., & Wang, Q. D. 2006, ApJS, 165, 173

Muno, M. P., Baganoff, F. K., Brandt, W. N., Park, S., & Morris, M. R. 2007, ApJ, 656, L69

Muno, M. P., Baganoff, F. K., Brandt, W. N., Morris, M. R., & Starck, J. 2008, ApJ, 673, 251

Murakami, H., Koyama, K., Sakano, M., Tsujimoto, M., & Maeda, Y. 2000, ApJ, 534, 283

Murakami, H., Koyama, K., Tsujimoto, M., Maeda, Y., & Sakano, M. 2001, ApJ, 550, 297

Nagano, M., & Watson, A. A. 2000, Reviews of Modern Physics, 72, 689

Nagata, T., Woodward, C. E., Shure, M., & Kobayashi, N. 1995, AJ, 109, 1676

Nakajima, H., Tsuru, T. G., Nobukawa, M., et al. 2009, PASJ, 61, 233

Nandra, K., George, I. M., Mushotzky, R. F., Turner, T. J., & Yaqoob, T. 1997, ApJ, 477, 602

Narayan, R., Quataert, E., Igumenshchev, I. V., & Abramowicz, M. A. 2002, ApJ, 577, 295

Nobukawa, M., Koyama, K., Tsuru, T. G., Ryu, S. G., & Tatischeff, V. 2010, PASJ, 62, 423

Nord, M. E., Lazio, T. J. W., Kassim, N. E., et al. 2004, AJ, 128, 1646

Oka, T., Hasegawa, T., Sato, F., Tsuboi, M., & Miyazaki, A. 1998, ApJS, 118, 455

Oka, T., Hasegawa, T., Hayashi, M., Handa, T., & Sakamoto, S. 1998, ApJ, 493, 730

Oka, T., Hasegawa, T., Sato, F., et al. 2001, ApJ, 562, 348

Oka, T., Geballe, T. R., Goto, M., Usuda, T., & McCall, B. J. 2005, ApJ, 632, 882

Oka, T., Nagai, M., Kamegai, K., Tanaka, K., & Kuboi, N. 2007, PASJ, 59, 15

Oka, T., Tanaka, K., Matsumura, S., et al. 2010, ArXiv e-prints

Osterbrock, D. E., & Ferland, G. J. 2006, Astrophysics of gaseous nebulae and active galactic nuclei, 2nd. ed. by D.E. Osterbrock and G.J. Ferland. Sausalito, CA: University Science Books, 2006,

Park, S., Muno, M. P., Baganoff, F. K., Maeda, Y., Morris, M., Howard, C., Bautz, M. W., & Garmire, G. P. 2004, ApJ, 603, 548

Peters, B. 1960, Moscow Cosmic Ray Conference, Volume III, 157

Phiwe series of Publication, Laboratory Experiments, Physical structure of matter

Pierce-Price, D., et al. 2000, ApJ, 545, L121

Pogge R.W., the Ohio State University, Course in the Physics of the Insterstellar medium (http://www.astronomy.ohio-state.edu/ pogge/Ast871/)

Ponti, G., Terrier, R., Goldwurm, A., Belanger, G., & Trap, G. 2010, ApJ, 714, 732

Porquet, D., Predehl, P., Aschenbach, B., et al. 2003, A&A, 407, L17

Porquet, D., Grosso, N., Bélanger, G., et al. 2005a, A&A, 443, 571

Porquet, D., Grosso, N., Burwitz, V., et al. 2005b, A&A, 430, L9

Porquet, D., et al. 2008, A&A, 488, 549

Predehl, P., & Schmitt, J. H. M. M. 1995, A&A, 293, 889

Predehl, P., Costantini, E., Hasinger, G., & Tanaka, Y. 2003, Astronomische Nachrichten, 324, 73

Eisberg, R., & Resnick, R. 1985, Quantum Physics of Atoms, Molecules, Solids, Nuclei, and Particles, 2nd Edition, by Robert Eisberg, Robert Resnick, pp. 864. ISBN 0-471-87373-X. Wiley-VCH , January 1985.,

Quarles, C. A. 1976, Phys. Rev. A, 13, 1278

Quataert, E. 2003, Astronomische Nachrichten Supplement, 324, 435

Raga, A. C., Velázquez, P. F., Cantó, J., Masciadri, E., & Rodríguez, L. F. 2001, ApJ, 559, L33

Ramaty, R., Kozlovsky, B., & Lingenfelter, R. E. 1996, ApJ, 456, 525

Reid, M. J. 1993, ARA&A, 31, 345

Revnivtsev, M. G., Churazov, E. M., Sazonov, S. Y., et al. 2004, A&A, 425, L49

Revnivtsev, M., Sazonov, S., Gilfanov, M., Churazov, E., & Sunyaev, R. 2006, A&A, 452, 169

Revnivtsev, M., Vikhlinin, A., & Sazonov, S. 2007, A&A, 473, 857

Revnivtsev, M., Sazonov, S., Churazov, E., Forman, W., Vikhlinin, A., & Sunyaev, R. 2009, Nature, 458, 1142

Rybicki, G. B., & Lightman, A. P. 1979, New York, Wiley-Interscience, 1979. 393 p.,

Robson Greg, Creative Commonns License

Rodríguez-Fernández, N. J., Martín-Pintado, J., Fuente, A., de Vicente, P., Wilson, T. L., Hüttemeister, S. 2001, A&A, 365, 174

Rodríguez-Fernández, N. J., Martín-Pintado, J., Fuente, A., & Wilson, T. L. 2004, A&A, 427, 217

Rodríguez-Fernández, N. J., & Martín-Pintado, J. 2005, A&A, 429, 923

Rodríguez-Fernández, N. J. 2006, Journal of Physics Conference Series, 54, 35

Ryu, S. G., Koyama, K., Nobukawa, M., Fukuoka, R., & Tsuru, T. G. 2009, PASJ, 61, 751

Sakano, M., Warwick, R. S., Decourchelle, A., & Predehl, P. 2004, MNRAS, 350, 129

Sakano, M., Warwick, R. S., & Decourchelle, A. 2006, Journal of Physics Conference Series, 54, 133

Schödel, R., Ott, T., Genzel, R., et al. 2002, Nature, 419, 694

Scoville, N. Z., & Solomon, P. M. 1975, ApJ, 199, L105

Shull, J. M., & van Steenberg, M. E. 1985, ApJ, 294, 599

Sidoli, L., Mereghetti, S., Treves, A., Parmar, A. N., Turolla, R., & Favata, F. 2001, A&A, 372, 651

Sidoli, L., Paizis, A., & Mereghetti, S. 2006, A&A, 450, L9

Simpson, J. A. 1983, Annual Review of Nuclear and Particle Science, 33, 323

Smith, A. M., & Stecher, T. P. 1971, ApJ, 164, L43

Smith, R. K., Brickhouse, N. S., Liedahl, D. A., & Raymond, J. C. 2001, ApJ, 556, L91

Snow, T. P., & McCall, B. J. 2006, ARA&A, 44, 367

Snowden, S. L., et al. 1997, ApJ, 485, 125

Snowden, S. L., Collier, M. R., & Kuntz, K. D. 2004, ApJ, 610, 1182

Spitzer, L., Jr. 1956, ApJ, 124, 20

Spitzer, L. 1978, New York Wiley-Interscience, 1978. 333 p.,

Stevens, I. R., & Hartwell, J. M. 2003, MNRAS, 339, 280

Strömgren, B. 1939, ApJ, 89, 526

Strong, A. W., Moskalenko, I. V., & Ptuskin, V. S. 2007, Annual Review of Nuclear and Particle Science, 57, 285

Strüder, L., Briel, U., Dennerl, K., et al. 2001, A&A, 365, L18

Su, M., Slatyer, T. R., & Finkbeiner, D. P. 2010, ApJ, 724, 1044

Sunyaev, R. A., Markevitch, M., & Pavlinsky, M. 1993, ApJ, 407, 606

Sunyaev, R. & Churazov, E. 1998, MNRAS, 297, 1279

Tanaka, Y. 2002, A&A, 382, 1052

Tatischeff, V., Ramaty, R., & Kozlovsky, B. 1998, ApJ, 504, 874

Tatischeff, V. 2003, in EAS Publications Series, Vol. 7, EAS Publications Series, ed. C. Motch & J.-M. Hameury, 79–+

Tatischeff, V. Cosmic Ray Interactions: Bridging High and Low Energy Astrophysics. Nonthermal X-rays from low energy cosmic rays: Application to the 6.4 keV line emission from the Arches cluster.

Terrier, R., Ponti, G., Bélanger, G., et al. 2010, ApJ, 719, 143

Townsley, L. K., Feigelson, E. D., Montmerle, T., Broos, P. S., Chu, Y.-H., & Garmire, G. P. 2003, ApJ, 593, 874

Tsuboi, M., Handa, T., & Ukita, N. 1999, ApJS, 120, 1

Tsuboi, M., Ukita, N., & Handa, T. 1997, ApJ, 481, 263

Tsujimoto, M., Hyodo, Y., & Koyama, K. 2007, PASJ, 59, 229

Turner, M. J. L., Abbey, A., Arnaud, M., et al. 2001, A&A, 365, L27

Uchiyama, Y., & Aharonian, F. A. 2008, ApJ, 677, L105

Valinia, A., Tatischeff, V., Arnaud, K., Ebisawa, K., & Ramaty, R. 2000, ApJ, 543, 733

van Dishoeck, E. F., & Black, J. H. 1986, ApJS, 62, 109

Wang, Q. D., Dong, H., & Lang, C. 2006, MNRAS, 371, 38

Warwick, R., Sakano, M., & Decourchelle, A. 2006, Journal of Physics Conference Series, 54, 103

Webber, W. R. 1998, ApJ, 506, 329

White, R. L. 1985, ApJ, 289, 698

White, G. J., et al. 1999, A&A, 342, 233

Wilms, J., Allen, A., & McCray, R. 2000, ApJ, 542, 914

Wollman, E. R., Geballe, T. R., Lacy, J. H., Townes, C. H., & Rank, D. M. 1977, ApJ, 218, L103

X-ray data booklet, 2009, Center for X-ray Optics and Advanced Light Source.

Yamauchi, S., Kawada, M., Koyama, K., Kunieda, H., & Tawara, Y. 1990, ApJ, 365, 532

Yamauchi, S., Ebisawa, K., Tanaka, Y., Koyama, K., Matsumoto, H., Yamasaki, N. Y., Takahashi, H., & Ezoe, Y. 2009, PASJ, 61, 225

Yusef-Zadeh, F., Purcell, W., & Gotthelf, E. 1997, in American Institute of Physics Conference Series, Vol. 410, Proceedings of the Fourth Compton Symposium, ed. C. D. Dermer, M. S. Strickman, & J. D. Kurfess, 1027–1033

Yusef-Zadeh, F., Law, C., Wardle, M., Wang, Q. D., Fruscione, A., Lang, C. C., & Cotera, A. 2002, ApJ, 570, 665

Yusef-Zadeh, F., Law, C., & Wardle, M. 2002, ApJ, 568, L121

Yusef-Zadeh, F., Nord, M., Wardle, M., Law, C., Lang, C., & Lazio, T. J. W. 2003, ApJ, 590, L103

Yusef-Zadeh, F. 2003, ApJ, 598, 325

Yusef-Zadeh, F., Muno, M., Wardle, M., & Lis, D. C. 2007a, ApJ, 656, 847

Yusef-Zadeh, F., Wardle, M., & Roy, S. 2007b, ApJ, 665, L123

Zatsepin, G. T., & Kuz'min, V. A. 1966, Soviet Journal of Experimental and Theoretical Physics Letters, 4, 78

Acknowledgements

During the three years of my Ph.D. studies I met many people that, in different ways, helped me in getting through this important step of my education. There is no doubt I have and I want to reserve the first place to whom first made all this possible; thank you Peter, for being the best supervisor I could have had. I still do not know how you offered to supervise me, but I am really grateful you did and it was an honour and a pleasure to work with you. Thank you for giving me the opportunity to work on one of the most exciting topics in modern astronomy, for being at the same time a strict boss and a friendly ear, for giving me the freedom to propose research directions, for making me feel capable and transmitting me the passion for our work. In particular I have to thank you very much for having trained me as you have: if there is one single thing I should highlight as having developed during my graduate studies is the skill to work independently. I do realise that this is not common, and I think it is a unique and valuable characteristic I am extremely grateful to have achieved. This is not only important in astronomy or work in general, it is a training for life that you did with me, and I am grateful to you for this!

The second person I would like to thank is Prof. Bob Warwick from the University of Leicester (UK). In the two years we have known each other we have never met, but you have always been a unique and invaluable source of support for the achievements of my scientific goals; thank you for the patience you had to reply to all the emails, although most of them might have seemed naive and foolish. I think that not many people in your position would have spent so much time to help on a student's project; I really appreciate that. Thank you for always trying to get the best from our work, to care about it as much as I do, not aiming to please but always aiming at the top. If I will achieve my doctoral degree, a significant part of the merit is also yours!

A special thank you also to Prof. Werner Becker, from the MPE/LMU. Thank you for having accepted me as an IMPRS student and allowed me to carry out my Ph.D. in one of the most stimulating working environments in the world. Thank you also for the support and the precious advice you gave me in these three years of work at MPE. I would also like to thank Dr. Delphine Porquet from the Strasbourg Observatory (France). Thank you for your presence and kindness in all the work we have developed together; thank you for believing so much in me and my work. I would have really liked to work with you for the beginning of my scientific postdoc career, but fate decided otherwise. I hope we can still collaborate in the future, to exchange projects and ideas as we have done in the last two years.

Thank you also to Dr. Stefan Gillessen, for the precious advice you gave me during the years I have been working at MPE. Your experience and love for Astronomy helped me in increasing the quality of my work, and this allowed me to be able to publish my work in international journals. I am also grateful to Prof. Yasuo Tanaka from MPE, for the many discussions we had during the last two years, for teaching me how to look at the smallest details, and to support me in the search for a further position in X-ray astronomy.

Although we did not develop my doctoral work together, I am also beholden to Dr. Lara Sidoli, who first believed in my capacities and skills to carry out a Ph.D in X-ray astronomy. Your support and your friendly ear has never been missing in the last three years either, and I really appreciate this too! You are a fixed point in my education, on which I feel I can always rely on!

I cannot miss a special thank you to a colleague that is more than a friend; we have studied together for four years at the University in Milano, and then spent three years as Ph.D. students in the same group at MPE. Thank you Dado, for all the chats and laughs we had; I think that our discussions about the radiative processes will never end ("how many photons does the bremmstrahlung emit?"). You have been a friendly arm I could "lean on".

I am very grateful to all the friends I had the chance to know in Munich; first of all my office mate Gregor, the bavarian Gregor from Marktoberdorf that, he says, is the most beautiful city in the world (I actually never heard about it before). Thank you for sharing with me the happiness and the sadness of the Ph.D. student life; I am only sorry that, because of all our Ph.D. duties, we could not continue the relaxing and amusing habit of playing ping-pong half an hour per day at the institute for all the three years; of course with me winning 21-19. And then the other friends: Behrang and Ati, the first Iranian people I have known and amongst the best friends I had during the three years of my life in Garching; the two Lucas, Graziani and Ricci, for the pleasure of the many chats we had and the many laughs we had about everything, that helped the time to be more enjoyable. And to David Gruber, for all the help he gave me with IDL programming and the shared coffees.

A very special thanks goes to my dear Katie, for sharing with me the most beautiful moments of these years; for sharing with me dreams and delusions. Also during the darkest periods, you encouraged me to not give up with anything and anyone. Thanks for showing me some other aspects, probably the most important, of life, which I did not care very much about before; I have learnt from you to be a better man, in all the moments of my day.

To move abroad and live far away from family and homeland is not easy for anyone; it has not been easy for me either, especially at the beginning. Among all my relatives, I want to first thank my grandma Olga; I will always remember what you said when I first told you I was moving to Germany: "You are made like this, I knew it. You do not miss the smoke of the chimney. I will miss you so much, but I am very happy you are going and I will be with you all the time". All the tears you had every time I came to visit you and afterwards left in these three years are the energy that drives me to always do the best I can, for being a man. They remind me of my roots, which I am very proud of. Thank you

also to my grandparents Mario and Gianina, for the infinite number of calls they gave me in three years in Munich and Garching. I really appreciated these, they made me feel less far from my affections.

I love my sisters and I missed them very much. I am sorry I could not be present to some of the important moments of your life: Eleonora's graduation, Alice's driving license. As an older brother, I always tried to be close to you with my thoughts, and hope I did it well and you appreciated it! I enjoyed very much the early and late calls on skype with both of you, talking about your studies and your experiences, to tease our parents or to prepare for a physics test at school.

I left them at the end on purpose, because I know they would say ”And us?!”. I feel a sense of profound gratitude for my parents, Gisella and Andrea; I know I owe you guys everything I have achieved in these 28 years. You have always supported me in everything I wished, a moral and practical support to every endeavour I wanted to attempt. You always encourage me to get to the best, to aim for the top in order to achieve my wills and dreams. Do you remember when I wanted to become an astronaut? Well, I did not get yet there, and probably I will never do, but this is kind of similar (on more ”earthly” scales). I feel privileged to have you as parents, and I think the education you gave me will always be the most important of my human and cultural heritage.